

Winter 2018

# Development of a Laser-Spark Multicharged Ion System – Application in Shallow Implantation of Sic by Boron and Barium

Md. Haider Ali Shaim  
*Old Dominion University*

Follow this and additional works at: [https://digitalcommons.odu.edu/ece\\_etds](https://digitalcommons.odu.edu/ece_etds)

 Part of the [Electrical and Computer Engineering Commons](#), and the [Physics Commons](#)

---

## Recommended Citation

Shaim, Md. H.. "Development of a Laser-Spark Multicharged Ion System – Application in Shallow Implantation of Sic by Boron and Barium" (2018). Doctor of Philosophy (PhD), dissertation, Electrical/Computer Engineering, Old Dominion University, DOI: 10.25777/kh2s-5r68  
[https://digitalcommons.odu.edu/ece\\_etds/42](https://digitalcommons.odu.edu/ece_etds/42)

This Dissertation is brought to you for free and open access by the Electrical & Computer Engineering at ODU Digital Commons. It has been accepted for inclusion in Electrical & Computer Engineering Theses & Dissertations by an authorized administrator of ODU Digital Commons. For more information, please contact [digitalcommons@odu.edu](mailto:digitalcommons@odu.edu).

**DEVELOPMENT OF A LASER-SPARK MULTICHARGED ION SYSTEM**  
**– APPLICATION IN SHALLOW IMPLANTATION OF SIC BY BORON**  
**AND BARIUM**

by

Md. Haider Ali Shaim  
MS, Applied Physics, July 2008, University of Chittagong  
B.Sc. Applied Physics, December 2006, University of Chittagong

A Dissertation Submitted to the Faculty of  
Old Dominion University in Partial Fulfillment of the  
Requirements for the Degree of

**DOCTOR OF PHILOSOPHY**

**ELECTRICAL AND COMPUTER ENGINEERING**

**OLD DOMINION UNIVERSITY**  
**DECEMBER 2018**

Approved by

Hani E. Elsayed-Ali (Director)

Helmut Baumgart (Member)

Gon Namkoong (Member)

Leposava Vuskovic (Member)

## ABSTRACT

### DEVELOPMENT OF A LASER-SPARK MULTICHARGED ION SYSTEM – APPLICATION IN SHALLOW IMPLANTATION OF SIC BY BORON AND BARIUM

Md. Haider Ali Shaim  
Old Dominion University, 2018  
Director: Dr. Hani E. Elsayed-Ali

A novel multicharged ion source, using laser ablation induced plasma coupled with spark discharge, has been investigated in this work. The designed and demonstrated ion source is cost-effective, compact and versatile. Experiments are described with the intention of demonstrating the practicability of ion implantation via laser ion source.

Multicharged aluminum ions are generated by a ns Q-switched Nd:YAG laser pulse ablation of an aluminum target in an ultrahigh vacuum. The experiments are conducted using laser pulse energies of 45–90 mJ focused on the Al target surface by a lens with an 80-cm focal length to 0.0024 cm<sup>2</sup> spot area and incident at 45° with the Al target surface. With the increase in the laser pulse energy, a slow increase in the number of ions generated is observed. The generation of ions with a higher charge state is also observed with the increase in the laser pulse energy. For 5 kV accelerating voltage applied to the Al target and using laser energy of 90 mJ, up to Al<sup>4+</sup> charge is delivered to the detector which is located 140 cm away from the Al target. Raising accelerating voltage increases the charge extraction from the laser plasma and the energy of multicharged ions.

The components of a transport line for a laser multicharged ion source are described. Aluminum and carbon multicharged ions are generated by a Q-switched, nanosecond Nd:YAG laser (wavelength  $\lambda = 1064$  nm, pulse width  $\tau = 7.4$  ns, and pulse energy up to 82 mJ) ablation of a target in a vacuum chamber. Time-of-flight and three-grid retarding ion energy analyzers are used to determine the velocity and the charge state of the ions. A three-electrode cylindrical einzel lens is used to focus the ions. At 30 cm from the center of the focusing electrode of the einzel lens, Al<sup>1+</sup> and Al<sup>2+</sup> have a minimum beam diameter of ~1.5 mm, while for Al<sup>3+</sup> and Al<sup>4+</sup> the minimum beam diameter is ~2.5 mm. The simulation of the ion trajectories is done using SIMION 8.1. A high voltage pulse applied to a set of two parallel deflecting plates is used

for the pickup of ions with different charge states according to their time-of-flight. An electrostatic cylindrical ion deflector is used for analysis and selection of charges with specific energy-to-charge ratio. The design of these transport line components and their operation are described.

A spark discharge is coupled to a laser multicharged ion source to enhance ion generation. The laser plasma triggers a spark discharge with electrodes located in front of the ablated target. For an aluminum target, the spark discharge results in significant enhancement in the generation of multicharged ions along with higher charge states than observed with the laser source alone. When a Nd:YAG laser pulse (wavelength 1064 nm, pulse width 7.4 ns, pulse energy 72 mJ, laser spot area on target  $0.0024 \text{ cm}^2$ ) is used, the total multicharged ions detected by a Faraday cup is 1.0 nC with charge state up to  $\text{Al}^{3+}$ . When the spark amplification stage is used (0.1  $\mu\text{F}$  capacitor charged to 5.0 kV), the total charge measured increases by a factor of  $\sim 9$  with up to  $\text{Al}^{6+}$  charge observed. Using laser pulse energy of 45 mJ, charge amplification by a factor of  $\sim 13$  was observed for a capacitor voltage of 4.5 kV. The spark discharge increases the multicharged ion generation without increasing target ablation, which solely results from the laser pulse. This allows for increased multicharged ion generation with relatively low laser energy pulses and less damage to the surface of the target.

Laser plasma generated by ablation of an Al target in vacuum is characterized by ion time-of-flight combined with optical emission spectroscopy. A Q-switched Nd:YAG laser (wavelength  $\lambda = 1064 \text{ nm}$ , pulse width  $\tau \sim 7 \text{ ns}$ , and fluence  $F \leq 38 \text{ J/cm}^2$ ) is used to ablate the Al target. Ions are accelerated according to their charge state by the double-layer potential developed at the plasma-vacuum interface. The ion energy distribution follows a shifted Coulomb-Boltzmann distribution. Optical emission spectroscopy of the Al plasma gives significantly lower plasma temperature than the ion temperature obtained from the ion time-of-flight, due to the difference in the temporal and spatial regions of the plasma plume probed by the two methods. Applying an external electric field in the plasma expansion region in a direction parallel to the plume expansion increases the line emission intensity. However, the plasma temperature and density, as measured by optical emission spectroscopy, remain unchanged.

Aluminum multicharged ion generation from femtosecond laser ablation is studied. A Ti:sapphire laser (wavelength 800 nm, pulse width  $\sim 100$  fs, and maximum laser fluence of  $7.6 \text{ J/cm}^2$ ) is used. Ion yield and energy distribution of each charge state are measured. A linear relationship between the ion charge state and the equivalent acceleration energy of the individual ion species is observed and is attributed to the presence of an electric field within the plasma-vacuum boundary that accelerates the ions. The ion energy distribution follows a shifted Coulomb-Boltzmann distribution. For  $\text{Al}^{1+}$  and  $\text{Al}^{2+}$ , the ion energy distributions have two components; the faster one can be attributed to multiphoton laser ionization, while the slower one is possibly due to collisional processes. Ion extraction from the plasma is increased with an applied external electric field, which is interpreted to be due to the retrograde motion of the plasma edge because of the external electric field. Multicharged ion generation by femtosecond laser ablation is compared to previously reported ion generation with nanosecond laser ablation and is shown to require significantly lower laser fluence and generates higher charge states and more energetic ions.

Fully-stripped boron ions are generated by a nanosecond Nd:YAG laser (wavelength  $\lambda = 1064$  nm, pulse width  $\tau = 7$  ns, and maximum laser pulse energy  $E = 175$  mJ) ablation of a B target in vacuum. Higher charge states, along with the increase in the number of ions detected, are observed with the increase in the laser fluence. An external electric field between the end of the expansion chamber and a grounded grid is used to extract the ions and accelerate them according to their charge state. For 5 kV accelerating voltage applied to the B target and using a laser fluence of  $115 \text{ J/cm}^2$ ,  $\sim 1.5$  nC of total charge is delivered to the detector which is located  $\sim 150$  cm away from the B target. Ion deflection by an electrostatic field separates the ions from the neutrals and makes this geometry suitable for ion implantation.

The developed multicharged ion deposition and implantation system was used to perform interfacial treatment of the SiC/SiO<sub>2</sub> interface using boron and barium ions. SRIM simulation was used to estimate the ion penetration depth in the SiC substrate. The multicharged ions were used for shallow ion implantation in 4H SiC. The optical bandgap of the 4H SiC was reduced due to boron ion implantation. Several MOSCAP devices were fabricated with a combination of boron and barium shallow implantation. High-low C-V measurements were used to characterize the MOSCAPs. Boron implantation affects the flatband voltage significantly, while the effect of

barium ion implantation is negligible. Shallow boron implantation in the SiC/SiO<sub>2</sub> interface reduces the flatband voltage from 4.5 V to 0.04 V.

Copyright, 2018, by Md Haider Ali Shaim, All Rights Reserved.

This thesis is dedicated to my family, friends, and colleagues whose continuous support and encouragement has helped to guide and motivate me through this process.



## ACKNOWLEDGMENTS

I would like to express my acknowledgement to several people, without whose continuous support and encouragement it was impossible for me to travel this long journey.

First and foremost, I thank my Ph.D. supervisor, Dr. Hani E. Elsayed-Ali, for his guidance and feedback throughout my doctoral studies. I thank him for offering me the opportunity to conduct the research that ultimately concluded into this dissertation. Without his involvement and enthusiasm, this work would not have been possible. I am thankful for his untiring support and inspiration during my Ph. D. program.

I also thank Dr. Helmut Baumgart, Dr. Gon Namkoong, and Dr. Leposava Vuskovic for their valuable comments on my work, and for participating as members of my thesis committee, despite their busy schedules.

A special thanks to Md Mahmudur Rahman, Oguzhan Balki, and Md Nizam Sayeed for the support provided throughout my graduate studies. This thesis would not have been possible without the help and feedback you provided. I would also like to thank Dr. Wei Cao for the training and assistance that makes me able to run different instruments.

I would like to offer special thanks to Abdullah Al Mamun and Tanzila Tasnim Ava for their continuous support and encouragement. Your inspiration always helps me in my professional and personal life.

I wish to extend a heartfelt thank you to all my family members and friends for their everlasting backing and encouragement. Thank you to my mother, father, siblings and especially thank you my wife, Al Aqsa, and my son, Md Arham Ali Shaim. I am truly blessed and grateful to have all of you in my life and I love you all immensely.

## TABLE OF CONTENTS

	<b>Page</b>
LIST OF TABLES.....	xii
LIST OF FIGURES.....	xiii
CHAPTER 1 INTRODUCTION.....	1
1.1 Multicharged ion source.....	2
1.2 Laser multicharged ion source.....	3
1.3 Literature review.....	5
1.4 Scope of research.....	7
CHAPTER 2 LASER MULTICHARGED ION SOURCE.....	8
2.1 Introduction.....	8
2.2 Experimental.....	9
2.3 Results and discussion.....	10
2.3.1 Laser pulse energy.....	13
2.3.2 Accelerating voltage.....	16
2.3.3 Incident laser angle.....	19
2.4 Summary.....	20
CHAPTER 3 ION TRANSPORT LINE COMPONENTS.....	21
3.1 Introduction.....	21
3.2 Experimental.....	22
3.3 Design and operation of the transport line components...	23
3.3.1 Faraday cup and three-electrode retarding field analyzer.....	23
3.3.2 Einzel lens.....	28
3.3.2.1 Fabrication.....	29
3.2.2.2 Testing.....	30
3.2.2.3 Simulation.....	31
3.3.3 Ion selection.....	34
3.3.3.1 Fabrication.....	34
3.3.3.2 Testing.....	35
3.3.4 Electrostatic ion analyzer.....	36
3.3.4.1 Fabrication.....	37
3.3.4.2 Testing.....	38

	3.3.4.3 Simulation.....	40
	3.4 Summary.....	42
CHAPTER 4	LASER-SPARK MULTICHARGED ION SOURCE.....	43
	4.1 Introduction.....	43
	4.2 Experimental.....	43
	4.3 Results and discussion.....	45
	4.3.1 Effect of spark energy.....	47
	4.3.2 Effect of laser energy.....	50
	4.4 Summary.....	53
CHAPTER 5	TIME-OF-FLIGHT AND OPTICAL EMISSION SPECTROSCOPY.....	54
	5.1 Introduction.....	54
	5.2 Experimental.....	56
	5.3 Results and discussions.....	59
	5.3.1 Effect of laser energy for a grounded	59
	5.3.2 Effect of laser energy for positively biased target.....	64
	5.3.3 Effect of target bias voltage.....	68
	5.3.4 Retarding field ion energy analysis..	70
	5.3.5 Optical emission spectroscopy.....	71
	5.4 Summary.....	76
CHAPTER 6	FEMTOSECOND LASER PLASMA.....	77
	6.1 Introduction.....	77
	6.2 Experimental.....	80
	6.3 Results and discussions.....	81
	6.3.1 Ions detected without external acceleration.....	82
	6.3.2 Ions detected with external acceleration.....	88
	6.3.3 Effect of laser fluence.....	92
	6.3.4 Effect of focal length.....	93
	6.4 Summary.....	96
CHAPTER 7	GENERATION OF B <sup>5+</sup> IONS.....	98
	7.1 Introduction.....	98

7.2	Experimental.....	99
7.3	Results and discussions.....	102
	7.3.1 Ions detected without external acceleration.....	102
	7.3.2 Ions detected with external acceleration.....	104
	7.3.3 Effect of laser fluence.....	106
	7.3.4 Ion energy.....	107
	7.3.5 Ion deflection out of neutral beam path.....	108
7.4	Summary.....	109
CHAPTER 8	SHALLOW IMPLANTATION ON SILICON CARBIDE.....	111
8.1	Introduction.....	111
8.2	Procedure.....	112
8.3	SRIM simulation of boron ion implantation on silicon carbide.....	112
8.4	Implantation of boron ion on silicon.....	116
8.5	B and Ba shallow ion implantation on SiC.....	117
	8.5.1 Optical bandgap measurement.....	117
	8.5.2 MOSCAP preparation.....	118
	8.5.3 MOSCAP characterization.....	119
8.6	Summary.....	122
CHAPTER 9	CONCLUSION.....	123
REFERENCES	.....	127
APPENDICES		
A	Vacuum system.....	143
B	Multicharged ion source.....	144
C	Nd:YAG nanosecond laser operation and maintenance....	155
D	Ti:Sapphire femtosecond laser operation and maintenance	156
E	Ion energy distribution measurement.....	163
F	Fabrication of SiC MOSCAP.....	165
G	XY deflecting stage flange design.....	166
H	Ion selection steps.....	167
I	List of vendors and different components used.....	168
VITA	.....	169

**LIST OF TABLES**

<b>Table</b>		<b>Page</b>
6.1	Comparison of Al MCI generated by femtosecond and nanosecond laser.....	96
8.1	Flat-band voltage with the implantation variation.....	121

## LIST OF FIGURES

Figure		Page
1.1	Illustration showing the properties of MCI.....	1
2.1	A schematic of the laser multicharged ion source showing the target chamber and the electrostatic time-of-flight energy analyzer, EB: the electrostatic barrier, SE: suppressor electrode, and FC: Faraday cup....	10
2.2	Dependence of the generated multicharged ions on barrier voltage when no accelerating voltage is applied. Inset shows the reduction of total charge with the increase of barrier voltage when no accelerating voltage is applied to the target.....	11
2.3	Generation of Al multicharged ions for 5 kV accelerating voltage with a laser pulse energy of 90 mJ shows charge state up to Al <sup>4+</sup> .....	13
2.4	(a) Total charge generation for different laser pulse energies. (b) Charge state generation with laser pulse energy (Y-axis: 5 mV per division); Accelerating voltage is 5 kV and the laser pulse energy of 45 to 90 mJ.....	14
2.5	The energy distribution of the generated Al multicharged ions for different laser pulse energies (a) 55 mJ (b) 60 mJ (c) 65 mJ and (d) 90 mJ. An accelerating voltage of 5 kV was applied to Al target.....	15
2.6	Effect of change of accelerating voltage from 4 to 6 kV on the TOF and the extraction of ions from the laser plasma. The laser pulse energy is 65 mJ.....	17
2.7	Energy distribution of Al <sup>1+</sup> , Al <sup>2+</sup> and Al <sup>3+</sup> ions for accelerating voltage of (a) 4 kV (b) 5 kV, and (c) 6 kV. The laser pulse energy is 65 mJ.....	18
2.8	Angular distribution of Al multicharged ions when target was rotating. At 45° the target faced the extraction grounded mesh while the laser incidence angle to the target surface is 45°. At 90° the target surface has a 45° angle with the extraction grounded mesh and the laser is incident perpendicular to the target.....	19
3.1	A schematic of the laser MCI source showing the target chamber, $V_c$ is the Faraday cup voltage, and $V_s$ is the suppressor voltage, and $V_b$ is the barrier voltage.....	23
3.2	(a) Schematic of the TOF mass-spectrometer, (b) TOF spectrum for suppressor voltage of -40, -60, and - 90 eV.....	24
3.3	(a) Time-of-flight analyzer signal for MCIs generating up to Al <sup>4+</sup> for 7 kV accelerating voltage and 82 mJ laser energy on target, (b) energy	26

	distribution of the MCIs.....	
3.4	Schematic of the three-electrode einzel lens.....	29
3.5	Experimental results of the effect of einzel lens voltage on the beam diameter of Al <sup>1+</sup> to Al <sup>4+</sup> at knife edge. Inset shows beam diameter of Al <sup>3+</sup> and Al <sup>4+</sup> with focusing voltage in a narrow voltage region where best focus is obtained.....	31
3.6	SIMION simulation showing the Al <sup>1+</sup> , Al <sup>2+</sup> , Al <sup>3+</sup> , and Al <sup>4+</sup> charges are indicated by blue, red, green and yellow respectively.....	32
3.7	Effect on ion trajectory for ion source distribution. Al <sup>4+</sup> ions are focusing with applied voltage -3.5 kV with the input ions having a Gaussian energy distribution with mean of 11.5 kV and FWHM of 2.7 kV. (a) A cylindrical spatial distribution for ion source center position at (0, 0, 0) with radius 21 mm. (b) Gaussian 3D spatial distribution with center at (0, 0, 0) and FWHM of 19 mm on each axis.....	33
3.8	Simulation of the effect of change of einzel lens voltage on (a) beam diameter of Al <sup>1+</sup> , Al <sup>2+</sup> , Al <sup>3+</sup> , Al <sup>4+</sup> ions measured at 30 cm distance from the central electrode of the einzel lens.....	33
3.9	Selection of MCI from Al <sup>1+</sup> to Al <sup>4+</sup> for deflection plate voltage -10 kV with pulse width 1 $\mu$ s. The delay of the deflection pulse is determined by the TOF of the ions. Inset shows the voltage pulse for selecting Al <sup>3+</sup> . Without ion selection, the TOF spectrum consists of all the MCIs generated traveling towards the FC, is shown in Fig. 3.2(a).....	36
3.10	Schematic of EIA analyzer and Faraday cup for ion selection with $E/z$ . RE is the retarding electrodes, SE is the suppressor electrode, and FC is the Faraday cup. The system can be configured with and without the electrostatic ion energy analyzer (EIA) while maintaining the same distance between the target and the Faraday cup.....	37
3.11	Carbon ion signal detected by the Faraday cup placed without (black), and with (red, intensity x 5) the electrostatic ion analyzer. The MCI signal is produced by a single pulse from a Nd:YAG laser ( $\lambda = 1064$ nm, pulse energy 34 mJ). The voltage applied to target is 5 kV, and the EIA is set to central $E/z = 2.8$ keV.....	38
3.12	EIA spectrum of C <sup>2+</sup> (a) and C <sup>3+</sup> (b) with varying $E/z$ . The energy resolution $\Delta E/E$ of the EIA is 7-9%, depending on the voltage applied across the EIA plates.....	40
3.13	Ion trajectory path for C <sup>4+</sup> through the EIA. The applied voltage to the EIA (a) $\pm 500$ V, (b) $\pm 300$ V.....	41
3.14	Simulated TOF spectrum for C <sup>1+</sup> , C <sup>2+</sup> , C <sup>3+</sup> , and C <sup>4+</sup> . The applied	41

	voltage to the EIA is $\pm 500$ V.....	
4.1	A schematic of the spark discharge coupled laser multicharged ion (SD-LMCI) source showing the target chamber, and a spark system to deposit energy into the plasma plume; $V_c$ is the Faraday cup voltage and $V_s$ is the suppressor voltage. Inset shows the experimental setup used for the spark discharge; $C$ is capacitor, $V$ is voltage applied to the capacitor, $R$ is current limiting resistor, and $L$ is inductor.....	44
4.2	(a) Voltage measured across the spark electrodes. (b) Discharge current. (c) Deposited electric power in the plasma. The spark was triggered by the Al plasma plume when a 72 mJ laser pulse ablated the Al target. The capacitor $C$ was charged to 5.0 kV.....	46
4.3	Spark discharge enhancement of multicharged ion generation for 72 mJ laser energy. (a) Only the laser is used. (b)-(d) Spark discharge operating with energy stored in $C$ of 0.05, 0.80, and 1.25 J, respectively.....	48
4.4	Energy distribution of $\text{Al}^{1+}$ without spark (square) and with spark energy of 0.05 (triangle), 0.8 (circle), and 1.25 J (pentagon) coupled with the 72 mJ laser pulse energy. Spark energy refers to energy stored in $C$ .....	49
4.5	Effect of spark energy deposited into the plasma plume on total charge detected. Error bars represent standard deviation. Spark energy refers to energy stored in $C$ .....	50
4.6	(a) Measured total charge delivered to the Faraday cup for different laser pulse energies without the spark (squares) and with 1.0 J spark energy (circles). The error bars represents the standard deviation. The MCI spectra for laser energy only (red) and for the combined effect of 1.0 J spark energy and laser pulse energy (black) of (b) 45 and (c) 63 mJ.....	52
5.1	Schematic of the experimental setup, EB denotes the electrostatic barrier of the three-grid retarding field analyzer, SE the suppressor electrode to suppress the effect of secondary emission from the Faraday cup (FC).....	57
5.2	Ion TOF signal for different laser energies ablating the Al target. The Al target was at ground potential. The inset shows the dependence of the number of charges measured by the Faraday cup (FC) on the laser pulse energy.....	59
5.3	Deconvolution of the ion time-of-flight signal. (a) For a laser fluence of $28 \text{ J/cm}^2$ showing charge states up to $\text{Al}^{3+}$ . (b) For a laser fluence of $38 \text{ J/cm}^2$ showing charge states up to $\text{Al}^{4+}$ . $V_0$ is the double-layer potential, $kT_i$ is the ion plasma temperature, whereas $V_{0S}$ is the	63



	equivalent accelerating voltage for the slow $\text{Al}^{1+}$ ions.....	
5.4	Deconvolution of the TOF signal for different ion charge states for 5 kV applied to target. The laser fluence is (a) $28 \text{ J/cm}^2$ and $38 \text{ J/cm}^2$ (b). $V_T$ is the total effective voltage accelerating the ions and $kT_{ie}$ represents the spread in ion energy due to the plasma ion temperature and ion spread during plume expansion and ion extraction in the target-grid region, $V_{TS}$ is the effective accelerating voltage for the slow ions.....	67
5.5	The effect of varying the total accelerating voltage $V_T$ and $kT_{ie}$ on the deconvolution of the ion pulse when 5 kV accelerating voltage is applied. The $\text{Al}^{4+}$ ion pulse obtained by deconvolution is shown for (i) $V_T \sim 1300 \text{ V}$ and $kT_{ie} \sim 27 \text{ eV}$ (red dotted line), (ii) $1600 \text{ V}$ and $14 \text{ eV}$ (blue dotted line), (iii) $1600 \text{ V}$ and $27 \text{ eV}$ (black straight line), (iv) $1600 \text{ V}$ and $40 \text{ eV}$ (blue dash line), and (v) $1900 \text{ V}$ and $27 \text{ eV}$ (red dash line).....	68
5.6	Deconvolution of the ion TOF signal into different charge states for a voltage applied to target of (a) 4 kV and (b) 6 kV. The ablating laser fluence is $28 \text{ J/cm}^2$ . The TOF signal is plotted in black. The deconvolution fit for $\text{Al}^{1+}$ , $\text{Al}^{2+}$ , $\text{Al}^{3+}$ , $\text{Al}_s^{1+}$ are plotted in red, green, navy, and blue, respectively. The sum of the individual de-convoluted ion species is plotted in pink. Inset shows the TOF signal converted into energy distribution of the ions.....	70
5.7	Effect of retarding voltage on the TOF spectrum for a laser fluence of $28 \text{ J/cm}^2$ and 5 kV applied to target.....	71
5.8	Al emission spectra for laser fluence of $21 \text{ J/cm}^2$ , when no external electric field (black line) and when 7 kV external field (red line) is applied.....	73
5.9	Effect of target bias voltage on (a) electron density $N_e$ and (b) electron temperature $kT_e$ as measured by OES. Laser pulse energy of 21, 25, 28, and $38 \text{ J/cm}^2$ is represented by black-square, red-diamond, blue-hexagon and green-circle, respectively.....	75
6.1	An illustration of the laser MCI ion source showing the laser irradiating the Al target, and the electrostatic TOF energy analyzer. EB is the electrostatic barrier electrode, SE suppressor electrode, and FC Faraday cup.....	80
6.2	Ion signal for various EB voltage biases at laser fluence of $7.6 \text{ J/cm}^2$ ...	83
6.3	Deconvolution of TOF spectrum into individual ion species for laser fluence of $7.6 \text{ J/cm}^2$ when no accelerating voltage is applied to target. $\text{Al}_s^{1+}$ and $\text{Al}_s^{2+}$ are the slower ions.....	86

6.4	Al MCI detected with (a) 5 kV and (b) 6 kV accelerating voltage. The laser fluence is $7.6 \text{ J/cm}^2$ . The deconvolution of the extracted ion is based on a shifted Coulomb-Boltzmann distribution. (c) The effect of varying the total accelerating voltage ( $V_0 + V_{eff}$ ) and equivalent plasma temperature $kT$ on the deconvolution of the ion pulse when 5 kV accelerating voltage is applied. In (c), the $\text{Al}^{4+}$ ion pulse obtained by deconvolution is shown for ( $V_0 + V_{eff}$ ) = 2300 V and $kT = 40 \text{ eV}$ (black straight line), 2300 V and 20 eV (blue dot line), 2300 V and 60 eV (blue dash line), 2000 V and 40 eV (red dot line), and 2600 V and 40 eV (red dash line).....	90
6.5	(a) TOF spectrum of MCIs for laser fluence variation from 1.4 to $7.4 \text{ J/cm}^2$ , (b) total charge generation as a function of laser fluence. The accelerating voltage applied to the target was 5 kV.....	92
6.6	Al total ion charge detected versus distance from optical focus of the lens on target surface.....	94
7.1	An illustration of the laser ion source showing the laser irradiating the B target, and the electrostatic TOF energy analyzer. EC expansion chamber, EB electrostatic barrier, SE suppressor electrode, FC-1 Faraday cup-1, and FC-2 is Faraday cup-2. In Region I, the plasma plume expands in a field-free region and the ions separate from the plume and are accelerated by the double-layer potential at the plasma-vacuum interface. In Region II, the ions can be accelerated by an external electric field between the end of the EC and the grounded mesh parallel to it. Region III is a field-free ion drift region.....	99
7.2	TOF signal for 1800 consecutive laser pulses hitting on the same target spot for a laser fluence of $135 \text{ J/cm}^2$ .....	101
7.3	(a) Ion signal detected by the FC-1 for increasing laser fluence. (b) Ion signal for a laser fluence of $135 \text{ J/cm}^2$ with different applied barrier voltages. Inset shows the total charge detected with the increase of barrier voltage.....	103
7.4	External acceleration voltage accelerates and separate the ions in their TOF. The accelerating voltage applied is 5 – 7 kV, and the laser fluence is $135 \text{ J/cm}^2$ .....	105
7.5	Higher charge states are generated with the increase of the laser fluence from 77 to $135 \text{ J/cm}^2$ . The accelerating voltage applied to the EC is 5 kV.....	106
7.6	Time-of-flight ion signals for different barrier voltages applied to the central grid of the retarding field analyzer.....	107
7.7	Ion signal detected by the two Faraday cups with and without ion deflection. The TOF signal shown are for (i) FC-1 without ion	108

	deflection, (ii) FC-2 with ion deflection, and (iii) FC-1 with ion deflection.....	
8.1	Image and schematic of the laser ion implanter showing the plasma generation chamber, ion deflecting stage, sample holder, and Faraday cup to detect the MCI.....	110
8.2	Block diagram shows the steps followed to fabricate MOSCAP.....	111
8.3(a)	SRIM simulation of 2000 B ions implanted in the SiC wafer with energy 150 eV.....	112
8.3(b)	SRIM simulation of 2000 B ions implanted in the SiC wafer with energy 300 eV.....	112
8.3(c)	SRIM simulation of 2000 B ions implanted in the SiC wafer with energy 450 eV.....	113
8.3(d)	SRIM simulation of 2000 B ions implanted in the SiC wafer with energy 600 eV.....	113
8.3(e)	SRIM simulation of 2000 B ions implanted in the SiC wafer with energy 750 eV.....	114
8.3(f)	SRIM simulation of 10,000 B ions with five energy groups of (a)–(e), with 2000 B ions in each group.....	114
8.4	(a) and (b) FESEM image of the boron film on Si, (c) transmission characteristics of the film on glass sample measured using UV-Vis spectrophotometer.....	115
8.5	Film thickness measured by FESEM of ~40 nm Ba film.....	116
8.6	Effect of B implantation on the bandgap of SiC, (a) UV-Vis photo-spectroscopy of the bare SiC and SiC with 2 nm boron layer, (b) Tauc plot to calculate the optical bandgap.....	117
8.7	Cross-section schematic of the MOSCAP.....	118
8.8	100 kHz C-V for n-type MOS capacitor with different B and Ba dose.....	119
8.9	High-Low C-V curve for bare SiC (a) and 2 nm boron implanted SiC (b).....	121
B.1	The MCI system with its transport line components.....	143
B.2	The ion energy analyzer.....	143
B.3	Schematic of the faraday cup.....	144

B.4	Image and schematic of the CF flange used from Kurt J. Lesker.....	145
B.5	Schematic of the top view of the customized CF flange.....	146
B.6	AutoCAD schematic of the FC components.....	147
B.7	AutoCAD schematic of the FC components.....	148
B.8	AutoCAD schematic of the FC components.....	149
B.9	Einzel lens.....	150
B.10	Design of the einzel and its components. 1. CF Full Nipple; 2. 1-1/3" OD CF Flanges; 3. Ceramic spacer; 4. 304 Stainless steel 2"OD seamless tubes; 5. Power Feedthroughs CF Flanged 20 000V; 6. 8-32x3/4" Bolt & Nut Sets; 7. Annealed Copper Gaskets 1-1/3" CF; 8. Barrel Connector for 0,120" wire; 9. UNC 1/4" stainless steel connecting rods; 10. Ceramic isolating tubes; 11. Stainless steel hex nuts; 12. Stainless steel washers; 13. Annealed copper gaskets 6"CF; 14. Stainless steel hex bolt/plate -nut sets; 15. Socket head screws 4-40; 16. Isolating tube.....	150
B.11	AutoCAD drawing of the CF flange.....	151
B.12	AutoCAD drawing of customized ceramic Spacer.....	152
B.13	Cylindrical ion deflector.....	153
B.14	Schematic and image of the MCI system with ion deflection plates to avoid neutral deposition.....	153
D.1	(a) power supply with chiller, (b) chiller temperature, (c) chiller for regen and oscillator and (d) pumping oscillator, oscillator, and regen.....	155
D.2	(a) Pulse generator, (b) oscilloscope, (c) Q-switched controller, (d) mode locked output in the computer screen.....	156
D.3	Fig. D.3 Beam path in the Regen.....	158
D.4	Beam shape observed in the concave mirror (compressor).....	159
D.5	Beam share observed in the compressor Retro-reflector.....	159
D.6	Beam shape in the stretcher grating.....	160
D.7	Beam shape in the retro-reflector mirror (compressor).....	160
D.8	Beam shape on the mirror (stretcher).....	161
D.9	Beam shape on the mirror (stretcher).....	161

E.1	Deconvolution of the TOF spectrum.....	162
E.2	(a) Extension of the signal to the base line, (b) energy distribution of the $Al^{4+}$ .....	162
G.1	AutoCAD drawing of XY deflecting flange.....	164
G.2	(a) assembled deflecting plate design and (b) separate plate and rod.....	164

## CHAPTER 1

### INTRODUCTION

Multicharged ions (MCI) sources are of interest for their utilization in surface modification, e.g., etching and deposition, for ion implantation, and for fundamental studies of ion-surface interactions. The intersection of MCIs with solids is different from that of singly charged ions. For singly charged ions, the ion projectile mainly interacts with the target nuclei causing surface sputtering, intermixing, and defect generation [1]. The total energy of an ion beam depends on the charge state of the ions (potential energy) and its velocity (kinetic energy). During interaction with a solid, the potential energy carried by the MCIs is released along with its kinetic energy. This potential energy can be significant for highly-charged ions and can exceed that of the ion kinetic energy. The release of the ion potential energy causes electronic exchange interaction in the target material and electronic excitation [2]. For sufficiently slow MCI, this released potential energy can be localized to a depth of few nm causing surface nano-features.

One attractive application of MCIs is ion implantation. MCIs can allow for ion implantation at different depths in a single step since different charge states are accelerated to different kinetic energies with the same potential [3]. Also, the ability to control both kinetic and potential energy of the MCIs could possibly be used to minimize implantation damage by ion recoil [3]. The higher charge state allows reaching higher kinetic energies with lower potential, therefore, reducing the requirement on the high voltage power supply making it possible to develop comparatively low-cost and compact ion implanter. The properties of MCIs are depicted in Fig. 1.1.

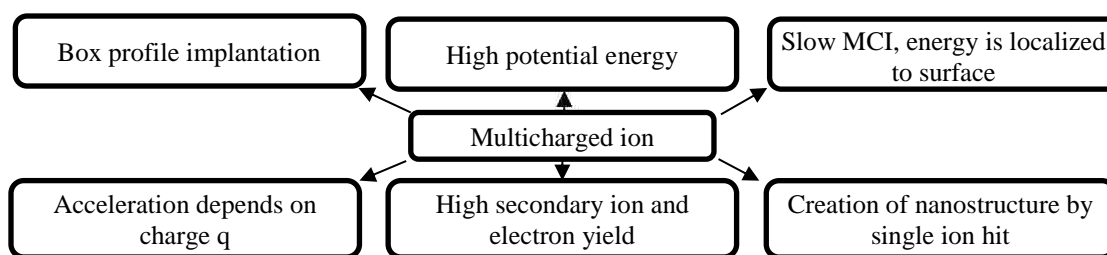


Fig. 1.1 Illustration showing the properties of MCI

1. Due to the high charge state, MCI possess a great amount of potential energy. For example,  $\text{Ag}^{15+}$  has a potential energy of  $\sim 5$  keV, while  $\text{Xe}^{52+}$  has a potential energy of more than 100 keV [2].
2. For a sufficiently slow MCI, the potential energy can be localized to the surface. During interaction with a solid the potential energy can be released within a few 10 fs and over an area of  $\sim 100$  nm<sup>2</sup>, providing a power density of  $10^{12}$  to  $10^{14}$  Wcm<sup>-2</sup> [2].
3. During ion-surface interaction, due to high power density at the surface, a single MCI can create Nano-crater.
4. Due to the high-power density at the surface, MCI can produce secondary particles such as neutrals as well as secondary ions and electrons.
5. MCI can be accelerated effectively compared to a singly charge state. The acceleration is proportional to the charge state  $q$  for linear accelerators and proportional to  $q^2$  for circular accelerators, where  $q$  is the charge state.
6. The use of ions with different charge states for implantation makes it possible to implant with different ion kinetic energies in one-step. This feature can be used to control the implanted ion depth profile producing a uniform concentration over a certain depth or a tailored gradient when needed.

## 1.1 MULTICHARGED ION SOURCE

Multicharged ions are mainly generated by electron cyclotron resonance ion sources (ECRIS), [4, 5] electron beam ion sources (EBIS), [6, 7] and laser multicharged ion (LMCI) sources [8, 9]. ECRIS and EBIS operate only with gases and, therefore, for elements with low vapor pressures, they require introducing gaseous compounds or some vaporization mechanism. Introduction of gases inside the MCI system requires additional pumping capacity to avoid recombination of the MCIs in the generation chamber and the transport beam line. ECIRS and EBIS can produce a continuous beam of MCIs. LMCI sources generate many ions per pulse and can generate MCIs from any solid even from nonconductive or refractory targets [8, 10]. LMCI sources can operate in an ultrahigh vacuum with a relatively small pumping capacity since no gas load is required for most elements. In principle, LMCI sources can also be used with gas targets since ultrafast laser pulses can induce gas breakdown generating dense plasma [9]. Laser

ion sources have been tested as potential ion sources for injection into ion accelerators [11]. Moreover, many pulsed laser deposition systems can be reconfigured into LMCI sources.

## **1.2 LASER MULTICHARGED ION SOURCE**

Laser ablation of a solid target results in the formation of dense plasma that is a source of multicharged ions (MCIs). The laser-matter interaction produces dense plasma consisting of ions, electrons, clusters, and neutral particles. The laser plasma plume expands in the perpendicular direction to the ablated surface. The ions are accelerated in the plasma sheath and can be additionally accelerated by an external electric field forming an ion beam [12-14]. The LMCI source produces ions from a small spot on the target, which gives control on the ion beam divergence and emittance. The produced MCIs can then be collimated and focused in an ion transport line. The study of MCIs generation from laser plasma is a topic of interest because these MCIs provide valuable information on the laser-plasma characteristics in addition to their applications in ion implantation [1], ion surface cleaning and patterning [1], secondary ion mass-spectrometry [2], extreme ultraviolet lithography [3], and for injection in electron cyclotron resonance ion sources and ion accelerators [4, 5]. Moreover, the ions generated by laser ablation impact thin film growth by pulsed laser deposition as these ions interact with the substrate [6]. The characterization of the different laser-generated ions involves measuring their number, charge state, energy distribution, and angular distribution. These measurements make use of a combination of different techniques such as time-of-flight (TOF) ion detection [7], electrostatic retarding field analyzers [8], and different configurations of electrostatic [8], and magnetic [2] ion spectrometers based on ion bending.

Nanosecond (ns) lasers are often used to generate ions by ablation of a solid target in a vacuum. During laser-matter interaction, the electromagnetic energy is converted into electronic excitation and then into thermal, chemical, and kinetic energies [15]. The process of ns laser ablation consists of three main stages: evaporation of the target material, interaction between the evaporated material and the laser pulse resulting in the formation of partially ionized vapor that absorbs the incident laser radiation, and plasma plume expansion and rapid cooling [16]. The laser energy is converted into internal energy of the plasma and emitted or absorbed during the hydrodynamic motion of the plume. Intense collisional ionization takes place in the hot plasma. Near the target surface, the residual recombination releases recombination energy acting against



the adiabatic cooling, thus slowing down the recombination rate. Due to the rapid expansion of the plume, the plasma density is reduced before the recombination eliminates the ionized species, despite a rapid increase in the three-body recombination rate due to electron temperature decrease in the adiabatic expansion [15]. In the expanding plasma, different charge states become frozen. Hence, some of the MCIs generated in the hot plasma core survive and are ejected from the expanding plume.

In laser-plasma, three groups of ions have been reported, depending on the laser conditions [15]. The main group is composed of thermal ions that gain their energy from the thermalization processes followed by plasma expansion into the vacuum [17]. The fast ions are attributed to the presence of super-thermal electrons formed by the electrostatic waves [18]. The number of fast electrons is dependent on the laser intensity and wavelength [18]. Slow ion groups can be generated by secondary collisional processes during plume expansion or due to reabsorption of emitted x-rays outside the laser focus [15, 19, 20].

Various processes have been proposed to explain the physical mechanisms of ion acceleration during ns laser ablation. The laser interaction with the plasma heats the plasma electrons by inverse bremsstrahlung. The energy of the heated electrons is then transferred to the neutrals and ions through collisions. The time needed to transfer the energy from the electrons to the ions, *i.e.* the electron-ion thermalization time scale ( $10^{-10}$  to  $10^{-11}$  s) [21], is much shorter than the ns laser pulse duration resulting in the establishment of local thermal equilibrium (LTE) between the electrons and the ions during the early portion of the laser pulse [21, 22]. Due to the mass differences between the electrons and the ions, fast electrons escape the plasma plume much earlier than the ions. The space-charge separation between the fast electrons and the ions that are lagging prevents some electrons from escaping the plasma resulting in the establishment of a self-electrostatic field at the expanding plasma-vacuum interface. This field is referred to as the ambipolar electric field or the double-layer potential [23]. The ions, which enter in the region of this electric field, are accelerated according to their charge state.

Generation of a large number of high-energy (hot) electrons during interaction of the laser pulse with the solid target and their subsequent escape from the expanding plume is the responsible mechanism for the formation of the double-layer potential. The hot electrons are formed in the plasma by three-body recombination or absorption of the remaining laser pulse by inverse bremsstrahlung. Some of these hot electrons escape the target, leaving behind a positive

electric charge region at the boundary of the expanding plasma-vacuum interface. The lifetime of the laser ablated plume is determined by the velocity of the plume expansion, which in turn is related to the hydrodynamic pressure inside the plume [24].

The structure of the double-layer potential depends on the ratio of the hot electrons to thermal electrons, which is dependent on the laser fluence. With the increase in the laser fluence, more hot electrons are generated and the double-layer structure changes from a layer formed by the escaping electrons and the excess ions at the front of the expanding plasma core to a more complex two-peak structure with two double-layers [23]. The developed two-electron-distribution and the role of prompt electrons in the development of this complex double-layer structure was studied, both experimentally and by numerical simulations [25]. As the initial electron density at the front of the expanding plasma increases, electron compression in the plasma occurring by the forces of the prompt electrons, cannot be compensated for by the ion oscillation frequency. This results in ion cloud fragmentation and a complex ion acceleration mechanism [25].

### 1.3 LITERATURE REVIEW

Several groups have developed LMCI sources. Abdellatif *et al.* reported that, for aluminum target ablation using a Nd:YAG laser ( $\lambda = 1064$  nm,  $\tau = 7$  ns, and laser intensity of  $8.7 \times 10^{10}$  Wcm<sup>-2</sup>), the plasma density was  $\sim 1.13 \times 10^{18}$  cm<sup>-3</sup> at a distance 100  $\mu$ m from the Al target surface [26]. At 1200  $\mu$ m from the target surface, the plasma density was reduced to  $0.55 \times 10^{18}$  cm<sup>-3</sup>. The plasma temperature was  $\sim 1.17$  eV at the target surface, and at 500  $\mu$ m, the plasma temperature increased to 4.2 eV then decreased beyond this point. In their experiment, an Al charge up to 3+ was generated [26]. Nassisi *et al.* reported on a Cu LMCI source with a charge state up to 5+ with most ions generated in the singly and doubly charged states, with ionization of the plasma estimated to be 16%. In their experiment, an excimer laser providing 70 mJ/pulse, corresponding to  $3.5 \times 10^8$  Wcm<sup>-2</sup> was used [27-29]. An Nd:YAG laser ( $\lambda = 532$  nm,  $\tau = 3$  ns, and maximum energy of 170 mJ/pulse) was used to ablate carbon plasma creating in excess of 70% ionization [30].

To increase the production of MCIs from LMCI sources, higher plasma density and temperature are needed. This is achieved using larger laser pulse energies, shorter pulse widths, and shorter laser wavelengths to penetrate the formed dense plasma [15, 31-37]. High laser

intensity ( $\geq 10^{14}$  Wcm<sup>-2</sup>), causes nonlinear interactions, e.g., self-focusing, with the plasma formed by a pre-pulse or the initial part of the laser pulse resulting in higher charge state generation [31, 32]. Laska *et al.* observed charge state of >50 for Ta with high kinetic energies (up to 100 keV/amu) using a high-power iodine photo-dissociation laser ( $\lambda = 1315$  nm, pulse energy 40-750 J,  $\tau \sim 400$  ps, intensity  $\leq 6 \times 10^{16}$  Wcm<sup>-2</sup>) [31-33]. A strong increase in MCI production was observed for laser intensities of  $\sim 2 \times 10^{14}$  Wcm<sup>-2</sup> when the laser focus was above the target surface. They also reported on the production of MCIs from different elements by a Nd:YAG laser ( $\lambda = 1064$  nm, pulse energy  $\leq 0.9$  J, pulse width  $\sim 9$  ns, intensity  $\sim 1 \times 10^9$  to  $\sim 5 \times 10^{10}$  Wcm<sup>-2</sup>) and an iodine laser (2nd and 3rd harmonic of the fundamental  $\lambda = 1310.5$  nm, pulse energy  $\leq 50$  J, pulse width  $\sim 350$  ps) [15]. For the Nd:YAG laser, which provided low laser intensity, the maximum ion charges reported were Nb<sup>8+</sup>, Ta<sup>8+</sup>, W<sup>9+</sup>, Au<sup>10+</sup>, and Pb<sup>9+</sup>. For the iodine laser, the maximum charges observed were Co<sup>25+</sup>, Ni<sup>26+</sup>, Ag<sup>36+</sup>, Sn<sup>38+</sup>, Ta<sup>55+</sup>, W<sup>49+</sup>, Pt<sup>50+</sup>, Au<sup>51+</sup>, Pb<sup>51+</sup>, and Bi<sup>51+</sup> ion [15]. Lorusso *et al.* used frequency tripled pulses of the iodine laser ( $\lambda = 438$  nm,  $\tau = 400$  ps, pulse energy  $\leq 250$  J) to generate up to Ge<sup>25+</sup> ion [38]. A theoretical model of a hybrid ion source composed of a Nd:YAG laser ( $\lambda = 1064$  nm,  $\tau = 9$  ns, and maximum pulse energy of 0.9 J) coupled with ECRIS to boost the charge state was developed [34]. These calculations showed that this approach could be effective if the ion energy from the laser source is maintained below a few hundred eV. However, precise control of ion energy in laser ion sources is complicated by ion acceleration in the sheath and plasma shielding effects. In addition, contaminations for the first laser shot can require further outgassing and target etching [34]. Woryna *et al.* reported the generation of up to Ag<sup>37+</sup> with an iodine laser ( $\lambda = 1315$  nm,  $\tau = 300$ -700 ps, pulse energy  $\sim 45$  J, intensity  $\sim 1 \times 10^{14}$  Wcm<sup>-2</sup>) [35]. Using iodine laser ( $\lambda = 1315$  nm, pulse width 350-600 ps, pulse energy 40 J, and intensity  $\sim 10^{15}$  Wcm<sup>-2</sup>), Rohlena *et al.* reported the generation of charge state up to Ta<sup>45+</sup> with energies >4 MeV [36]. At CERN, production of high current and high charge state ion beam with maximum charge state of Ta<sup>23+</sup> was reported using a CO<sub>2</sub> laser ( $\lambda = 10.6$   $\mu$ m,  $\tau = 70$  ns, pulse energy  $\leq 50$  J) [37]. Clearly, using lasers with large pulse energies is effective in increasing the plasma density and temperature resulting in higher ionization states and more ion production. However, this approach requires expensive lasers that are typically available only in limited laser laboratories. Therefore, it is desirable to develop LMCI sources capable of delivering high charge states without the complication and cost associated with large laser systems.

## 1.4 SCOPE OF RESEARCH

The research presented in this dissertation provides a detailed experimental procedure for MCI production by means of a laser-spark ion source. The main goal is to increase the plasma ionization by coupling a spark discharge with the laser plasma. The increase in the plasma ionization enhances the total ion generation along with the increase in maximum charge state. This dissertation is organized as follows:

Chapter 1 deals with the MCIs, mechanism of laser ion source, some literature review of previous work done on laser multicharged ion source, and presently used methods to enhance the ion production.

Chapter 2 explains the details of the experimental setup of a LMCI source for Al MCI generation. The plasma is characterized in terms of laser fluence, accelerating voltage, incident laser angle on target, and ion energy distribution.

Chapter 3 covers the details of the ion transport line module fabrication. Faraday cup with three-grid retarding field ion energy analyzer, einzel lens, cylindrical ion deflector, and parallel plate ion selector were fabricated and tested.

Chapter 4 explains the details of the laser-spark MCI source. The laser produced plasma is reheated by deposition of external energy from a capacitor. The laser-spark plasma is characterized in terms of spark energy, and laser fluence.

Chapter 5 describes the characterization of the nanosecond laser-generated aluminum plasma using ion time-of-flight and optical emission spectroscopy.

Chapter 6 provides a detailed account of the experimental production of aluminum MCIs by means of femtosecond laser produced plasma.

Chapter 7 covers the details of the modified LMCI source for ion implantation without neutral particle deposition. The system also generated fully stripped boron ions.

Chapter 8 explains the effect of shallow implantation of boron and barium ions in 4H-SiC. Silicon carbide-metal oxide semiconductor capacitors (SiC-MOSCAPs) are fabricated with boron and/or barium shallow implantation in the SiC/SiO<sub>2</sub> interface.

Chapter 9 covers the conclusion and a summary of the work presented along with suggestions for future work.

## CHAPTER 2

### LASER MULTICHARGED ION SOURCE

#### 2.1 INTRODUCTION

We report on the development of an aluminum laser MCI source in which a Q-switched ns Nd:YAG laser is used for target ablation and an ion extraction and accelerating voltage is applied to the target. The velocity and the charge state of the MCIs are determined by using time-of-flight (TOF) and a three-grid retarding ion energy analyzer. The use of TOF to characterize MCIs is suitable when the ion pulse is much shorter than the ion travel time from target to detector. The energy distribution of the ions generated from the laser plasma plume is measured by their TOF or the electrostatic energy analyzer. The energy distribution of ions for increasing ablation laser pulse energy shows an increase in the ion energy along with a narrowing of the distribution.

Aluminum ion implantation and deposition have many applications. For example, Al ion implantation followed by oxidation was used to reduce atomic oxygen degradation of polymers [39]. Increased conductivity of ZnO by Al ion implantation was reported to be due to the reduced effects of oxygen vacancies [40]. Al ion implantation of surgical AZ 31 and AZ91 magnesium alloys was used to increase their corrosion resistance [41, 42]. Plasma immersion ion implantation of Al on HfO<sub>2</sub> causes a reduction in the leakage current, smaller flatband shift, and steep transition from the accumulation to the depletion region in the C-V characteristics, indicating the reduction of both bulk oxide and interface traps [43]. All these applications were conducted with singly-charged Al ions. MCI potentially can offer advantages due to control on both their kinetic and potential energy. The availability of MCIs with different charge states makes it possible to control the implanted ion depth profile producing uniform concentration gradient, or a tailored gradient when needed. An example where a uniform Al concentration gradient is needed is in the p-type doping of SiC by ion implantation. To achieve this uniform concentration, implantation is conducted with singly-charged Al ions with different energies ranging from 25 to 300 keV [44]. SiC is an attractive material for high power and high

temperature fast devices because of its high thermal conductivity, large electron saturation drift velocity, high electric field breakdown, and thermal stability [45, 46]. Using an ion beam containing Al MCIs could enable implantation at different depths in a one-step process. Also, the ability to control both kinetic and potential energy of the Al ions could conceivably be used to minimize implantation damage by ion recoil. The higher charge states also reduce the required potential to reach a certain kinetic energy, thus reducing the requirement on the high voltage power supplies and allowing development of a compact and cost-effective implanter.

## 2.2 EXPERIMENTAL

The experimental setup used in this study is shown in Fig. 2.1. It consists of a Q-switched Nd:YAG laser, operating at the fundamental wavelength ( $\lambda = 1064$  nm) with a pulse duration (FWHM) of 7.4 ns. An aluminum disc target of 99.9 % purity, 0.5 mm thickness and with a surface roughness (rms) of 261.77 nm, as characterized by the manufacturer (Alfa Aesar), is placed on a multi-axes translational stage and the laser beam is focused on the Al target surface by a lens with an 80-cm focal length. The laser energy on the target was controlled by a combination of half-wave-plate and thin film polarizer. An insulating connector is used to mount the Al target support inside the MCI generation chamber. This arrangement allows for applying an accelerating voltage directly to the Al target keeping the experimental chamber at ground. An extraction nickel mesh of 10 cm diameter, 100  $\mu$ m thicknesses, and 70% open area from Precision Eforming is placed 10 cm in front of the target. The beam strikes the Al target surface at an angle  $\vartheta = 45^\circ$  with a laser spot area, at focus, of 0.0024 cm<sup>2</sup>, as measured by the knife-edge method at target-equivalent plane with the edge scanned at 45° to the laser beam. The knife edge was used to scan the laser beam in both horizontal and vertical directions. The Faraday cup is made of Al and has a diameter of 5 cm. The retarding field ion energy analyzer consists of three nickel meshes, similar to the extraction mesh but with a diameter of 5 cm, separated by 1 cm and placed with the closest mesh to target at a distance of 130-cm away from the Al target. The diameter of the MCI generation chamber is 15 cm. A 125 cm long transport tube with inner diameter of 10 cm is connected to the chamber. The suppressor electrode is biased with negative voltage to suppress the secondary electron emission from the Faraday cup due to positive ion collisions. Throughout the experiment, the Faraday cup voltage was maintained at -70 V and the suppressor electrode voltage was at -80 V. The electrostatic barrier mesh is biased with variable

positive voltage and is used to analyze the ion energy distribution. To observe the effect of consecutive laser pulses hitting the target, we calculated the total ions generated per pulse for pulses hitting the same spot on the target. The second pulse on the Al target reduces the total number of ions generated by 10 – 20% compared to the first one. With further pulses, the change in the number of ions generation per pulse is within the experimental shot-to-shot fluctuations of  $\sim 5\%$ . The reported data were obtained from the 3<sup>rd</sup> laser pulse.

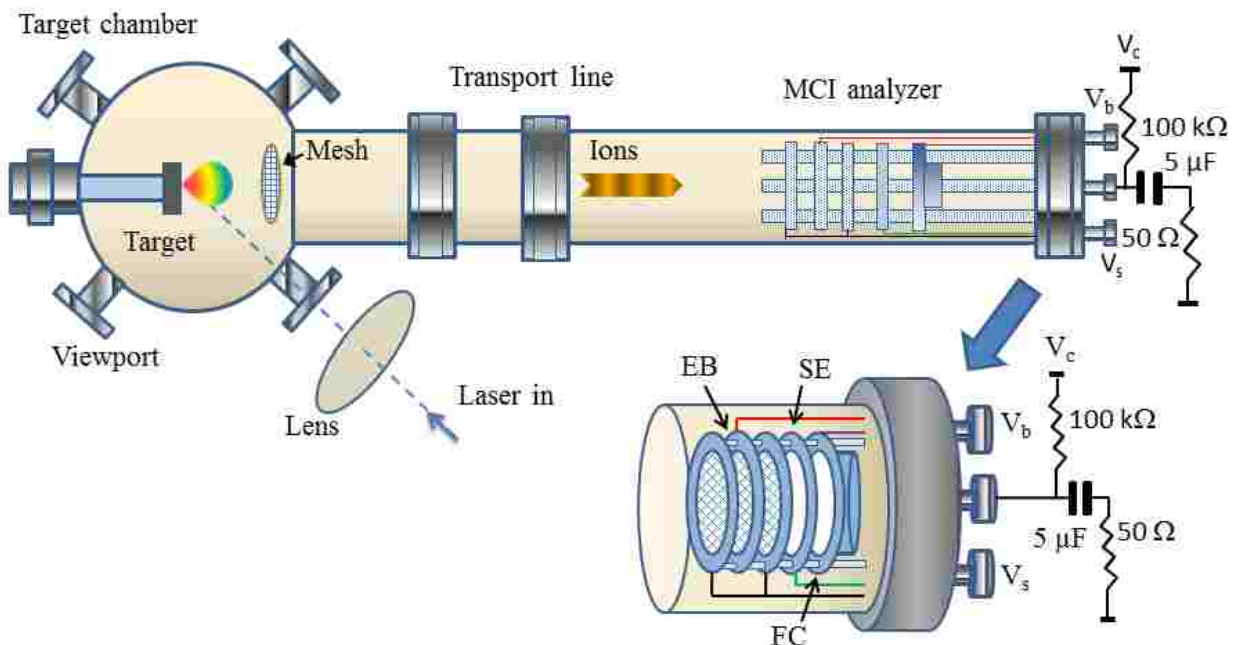


Fig. 2.1 A schematic of the laser multicharged ion source showing the target chamber and the electrostatic time-of-flight energy analyzer, EB: the electrostatic barrier, SE: suppressor electrode, and FC: Faraday cup.

## 2.3 RESULTS AND DISCUSSION

We characterized the generated ions from the laser plasma with and without applying accelerating voltage to the Al target. Fig. 2.2 shows the Faraday cup signal that is dependent of barrier voltage. At the instant of the laser trigger, a positive signal is observed due to the photoelectric effect where photons generated from the laser plasma with energy above the work

function of the Faraday cup material cause photoemission. The plasma ion peak drifts towards the Faraday cup with a velocity of  $\sim 2.8 \times 10^4 \text{ ms}^{-1}$ . The ions generated by pulsed laser ablation reach the Faraday cup as a bunch containing the different ion states. As expected, increasing the barrier voltage stops more of the slower ions. From Fig. 2.2, we also observe that the arrival time of the fastest ions in the bunch becomes longer with the increasing barrier voltage, changing from  $\sim 30 \text{ }\mu\text{s}$  at 0 barrier voltage to  $\sim 38 \text{ }\mu\text{s}$  at 70 V. Also, with applied barrier voltage, the number of ions in the plasma with energies sufficient to overcome that barrier voltage and reach the Faraday cup is reduced. Increasing the barrier voltage slows down all ions which causes an increase in ion loss due to enhanced recombination and ion scattering out of the propagating plume. Similar trends were also observed in excimer laser generation of Cu MCI conducted by Nassisi *et al.* [27]. The inset in Fig. 2.2 shows the reduction in the total charge with the increase of barrier voltage.

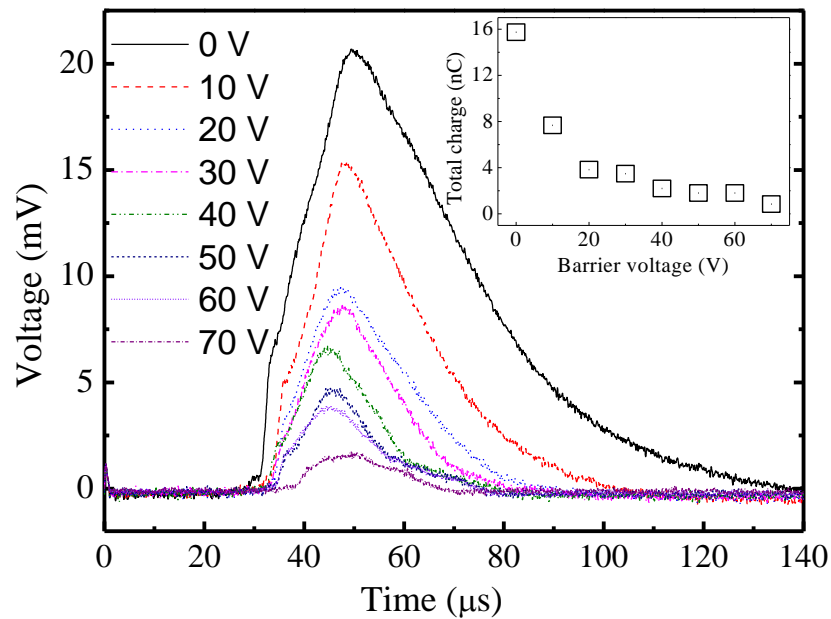


Fig. 2.2 Dependence of the generated multicharged ions on barrier voltage when no accelerating voltage is applied. Inset shows the reduction of total charge with the increase of barrier voltage when no accelerating voltage is applied to the target.

For nanosecond lasers, the laser ablation mechanism consists of three main regimes: target material evaporation, interaction of the laser pulse with evaporated material which results



in material heating and plasma formation, and plasma plume expansion and rapid cooling [16]. During laser ablation, the electrons are heated through laser absorption by inverse bremsstrahlung, and then the heated electrons transfer their energy to ions and neutrals through collisions. The time to transfer energy from electrons to ions is much shorter than the ablation laser pulse duration for our experimental condition. Due to the hydrodynamic pressure in the plume, the velocity of the plume expansion determines its lifetime. The ion mass affects the average velocity of plume expansion [47].

The total charge reaching the Faraday cup,  $C_i$  is given by  $C_i = \frac{1}{R} \int V_F(t) dt$ , where  $V_F(t)$  is the voltage signal on the Faraday cup and  $R$  is 50  $\Omega$  internal resistance of the oscilloscope. The ion energy distribution function  $f(E)$  is calculated from the kinetic energy  $E = \frac{1}{2}mv^2$  with  $v$  obtained from the TOF signal. For 5 kV accelerating voltage, 500 V of barrier voltage, and a laser pulse energy of 90 mJ, charge state, up to  $Al^{4+}$  is generated, as shown in Fig. 3. Beside the identified MCI peaks, slow  $Al^{1+}$  ions are present. The main groups of ions are the thermal ions generated due to direct laser interaction processes. These ions establish an energy distribution by collisional thermalization in the dense laser plasma. The slow ions were suggested to be generated by X-rays reabsorbed outside the laser focus spot [48]. To measure the total charge per charge state, we separate the TOF for individual MCI of Fig. 2.3 by roughly estimating the tail position using the peak fitting option in Origin-lab 9.1 software. Integrating the area of individual charge state gives us the total charge delivered to the Faraday cup for that MCI, while its energy distribution is calculated from the TOF signal. For  $Al^{1+}$ , we have  $\sim 0.45$  nC charge with most probable energy  $E_{mp} \sim 2.0$  keV,  $Al^{2+}$  has  $\sim 0.07$  nC charge with  $E_{mp} \sim 3.0$  keV,  $Al^{3+}$  has  $\sim 0.05$  nC charge with  $E_{mp} \sim 4.0$  keV and  $\sim 0.08$  nC of  $Al^{4+}$  ions with  $E_{mp} \sim 6$  keV.

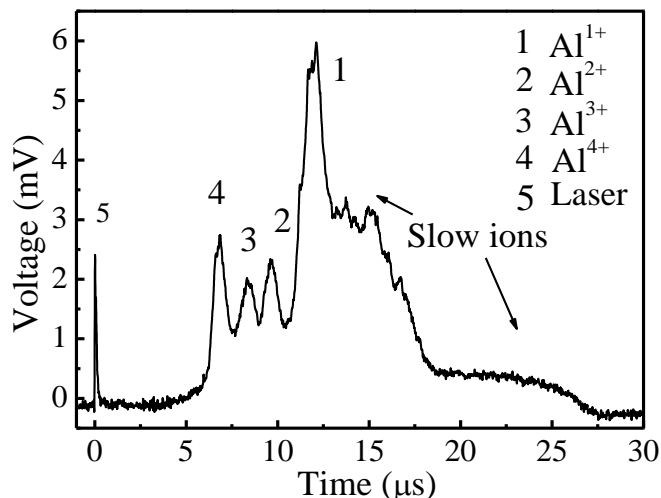


Fig. 2.3 Generation of Al multicharged ions for 5 kV accelerating voltage with a laser pulse energy of 90 mJ shows charge state up to  $\text{Al}^{4+}$ .

### 2.3.1 Laser Pulse Energy

In laser produced plasma the laser parameters (pulse energy, intensity, and pulse width) can affect the plasma density, temperature, ablated mass, and the ion and electron energy. Fig. 2.4(a) shows the relationship between total charge generated and the laser pulse energy incident on the target when 5 kV accelerating voltage is applied. The laser focus spot, angle of incidence, and pulse width were kept constant as described in the experimental section. Initially, the total number of charges rises with the increase of laser pulse energy. For laser pulse energies  $\geq 65$  mJ, the charge reaching the Faraday cup nearly saturates at  $\sim 0.6$  nC. From Fig. 2.4(b) we observe that, as the laser pulse energy is increased, higher Al charge states are observed. Laser pulse energies 60, 65 and 90 mJ generate charges up to  $\text{Al}^{2+}$ ,  $\text{Al}^{3+}$  and  $\text{Al}^{4+}$ , respectively. The laser pulse energy is measured before the UHV chamber window which has  $\sim 8\%$  loss.

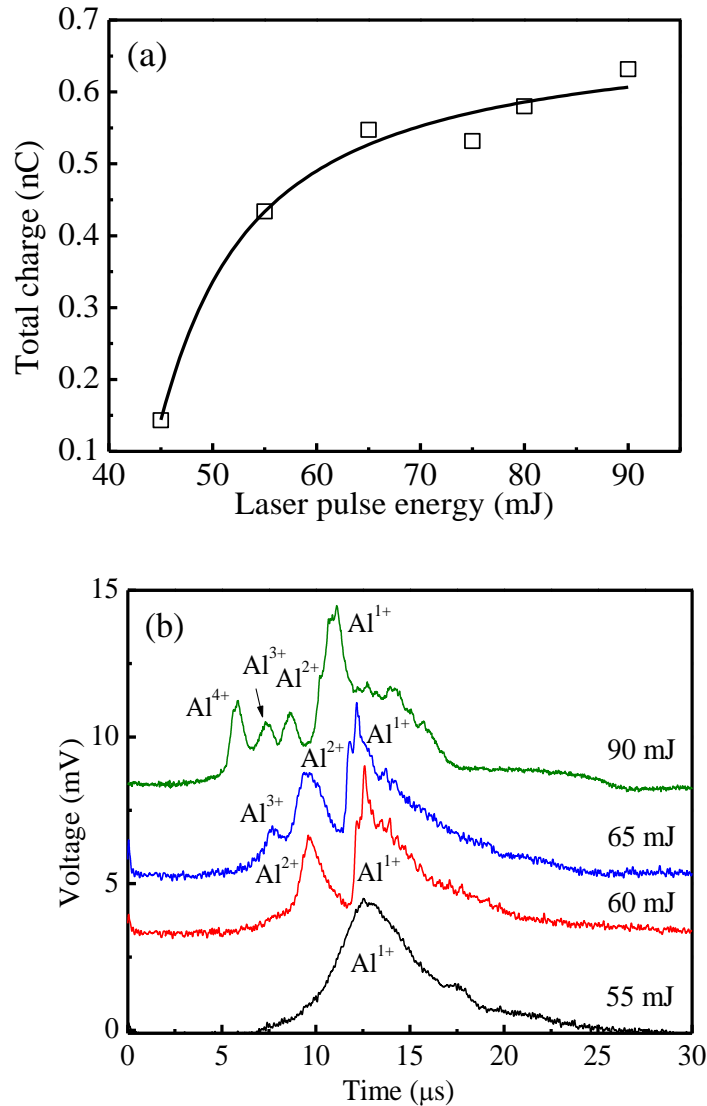


Fig. 2.4 (a) Total charge generation for different laser pulse energies. (b) Charge state generation with laser pulse energy; Accelerating voltage is 5 kV and the laser pulse energy of 45 to 90 mJ

The saturation in charge yield with the laser pulse energy in Fig. 2.4(a) is well explained by the plasma shielding effect, which is frequently observed in experiments on laser drilling [49]. As the laser pulse energy is increased, the plasma density increases as well, reaching a density where the plasma plume absorbs a significant part of the remaining laser pulse energy. At this condition, the degree of plasma ionization increases, producing a higher state ion charge. The main absorption mechanisms of the plasma consist of the electron-atom inverse bremsstrahlung, the electron-ion inverse bremsstrahlung, photoionization, and Mie absorption [50]. Plasma

absorption results in the saturation of charge generation, as shown in Fig. 2.4(a). The energy distribution of Al ions up to  $\text{Al}^{4+}$  for different laser pulse energies is shown in Fig. 2.5. The peak kinetic energy of the Al ions increases with the laser pulse energy. This ion energy distribution gives information on the relative abundance of MCIs. The peak ion energy is increased for the higher charge state ions. The shoulder present at  $\sim 1$  keV in Fig. 2.5(a) in the energy distribution is due to the slow ions.

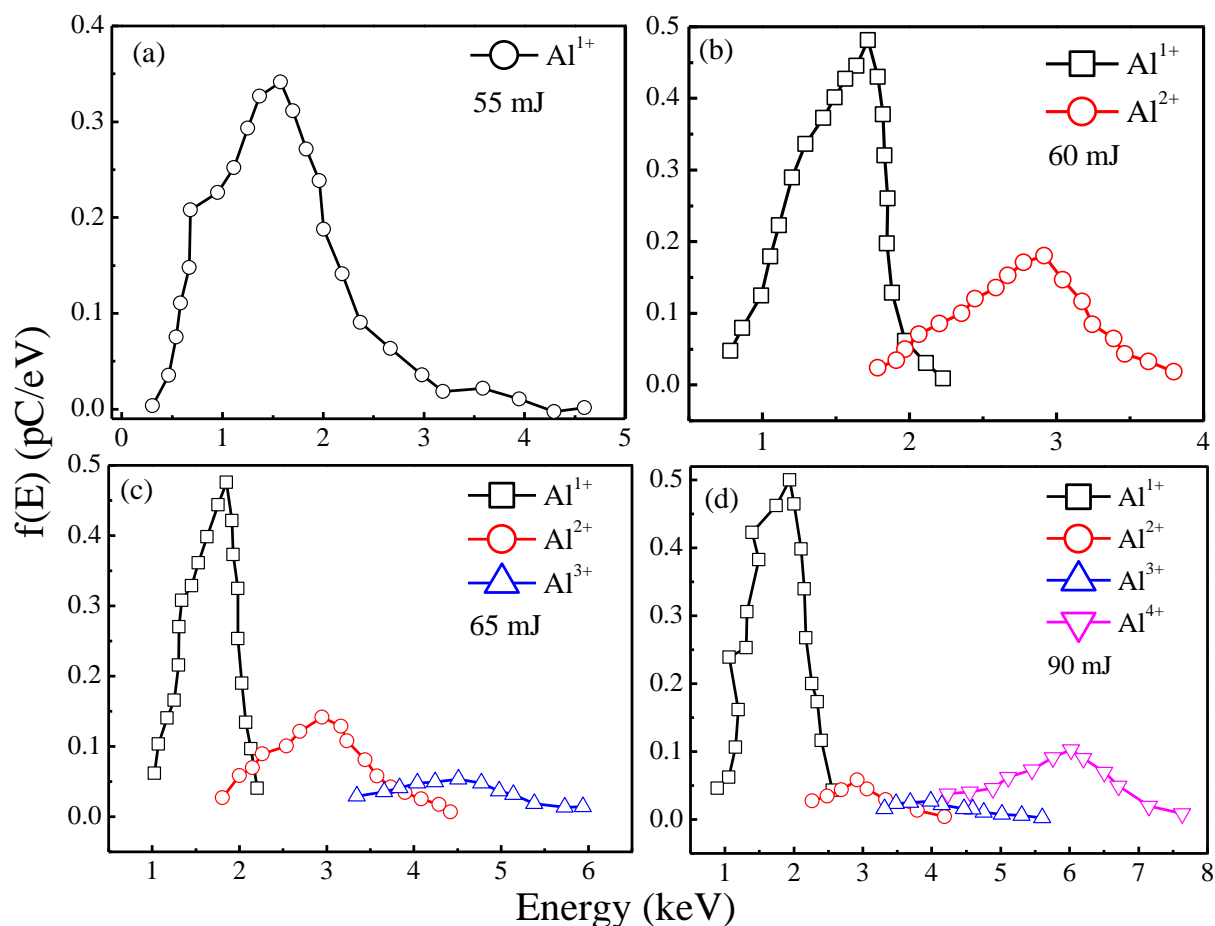


Fig. 2.5 The energy distribution of the generated Al multicharged ions for different laser pulse energies (a) 55 mJ (b) 60 mJ (c) 65 mJ and (d) 90 mJ. An accelerating voltage of 5 kV was applied to Al target.

### 2.3.2 Accelerating Voltage

The ions are accelerated according to their mass-to-charge ratio. During the plume expansion, the thermal interactions, the adiabatic expansion, and the Coulomb interactions are responsible for the ion acceleration in plasma [51]. An applied accelerating voltage allows resolving higher charge states. Fig. 2.6 shows the ion signals for accelerating voltage 4, 5, and 6 kV with laser pulse energy of 65 mJ. Due to plasma shielding, the electric field established between the target and the grounded extraction mesh does not fully penetrate the plasma plume resulting in ion acceleration to energies less than the potential applied to the target. If plasma shielding effects are not considered, the TOF signal varies with the accelerating voltage according to  $TOF = t_a + t_d = \sqrt{\frac{2m}{ZqV}}d + \sqrt{\frac{m}{ZZqV}}S$ , where  $t_a$  is the time that an ion is accelerated from zero velocity at target to velocity  $v$  at the extraction mesh,  $t_d$  is the time that ions drift at constant velocity from extraction mesh to Faraday cup,  $d$  is the distance from target to extraction mesh,  $S$  is the distance from the extraction mesh to the Faraday cup in meters,  $m$  is the mass of Al atom,  $q$  is electron charge,  $Z$  is the charge state, and  $V$  is the applied accelerating voltage. The above equation does not account for the initial ion velocity gained in the plasma sheath. The ion accelerating time  $t_a$  is small compared to ion drift time  $t_d$ . Experimentally, we identified the MCIs using the ratio of calculated TOF of individual MCIs. It is also observed that increasing the accelerating voltage increases the amplitude of the ion signal due to an increase in the charge extraction from the Al plasma due to the electric field between the target and extraction mesh.

With the increase of acceleration voltage from 4 to 5 kV and from 5 to 6 kV, total charge generation increased from  $\sim 0.25$  to  $\sim 0.5$  nC then to  $\sim 0.65$  nC, respectively. When the target-to-Faraday cup distance is reduced to 80-cm, the ratio of the ions detected compared to that for 140-cm distance varied between 2.4 to 2.0 when 1 to 6 kV are applied to the target. For ions extracted by an applied electric field, the main transport loss is due to ion divergence rather than recombination in the UHV chamber. With no accelerating voltage, the plasma ions detected at the two Faraday cup locations differ by a factor of  $\sim 4$  due to both ion divergence and recombination. Therefore, ion transport loss is dependent on the electric field between the target and mesh. The energy distribution of  $Al^{1+}$ ,  $Al^{2+}$  and  $Al^{3+}$  for 4, 5 and 6 kV accelerating voltages

is shown in Fig. 2.7. The ion energy depends on the potential applied to the target and how much of the electric field is shielded by the laser plasma.

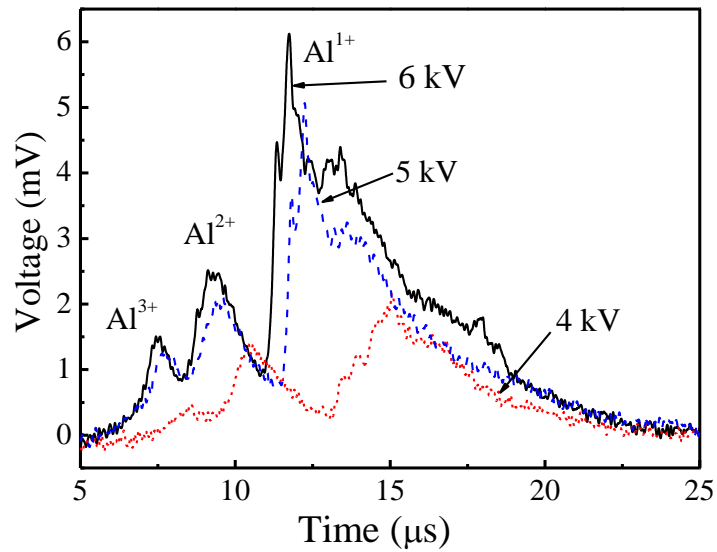


Fig. 2.6 Effect of change of accelerating voltage from 4 to 6 kV on the TOF and the extraction of ions from the laser plasma. The laser pulse energy is 65 mJ.

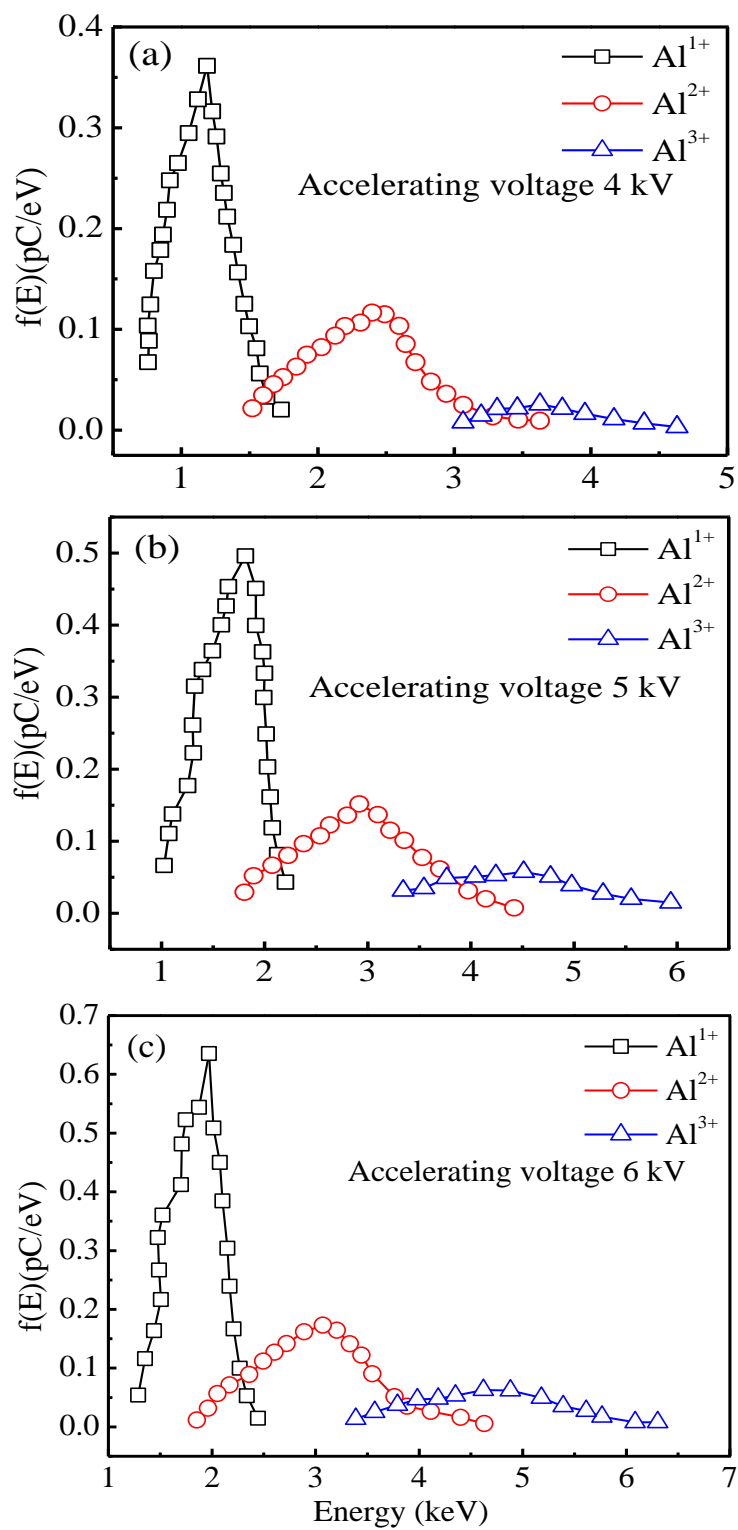


Fig. 2.7 Energy distribution of  $\text{Al}^{1+}$ ,  $\text{Al}^{2+}$  and  $\text{Al}^{3+}$  ions for accelerating voltage of (a) 4 kV (b) 5 kV, and (c) 6 kV. The laser pulse energy is 65 mJ.

The enhancement of the ion extraction with increasing electric field between the Al target and the extraction grounded mesh is due to the retrograde motion of the plasma edge, which exposes more ions to the accelerating field and repels electrons [52]. This phenomenon can be explained using the sheath structure at the plasma edge. The retrograde motion of the plasma and the ion current introduced in the presheath cause the space-charge limited flow in the ion sheath that controls the ion extraction [53].

### 2.3.3 Incident laser angle

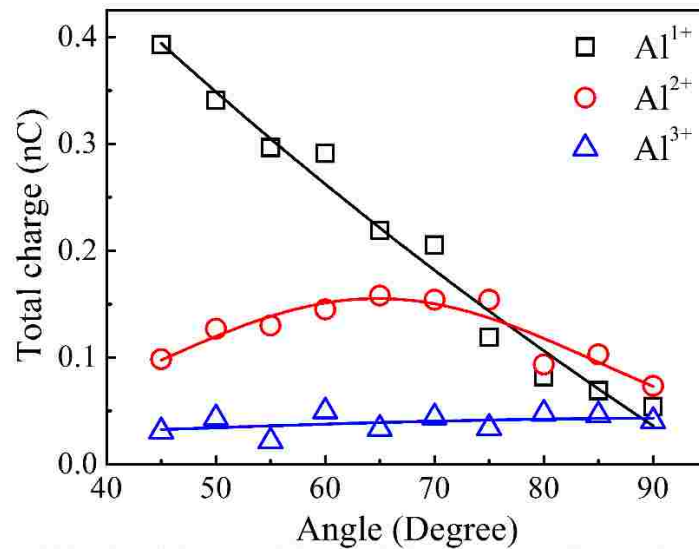


Fig. 2.8. Angular distribution of Al multicharged ions when target was rotating. At 45° the target faced the extraction grounded mesh while the laser incidence angle to the target surface is 45°. At 90° the target surface has a 45° angle with the extraction grounded mesh and the laser is incident perpendicular to the target.

The spatial distribution of MCIs in the plasma plume is not uniform. The laser incident angle was changed by rotating the target relative to the geometrical axis of the drift tube, and the number of the charged ions was collected by the Faraday cup. In Fig. 2.8, the dependences of the number of Al<sup>1+</sup>, Al<sup>2+</sup> and Al<sup>3+</sup> ions collected by the Faraday cup with the change of the target angle for accelerating voltage of 5 kV and laser pulse energy 65 mJ are shown. By changing the target angle, the laser incidence angle  $\theta$  on the target is changed from 45° to 90°, which increases the laser energy density on target by a factor of  $\sim 1.4$  as the laser is incident perpendicular to the



target surface ( $\theta = 90^\circ$ ). This change in laser energy density is not significant enough to cause the behavior observed in Fig. 2.8, which shows significant differences in the spatial distribution of the ions extracted from the plume with  $\text{Al}^{1+}$  showing much higher directionality compared to  $\text{Al}^{2+}$  and  $\text{Al}^{3+}$ . These preliminary results showing different spatial distributions depending on ion charge could be due to the influence of the electric field developed in the plasma sheath. Further studies are needed to characterize the ion charge-dependent angular distribution in laser MCI sources.

## 2.4 SUMMARY

A Q-switched Nd:YAG laser (wavelength  $\lambda = 1064$  nm, pulse  $\tau = 7.4$  ns) was used to generate Al multicharged ions by laser ablation. The total number of ion generation, the maximum charge state, and their kinetic energy are influenced significantly by the incident laser pulse energy. For 5 kV extraction and accelerating voltage applied to the target and a laser pulse energy of 90 mJ, charge state up to  $\text{Al}^{4+}$ , with most probable energy for  $\text{Al}^{4+}$  of 6 keV and total charge of  $\sim 0.65$  nC were detected. Plasma shielding reduces the effective accelerating field established between the target and the grounded extraction mesh resulting in ion acceleration to energies less than the potential applied to the target.

## CHAPTER 3

### ION TRANSPORT LINE COMPONENTS

#### 3.1 INTRODUCTION

We discuss the design and operation of transport line components used in the LMCI source [54, 55]. These components are: (1) A time-of-flight (TOF) ion energy analyzer combined with a three-grid retarding field analyzer used to resolve the various charge states and analyze their energy distributions; (2) Three-electrode electrostatic einzel lens used to focus the MCIs; (3) A set of parallel deflection plates used with a pulsed high-voltage source for MCI pick up based on their TOF; and (4) An electrostatic cylindrical deflector ion energy analyzer (EIA) for MCI selection with energy-to-charge  $E/z$  ratio. The EIA selects ions according to the  $E/z$  ratio from an MCI beam and allows measuring the energy distribution of each charge state. Ion trajectory simulations are done to design transport line components compatible with our experimental conditions and for better understand the operations of the designs. These simulations are carried out utilizing SIMION 8.1 ion optics software [56].

Several groups have reported on the design and operation of ion transport line components. For example, a laser ion source utilizing an Nd:YAG ( $\lambda = 532$  nm,  $\tau = 8$  ns, repetition rate 20 Hz, and maximum laser energy per pulse 30 mJ), Trinczek *et al.*, generated a charge state up to  $\text{Al}^{4+}$  and focused the charges using a three-electrode einzel lens [57]. A pulsed extraction voltage was used to extract and accelerate the ions. The maximum voltage applied for the pulsed extraction and the einzel lens was 30 kV [57]. Yeates *et al.* reported a laser ion source based on Q-switched Ruby laser ( $\lambda = 532$  nm,  $\tau = 8$  ns, laser fluence of 0.1 - 3.9 kJ/cm<sup>2</sup>) to generate charge state up to  $\text{Cu}^{6+}$ . Einzel lenses were utilized to transport and collimate the ion beam, which was detected by a Faraday cup [58]. Nagaya *et al.* reported on an ECRIS to generate fullerene up to a charge state of  $\text{C}_{60}^{3+}$ . The transport line consisted of three electrode extraction system, einzel lens, analyzing magnet, slit assembly, and Faraday cup [59].

### 3.2 EXPERIMENTAL

Two LMCI sources are constructed; one is used to produce aluminum MCIs, while the other is used for carbon MCIs. The transport line components in both systems are similar. A schematic of the MCI source used for the aluminum source is shown in Fig. 3.1. A Q-switched Nd:YAG laser pulse (wavelength  $\lambda = 1064$  nm, pulse width  $\tau = 7.4$  ns (full-width at half maxima (FWHM)), pulse energy 82 mJ on target, with maximum repetition rate of 10 Hz) is used to ablate the Al target. An aluminum disc target of area  $\sim 1$  cm<sup>2</sup>, 99.9% purity, 0.5 mm thickness and with a surface roughness (rms) of 261.77 nm, as characterized by the manufacturer (Alfa Aesar), is placed on a multi-axis translational stage. The laser beam is incident on the Al target surface at an angle of  $\theta = 45^\circ$ . A 50 cm focal length convergent lens is used to focus the laser beam on the Al surface. The laser spot area at focus is  $\sim 0.0024$  cm<sup>2</sup>, as measured by the knife-edge method with the edge scanned at  $45^\circ$  to the laser beam. Throughout the experiment, the Al target is biased at 7 kV. The distance from the target to mesh is 10 cm, and from the center of the target to the chamber wall is 15 cm. This experimental chamber was described in our recent publications [54, 55]. The transport line consists of an einzel lens to focus the ion beam, a pair of deflection plates to select ion charge, a knife edge to measure the ion beam diameter and a Faraday cup (FC) to collect the ions. The distance from the Al target to the center of the middle electrode of the einzel lens is  $\sim 94$  cm; the knife edge is placed  $\sim 30$  cm away from the center electrode of the einzel lens. The deflection plates are at  $\sim 120$  cm away from the Al target and the FC is at 33 cm from the deflection plates. The distance from the Al target to the FC is  $\sim 153$  cm. An EIA can be added before the retarding field MCI analyzer. The EIA allows for the selection of ions with  $E/z$  ratio from an ion beam and can also be used to measure the energy distribution of each charge state. The ion energy distribution can also be obtained from the TOF signal.

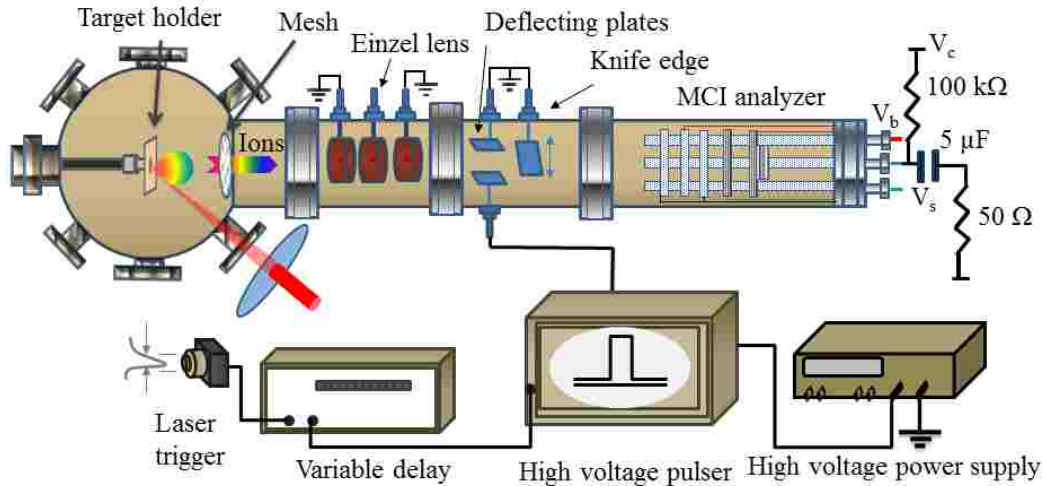


Fig. 3.1 A schematic of the laser MCI source showing the target chamber,  $V_c$  is the Faraday cup voltage, and  $V_s$  is the suppressor voltage, and  $V_b$  is the barrier voltage.

### 3.3 DESIGN AND OPERATION OF THE TRANSPORT LINE COMPONENTS

#### 3.3.1 Faraday cup and three-electrode retarding field analyzer

A time-of-flight energy-to-mass  $E/m$  analyzer consists of a drift tube terminated by a Faraday cup (FC) with secondary electron suppressor electrode (SE). A three-grid retarding field ion energy analyzer (RIA) is used to analyze the energy of the MCIs. The FC and the SE are made of aluminum and have a diameter of 5 cm. The RIA consists of three nickel mesh with a diameter of 5 cm, 100  $\mu\text{m}$  thickness and 70% opening area, separated by 1 cm and placed with the closest mesh to aluminum target at 143 cm. The outer two electrodes of the RIA are grounded while a variable positive voltage is applied to the center electrode to measure the energy distribution of the ions. The effect of voltage on the RIA was recently discussed [54]. The FC, SE, and the retarding field ion energy analyzer are placed on a 6-inch CF flange attached to the end of the drift tube. Fig. 3.2(a) shows a schematic of the FC with suppressor electrode connected to the three-electrode retarding field analyzer. A negatively biased suppressor electrode is used to suppress the signal from secondary electrons due to ion bombardment of the FC. The suppressor electrode keeps the electrons from leaving the FC. We applied -70 V to the Faraday cup. By applying a variable negative voltage to the suppressor electrode, starting from ground potential, while observing the shape of the ion signal, we can detect the voltage needed to

suppress the effect of secondary electrons. The time-of-flight signal is affected by the secondary electron emission for up to  $-70$  V applied to the suppressor electrode. That effect is reduced as we increase the negative voltage applied to the suppressor. At  $-80$  V, there is no effect due to secondary electron emission. With more negative voltage applied to the suppressor, the shape of the ion signal does not change. In our experiment, we use  $-140$  V for the suppressor voltage. Fig. 3.2(b) shows the effect of suppressor voltage for  $-40$ ,  $-60$ , and  $-90$  V, respectively. The TOF signal shown is for  $82$  mJ laser energy on target and no acceleration voltage applied.

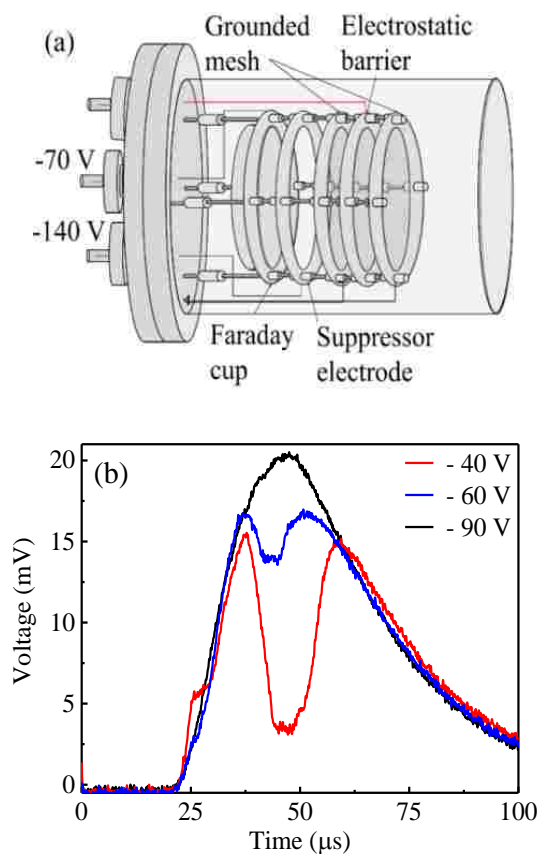


Fig. 3.2 (a) Schematic of the TOF mass-spectrometer, (b) TOF spectrum for suppressor voltage of  $-40$ ,  $-60$ , and  $-90$  eV.

The total charge delivered to the Faraday cup  $Q_i$  is given by  $Q_i = \frac{1}{R_L} \int V_F(t) dt$ , where  $V_F(t)$  is the voltage applied to the Faraday cup, and  $R_L$  is the  $50 \Omega$  internal resistance of the

oscilloscope. Fig. 3.3(a) shows the MCI signal with charge state up to  $\text{Al}^{4+}$  for accelerating voltage of 7 kV and laser pulse energy on target of 82 mJ. A fast-positive signal is observed due to the photoelectric effect where photons generated from the laser plasma with energy above the work function of the FC material cause photoemission. The extracted ions from the plasma plume by the electric field between the target and the grounded mesh are detected by their TOF signal measured by the FC. An ion generated at the target with zero energy would reach the FC after a time-of-flight  $TOF = t_a + t_d = \sqrt{\frac{2m}{ZeV}}d + \sqrt{\frac{m}{2ZeV}}S$ , where  $t_a$  is the time that an ion is accelerated from zero velocity at target to velocity  $v$  at the extraction mesh,  $t_d$  is the time that ions drift at constant velocity  $v$  from the extraction mesh to the FC,  $d$  is the distance from the target to the extraction mesh,  $S$  is the distance from the extraction mesh to the FC,  $m$  is the mass of Al atom,  $e$  is the electron charge,  $Z$  is the charge state, and  $V$  is the applied accelerating voltage. The above equation does not account for plasma ion shielding, voltage drop on target, and ion acceleration in the expanding plasma. The ion accelerating time  $t_a$  is small compared to the ion drift time  $t_d$ . The procedure to determine the charge state of the ions using their TOF was previously discussed [54, 55]. The process followed for deconvolution of the total TOF spectrum in Fig. 3.3(a) into separate ion charges is accomplished by, first, assigning a curve fit to the TOF signal using the peak fitting option in Origin-lab 9.1 software. Then, the TOF signal for each charge is separated using the selected peak position obtained by Origin-lab. Integrating over the time range and dividing the integral by the  $50 \Omega$  terminal resistance of the oscilloscope gives the total charge for each charge state delivered to the FC. The signal observed by the FC is the sum of these separated ion signals. The energy distribution for each charge state is calculated for the selected peak position. Peak position selection for the TOF signal corresponding to each charge can be also obtained directly from the TOF signal without curve fitting. These two approaches give almost similar total charge (within 5%) and energy distribution for each charge state.

The total charge reaching the FC is  $\sim 640$  pC when no einzel lens voltage is applied. Fig. 3.3(b) shows the energy distribution of the MCIs calculated from the TOF signal of the ions. For  $\text{Al}^{1+}$ , we detect  $\sim 150$  pC charge per pulse with most probable energy  $E_{mp} \sim 2.8$  keV,  $\sim 180$  pC for  $\text{Al}^{2+}$ ,  $E_{mp} \sim 5.5$  keV,  $\sim 260$  pC for  $\text{Al}^{3+}$ ,  $E_{mp} \sim 8.2$  keV and  $\sim 50$  pC for  $\text{Al}^{4+}$ ,  $E_{mp} \sim 11$  keV. The peak ion currents are  $55 \mu\text{A}$  for  $\text{Al}^{1+}$ ,  $103 \mu\text{A}$  for  $\text{Al}^{2+}$ ,  $150 \mu\text{A}$  for  $\text{Al}^{3+}$  and  $100 \mu\text{A}$  for  $\text{Al}^{4+}$ . The ion energy depends on the plasma parameters, the potential applied to the target, and the

shielding effect of the laser plasma. The ion energy distribution  $f(E)$  is calculated from the ion kinetic energy  $E_K = \frac{1}{2}mv^2$ , where the velocity  $v$  is measured from the TOF signal of the MCIs.

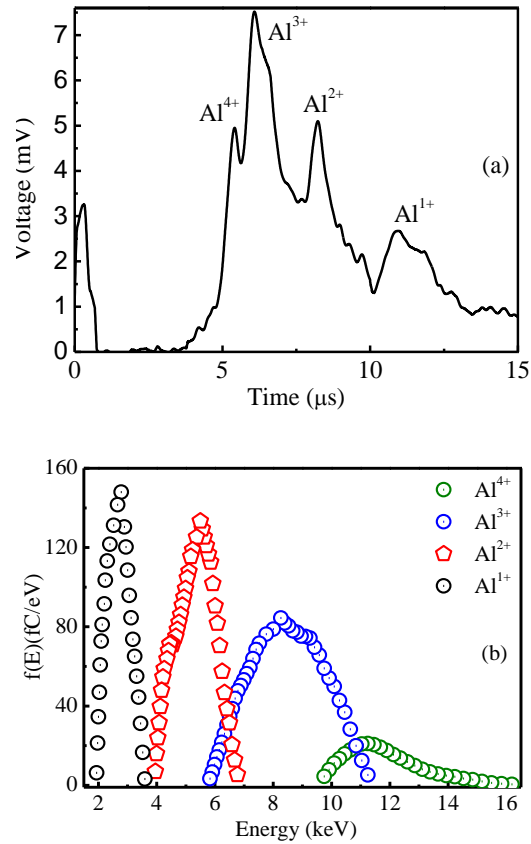


Fig. 3.3 (a) Time-of-flight analyzer signal for MCIs generating up to  $\text{Al}^{4+}$  for 7 kV accelerating voltage and 82 mJ laser energy on target, (b) energy distribution of the MCIs.

The average current that the described laser MCI source can deliver depends on the laser pulse repetition rate and the current rating of the power supply providing high voltage bias to the target. Due to their higher velocity, the ions pass the grounded grid before the expanding plasma. As the expanding plasma plume from the target reaches the grounded grid, the high voltage power supply is connected to the ground potential through the plasma resistance. This resistance can be low, resulting in a drop-in power supply voltage. In our system, the Q-switched Nd:YAG laser used has a maximum repetition rate of 10 Hz, while the power supply limits the repetition

rate to  $\sim 5$  Hz due to time required for the voltage to recover after each pulse. At 5 Hz operation, the average current for each charge states are  $\sim 0.75$  nA for  $\text{Al}^{1+}$ ,  $\sim 0.9$  nA for  $\text{Al}^{2+}$ ,  $\sim 1.3$  nA for  $\text{Al}^{3+}$ , and  $\sim 0.25$  nA for  $\text{Al}^{4+}$ .

One application of the Al LMCI source is in implantation of SiC to form a *p*-type layer. Saks *et al.*, implanted SiC with 30-keV Al ions to a dose of  $\sim 4 \times 10^{11}$  ions/cm<sup>2</sup> [60]. The implant layer doping was  $1 \times 10^{17}$  ions/cm<sup>3</sup> with thickness (box profile) of 500 nm. At  $\sim 5$  Hz repetition rate, our LMCI source can provide a dose rate of  $\sim 5 \times 10^8$  ions/(cm<sup>2</sup>.s) for an ion beam area of  $\sim 20$  cm<sup>2</sup> obtained without focusing. Therefore, a SiC wafer of  $\sim 20$  cm<sup>2</sup> area can be implanted with Al MCI to form a shallow *p*-doped layer in  $\sim 2.8$  hour. This dose can be further increased by implanting before the ions pass the three meshes of the retarding ion energy analyzer which combined allows only  $\sim 34\%$  of the ions to pass to the Faraday cup.

The ion yield and charge state from laser sources vary widely depending on the laser source and irradiation conditions [61]. Using a table-top femtosecond Ti:sapphire laser (wavelength  $\lambda = 800$  nm, pulse width  $\tau = 200$  fs, pulse energy up to 0.5 mJ, and repetition rate 1 kHz), it was possible to generate up to  $\text{Si}^{12+}$  and  $\text{W}^{26+}$  with maximum energies in the keV range per charge state [62, 63]. An XeCl excimer ( $\lambda = 308$  nm,  $\tau = 20$  ns) laser-based MCI source was developed, and extensive studies on the characteristic of the produced MCI were reported [27, 28]. Ablation of the Cu target using 70 mJ ( $56 \text{ J/cm}^2$   $3.5 \times 10^8 \text{ W/cm}^2$ ) laser energy per pulse, maximum charge state generation was  $\text{Cu}^{5+}$ , with most ions singly and doubly ionized and 16 % ionization of the plasma [27, 28]. An Nd:YAG (wavelength  $\lambda = 1064$  nm, pulse width  $\tau = 7$  ns, and laser fluence of  $10\text{-}110 \text{ J.cm}^{-2}$ ) was used to produce carbon MCI up to charge state  $\text{C}^{4+}$  with the total maximum charge was  $\sim 25$  nC [64].

Electron cyclotron ion sources (ECRIS) and electron beam ion sources (EBIS) generate MCI from gases or external ion or laser ablation sources [65-68]. An ECR ion source operating at 18 GHz microwave of power 1.6 kW generated 560  $\mu\text{A}$  of  $\text{O}^{7+}$ , 620  $\mu\text{A}$  of  $\text{Ar}^{11+}$ , 430  $\mu\text{A}$  of  $\text{Ar}^{12+}$ , 430  $\mu\text{A}$  of  $\text{Xe}^{20+}$  [65]. A maximum current of 1.42 mA  $\text{Ar}^{12+}$  and 1.1 mA  $\text{Xe}^{26+}$  was reported for an ECRIS operating at 24 GHz with 7 kW power [66]. Production of currents at the mA level (10  $\mu\text{s}$  pulse length) of different ion charges was reported for an EBIS equipped with 5 T, 2-m long and 204 mm diameter warm bore superconducting solenoid magnet and electron gun operating at 10 A. This EBIS can produce high charge state ions of practically any species,



however, it was mainly used to generate  $\text{Au}^{32+}$  and  $\text{Fe}^{20+}$  [67]. An EBIT with 5 T magnetic field, 800 mA electron beam current, and 200  $\mu\text{m}$  electron beam radius was able to produce  $\text{Ar}^{17+}$  [68]. Commercial ECRIS made by *Pantechnik* operate in a continuous mode [69]. When using superconducting magnets, they can produce high continuous current, e.g., ECRIS model *Supernannogan* can generate 200  $\mu\text{A}$   $\text{C}^{4+}$  [69]. The EBIS are generally pulsed (10-300 Hz), although they can operate in a continuous mode with a low ion yield. For example, *DREEBIT* EBIS can produce  $2 \times 10^6$   $\text{C}^{6+}$  ions/pulse [70]. The laser MCI sources produce plasma plume by laser ablation and ionization of a solid target. The ion yield from LMCI sources vary significantly with the laser source used. LMCI sources are mostly experimental and have not been so far commercialized. The availability of many pulsed laser deposition (PLD) systems makes the development of LMCI systems for labs equipped with PLD relatively straightforward, with mainly the ion transport line components needed. The laser MCI system and its transport line can operate in ultrahigh vacuum with a relatively small pumping capacity since no gas load is handled and no differential pumping is needed. High ion yield per laser pulse can be generated. With a relatively small Nd:YAG laser (wavelength 1064 nm, 15 ns pulse width, 400 mJ pulse energy), it is possible to generate  $\sim 8 \times 10^9$   $\text{C}^{6+}$  ions/pulse [71].

### 3.3.2 Einzel lens

A three-electrode electrostatic einzel lens is used to focus the MCIs. An einzel lens is a three-element lens with the outer two electrodes held at the same potential (in our case grounded), while the central electrode is held at a potential that can be varied for focusing at different distances. This lens does not vary the energy of the charged particles. Several groups reported on the simulation and analytical solutions of charged particle trajectory in einzel lenses. Sise *et al.*, modeled multi-element cylindrical electrostatic lenses for focusing and controlling charged particles. Numerical modeling was done using SIMION [56] and LENSYS [72], and the results were described in terms of the ratios of the electrode lengths and gaps, and the ratios of the controlling voltages [73]. For three, four, and five cylindrical electrode lenses, higher voltage ratios for middle electrodes were shown to result in the lowest spherical and chromatic aberration coefficients [74]. Abdelrahman used SIMION to design a three electrode einzel lens system for focusing 5 keV singly-charged oxygen ions [75]. Different lens parameters were investigated with and without space-charge effects [75]. For 40 mm aperture diameter lens separated by 20

mm gaps, the best focal length was 550 mm from the end of the lens, which was achieved for an applied voltage of -4.5 kV [75]. An analytical method to evaluate the potential and the fields for a cylindrical einzel lens was described and the solution compared well to SIMION modeling [76]. We describe the construction and testing of a three-electrode einzel lens for MCI focusing.

### 3.3.2.1 Fabrication

Fig. 3.4 shows the schematic of the einzel lens consisting of three electrodes, of which the outer two electrodes are grounded, and the ion beam focusing is done by varying the voltage on the center electrode. These electrodes are made out of stainless-steel tubes of 33 mm length and 43 mm inside diameter and separated by ~1 cm. A high voltage power supply provides variable negative voltage to the central electrode of the einzel lens. The grounded knife edge, shown in Fig. 3.1, has a dimension of 5 x 5 cm and can be move up and down by an external linear feedthrough to intercept the ion beam path to the FC. The ion beam diameter delivered to the FC is measured with the knife-edge intersecting the ions beam from a fully open position, through the beam, to the position where the beam is fully blocked. The TOF signal of different MCIs are observed and used to calculate MCI transmission at certain knife-edge positions. The number of ions reaching the FC with respect to knife-edge position is plotted. The full-width and half-maximum (FWHM) value of the derivative of that curve gives an estimate of the diameter of the ion beam. Due to ion divergence, with the central electrode of the einzel lens at ground, the ion beam width is large enough to fill the 43 mm ID of the lens resulting in a portion of the generated MCIs hitting the einzel lens and other parts of the transport line rather than reaching the FC. Focusing the ion beam increases the total charge delivered to the FC.

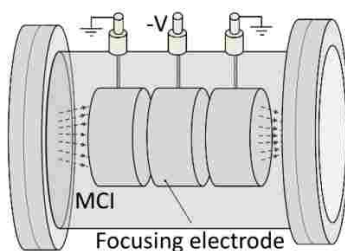


Fig 3.4 Schematic of the three-electrode einzel lens.

### 3.3.2.2 Testing

Changing the einzel lens voltage affects the total number of charges delivered to the FC. Initially, with the increase of einzel lens voltage, the total charge reaching the FC increases because the electric field focuses the ion beam, reducing the ion lost in the transport line due to the divergence of the ion beam. After a certain high voltage applied to the central electrode of the einzel lens, the number of charges, with a specific charge state, delivered to the FC decreases as the ion beam is defocused at the location on the FC to an area larger than the FC diameter. The maximum charge delivered to the FC for  $\text{Al}^{1+}$  is  $\sim 224$  pC at  $-2.4$  kV, for  $\text{Al}^{2+}$   $\sim 270$  pC at  $-2.2$  kV, for  $\text{Al}^{3+}$   $\sim 400$  pC at  $-2.8$  kV, and for  $\text{Al}^{4+}$   $\sim 90$  pC at  $-2.0$  kV. The ratio of maximum charge reaching the FC and the total charge when no voltage is applied to the einzel lens is  $\sim 1.5$  for  $\text{Al}^{1+}$ ,  $\text{Al}^{2+}$ , and  $\text{Al}^{3+}$ , while for  $\text{Al}^{4+}$  the ratio is  $\sim 1.8$ . Ion divergence from the einzel lens to FC is  $\sim 0.5^\circ$  for  $\text{Al}^{1+}$ ,  $\text{Al}^{2+}$ ,  $\text{Al}^{3+}$  and for  $\text{Al}^{4+}$  the divergence is  $\sim 0.75^\circ$  estimated by the ratio of maximum charge reaching the FC and the total charge when no einzel lens voltage is applied. At higher einzel lens voltage, the number of charges delivered to the FC is decreased. This decrease in the total charge delivered to the FC is because the defocused ion beam diameter at the location of the FC is increased and is larger than the FC diameter.

Fig. 3.5 shows measurements of the ion beam diameter at the knife edge location (300 mm away from the center of the focusing lens) for different voltages applied to the einzel lens. When the central electrode of the einzel lens is grounded, the different MCIs fill the transport line and the beam diameter measured at knife edge is nearly equal to the inner diameter of the einzel lens. For  $\text{Al}^{1+}$  and  $\text{Al}^{2+}$ , varying the einzel lens voltage from zero to  $-4.0$  kV decreases the beam diameter at the knife edge. At  $-4.0$  kV, the ion beam diameter for  $\text{Al}^{1+}$  and  $\text{Al}^{2+}$  is  $\sim 1.5$  mm, while  $\text{Al}^{3+}$  ion has a minimum beam diameter of  $\sim 2.8$  mm at  $-3.2$  kV einzel lens voltage, and  $\text{Al}^{4+}$  has a minimum ion beam diameter of  $\sim 2.6$  mm at  $-2.7$  kV. The difference in the focused beam diameter for different charge states is due to their different energy distributions and beam divergence. The inset of Fig. 3.5 shows the ion beam diameter for  $\text{Al}^{3+}$  and  $\text{Al}^{4+}$  for einzel lens voltage range from  $-2.5$  to  $-3.5$  kV with a step change of  $100$  V. At  $-4.0$  kV the ion beam diameters of  $\text{Al}^{3+}$  and  $\text{Al}^{4+}$  are increased to  $\sim 11$  and  $\sim 13$  mm, respectively. Due to the distance from the einzel lens to FC and ion beam defocusing, all the ions passing through knife do not reach the FC. When the ions are focused to minimum beam diameter at the knife edge, the

number of ions reaching the FC for each charge state is more than 85% of their value when the ions are focused on the FC surface. This loss in the total number of ions detected when measuring the ion focus diameter by the knife edge underestimates the beam diameter at focus by  $\sim 15\%$  when assuming a Gaussian ion beam shape. The voltage applied to the einzel lens for minimum beam diameter and the resulting beam diameter depends on the charge state because the different charge states have different spatial beam divergence starting from the source [77]. Although each charge state is accelerated to a potential that is almost directly dependent on their charge state, the energy distribution of ions with different charge states vary [78].

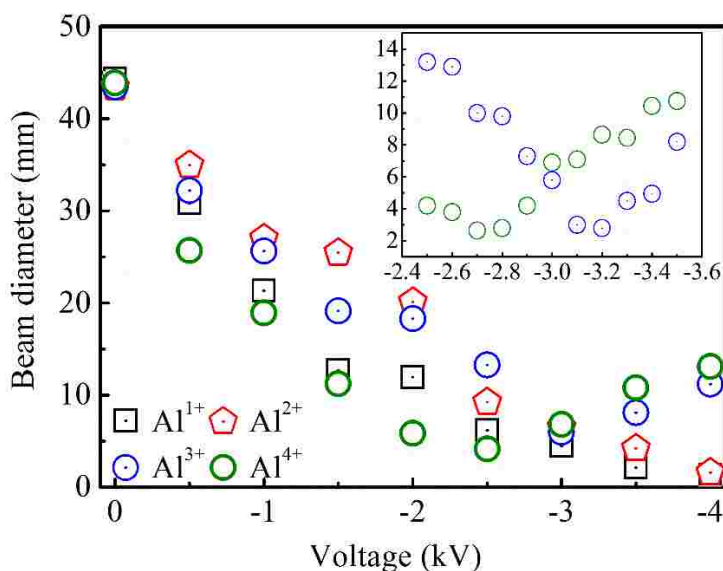


Fig 3.5 Experimental results of the effect of einzel lens voltage on the beam diameter of Al<sup>1+</sup> to Al<sup>4+</sup> at knife edge. Inset shows beam diameter of Al<sup>3+</sup> and Al<sup>4+</sup> with focusing voltage in a narrow voltage region where best focus is obtained.

### 3.2.2.3 Simulation

SIMION 8.1 ion optics simulation software is used for the modeling of the einzel lens. SIMION uses the 3D potential array approach to estimate the electrostatic fields created by the electrode geometry. A potential array contains a collection of square mesh of points. The potential at points outside of the electrodes is determined by solving the Laplace equation via the finite difference method [79]. For computation, we choose a geometry closely representing the actual experimental chamber used. The model simulates a three-electrode einzel lens with

dimensions similar to our experiment. To simulate the ion source, the experimentally obtained ion divergence for each charge state and the spatial distribution (fitted with Gaussian distribution) at the knife edge is used. In the SIMION model, we defined the spatial distribution of the ions with Gaussian 3D distribution with mean at origin and FWHM of 40 mm, as calculated from the knife edge experiment. Fig. 3.6 shows the lens geometry and ion beam trajectories in the SIMION model. From the experimental results the mean energy and FWHM of the energy distribution are:  $\text{Al}^{1+}$  2.8 kV and 1.1 kV;  $\text{Al}^{2+}$  5.5 kV and 1.5 kV;  $\text{Al}^{3+}$  8.2 kV and 3.6 kV, and for  $\text{Al}^{4+}$  11 kV and 2.7 kV, respectively. For modeling the ion focusing distance and focus spot size, using an accurate ion energy source distribution is crucial. Fig. 3.7 shows the difference in ion trajectories between a cylindrical ion energy distribution (a) and a Gaussian 3D ion energy distribution when -3.5 kV is applied to the center electrode (b). For the cylindrical ion distribution, the  $\text{Al}^{4+}$  ions focus at a distance of 156 mm from the center electrode, while when a Gaussian ion distribution is used, that distance is 167 mm. The minimum beam diameter for the cylindrical ion source is 1.2 mm, whereas for the 3D Gaussian distribution it is 1.9 mm.

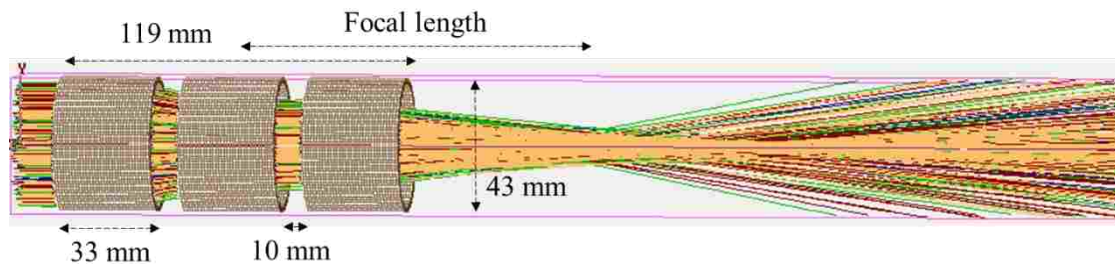


Fig. 3.6 SIMION simulation showing the  $\text{Al}^{1+}$ ,  $\text{Al}^{2+}$ ,  $\text{Al}^{3+}$ , and  $\text{Al}^{4+}$  charges are indicated by blue, red, green and yellow respectively.

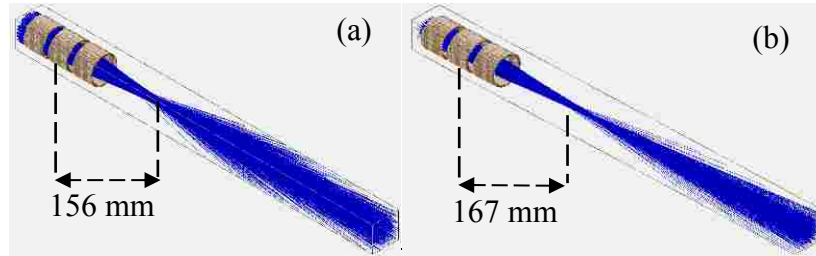


Fig. 3.7 Effect on ion trajectory for ion source distribution.  $\text{Al}^{4+}$  ions are focusing with applied voltage - 3.5 kV with the input ions having a Gaussian energy distribution with mean of 11.5 kV and FWHM of 2.7 kV. (a) A cylindrical spatial distribution for ion source center position at (0, 0, 0) with radius 21 mm. (b) Gaussian 3D spatial distribution with center at (0, 0, 0) and FWHM of 19 mm on each axis.

The ion beam diameter is measured at 30 cm from the central electrode of the einzel lens. This distance is like the distance from the central electrode to the knife edge in the experiment. Fig. 3.8 shows simulated results for the effect of change of einzel lens voltage on the ion beam focus diameter at knife edge using SIMION. Increasing the einzel lens focusing voltage from zero to -3.5 kV continuously decreases the beam diameter of the ions. The minimum beam diameter for  $\text{Al}^{1+}$ ,  $\text{Al}^{2+}$ ,  $\text{Al}^{3+}$  and  $\text{Al}^{4+}$  is  $\sim 2$  mm observed for einzel lens voltage of -2.7 kV. In the SIMION simulation, ions with different charges focus to the same beam diameter because the ions are assumed to have the same energy per charge.

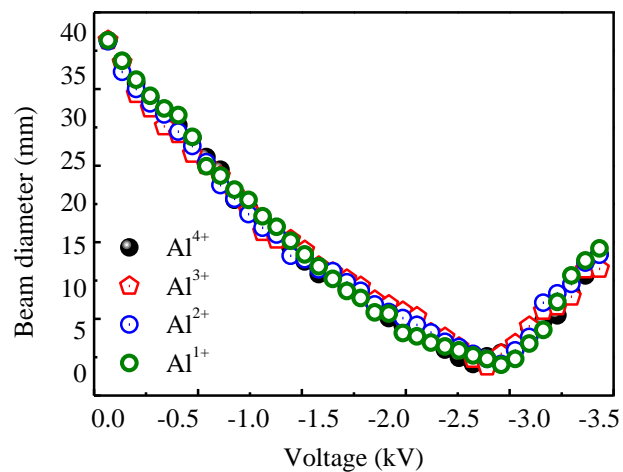


Fig. 3.8 Simulation of the effect of change of einzel lens voltage on (a) beam diameter of  $\text{Al}^{1+}$ ,  $\text{Al}^{2+}$ ,  $\text{Al}^{3+}$ ,  $\text{Al}^{4+}$  ions measured at 30 cm distance from the central electrode of the einzel lens.

### 3.3.3 Ion selection

Ion acceleration by the internal electric field generated in the plume and by the external applied electric field depends on the charge state. The higher charge states for an element are accelerated to a higher drift velocity than the lower charge states. Therefore, selection of ions with certain mass-to-charge ratio  $m/z$  can be accomplished by applying a voltage pulse to a set of deflection plates that is synchronized to pick a subset of the ions during their TOF. Several groups reported on the use of pulsed ion deflection for selection or removal of ions with  $m/z$ . Vlasak *et al.*, reported on the design and operation of an interleaved comb ion deflection gate device for selection of ions for particular  $m/z$  for TOF mass spectroscopy [80]. With a temporary and short-range deflection field, Guilhaus *et al.*, removed the selected ions with certain  $m/z$  ratio from the TOF signal [81]. Toker *et al.*, reported on a mass selection technique to clean a keV ion beam of undesirable ion masses using an electrostatic deflector and two grounded shielding electrodes placed before and after the electrostatic deflector [82]. A deflection device consists of two parallel plates for ion injection followed by two sleeve plates to reduce the ion scattering was reported [83].

We have used a pair of deflection plates to select a subset of the ions based on their TOF. For example, if one ion charge is to be selected, the deflection plates are operated to deflect the ions except the selected ion charge, which drifts to the FC. The applied voltage pulse width on the deflecting plates determines the ion pulse width reaching the FC. Therefore, it is possible to select a subset of ions that can contain more than one charge or to select a kinetic energy range of a certain charge.

#### 3.3.3.1 Fabrication

The deflecting plates are made of aluminum and have a length of 6 cm, width of 5 cm, a thickness of 0.5 cm, and are separated by 10 cm. Insulated feedthroughs are used to mechanically support the deflection plates and apply voltage to them. One deflection plate is grounded while a voltage pulse is applied to the other plate. The location of the deflection plates in the transport line is schematically shown in Fig. 3.1. The distance from the Al target to the center of the deflecting plates is ~120 cm. The high-voltage pulse to select specific charge is generated using a combination of a delay generator, a high-voltage power supply, and a high-voltage pulse

generator (IXYS Colorado, PVX-4110). The external trigger from the laser power supply, which controls the Q-switching of the laser, is used to trigger the pulsed delay generator, which in turn triggers the high-voltage pulse generator at a specific delay time from the laser pulse. The delay and the width of the high-voltage pulse are determined by the delay generator pulse and can be varied. We apply up to -10 kV pulse with variable pulse width and delay to the deflection plates.

### 3.3.3.2 Testing

The vertical deflection of ions due to the electric field of the deflecting plates can be calculated from  $S = \frac{V_d L}{2dV_{acc}} (D + \frac{L}{2})$ , where  $S$  is the deflection of ion vertically from the center of the two plates at a distance of  $D$  from the end of the deflecting plates,  $V_d$  is the deflecting voltage,  $L$  is the deflecting plate length,  $d$  is the separation between plates, and  $V_{acc}$  is the ion accelerating voltage. MCIs with different charges will be deflected together as long as they experience the same accelerating voltage (their kinetic energy is proportional to their charge). We apply -10 kV voltage to deflect all ions outside the Faraday cup. Then, to select  $\text{Al}^{1+}$ ,  $\text{Al}^{2+}$ ,  $\text{Al}^{3+}$ , and  $\text{Al}^{4+}$ , the high-voltage pulse is applied to the deflection plate at 8.0, 5.8, 4.5, and 3.4  $\mu\text{s}$  after the laser trigger. The energy distribution of the selected MCI depends on the selected ion pulse width. By selecting a subset of an ion charge, that energy distribution can be smaller than the distribution before the deflection plates.

Fig. 3.9 shows signal from  $\text{Al}^{1+}$  to  $\text{Al}^{4+}$  ions as they are picked up by the applied high-voltage pulse with a width of 1  $\mu\text{s}$ . The TOF signal of the Al ions after charge selection with the pulsed deflection plates is shown. The inset shows the applied high-voltage pulse for selecting  $\text{Al}^{3+}$  MCI when 7 kV is applied to the Al target. The deflection plate voltage is maintained high enough to deflect all ions away from the FC. Then, a negative high-voltage pulse is applied to allow only the  $\text{Al}^{3+}$  ions. For example, a pulse delay by 4.5  $\mu\text{s}$  to the laser trigger allows only the  $\text{Al}^{3+}$  MCI to reach the Faraday cup.



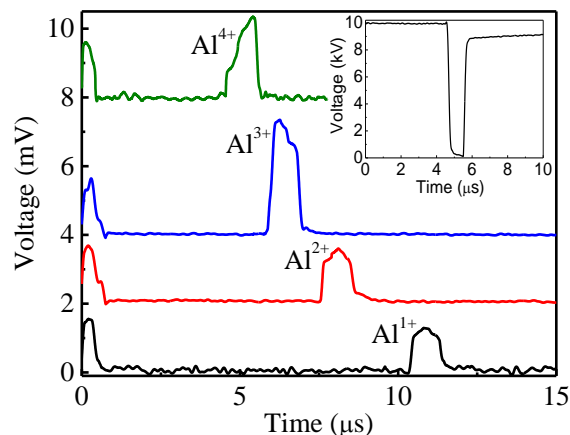


Fig. 3.9 Selection of MCI from Al<sup>1+</sup> to Al<sup>4+</sup> for deflection plate voltage -10 kV with pulse width 1 μs. The delay of the deflection pulse is determined by the TOF of the ions. Inset shows the voltage pulse for selecting Al<sup>3+</sup>. Without ion selection, the TOF spectrum consists of all the MCIs generated traveling towards the FC, is shown in Fig. 3.2(a).

### 3.3.4 Electrostatic ion analyzer

Electrostatic cylindrical ion energy analyzers (EIA) are often used for analysis or selection of ions with a specified range of energy-to-charge ratio  $E/z$  [84]. The EIA consists of two curved parallel plates held at different potentials and a radial cylindrical design with a deflection angle that varies depending on the application. A total deflection angle of 127° is often used in energy analysis because this angle allows an ion beam focused onto the entrance slit to be also focused onto the exit slit, improving ion transmission through the EIA [85]. The EIA operated with TOF detection of MCIs allows  $E/z$  ratio and  $z$  to be identified independently. Therefore, the energy distribution of ions in each charge state can be obtained by applying different voltages between the EIA electrodes. An EIA was previously used to separate laser-generated MCIs and analyze their energy distribution. An EIA was used to probe Si MCIs, generated by femtosecond ablation, with  $E/z$  of 0.4-33 keV and energy resolution of 8% FWHM [62]. Torrisi *et al.*, used an EIA, with 90° bending angle, followed by TOF detection to study ion emission from Ta laser-generated plasma [86]. Using a Nd:YAG laser with 270 mJ/pulse, they detected up to Ta<sup>5+</sup> in the ablation plume without external ion acceleration. Mean ion energies were 250 eV/ $z$ . Shan *et al.*, used an EIA combined with TOF detection, equipped with an

electron multiplier, to probe charge state and energy distribution of the ions produced by a laser ion source [87]. Using Nd:YAG laser operating at 1064 nm with 8 ns pulse width and an energy of 1 J/pulse, up to  $\text{Al}^{12+}$  and  $\text{Pb}^{7+}$  were observed. We have constructed an EIA and used it to detect MCIs of Al and C.

### 3.3.4.1 Fabrication

The EIA is placed before the three-grid energy analyzer and Faraday cup without changing the distance from the target to the Faraday cup, as shown in Fig. 3.10. Ions enter the analyzer at one side and either pass through the other side or collide with the walls of the analyzer, depending on their initial kinetic energy. The ions selected by the EIA have a range of  $E/z$  obtained from the equation  $\frac{E}{z} = \frac{eU}{[2 \ln(\frac{R_2}{R_1})]}$ , where  $E$  is the kinetic energy of the ion,  $e$  is the electron charge,  $U$  is the total potential across the plates,  $R_1 = 145$  mm is the inner radius, and  $R_2 = 183$  mm is the outer radius [24]. The width of the plates is 38 mm and the bend angle is  $90^\circ$ . Ion entrance and exit slits can be placed in the EIA to reduce the spread in  $E/z$  selected, however, all results reported are without slits in order to increase ion transmission.

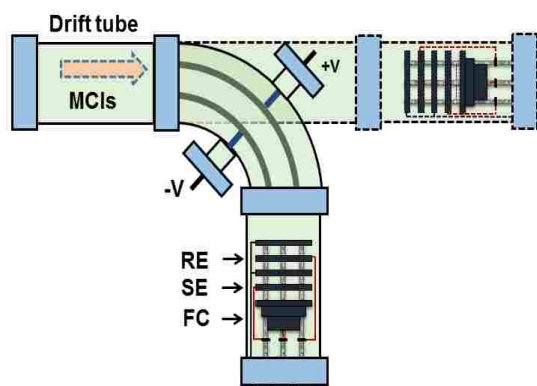


Fig. 3.10 Schematic of EIA analyzer and Faraday cup for ion selection with  $E/z$ . RE is the retarding electrodes, SE is the suppressor electrode, and FC is the Faraday cup. The system can be configured with and without the electrostatic ion energy analyzer (EIA) while maintaining the same distance between the target and the Faraday cup.

### 3.3.4.2 Testing

A second LMCI system is used to generate carbon MCI. In this setup, the distance from the carbon target to EIA is 90 cm. The EIA is tested on that system and used to select carbon MCIs according to their  $E/z$  ratio. The EIA spectrum is obtained at a laser energy of 34 mJ per pulse with an Nd:YAG laser operating at  $\lambda = 1064$  nm and  $\tau = 7$  ns. The laser spot size at focus is  $\sim 200$   $\mu\text{m}$ . Fig. 3.11 shows the carbon ion spectra for 5 kV voltage applied to target without and with the EIA. The ion spectra in Fig. 3.11 is obtained when the  $E/z$  selection is set to allow transmission of ions with central  $E/z = 2.8$  keV. The voltage applied to the EIA plates are at  $\pm 655$  V. Different  $E/z$  selections are used to analyze the energy distribution of different MCIs. Comparison of the MCI spectra without and with the EIA shows that the carbon MCIs contain multiple peaks associated with the same ion charge. For example, the peak at  $\sim 6.5$   $\mu\text{s}$  could be due to  $\text{C}^{1+}$  that is accelerated more than the rest of the  $\text{C}^{1+}$  ions by the double layer potential established in the outer layer of the expanding plasma [23].

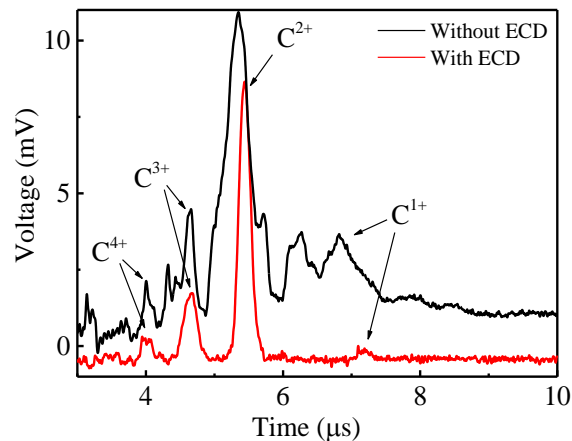


Fig. 3.11 Carbon ion signal detected by the Faraday cup placed without (black), and with (red, intensity  $\times 5$ ) the electrostatic ion analyzer. The MCI signal is produced by a single pulse from a Nd:YAG laser ( $\lambda = 1064$  nm, pulse energy 34 mJ). The voltage applied to target is 5 kV, and the EIA is set to central  $E/z = 2.8$  keV.

Fig. 3.12 shows EIA spectrum of the  $C^{2+}$  and  $C^{3+}$  ions detected from  $E/z = 1.7$  to  $5.1$  keV. The carbon target is kept at  $7$  kV acceleration voltage. The widths of  $C^{2+}$  and  $C^{3+}$  peaks before the EIA analyzer are both  $\sim 3$   $\mu$ s. The ions have some overlap in time before deflection. Ion signals of  $C^{2+}$  and  $C^{3+}$  are shown in Fig. 3.12(a), and 3.12(b), detected for the EIA analyzer voltage set to transmit ion energies centered from  $1.7$  to  $5.1$  keV. As the EIA voltage is increased, ions with higher energies appear in the energy spectrum. The intensities of  $C^{2+}$  and  $C^{3+}$  are maximized at  $E/z \sim 4.2$  keV. Plasma shielding of the ions during the plume expansion in the region between the target and grounded mesh limits the ion energy gained to less than the  $7$  kV voltage applied to target. Further increasing the biasing voltage up to  $E/z = 5.3$  keV shows the more energetic components of the  $C^{2+}$  and  $C^{3+}$  ions. The ion energy distributions can be reconstructed from the spectra obtained for different  $E/z$  selections. The energy resolution  $\Delta E/E$  of the EIA is  $7$ - $9\%$ , depending on the voltage applied across the EIA plates. The resolution is calculated by dividing FWHM of the ion peak transmitted through the EIA to the corresponding central kinetic energy of that ion. Introducing entrance and exit slits to the EIA can narrow the resolution.

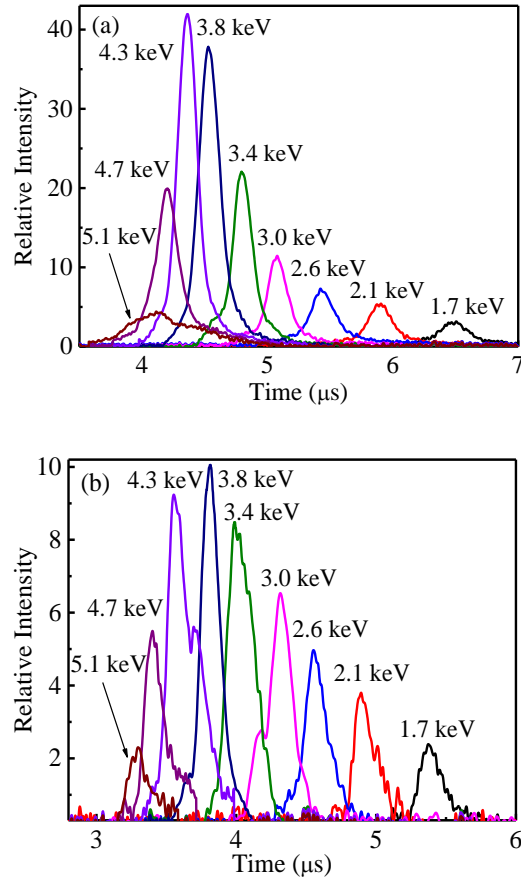


Fig. 3.12 EIA spectrum of  $C^{2+}$  (a) and  $C^{3+}$  (b) with varying  $E/z$ . The energy resolution  $\Delta E/E$  of the EIA is 7-9%, depending on the voltage applied across the EIA plates.

### 3.3.4.3 Simulation

SIMION is used to simulate the carbon ion trajectory in the EIA and obtain the  $E/z$  selectivity of the EIA. The EIA geometry in SIMION is set similar to the experiment with the inner radius  $R_1 = 145$  mm and outer radius  $R_2 = 183$  mm. The voltage across the plates is varied. The maximum number of ions detected for  $\pm 500$  V on the deflection electrodes with  $E/z = 2.2$  keV. Fig. 3.13 shows the ion trajectory path for  $C^{4+}$  passing through the EIA and reaching the FC for two different voltages applied to the EIA electrodes. Fig. 3.14 shows the TOF spectrum in terms of the number of ions reaching the FC with  $\pm 500$  V applied on the electrodes of the EIA. From the Fig. 3.14, we observe that the EIA ion transmission increases with the ion charge state. The number of particles in the ion source is 500 for each charge state. All the ions are simulated

with both energy distribution and special distribution obtained from the experiment. For ion energy distribution, a Gaussian three-dimensional distribution is used with a mean of 2.3, 4.2, 7 and 10.3 keV for  $C^{1+}$ ,  $C^{2+}$ ,  $C^{3+}$  and  $C^{4+}$ , respectively. The FWHM of the Gaussian energy distribution is 1.5, 2.9, 3.8, and 4.3 keV for  $C^{1+}$ ,  $C^{2+}$ ,  $C^{3+}$  and  $C^{4+}$ , respectively. The simulated TOF corresponding to peak signal for  $C^{1+}$ ,  $C^{2+}$ ,  $C^{3+}$  and  $C^{4+}$  are 7.9, 5.5, 4.6, and 3.9  $\mu\text{s}$ , respectively, whereas, the experimental TOF is 7.2, 5.4, 4.6, and 4  $\mu\text{s}$  as shown in Fig. 3.11.

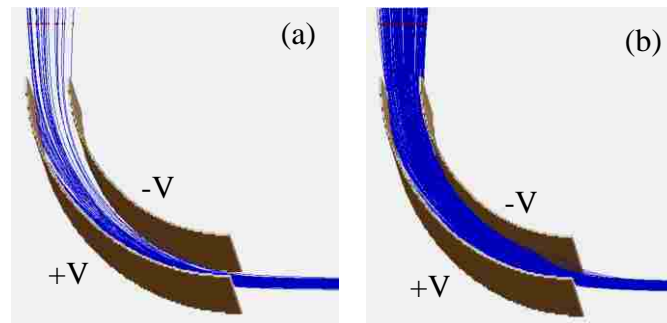


Fig. 3.13 Ion trajectory path for  $C^{4+}$  through the EIA. The applied voltage to the EIA (a)  $\pm 500$  V, (b)  $\pm 300$  V.

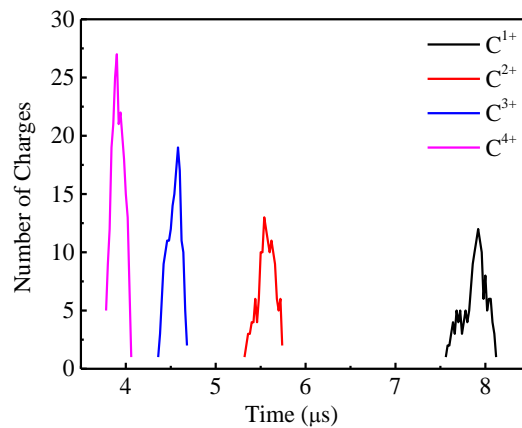


Fig. 3.14 Simulated TOF spectrum for  $C^{1+}$ ,  $C^{2+}$ ,  $C^{3+}$ , and  $C^{4+}$ . The applied voltage to the EIA is  $\pm 500$  V.

### 3.4 SUMMARY

Details of construction and operation of ion transport line components, e.g. einzel lens, parallel ion deflection plates, electrostatic ion energy analyzer, and three-grid retarding field ion energy analyzer, are reported. The minimum ion beam diameter detected of  $\sim 1.5$  mm is for charge  $\text{Al}^{4+}$ . With a combination of parallel deflecting plates and programmable pulse generator, ion charge states are selected from their TOF. The ion pulse width depends on the selected voltage pulse applied to the parallel plates. The EIA selects ions according to their  $E/z$ . The overall energy resolution of the EIA for the carbon MCI is 7-9%. This resolution can be reduced by using input and output slits.

## CHAPTER 4

### LASER-SPARK MULTICHARGED ION SOURCE

#### 4.1 INTRODUCTION

We report on the development of a spark discharge coupled laser multicharged ion (SD-LMCI) source to enhance the plasma ionization by depositing spark energy into the laser ablated plume. A similar type of experiment was conducted by Nassef and Elsayed-Ali to enhance the spectral line intensity and signal/background ratio using spark discharge coupled laser induced breakdown spectroscopy [88]. The SD-LMCI source is composed of a laser MCI source and a separate spark stage to deposit energy into the laser ablated plasma. A Q-switched 7.4 ns pulse width Nd:YAG laser is used to ablate Al target. The electrodes of the spark system are placed in front of the Al target and the laser beam is incident on the target through the gap of the electrodes. An accelerating voltage is applied to the target while a grounded mesh is placed in front of the target to extract, accelerate and direct the generated MCIs towards the Faraday cup. The velocity and the charge state of the extracted MCIs are measured using ion time-of-flight (TOF) as detected by a Faraday cup. The results show that a simple spark discharge, triggered by the laser plasma, can be effectively used to amplify the number of ions produced and increase the ion charge state achieved.

#### 4.2 EXPERIMENTAL

A schematic of the SD-LMCI source is shown in Fig. 4.1. The target is ablated with a Q-switched Nd:YAG laser pulse ( $\lambda = 1064$  nm, 7.4 ns pulse width (full-width at half maxima (FWHM)), and pulse energy 72 mJ). The laser beam strikes the Al target surface at an angle  $\vartheta = 45^\circ$ . The laser beam is focused on the Al surface by a convergent lens with 50 cm focal length. The laser spot area at focus was  $0.0024$  cm<sup>2</sup>, as measured by the knife-edge method at target-equivalent plane with the edge scanned at  $45^\circ$  to the laser beam. The knife edge was used to scan the laser beam in both horizontal and vertical directions. A combination of half-wave plate and thin film polarizer is used to control the focused laser energy on the target. The data reported here were all obtained using a single laser pulse. A 99.9% pure, 0.5 mm thick aluminum disc target (Alfa Aesar) with a surface roughness of 261.77 nm is placed on a multi-axes translational



stage. An insulating connector is used to mount the Al target support inside the MCI generation chamber. This arrangement allows applying accelerating voltage directly to the Al target, keeping the experimental chamber at ground. Throughout the experiment, 5 kV bias voltage was applied to the Al target. A nickel mesh of diameter 10-cm, thickness of 100  $\mu\text{m}$  and with an open area of 70% (Precision Eforming) is placed 15-cm in front of the target. A laser pulse is directed at the target to create a plasma plume. The ions are then accelerated through a transport line and analyzed by the MCI Analyzer. The Faraday cup voltage  $V_c$  is measured through a 100 k $\Omega$  resistor and a 5  $\mu\text{F}$  capacitor, and the suppressor voltage  $V_s$  is measured through a 50  $\Omega$  resistor.

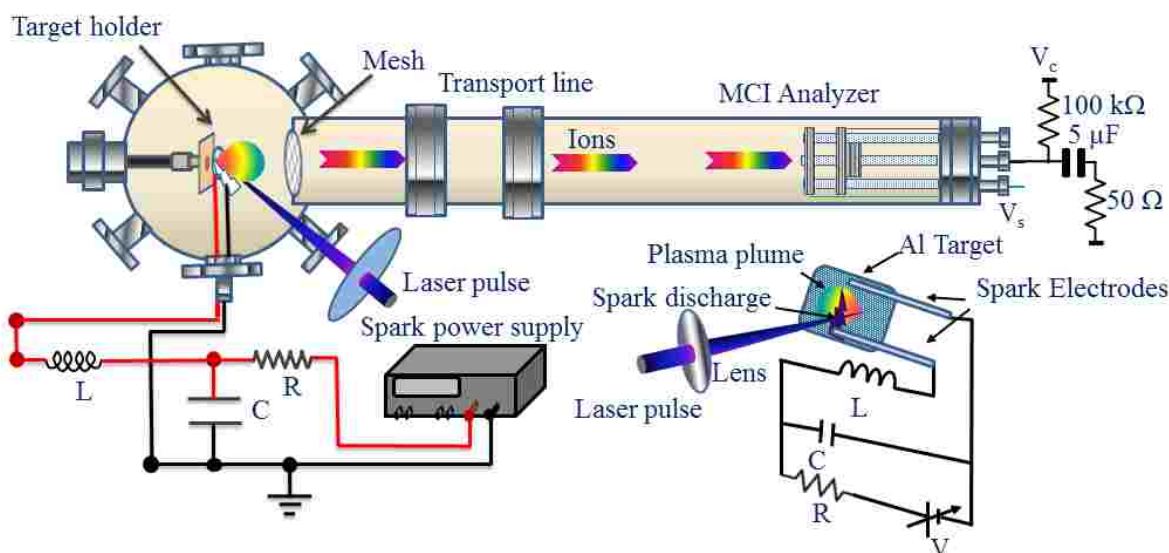


Fig. 4.1 A schematic of the spark discharge coupled laser multicharged ion (SD-LMCI) source showing the target chamber, and a spark system to deposit energy into the plasma plume;  $V_c$  is the Faraday cup voltage and  $V_s$  is the suppressor voltage. Inset shows the experimental setup used for the spark discharge;  $C$  is capacitor,  $V$  is voltage applied to the capacitor,  $R$  is current limiting resistor, and  $L$  is inductor.

The spark is composed of two parallel Al electrodes of diameter 3.2 mm, separated by  $\sim 3$  mm, and placed  $\sim 5$  mm in front of the Al target, as shown in the inset of Fig. 4.1. The 0.1  $\mu\text{F}$  capacitor is connected to a variable DC power supply through a 5 M $\Omega$  current limiting resistor. One of the electrodes is connected to the capacitor through a 0.15  $\mu\text{H}$  inductor. The other electrode is grounded through a 25 cm long wire. The capacitor was charged up to 5 kV. No self-breakdown occurred for these voltages. A high voltage probe (Tektronix P6015A) and a current pick up coil (Pearson Electronics, Inc., 0.001 V/A current monitor) are used to record the voltage drop across the discharge and the discharge current using an oscilloscope. The laser beam strikes

the Al sample through the ~3-mm electrode separation. The laser plasma plume expands between the electrodes triggering the spark discharge.

The diameter of the MCI generation chamber is 15 cm. A 125 cm long, 10.2 cm ID transport tube is connected to the chamber. A Faraday cup of diameter 5 cm made from Al is placed at the end of the drift tube to collect the MCIs. The interaction of the ions with the Faraday cup emits secondary electrons. To suppress these electrons, a higher negative voltage than the Faraday cup biasing is applied to the suppressor electrode. Throughout the experiment, the Faraday cup voltage was maintained at -70 V and the suppressor electrode voltages was at -110 V. The Faraday cup is connected to the oscilloscope through a capacitor (5  $\mu$ F), to remove the bias voltage from the recorded MCI signal. The MCI system is operating in high vacuum (background pressure in  $10^{-7}$  Torr range) by using a combination of a turbo-molecular pump for initial pumping followed by an ion pump). The total scattering cross-section for different MCIs was measured and reported by several groups [89-91]. According to their results, for our experimental condition the ion travel distance from the Al target to the Faraday cup is much shorter than the mean free path of the generated different MCIs, reducing the MCI loss due to charge transfer with the background gas to a negligible value.

### 4.3 RESULTS AND DISCUSSIONS

The spark discharge operation depends on the circuit parameters, separation of the electrodes, electrode distance from target, and the laser ablation plume characteristics [92, 93]. The value of the inductor  $L$  was adjusted in order to best couple the spark discharge energy to the ablated plume. Fig. 4.2 shows the voltage measured across the spark discharge (a), current through the discharge (b), and the power dissipated in the plume by the spark (c) when the capacitor  $C$  was charged to 5.0 kV and a laser energy pulse of 72 mJ used to ablate the Al target. At this voltage, the total stored energy in  $C$  is 1.25 J. As the spark is initiated, the voltage across the two electrodes shows a sudden decay in 1.2  $\mu$ s. The corresponding current shows damped oscillations with a maximum of ~670 A, as shown in Fig. 4.2(b). The peak power deposited into the plasma plume is ~0.67 MW, which decays to ~0.1 MW in ~1  $\mu$ s then oscillates while diminishing with time as shown in Fig. 4.2(c). Integrating the power dissipating in the discharge, shown in Fig. 4.2(c), the total energy deposited into the plasma plume is 0.9 J with 0.4 J deposited in 1.0  $\mu$ s after initiation of the spark discharge. Discharge power dissipation time of ~1

$\mu\text{s}$  or less can best couple the discharge energy with the laser plume and is needed to preserve the shape of the ion signal showing the different ion states separated in time for time-of-flight detection.

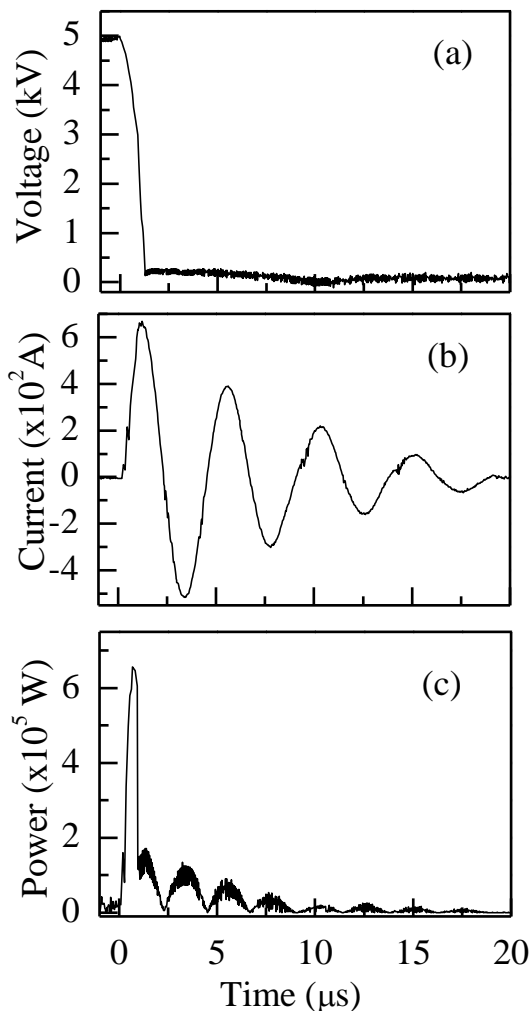


Fig. 4.2 (a) Voltage measured across the spark electrodes. (b) Discharge current. (c) Deposited electric power in the plasma. The spark was triggered by the Al plasma plume when a 72 mJ laser pulse ablated the Al target. The capacitor  $C$  was charged to 5.0 kV.

The total charge reaching the Faraday cup  $Q_i$  is given by  $Q_i = \frac{1}{R_L} \int V_F(t) dt$ , where  $V_F(t)$  is the voltage signal on the Faraday cup and  $R_L$  is the  $50 \Omega$  internal resistance of the

oscilloscope. The process we use to deconvolve the Faraday cup signal into curves for each charge state has been explained in a recent publication on the LMCI source without the spark [54]. The ions, extracted from the plasma plume by the electric field between the target and the grounded mesh, are detected by their TOF signal measured by the Faraday cup. Due to plasma shielding, the ions are not accelerated to the full potential applied between target and grid. The electric field due to the voltage applied to the spark also decelerates the MCIs. If effects due to plasma shielding and the spark electrodes are not considered, an ion generated at the target with zero energy would reach the Faraday cup after a time-of-flight of  $TOF = t_a + t_d = \sqrt{\frac{2m}{ZeV}}d + \sqrt{\frac{m}{2ZeV}}S$ , where  $t_a$  is the time that an ion is accelerated from zero velocity at target to velocity  $v$  at the extraction mesh,  $t_d$  is the time that ions drift at constant velocity  $v$  from the extraction mesh to the Faraday cup,  $d$  is the distance from the target to the extraction mesh,  $S$  is the distance from the extraction mesh to the Faraday cup,  $m$  is the mass of Al atom,  $e$  is the electron charge,  $Z$  is the charge state, and  $V$  is the applied accelerating voltage. The above equation does not account for ion acceleration in the plasma which, for our laser parameters, is mainly due to the sheath potential. The ion accelerating time  $t_a$  is small compared to the ion drift time  $t_d$ . Identifying the charge state from the TOF spectra was performed as follows: Since the  $Al^{1+}$  has the lowest velocity, the arrival time of these ions corresponds to the longest TOF. The effective acceleration potential that the  $Al^{1+}$  ions were subjected to is obtained by calculating the accelerating voltage required to achieve this TOF for  $Al^{1+}$  and applying this accelerating voltage in the above TOF equation. This potential is then used in the TOF equation to determine the TOF of MCIs with other charges. The estimated TOF for MCIs with different charge states matches well the TOF spectra.

#### **4.3.1 Effect of spark energy**

The TOF ion signals without and with the spark discharge are shown in Fig. 4.3. The pulse laser energy used was 72 mJ while the spark discharge was operated at different capacitor  $C$  voltages. Without the spark, up to  $Al^{3+}$  MCI with a total charge of  $\sim 1$  nC is detected as shown in Fig. 4.3(a). When using the same laser pulse energy of 72 mJ and activating the spark by charging the capacitor  $C$  to 1.0, 4.0, and 5.0 kV (corresponding to stored energy of 0.05, 0.80 and 1.25 J, respectively), the total charge detected is enhanced and higher charge states are

observed. For capacitor voltages of 1.0, 4.0, and 5.0 kV, the total charges generation are 2.0, 6.6, and 9.2 nC, respectively as shown in Figs. 4.3(b)-(d). The maximum charge states observed also increases reaching  $\text{Al}^{6+}$  for  $V = 5.0$  kV. The initial noise in the TOF signal before the arrival of the MCIs to the Faraday cup is due to the spark generated RF noise that interferes with the signal detected by the Faraday cup [94]. The TOF of the MCIs also shows some peaks with complex shapes, for example, in Fig. 4.3(d)  $\text{Al}^{3+}$  and  $\text{Al}^{4+}$  MCIs show double peaks. The shape of the MCI signal depends on the energy characteristics of the ions, which could involve slower and faster ions depending on the ion generation mechanism and the propagation of MCIs through the spark discharge electrodes [95].

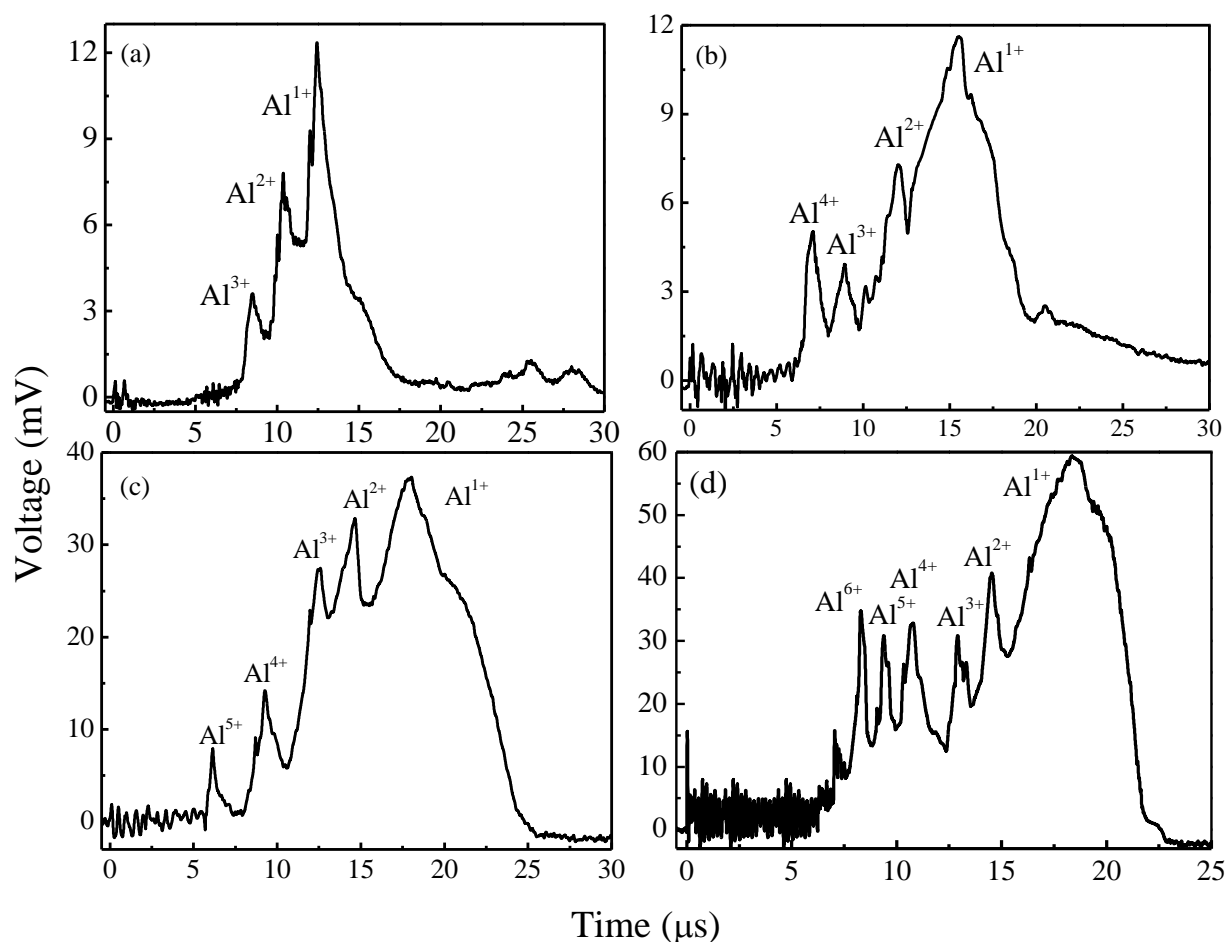


Fig. 4.3 Spark discharge enhancement of multicharged ion generation for 72 mJ laser energy. (a) Only the laser is used. (b)-(d) Spark discharge operating with energy stored in  $C$  of 0.05, 0.80, and 1.25 J, respectively.

The effect of the spark is to enhance ion generation and increase the maximum ion charge state. By integrating the area under each charge state in Fig. 4.3, one can determine the abundance of each charge state. From Fig. 4.3(a), without the spark, the ion charges detected are 72%  $\text{Al}^{1+}$ , 21%  $\text{Al}^{2+}$ , and 7%  $\text{Al}^{3+}$ , while with the spark with  $C$  charged at 1.25 J, the ion charges were 56%  $\text{Al}^{1+}$ , 12%  $\text{Al}^{2+}$ , 7%  $\text{Al}^{3+}$ , 11%  $\text{Al}^{4+}$ , 7%  $\text{Al}^{5+}$  and 7%  $\text{Al}^{6+}$ . The TOF of MCIs is increased when the spark is used since the spark voltage decelerates the extracted ions in the gap between the target and the extraction mesh. In Fig. 4.4, we show calculation of the most probable energy of the  $\text{Al}^{1+}$  based on TOF data in Fig. 4.3. When the laser pulse was used without the spark, the most probable energy of  $\text{Al}^{1+}$  is  $\sim 1.8$  keV. As the capacitor  $C$  was charged to 1.0, 4.0, and 5.0 kV (corresponding to stored energy of 0.05, 0.80 and 1.25 J, respectively), the most probable energy of  $\text{Al}^{1+}$  became  $\sim 1.1$ ,  $\sim 0.9$ , and  $\sim 0.8$  keV, respectively. The FWHM of the kinetic energy distribution of  $\text{Al}^{1+}$  remains unchanged at  $\sim 0.6$  keV regardless of the spark operating voltage showing that the spark discharge did not introduce additional energy spread in the ion distribution from the laser plasma.

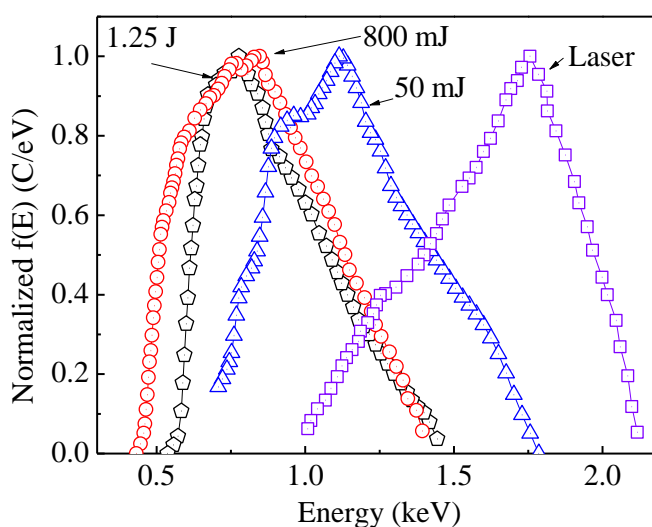


Fig. 4.4 Energy distribution of  $\text{Al}^{1+}$  without spark (square) and with spark energy of 0.05 (triangle), 0.8 (circle), and 1.25 J (pentagon) coupled with the 72 mJ laser pulse energy. Spark energy refers to energy stored in  $C$ .

Fig. 4.5 shows the increase in total charge detected with the increase of energy stored in spark capacitor  $C$ . The laser pulse energy is fixed at 72 mJ. We observed that, with the increase of spark energy, total charge generation increased slowly, and for 1.25 J spark energy, the total charge generation increased by a factor of  $\sim 9$  compared to charge generation with the laser pulse alone. Increasing the spark energy deposited into the laser plasma is expected to increase the plasma density and temperature, which in turn increases the total charge generation.

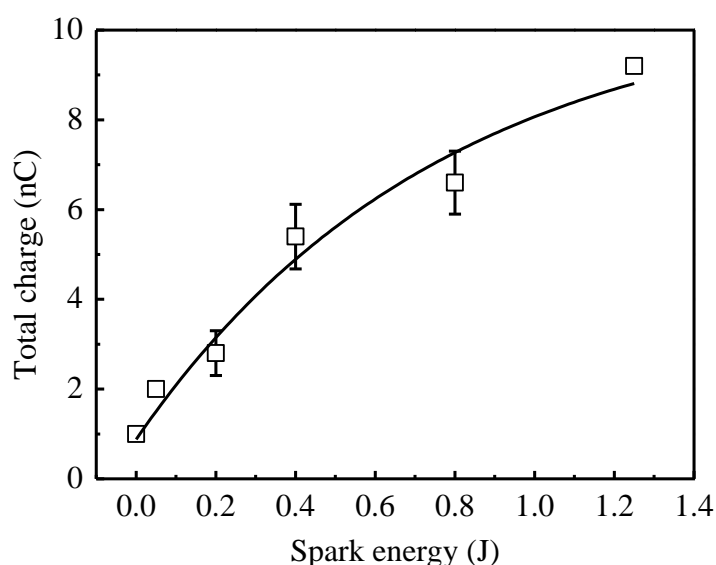


Fig. 4.5 Effect of spark energy deposited into the plasma plume on total charge detected. Error bars represent standard deviation. Spark energy refers to energy stored in  $C$ .

### 4.3.2 Effect of laser energy

In nanosecond laser-matter interaction, an incident laser pulse of enough energy causes evaporation of the target surface. Since the pulse width of the nanosecond laser is relatively long, the evaporated materials interact with the remaining part of the laser beam causing progressive ionization of the plasma plume [16, 96]. During this process, the electrons are heated by inverse-bremsstrahlung. The heated electrons transfer their energy to the ions and neutrals through collisions. In our experimental conditions, the ablation time is much longer than the time to

transfer energy from energetic electrons to ions [26, 97]. The lifetime of the laser ablated plume is determined by the velocity of the plume expansion, which in turn is related to the hydrodynamic pressure inside the plume. The average velocity of the plume expansion is affected by the ion mass [24]. In laser ablated plasma, the ablated plasma density, temperature, ablated mass, and the ion and electron energy is affected by the laser pulse energy, intensity, and pulse width. The spark energy deposited into the plasma plume is expected to increase the plasma density and temperature leading to higher ionization rate and higher state charge along with increase in the total number of MCIs generated.

Fig. 4.6(a) shows the total charge detected for increasing laser energy from 45 to 72 mJ without and with the spark discharge ( $C$  charged to 1.00 J). Without the spark, changing the laser pulse energy from 45 to 72 mJ increases the total charge detected from  $\sim 0.6$  to  $\sim 1.0$  nC. When 1.00 J spark energy is used in conjunction with the laser pulse, the total charge detected increased from  $\sim 8.0$  to  $\sim 8.3$  nC for laser pulse energies of 45 and 72 mJ, respectively. The almost lack of dependence on the laser pulse energy shows that most of the MCIs are generated by the spark discharge energy with the spark causing amplification of the laser-generated MCIs by a factor of  $\sim 13$  for a laser pulse energy of 45 mJ. Fig. 4.6(b) and 4.6(c) show the MCI generation for 45 and 63 mJ laser pulse energy without and with the spark discharge. Without the spark, 45 and 63 mJ laser energy generate Al MCIs with charge states up to  $\text{Al}^{1+}$  and  $\text{Al}^{3+}$ , respectively. With a 1.00 J spark, MCI charge states up to  $\text{Al}^{5+}$  are generated for both laser pulse energies. The increased TOF for ions when the spark is operated is due to the ion deceleration by the spark voltage reducing ion kinetic energy. During the experiment the laser focus spot, angle of incidence on Al target, and pulse width of the laser were kept constant, as described in the experimental section.



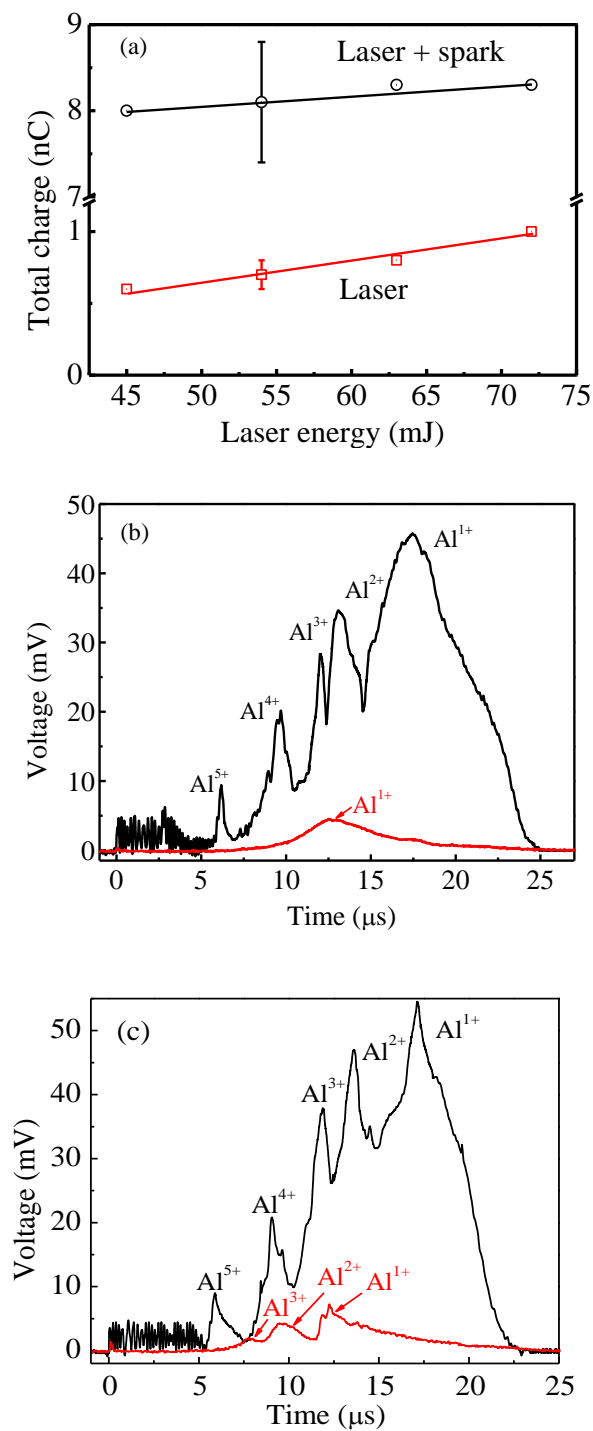


Fig. 4.6 (a) Measured total charge delivered to the Faraday cup for different laser pulse energies without the spark (squares) and with 1.0 J spark energy (circles). The error bars represents the standard deviation. The MCI spectra for laser energy only (red) and for the combined effect of 1.0 J spark energy and laser pulse energy (black) of (b) 45 and (c) 63 mJ.

#### 4.4 SUMMARY

A spark discharge is coupled to the Nd:YAG laser generated Al plasma to enhance the plasma ionization. A self-triggered mechanism, by shortening of the electrodes due to laser plasma plume expansion, is demonstrated to deposit spark energy to the laser plasma. The spark discharge significantly enhances the total ion generation along with higher charge states. For a laser-spark ion source, laser energy initiates the plasma, but the maximum charge state and total ion generation depends mostly on the spark energy. For 5 kV accelerating voltage, when 72 mJ laser pulse energy is coupled with 1.25 J spark energy, Al charge state up to 6+ is detected with total charge of ~9.2 nC. While without spark energy for the same condition, the maximum charge state is Al<sup>3+</sup> and total charge is ~1 nC.

## CHAPTER 5

### TIME-OF-FLIGHT AND OPTICAL EMISSION SPECTROSCOPY

#### 5.1 INTRODUCTION

We extend our previous work on Al laser MCI generation [54, 98] through a combined ion TOF measurement and OES of the laser plasma. The double-layer potential generated at the plasma-vacuum interface is estimated from the deconvolution of the TOF ion signal into individual ion species. From optical emission spectroscopy (OES), the  $N_e$  is calculated by Stark broadening, while the  $kT_e$  is calculated using the relative intensity ratio of two emission lines belonging to the same atomic species. Although LTE is assumed valid for ablation conditions similar to ours [99], the  $kT_i$  obtained from the deconvolution of the ion TOF signal is significantly higher than the electron temperature obtained from OES. This is attributed to the difference in time and location at which the plasma is probed. MCI generation occurs mainly when the plasma is at its highest temperature and at a high density near the surface and the core of the plume. Ions escaping from the plasma and accelerated by the double-layer potential reflect these conditions and therefore their TOF ion signal corresponds to the high temperature used to generate the ions. Whereas, OES probes time and spatially integrated line emissions, which becomes prominent after decay of the black-body radiation from the initial laser plasma. During this time, the plasma is providing strong line emission, the plume is expanding, and the plasma is cooling. Therefore, the spatially and temporally integrated line emission, as detected by the spectrometer, provides a much cooler electron temperature. The peak intensity of the spectral lines, and the ion energy spread show dependence on the external electric field in which the plume expands.

Ion emission for ns laser ablation was characterized by their TOF [22, 64, 86, 100-108]. The charge state, kinetic energy and angular distribution of the ions ejected from the laser plasma depend on the laser parameters (e.g., laser pulse energy, wavelength, and pulse duration), the ablated material, and the surrounding environment [22]. The general trend is that increasing the laser pulse energy increases ion generation. For example, laser ablation of carbon and aluminum with an Nd:YAG laser ( $\lambda = 1.064 \mu\text{m}$ ) showed enhancement of the ion generation along with the

maximum charge observed with the increase in the laser pulse energy [64]. The effect of laser wavelength on the ion energy distribution from laser-ablated plasma in vacuum was studied. The Ablation of a Sn target by a Nd:YAG laser ( $\lambda = 1.064 \mu\text{m}$ ) and by a CO<sub>2</sub> laser ( $\lambda = 10.6 \mu\text{m}$ ) yielded a maximum charge state of Sn<sup>6+</sup> with an average ion energy of 792 eV for the Nd:YAG laser and Sn<sup>9+</sup> with an average ion energy of 680 eV for the CO<sub>2</sub> laser [101]. A combined Langmuir probe and an electrostatic ion energy analyzer study of Al ions generated by a nanosecond Nd:YAG laser and a femtosecond Ti:sapphire laser at a comparable ablation flux yielded maximum charge state by the ns and fs lasers of Al<sup>2+</sup> and Al<sup>3+</sup>, respectively [104]. For the ns laser, the ions had a lower kinetic energy than that for the fs laser [104]. For a Pd laser ion source generated by a Q-switched Nd:YAG laser and its second harmonic, the ablation threshold was reported to be 1.2 times higher for  $\lambda = 1064 \text{ nm}$  than for  $\lambda = 532 \text{ nm}$  due to the longer penetration depth of the  $\lambda = 1064 \text{ nm}$  in the metal [102]. For a laser pulse energy of 100 mJ, Pd<sup>5+</sup> ions were detected for  $\lambda = 1064 \text{ nm}$ , while Pd<sup>6+</sup> ions were detected for  $\lambda = 532 \text{ nm}$  [102]. The role of laser pulse duration on the ion emission from a Nd:YAG laser-generated Sn plasma was reported [100]. The ion kinetic energy profile shifted to higher energy with the reduction of the laser pulse width, while narrower energy distributions were obtained for the longest laser pulses used [100]. The average charge state decreased from Sn<sup>13+</sup> to Sn<sup>7+</sup> when the laser pulse duration was increased from 5 to 20 ns [100].

For ns laser ablation, Harilal *et al.* reported that the plasma plume expands spherically with smaller laser spot size on target; while for a larger spot size the plume propagation is more cylindrical due to the smaller lateral expansion [103]. Using a Faraday cup to study ion energy distribution, they showed narrower and higher energy ion distribution with the smaller spot size [103]. The dependence of the ion angular distribution on the laser parameters and the ablated material were reported by several groups [105-107]. The fs laser-ablated plume was more elongated along the direction normal to the target compared with that for ns laser ablation [105], resulting in significantly narrower ion angular distribution at a similar laser fluence [106]. A narrower angular distribution of the plume occurs with increasing laser fluence [106]. Elsieid *et al.* reported differences in the spatial and temporal distribution of slow and fast ions for various metals and related that observation to the different mechanisms in ion generation [107]. For Mo, the slow ion flux peaked at a direction normal to the target, whereas the fast ion flux peaked at relatively larger angles. For Al, the slow ions also peaked normal to the target while the fast ions

were absent [107]. Torrisi *et al.*, utilizing a Nd:YAG laser, reported that the energy peaks of the singly-charged ions increase with the melting point of the ablated material, while the ablation yield showed the reverse trend [86]. Freeman *et al.* reported that the maximum kinetic energies of the ions generated by an Nd:YAG laser using its fundamental, second, and fourth harmonic with the same laser intensity were similar [108]. The kinetic energy distributions became broader as the laser wavelength was reduced, while the angular distribution of the ions showed a similar trend for all laser wavelengths [108].

Several groups have studied ion emission from ns laser plasma using optical emission spectroscopy (OES) [26, 109, 110]. Caridi *et al.* reported on ion generation by laser ablation of Al, Ti, Mo, Au and polyethylene targets in vacuum using a Nd:YAG laser. For laser energy of 180 mJ, the electron temperature  $kT_e$ , obtained using optical emission spectroscopy is  $\sim 1.3$  eV, while the equivalent ion plasma temperature  $kT_i$ , as evaluated by TOF deconvolution using shifted Coulomb-Boltzmann distribution, varies from 30 to 44 eV. The difference in plasma temperatures was attributed to the difference in the plasma region probed [109]. Abdellatif *et al.* studied Al plasma generated in vacuum by an Nd:YAG laser. The plasma density  $N_e$  was measured to be  $1.13 \times 10^{18}$  cm<sup>-3</sup> at 100  $\mu$ m from the Al target surface and  $0.55 \times 10^{18}$  cm<sup>-3</sup> at 1200  $\mu$ m from the surface. The measured  $T_e$  at the target surface was  $\sim 1.17$  eV and increased to 4.2 eV 500  $\mu$ m away from the surface, then it decreased beyond that point. Charge states up to Al<sup>2+</sup> were observed [26]. Harilal *et al.* reported on OES studies of a Sn plasma generated in vacuum using a Nd:YAG laser. The  $kT_e$  and  $N_e$  measured 1 mm from the target surface were 3.2 eV and  $7.7 \times 10^{17}$  cm<sup>-3</sup>, respectively [16]. The time-integrated  $kT_e$  near the target surface remained nearly constant with distance from the surface but increased significantly for a distance  $> 7$  mm [16]. The spatial variation of  $N_e$  showed approximately inverse dependence on distance. Applying a negative potential to a gold target was shown to increase ultraviolet line emission from the laser plasma produced by a KrF excimer laser, which was attributed to electric field enhanced recombination near the target surface [110].

## 5.2 EXPERIMENTAL

The laser ion source is composed of a Q-switched Nd:YAG laser ( $\lambda = 1064$  nm,  $\tau \sim 7$  ns, and laser fluence  $F \leq 38$  J/cm<sup>2</sup>) with associated laser beam delivery optics, target ablation chamber, ion drift tube, three-grid retarding field ion energy analyzer, and Faraday cup (FC). The

laser was  $p$ -polarized and incident on the target at an angle  $\theta = 45^\circ$ . The laser was focused on the target using a lens with 80 cm focal length. The laser pulses pass to the Al target through a viewport which has  $\sim 8\%$  loss due to Fresnel reflections. The laser was focused on the Al target forming an elliptical spot (semi major axis radius 0.3 mm, and semi minor axis radius 0.25 mm) with an area of  $\sim 0.0024 \text{ cm}^2$ . A fast-high voltage probe (Tektronix P6015A) is used to observe the voltage fluctuations of the biased target during plasma plume expansion. The currents flowing through the Al target and the externally grounded extraction mesh are measured separately using two current pickup coils (Pearson current monitor, model 4118). The pressure in the vacuum chamber was maintained at low  $10^{-9}$  Torr.

The ions are accelerated towards the FC through a drift tube. The diameter of the MCI generation vacuum chamber is 30 cm. A 125-cm long transport tube with inner diameter of 10 cm is connected to the MCI generation chamber making the distance from the Al target to the FC 140 cm. The FC biased at  $-70 \text{ V}$  detects the TOF ion signal, which is used to calculate the total charge delivered to the FC and their kinetic energy. The TOF signal can be used to identify the charge state of the ions generated. The ion signal is acquired by a fast-digital oscilloscope triggered by a photodetector observing the optical leak in the last mirror before the focusing lens. An illustration of the experimental setup is shown in Fig. 5.1. More details on the experimental setup for ion generation and detection are given in our previous publications [54, 55, 111].

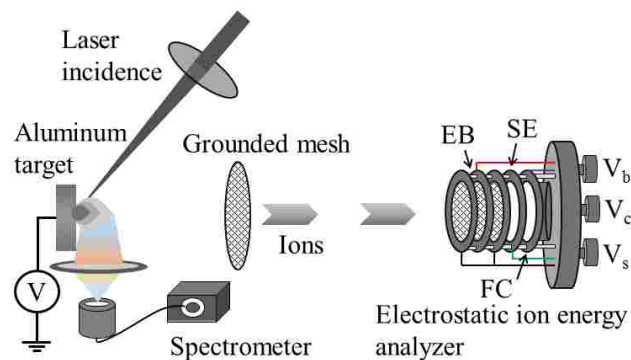


Fig. 5.1 Schematic of the experimental setup, EB denotes the electrostatic barrier of the three-grid retarding field analyzer, SE the suppressor electrode to suppress the effect of secondary emission from the Faraday cup (FC).

To further accelerate the extracted ions, the target is biased positively while a grounded mesh is placed in front of it. The extraction mesh is placed at 10 cm away from the Al target towards the FC, where the density of the plasma is several orders of magnitude lower than at the target surface. The plasma plume expands in the electric field generated between the target and the grounded mesh. The adiabatic expansion, thermal interactions, and the Coulomb acceleration due to the double-layer potential at the plasma-vacuum interface are mainly responsible for the initial ion acceleration. The external electric field accelerates ions separated from the plume. The ion acceleration by the external electric field is reduced due to plasma shielding. The location between the target and the grounded mesh at which an ion experiences the electric field also affects the ion acceleration by the external electric field. The ion flux extracted increases with the electric field due to the retrograde motion of the plasma edge exposing more ions to the accelerating field and repelling the electrons [53]. In the drift region, the temporal ion pulse width is increased.

An optical spectrometer (Princeton Instruments, Acton SP2300 (grating size 68 x 68 mm, 150 grooves/mm, blaze wavelength 500 nm, and a resolution of 1.27 nm as provided by the manufacturer)) is used to obtain the optical spectra from the laser plasma. The optical spectra were collected for 1 ms using a single-shot mode and without any set delay between capturing the optical spectra and the laser pulse. The emission from the formed plasma is imaged onto the open end of an optical fiber bundle using a lens of 5 cm diameter with a focus length of 5 cm. The optical fiber bundle has 19 optical fibers, each 200  $\mu\text{m}$  in diameter and 1 m long with a numerical aperture of 0.2. The spectra were observed in a direction parallel to the target surface (i.e.  $90^\circ$  with respect to the direction of the plasma expansion) with its axis centered  $\sim 1$  mm from the surface of the sample and the fiber is placed  $\sim 250$  mm away from the produced plasma. The position of the fiber is far enough to obtain spatially-integrated spectra from the plasma. The spatially-integrated, time-integrated spectra from each pulse is detected and the final spectra used in the analysis was an average of 10 laser pulses. For a similar experimental condition, the plasma emitting region is  $>5$  mm above the sample surface [112].

## 5.3 RESULTS AND DISCUSSIONS

### 5.3.1 Effect of laser energy for a grounded target

Fig. 5.2 shows the TOF ion signal for laser fluence of 21, 25, 28, and 38 J/cm<sup>2</sup>. The inset of Fig. 5.2 shows that the total number of charge generated increases linearly with the increase in the laser fluence. The ion pulse that reaches the FC contains different ionic states. The double-layer potential, developed at the expanding plasma-vacuum interface, accelerates the ions. Higher charge state ions reach the FC earlier than those with a lower charge, since the ions with higher charge gain more kinetic energy by the double-layer potential. From analysis of the shape of the ion signal, we show that with the increase in the laser fluence, the ion energy distribution shifts to higher energies along with the generation of higher charge-state ions. Increasing the laser fluence from 21 to 38 J/cm<sup>2</sup> increases the peak ion drift velocity from  $\sim 1.9 \times 10^4$  to  $\sim 2.4 \times 10^4$  ms<sup>-1</sup>, resulting in a peak ion energy increase from  $\sim 50$  to  $\sim 80$  eV.

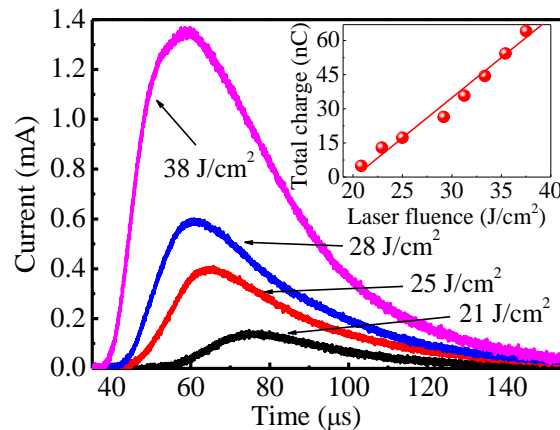


Fig. 5.2 Ion TOF signal for different laser energies ablating the Al target. The Al target was at ground potential. The inset shows the dependence of the number of charges measured by the Faraday cup (FC) on the laser pulse energy.

The ion energy distribution can be used to characterize the plasma temperature and the double-layer potential developed at the plasma-vacuum interface of the expanding plume. The ion TOF signal is detected by the FC. The ion TOF signal and the retarding field energy analyzer are used to obtain the ion energy distribution. The TOF signal can be deconvoluted into



individual ion charge signals. For a transient laser-plasma satisfying LTE ( $T_i \sim T_e \sim T$ ), the electron-atom and electron-ion collisions establishes equilibrium with the particle velocities in the plasma following a Maxwell-Boltzmann distribution [16]. The validity of the LTE for ns laser plasma was previously considered [99]. Accordingly, our plasma conditions satisfy LTE. Away from the target, where recombination and collisional excitation processes are absent, the ion charge-states are frozen and the ions drift freely in the vacuum with a velocity distribution for each ion species characterized by a shifted Coulomb-Boltzmann (SCB) distribution [22]. For a laser-plasma where the TOF of the extracted ions is much longer than the laser pulse duration, the Kelley and Dreyfus function expressing the ion current based on the SCB distribution, including the effect of Coulomb energy (in terms of an equivalent accelerating voltage) can be applied for the analysis of the ion current [113, 114]. Both thermal and Coulomb interactions are considered in the SCB model. Therefore, the sum of the individual SCB distributions for each ion species with their characteristic equivalent accelerating voltage and ion plasma temperature provides the overall distribution of the ejected ions [109]:

$$F(t) = \sum_i A_i \left( \frac{m}{2\pi kT_i} \right)^{3/2} \left( \frac{L^4}{t^5} \right) \exp \left[ -\frac{m}{2kT_i} \left( \frac{L}{t} - \sqrt{YkT_i/m} - \sqrt{2zeV_{0,i}/m} \right)^2 \right] \quad (5.1)$$

where  $A_i$  are normalization constants,  $m$  is the mass of the ablated ions,  $t$  is the time-of-flight,  $L$  is the total distance from the target to the Faraday cup.  $v = \frac{L}{t}$  is the velocity along the normal to the target and is equal to the summation of the velocity components  $v_t, v_k, v_c$ . The component  $v_t = \sqrt{(3kT_i/m)}$  is the mean thermal velocity for monoatomic neutral species,  $v_k = \sqrt{YkT_i/m}$  is the adiabatic expansion velocity, and  $v_c = \sqrt{2zeV_0/m}$  is the velocity due to Coulomb acceleration. In the velocity components,  $Y$  is the adiabatic coefficient which for a monoatomic metal, e.g., aluminum, has the value of 5/3,  $z$  is the charge state,  $kT_i$  describes the velocity spread of the probed ions, which has been assumed equivalent to the ion plasma temperature (in eV) in previous laser MCI studies [22, 109], and  $V_0$  is the equivalent accelerating voltage developed at the plasma-vacuum interface. Eq. 5.1 applies under the condition of absence of significant recombination and collisional excitation processes; i.e., the ion species are frozen and freely drifting in the vacuum [115]. The curve fit of the TOF signal with Eq. 5.2

mostly depends on the  $kT_i$  and  $V_0$  developed at the plasma-vacuum interface due to the double-layer potential. We can estimate  $kT_i$  and  $V_0$  from the curve fit of the measured TOF signal with Eq. 5.1.

The ion pulse detected by the FC, shown in Fig. 5.2, consists of ions with different charge states. To determine the contribution of each ion charge to the TOF signal, deconvolution of the ion pulse signal for each ion charge state is accomplished. The best fit to the TOF signal is obtained for a combination of  $kT_i$  and  $V_0$  developed in the double-layer region of the plume. These two parameters can be used to estimate the effects of thermal energy, adiabatic expansion, and Coulomb potential on the energy distribution of the individual ion species. The deconvolution of the ion pulse into individual ion species is conducted as follows: first, we fix the value of the maximum charge state  $n$  (known by separating the charge states temporally using an externally applied electric field between the target and the grounded mesh). Then, we set the  $V_0$  and the  $kT_i$  as free variables to bring the total energy (sum of thermal, adiabatic, and Coulomb) to match with the ion pulse suppression potential applied to the central grid of the three-grid retarding field analyzer. Other conditions used for the fit are that the sum of the TOF de-convoluted signals of individual ion species fits with the measured TOF signal of the detected ion pulse. Also, the ratio of the ion charges detected for each charge state matches with that ratio as measured when an external electric field is used to separate signals from each charge state by their TOF. Details of the deconvolution procedure were given previously [54].

Previous ion TOF studies from ns laser plasma has shown that the ion energy distribution, for a certain ion charge, splits into two SCB distributions peaked at different energies [19, 20]. Bimodal energy distributions for metal ions at different peak energies were reported for ablation with a ns Nd:YAG laser. The SCB distribution of  $Al^{1+}$  ions with the higher velocity was correlated with the direct multiphoton laser ionization, while the slower distribution was associated with collisional processes. In the expanding plume, neutrals can be ionized, and ions can be converted into another charge state due to the collisions among ions, electrons, and neutrals leading to ionization, recombination, and ion charge transfer. Ions produced due to collisions have velocities that depend on their formation process and hence are observed as an independent energy distribution [19, 20]. The external energy gain also depends on the location between the target and grounded mesh, where the ion is generated, and the distance the ions travelled experiencing the external electric field. Ion acceleration by the external electric field is

reduced due to plasma shielding. For example, if electron-impact ionization is the dominant process ( $\text{Al}^0 + e^- \rightarrow \text{Al}^+ + 2e^-$ ), the kinetic energy of the  $\text{Al}^0$  involved in this reaction will contribute to the energy distribution of the resulting  $\text{Al}^{1+}$  ions. Recent studies of ns laser ablation observed the presence of fast and thermal ions following Gaussian and Maxwell-Boltzmann distributions, respectively [107]. The presence of fast ions depends on the atomic weight of the ablated material. For heavy metals, e.g. Mo, fast and thermal ions were observed. While for lighter metals, e.g. Al, only thermal ions were detected [107]. This phenomenon was attributed to the difference in both spatial and temporal ion distributions along with the fact that ns laser ablation of heavy metals emits prompt electrons, and these prompt electrons are responsible for the emission and acceleration of the fast ions. Similar results for ns laser ablation were reported by Farid *et al.*, where higher  $Z$  materials (Mo, T, and W) show multiple peaks containing fast and thermal ions, while lower  $Z$  materials (C, Al, Si, and Cu) show only a single peak containing thermal ions [116]. In our present experiment with Al, no fast ions were detected; only thermal and slow ions are detected and are fitted with SCB distribution.

The deconvolution of the ion pulse into individual ion species for laser fluence of 28 and 38  $\text{J}/\text{cm}^2$  is shown in Fig. 5.3(a) and (b). The higher charge state ions have higher velocities and, therefore, reach the FC earlier than the lower charge states. The sum of the signals from different ion charges gives the total ion signal, which is fitted to the experimental TOF signal. The ions generated with laser at a fluence of 28 and 38  $\text{J}/\text{cm}^2$  have energies up to  $\sim 70$  and  $\sim 80$  eV, respectively, as measured by the retarding field analyzer [54]. During retarding field analysis, the barrier voltage, applied to the central electrode of the three-mesh retarding field analyzer, was increased from 0 to 80 V. From the deconvolution, we obtain charge states up to  $\text{Al}^{3+}$  and  $\text{Al}^{4+}$  when the laser fluence is 28 and 38  $\text{J}/\text{cm}^2$ , respectively. This is confirmed by observing the individual ion peaks for each charge in the TOF signal when voltage is applied to the target setting an external electric field sufficient to separate the different charge states.

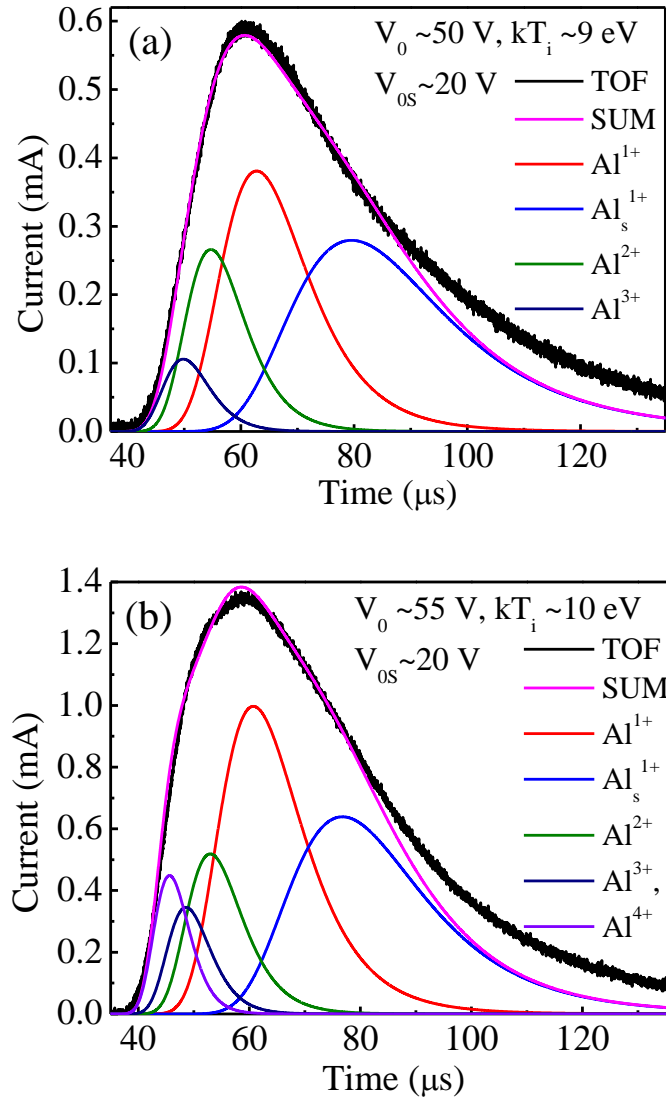


Fig. 5.3 Deconvolution of the ion time-of-flight signal. (a) For a laser fluence of  $28 \text{ J/cm}^2$  showing charge states up to  $\text{Al}^{3+}$ . (b) For a laser fluence of  $38 \text{ J/cm}^2$  showing charge states up to  $\text{Al}^{4+}$ .  $V_0$  is the double-layer potential,  $kT_i$  is the ion plasma temperature, whereas  $V_{os}$  is the equivalent accelerating voltage for the slow  $\text{Al}^{1+}$  ions.

The curve fit in Fig. 5.3(a) was done for  $V_0 = 50 \text{ V}$  and  $kT_i = 9 \text{ eV}$  and in Fig. 5.3(b) for  $V_0 = 55 \text{ V}$  and  $kT_i = 10 \text{ eV}$ . The slow ions  $\text{Al}_s^{1+}$  are fitted with  $V_{os} = 20 \text{ V}$  with similar  $kT_i$  as used to fit the thermal ions. For laser fluences of  $21$  and  $25 \text{ J/cm}^2$  (data not shown), the best fit to the TOF signal gave  $V_0 = 35$  and  $43 \text{ V}$  and  $kT_i = 6$  and  $8 \text{ eV}$ , respectively, while  $V_{os}$  was  $15 \text{ V}$  for both laser fluences. Other slow ion groups could also affect the ion TOF signal. With the target

grounded, for an ion with charge state  $z$ , the total energy gain of the ion  $E_{zT} = (E_t + E_k) + zE_c$ , where  $E_t = \frac{3}{2}kT_i$  is the thermal energy,  $E_k = \frac{\gamma}{2}kT_i$  is the adiabatic energy, and  $E_c = eV_0$  is the Coulomb energy associated with the equivalent accelerating voltage due to the double-layer potential. The most probable energy calculated from the TOF signal, and the adiabatic and thermal energy estimated from the deconvolution of the TOF signal are in good qualitative agreement with the results previously reported from ns laser ablation [117]. This fit is best at time scales extending from the onset of detecting the thermal ions by the FC and extends past the peak of the TOF signal. The slower ions forming the tail of the TOF signal are not as well fitted to the SCB distribution, representing the sum of the ion charges. This is because there are secondary mechanisms forming these slower ions, as was previously discussed [19, 20].

### 5.3.2 *Effect of laser energy for positively biased target*

When, the target is positively biased, establishing an electric field between the target and the grounded mesh, the ions that separate from the plume experience further acceleration. For sufficient acceleration, the ions detected by the FC appear as temporally separated peaks for each charge state. The extent of which the ions experience the external field depends on the distance away from the target that they are separated from the shielding plasma. If an ion is generated with zero energy near the target and is accelerated by the full potential applied, i.e. in the absence of plasma shielding, the ions TOF to the FC is  $TOF = t_a + t_d = \sqrt{\frac{2m}{zeV}}d + \sqrt{\frac{m}{2zeV}}S$ , where  $t_a$  is time to accelerate the ions in the extraction region,  $t_d$  is the ions drift time from the extraction mesh to FC,  $d$  is the length of the extraction region,  $S$  is the length of the drift region, i.e. from the grounded mesh to FC,  $m$  is the mass of Al atom,  $e$  is the electron charge,  $z$  is the charge state, and  $V$  is the external potential applied. This TOF equation does not account for the ion acceleration experienced by the double-layer potential, and due to the adiabatic and thermal expansion of the plume. The ions travel time in the extraction region is much smaller than the drift time. The effective acceleration experienced by the ions depends on the traveled distance of the plasma before the ions are extracted. Each ion charge state is accelerated in the double-layer potential region and by the external field according to the charge state.  $Al^{1+}$  gains the least energy compared to higher charge states and, therefore, has the lowest velocity and its TOF is the

longest. By calculating the accelerating potential required to achieve the TOF of  $\text{Al}^{1+}$ , the effective accelerating potential that the  $\text{Al}^{1+}$  experience is obtained. This potential is then used to determine the TOF of ions with higher charge states. The sum of the estimated TOF for Al ions with different charge states matches the experimental TOF signal well. By adding the effective external potential  $V_{eff}$  with the double-layer potential  $V_0$ , we can further extend the SCB distribution. To do so, we replaced the  $V_0$  term in Eq. 5.1 with total accelerating voltage  $V_T = (V_0 + V_{eff})$ . This results in ion pulses with peaks that are temporally separated with each pulse corresponding to a different charge state. The sum of these separated pulses is the signal observed by the FC. From the peak of the TOF signal of each charge state, the most probable energy can be calculated. The total energy of the ions with charge state  $z$  is equal to the sum of the ablation energy (sum of thermal and adiabatic expansion), Coulomb energy (from double-layer potential), and the effective accelerating voltage and can be written as  $E_{z-Total} = E_T + E_K + zE_c + zE_{eff}$ , where  $E_{eff}$  is the effective acceleration energy experienced by the ion from the external electric field. The value of  $E_{eff}$  is less than the voltage applied to the target due to the plasma shielding and secondary ion generation mechanism in the target-to-extraction grid region.

As the ions drift in the external electric field, they experience different acceleration by the external electric field depending on their generation location and the dynamics of plasma shielding in addition to the retrograde motion of the plan separating the neutral plasma from the non-neutral region established by the double-layer potential [23, 53]. The plasma expansion dynamics in an external electric field is complex and has been the subject of a few studies [52]. When the plasma expands in a field-free region,  $kT_i$  can be deduced from the fit of the ion signal, far away from the ablation point, as was shown in many publications [22, 109, 115]. However, when the plasma expands in an external electric field, obtaining  $kT_i$  from the SCB fit is problematic as the width of the TOF signal is affected by additional mechanisms occurring in the region between the target and the grounded grid causing ions with similar charge to experience slightly different electric field, thus, broadening the ion pulse. In this case, the TOF fit to the SCB distribution would not give an accurate  $kT_i$  of the ablated plume but rather a higher value that represents the spread in the kinetic energy of the detected ions as a result of their plasma ion energy and the complex plume and ion extraction dynamics in the target-grid region for an external applied field. Therefore, we refer to this parameter used in the fit as the effective ion

energy spread due to the combined plasma ion temperature and ion energy spread in the external electric field and refer to this quantity as  $kT_{ie}$  which is larger than the  $kT_i$  used for the SCB fit under plume expansion without an external field.

Fig. 5.4 shows the deconvolution of the ion signal into different ion charges for 5 kV applied to the target. When the laser fluence is  $28 \text{ J/cm}^2$ , the ratio of the ion charges  $\text{Al}^{1+}$ :  $\text{Al}^{2+}$ :  $\text{Al}^{3+}$  is  $\sim 6.2:3:1$ , and for a laser fluence of  $38 \text{ J/cm}^2$ , this ratio for  $\text{Al}^{1+}$ :  $\text{Al}^{2+}$ :  $\text{Al}^{3+}$ :  $\text{Al}^{4+}$  is  $\sim 6:1.6:1:1$ . The deconvolution of the TOF signal for a laser fluence of  $28 \text{ J/cm}^2$  yielded total accelerating voltage  $V_T \sim 1.55 \text{ kV}$  and  $kT_{ie} \sim 26 \text{ eV}$ . The increase in  $kT_{ie}$  with the applied voltage to the target reflects the spread in the energy of the ions probed by their TOF due to the dynamic nature of the plasma expansion in an external electric field. The external electric field is mostly shielded from the expanding plasma and would not cause plasma heating. When the laser fluence was  $38 \text{ J/cm}^2$ , as shown in Fig. 5.4(b), the deconvolution yielded total accelerating voltage  $V_T \sim 1.6 \text{ kV}$  and  $kT_{ie} \sim 27 \text{ eV}$ . The deconvolution of Fig. 5.4(a) and (b) also shows the presence of slow  $\text{Al}^{1+}$ . The slow ions were fitted for  $V_{TS} = (V_{0S} + V_{eff}) \sim 1.2 \text{ kV}$ .

The sensitivity of the deconvolution is checked by varying the values of  $z$ ,  $V_T$  and  $kT_{ie}$ . Fig. 5.5 shows the fit performed for  $\text{Al}^{4+}$  using different  $V_T$  and  $kT_{ie}$  values.  $kT_{ie}$  determines the ion pulse width for each charge state irrespective of the external electric field.  $V_0$  determines the ion pulse energy shift by the Coulomb energy associated with the double-layer potential, while  $V_T = (V_0 + V_{eff})$  adds the effect of the external electric field. The effect of  $V_T$  on the fit is more dominant than that for  $kT_{ie}$  and, for higher charge ions, the sensitivity of the fit to the value of  $V_T$  is higher. If  $kT_{ie}$  is kept constant, the energy shift in the SCB distribution is determined by  $V_T$ , whereas, for a fixed  $V_T$ ,  $kT_{ie}$  mainly determines the ion pulse width. As shown in Fig. 5.5, 300 V change in  $V_T$  shifts the  $\text{Al}^{4+}$  ion most probable energy by  $1200 \text{ eV}$ . Changes in  $kT_{ie}$  by  $13 \text{ eV}$  mostly affects the ion pulse width. For higher charge states, the accuracy of the fitting parameter  $V_T$  increases.

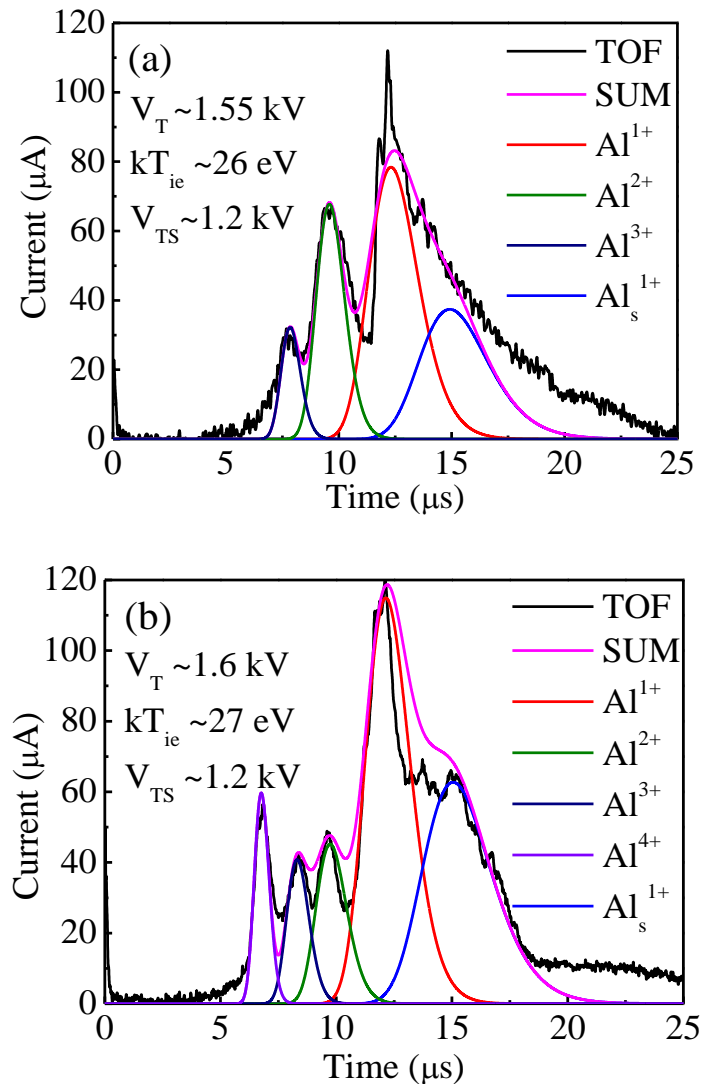


Fig. 5.4 Deconvolution of the TOF signal for different ion charge states for 5 kV applied to target. The laser fluence is (a)  $28 \text{ J/cm}^2$  and  $38 \text{ J/cm}^2$  (b).  $V_T$  is the total effective voltage accelerating the ions and  $kT_{ie}$  represents the spread in ion energy due to the plasma ion temperature and ion spread during plume expansion and ion extraction in the target-grid region,  $V_{TS}$  is the effective accelerating voltage for the slow ions.



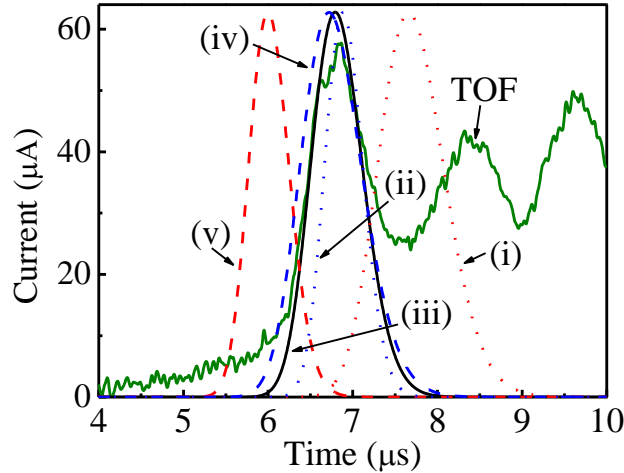


Fig. 5.5 The effect of varying the total accelerating voltage  $V_T$  and  $kT_{ie}$  on the deconvolution of the ion pulse when 5 kV accelerating voltage is applied. The  $\text{Al}^{4+}$  ion pulse obtained by deconvolution is shown for (i)  $V_T \sim 1300$  V and  $kT_{ie} \sim 27$  eV (red dotted line), (ii) 1600 V and 14 eV (blue dotted line), (iii) 1600 V and 27 eV (black straight line), (iv) 1600 V and 40 eV (blue dash line), and (v) 1900 V and 27 eV (red dash line).

### 5.3.3 Effect of target bias voltage

Fig. 5.6 shows the deconvolution of the ion TOF signal for 4 and 6 kV applied to the target when a laser fluence of  $28 \text{ J/cm}^2$  is used to ablate the target. The amplitude of the ion signal increases with the increase of the electric field between the Al target and the grounded mesh. For an acceleration voltage of 4, 5, and 6 kV, with all other conditions fixed, the total charges detected were 0.25, 0.5, and 0.65 nC, respectively. The ratio of the different ion charges detected remains nearly the same for the different target bias voltages. This indicates that changes in the external electric field between the target and mesh for our experimental conditions have negligible effects on the angular distribution of the detected ions. The applied electric field introduces retrograde motion of the expanding plasma edge exposing more ions to the accelerating field and repelling the electrons [53]. This is thought to be the main reason for the enhancement of the ion extraction with an increasing electric field between the Al target and the extraction grounded mesh. In Fig. 5.6(a), when 4 kV is applied to the target, the ion TOF signal has a best fit for  $V_T \sim 1100$  V and  $kT_{ie} \sim 20$  eV. When 6 kV is applied to the target, the best fit to the ion TOF signal is obtained for  $V_T \sim 1900$  V and  $kT_{ie} \sim 30$  eV, as shown in Fig. 5.6(b). The

deconvolution in Figs. 5.6(a) and (b) also shows a low energy tail in the ion TOF signal due to slow  $\text{Al}^{1+}$ . For 4 and 6 kV accelerating voltage, the TOF signal for the slow ions is fitted for  $V_{TS}$  of  $\sim 800$  and  $\sim 1400$  V, respectively. The insets of Fig. 5.6 (a) and (b) show the energy distribution of the ions as obtained from the ion TOF signal. The initial bumps present in the energy distribution is due to the slow energetic ions. The ion energy resolution,  $\frac{\Delta E}{E}$ , is dependent on the charge state, and is  $\sim 42\%$  for  $\text{Al}^{1+}$ ,  $\sim 32\%$  for  $\text{Al}^{2+}$ , and  $\sim 25\%$  for  $\text{Al}^{3+}$ . This resolution is not affected by the target biasing voltage.

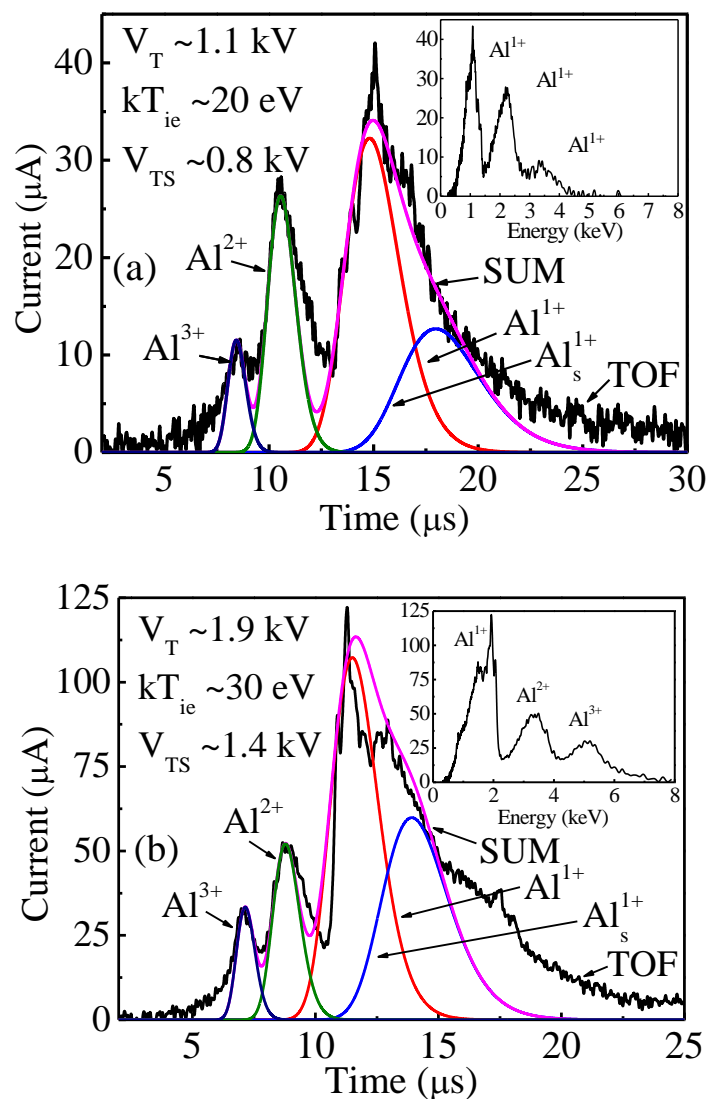


Fig 5.6 Deconvolution of the ion TOF signal into different charge states for a voltage applied to target of (a) 4 kV and (b) 6 kV. The ablating laser fluence is  $28 \text{ J/cm}^2$ . The TOF signal is plotted in black. The deconvolution fit for  $\text{Al}^{1+}$ ,  $\text{Al}^{2+}$ ,  $\text{Al}^{3+}$ ,  $\text{Al}_s^{1+}$  are plotted in red, green, navy, and blue, respectively. The sum of the individual de-convoluted ion species is plotted in pink. Inset shows the TOF signal converted into energy distribution of the ions.

### 5.3.4 Retarding field ion energy analysis

To characterize the ions from the laser plasma, the voltage applied to the electrostatic barrier (EB) mesh was incrementally increased from 0 V to a voltage that resulted in complete suppression of the ions detected. The laser fluence of  $28 \text{ J/cm}^2$  was used to ablate the Al target,

while 5 kV was applied to the target. Fig. 5.7 shows the TOF signal for 0, 0.6, 1.2, 1.8, 2.0 and 2.4 kV applied to the EB. The inset of Fig. 5.7 shows the reduction in the total number of charges reaching the FC with the increase in the EB voltage. Higher charge state ions reach the FC earlier than those with a lower charge since the ions gain kinetic energy from the double-layer potential and from the external electric field, proportional to their ion charge. The EB potential  $V_{EB}$  suppresses all ions having kinetic energy lower than  $zeV_{EB}$ . From Fig. 5.7, we observe that the EB bias of 1.8 kV suppresses more than  $\sim 80\%$  of the Al ions. The ion energy measured from the EB, TOF signal, and the deconvolution of the TOF signal are in good qualitative agreement.

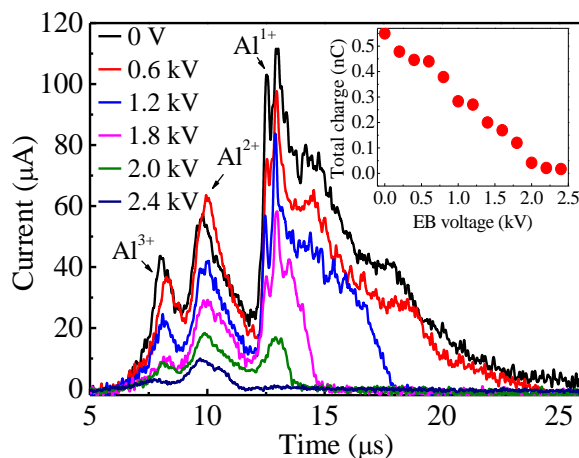


Fig. 5.7 Effect of retarding voltage on the TOF spectrum for a laser fluence of  $28 \text{ J/cm}^2$  and 5 kV applied to target.

### 5.3.5 Optical emission spectroscopy

We use the optical spectra of the laser plasma to estimate the  $kT_e$  and  $N_e$ . The emission spectra captured is time integrated but limited to the plasma observation location, which restricts the observation time depending on the plume expansion velocity. The plasma is moving in a direction perpendicular to the target surface. In our experiment, the fiber used has an acceptance angle of  $\sim 11^\circ$ . The lens that images the plume on the fiber optics bundle input is set to image the plume at and near the surface of the target. We estimate that optical emission from a distance up

to ~3 cm from the target is captured by the spectrometer. According to Harilal *et al.* [118], for Al ablation with nearly the same laser parameters, the plume has an expansion velocity of  $>10^7$  cm.s<sup>-1</sup>. With this velocity, the plume takes than 300 ns to pass the region imaged on by the fiber bundle connected to the spectrometer. For a ns laser ablation of Al by Nd:YAG laser in vacuum, Freeman *et al.* reported that the electron density and temperature measurement for time up to ~450 ns after the laser ablation satisfying the LTE condition [99]. Fig. 5.8 shows the optical spectra when the Al target is ablated by a laser fluence of 21 J/cm<sup>2</sup> without and with a voltage of 7 kV applied to the target. The NIST database is used to identify the atomic and ionic emission lines [119]. Line emission due to neutrals and ions with charge states up to Al<sup>2+</sup> are detected. The external electric field affects both the atomic and ionic spectral lines. There is a clear enhancement in the intensity of the spectral lines (both atomic and ionic) in the presence of an external electric field. The enhancement of the optical emission line intensities and the background is due to the shortening of the biased Al target to the grounded mesh, placed in front of the target, by the expanding plume. This shortening results in current flow from the power supply through the target and the plasma to the grounded grid. This current flowing between the biased Al target and grounded mesh is detected by a current pick-up coil detecting the current flow out of the grounded mesh. The current through the grounded mesh starts flowing at ~1 μs after the ablating laser pulse and is sustained for another ~1 μs corresponding to the time this glow discharge between the target and grid is extinguished as the plume passes that region. We believe that increased optical emission and its detection time is responsible for the increase in the integrated intensity in Fig. 5.8 when an external field is applied. In addition to enhancing the Al line emission intensity, a new emission line corresponding to the Ni I at 485.54 is detected when the target is biased at 5 and 7 kV. This line is probably due to the sputtering of Ni grounded mesh, placed in front of the target, which acts as the cathode of the discharge between the target and mesh. While, sputtering of the Ni mesh by the laser-generated ions would also occur without target bias, its rate will be significantly less due to the lower ion energy. As the optical detection geometry detects only a distance up to ~3 cm from the target, Ni lines will only be detected if Ni is present in that region during the discharge established between the target and the Ni grid.

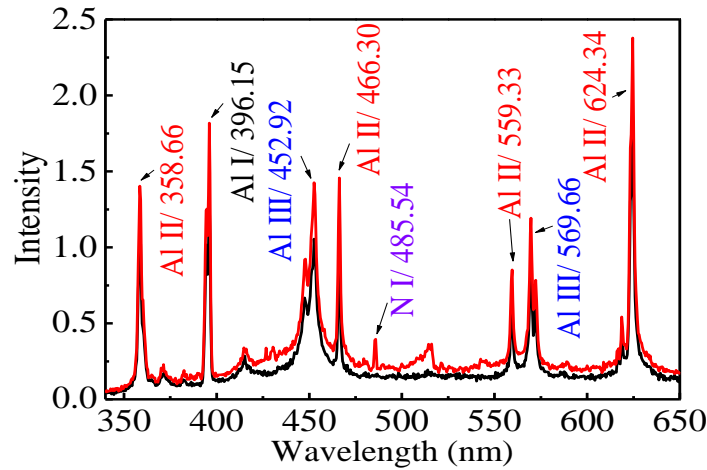


Fig. 5.8 Al emission spectra for laser fluence of  $21 \text{ J/cm}^2$ , when no external electric field (black line) and when 7 kV external field (red line) is applied.

For optically thin plasma, Stark broadening of line emission from neutrals or singly-charged ions is used to estimate the  $N_e$  [120]. Applying the procedure described by Radziemski *et al.*, for Al II lines at 704.21 and 705.66 nm, the statistical weight of the upper level of the lines are found to be proportional to the intensity ratio of the lines; therefore, the plasma was optically thin, and Stark broadening analysis can be applied [121]. In the present experiment, the Stark-broadened profile of the Al II line at 466.30 nm ( $4p^1P^0(1)-3p^2D(1)$ ) was used after fitting the line-shape to a Lorentzian profile, because of a comparatively lower self-absorption coefficient [122]. Three main broadening mechanisms contribute to line broadening, namely Doppler broadening, resonance pressure broadening, and Stark broadening. For laser plasma similar to ours, the effect of Doppler broadening and resonance broadening is very small compared to Stark broadening and can be neglected [123]. The mechanism causing Stark broadening of the Al II transitions is mainly due to perturbation of the energy levels of the ions by electron collisions leading to broadening of the emission lines. The instrumental response was obtained by fitting the line-shape of the 404.65 nm line from a low-pressure Hg lamp to a Lorentzian profile and was found to be 0.7 nm. This instrumental response was subtracted from the experimental linewidth of the Al II line at 466.30 nm that was also fitted to a Lorentzian profile. Eq. 5.2 can be used to correlate the full-width at half-maximum (FWHM) of the Stark-broadened line  $\Delta\lambda_{1/2}$  with the  $N_e$  [124];

$$\Delta\lambda_{1/2} = 2\omega \left( \frac{N_e}{10^{16}} \right) + 3.5A \left( \frac{N_e}{10^{16}} \right)^{\frac{1}{4}} (1 - 1.2N_D^{-1/3}) \omega \left( \frac{N_e}{10^{16}} \right) \text{Å}, \quad (5.2)$$

where  $\omega$  is the stark broadening parameter, and for Al II line at 466.30 nm, it has a value of 0.0538 nm at a temperature of 15,000 K [124],  $A$  is the ion broadening parameter. Both  $\omega$  and  $A$  are weak functions of temperature [120].  $N_e$  is the electron density in  $\text{cm}^{-3}$  and  $N_D$  is the number of particles inside the Debye sphere. The first term of the Eq. 5.2 accounts for the electron broadening, and the second term is the correction for the quasi-static ion broadening. The quasi-static ion broadening term is small in plasma, similar to our case as was estimated from the extrapolation of the estimates of  $\omega$  and  $A$  [120, 123]. Therefore, Eq. 5.2 becomes:

$$\Delta\lambda_{1/2} = 2\omega \left( \frac{N_e}{10^{16}} \right) \text{Å} \quad (5.3)$$

To determine the  $kT_e$ , we use the line emission intensity analysis. This method can be applied when the plasma satisfies LTE and is applicable to our laser plasma conditions, as described in previous studies using similar lasers [99]. The excitation temperature can be determined using Eq. 5.4 [120].

$$T_e = \frac{E_2 - E_1}{k} \left[ \ln \left( \frac{I_1 \lambda_1 g_2 A_2}{I_2 \lambda_2 g_1 A_1} \right) \right]^{-1} \quad (5.4)$$

where  $k$  is the Boltzmann constant,  $E_2$  and  $E_1$  are the energies of upper transition levels of two lines utilized for electron temperature estimation and belong to the same atomic species.  $I_l$ ,  $A_l$ ,  $g_l$ , and  $\lambda_l$  are total intensity (integrated over the line profile), transition probability, degeneracy, and wavelength of the line with upper level  $E_l$ , respectively. The subscript 2 refers to the line with upper level  $E_2$  for the corresponding quantities. Al II lines at 358.66, 466.30, 559.33, and 624.34 nm are used to calculate the plasma  $kT_e$ . Fig. 5.9 shows the  $N_e$  (a) and  $kT_e$  (b) with the increase in voltage applied to the target for laser fluence of 21 – 38  $\text{J}/\text{cm}^2$ . In Fig. 5.9(b), the average  $kT_e$  is plotted with the error bar representing the maximum and minimum values obtained from the line emission analysis. We observe that the  $N_e$  and  $kT_e$  increase significantly with the increase of laser fluence, but shows no change, within the experimental error, with the applied external electric field.

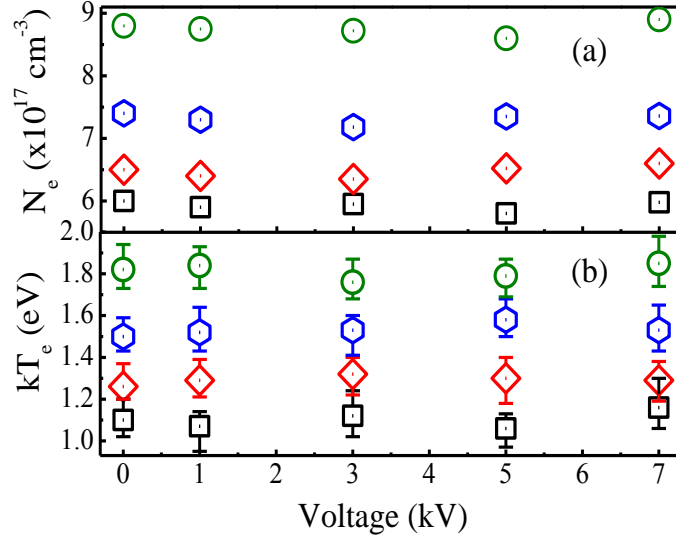


Fig. 5.9 Effect of target bias voltage on (a) electron density  $N_e$  and (b) electron temperature  $kT_e$  as measured by OES. Laser pulse energy of 21, 25, 28, and 38 J/cm<sup>2</sup> is represented by black-square, red-diamond, blue-hexagon and green-circle, respectively.

Using the value of  $N_e$  and  $kT_e$  in the McWhirter criterion, we can determine whether the generated plasma satisfies the LTE condition. To satisfy the LTE condition, the lower limit of the  $N_e$  has to fulfill the following condition [26]:

$$N_e(\text{cm}^{-3}) \geq 1.6 \times 10^{12} [T_e(\text{K})]^{1/2} [\Delta E(\text{eV})]^3 \quad (5.5)$$

where  $\Delta E$  is the largest energy transition from which the condition holds, and for our case it is 3.65 eV, and  $T_e$  is the plasma temperature [26]. The plasma temperature we obtained for a laser fluence of 21 J/cm<sup>2</sup> when no accelerating voltage is applied is  $\sim 1.1$  eV. Accordingly, the lower limit of  $N_e$  for the LTE condition using Eq. 5.5 is  $8.8 \times 10^{15}$  cm<sup>-3</sup>. The  $N_e$  value we obtained using OES is greater than the minimum LTE condition value leading to the conclusion that LTE is applicable to the studied plasma.

For the laser fluence range from 21 to 38 J/cm<sup>2</sup>,  $kT_i$  of the ejected ions evaluated by the TOF deconvolution varied between  $\sim 6$  to  $\sim 10$  eV when no accelerating voltage was applied, while when up to 6 kV accelerating voltage was applied  $kT_{ie}$  ranged from  $\sim 20$  to  $\sim 30$  eV whereas the  $kT_e$  calculated from the optical spectra varied between  $\sim 1.1$  to  $\sim 1.8$  eV for the same laser fluences. Without an external field applied, the difference in the values of  $kT_i$  measured by ion TOF and  $kT_e$  measured by OES is attributed to the difference in time and location at which the



plasma is probed. For ns laser pulse ablation, plasma reaches its highest temperature during the laser pulse with its highest density near the surface forming the core of the plasma and, therefore, the ions are generated during the laser pulse interaction with the target and the plume [22, 125, 126] and  $kT_i$  from the TOF deconvolution estimates the initial ion temperature. Also, for ns laser ablation at the earlier stage, before  $\sim 60$  ns, the intense continuum is dominant masking line emission [16]. Since  $kT_e$  probed by the OES is time and spatially integrated, it estimates lower temperature than the initial temperature. Thus, for a laser fluence of  $21 \text{ J/cm}^2$ , the plasma temperature cools from  $\sim 6$  to below  $\sim 1.1$  eV from initial plasma expansion until the plasma cools down. With an electric field applied between the target and the grounded mesh, temporal and spatial variations in ion acceleration by the field due to the dynamics of the plasma expansion causes a further spread in the ion velocity not associated with ion plasma temperature. Hence,  $kT_{ie}$  represents the combined ion energy spread due to plasma ion temperature and the ion extraction dynamics from the laser plume expanding in an external electric field.

#### 5.4 SUMMARY

Nd:YAG laser Al plasma is characterized using ion TOF and OES. Laser fluence of  $21 - 38 \text{ J/cm}^2$  is used to ablate the Al target. Production of ions up to  $\text{Al}^{4+}$  was observed. The extracted ions energy distributions are fitted with shifted-Coulomb Boltzmann distribution. The ions are accelerated according to their charge state by the double layer potential developed at the plasma-vacuum interface, in addition to the external electric field applied to accelerate the extracted ions. The plasma temperature measured by ion TOF and OES shows significant deviation. For a laser fluence increase from  $21 - 38 \text{ J/cm}^2$ , according to ion TOF measurement the  $kT_i$  increases from  $6 - 10$  eV, while OES yields  $kT_e$  of about  $1.1 - 1.8$  eV. The temperature measured by OES does not reflect the initial high temperature of the plasma in which the ions are generated, and at that time condition of optically thin plasma might not be maintained. In addition, temporal and spatial averaging of plasma emission influences the OES measurements and yield a lower plasma temperature than the early time of plume formation when the plasma was densest and hottest.

## CHAPTER 6

### FEMTOSECOND LASER PLASMA

#### 6.1 INTRODUCTION

Pulsed laser ablation of a solid target can be used to generate ions with different charges from a variety of target materials. The laser-ablated plasma can be considered as an instantaneous ion point source with the characteristic ion emission time smaller than the ion drift time and the plasma plume dimension much smaller than the source-to-ion collector distance [127]. Pulsed laser interaction with a solid is initiated by the absorption of part of the incident laser pulse causing target heating, melting, vaporization, ionization, particle ejection, and plasma formation and expansion. The laser pulse width, wavelength, and the pulse energy density determine the heat-affected zone, the ablation mechanism, plasma properties, and plasma expansion dynamics [128, 129]. Dense plasma consisting of electrons, ions, clusters, and neutrals are generated due to the laser-matter interaction. The interaction of a high-power density laser pulse with the target results in the ablation of the target surface. When the femtosecond laser intensity is  $10^{13}$ - $10^{14}$  W/cm<sup>2</sup>, ionization of the target material, occurring during the initial laser-solid interaction, is the dominant mechanism [130]. After the initial ionization by inverse bremsstrahlung and resonant absorption, electron-photon energy transfer takes place between the free electrons and the remaining femtosecond laser pulse [130]. During this time, a thin sheath of electrons and ions forms and begins to generate a bubble on the laser-irradiated surface. The electron cooling time ( $\tau_e \sim 1$  ps) is longer than the temporal duration of the 100-fs laser pulse; therefore, the interaction of the femtosecond laser pulse with the metal target is already completed before the excited electrons transfer their energy into the lattice of the target via electron-phonon coupling [131]. Evaporative ablation due to the energy transfer to the lattice by the electrons results in the formation of the plasma plume.

In femtosecond laser ablation, the laser pulse width is shorter than the electron-phonon coupling time and the heat transport time in the solid [131-133]. Therefore, femtosecond laser ablation causes a smaller heat affected zone compared to nanosecond ablation [134]. For laser intensities significantly higher than the ablation threshold, as is the case for MCI generation,

ablation proceeds mainly by thermal vaporization [135, 136]. In femtosecond laser ablation, plasma expansion occurs after absorption at the laser pulse.

Several groups reported on ion emission by femtosecond laser pulse irradiation of a solid target [129, 137-139]. Using a Ti:sapphire laser (wavelength  $\lambda = 800$  nm, pulse width  $\tau = 60$  fs, and laser fluence  $F = 8.5$  J/cm<sup>2</sup>), Irimicucic *et al.* performed Langmuir probe measurement on transient plasmas from several metallic targets. The time-of-flight (TOF) profile of the ion current was fitted to a shifted Maxwell-Boltzmann velocity distribution and used to reconstruct the probe I-V characteristics. This technique allowed for obtaining the temporal development of the ion and electron temperatures and densities up to 10  $\mu$ s after the laser pulse [129]. For an Al target, the electron temperature was  $\sim 1.6$  eV, measured 8  $\mu$ s after the laser pulse, while the ion temperature, determined from the shifted Maxwell-Boltzmann fit of the probe ion signal, was  $\sim 3$  eV. Anoop *et al.* used spatially and temporally-resolved optical emission spectroscopy of the laser plume to study the dynamics of ions and neutrals generated by ablating Cu using a Ti:sapphire laser ( $\lambda = 800$  nm, and  $\tau = 40$  fs, and  $F = 0.5$ – $77.5$  J/cm<sup>2</sup>). For  $F > 10$  J/cm<sup>2</sup>, splitting of the plasma plume is observed and was attributed to the fast-moving ions separating from the slow neutrals. For  $F > 50$  J/cm<sup>2</sup>, the maximum energy estimated for the ions and neutrals was  $\sim 800$  and  $\sim 30$  eV, respectively [137]. Their imaging results were correlated to Faraday cup and Langmuir probe measurements of the charged particles. Kelley *et al.* used a Faraday cup to study plasma from C, Al, and Cu targets ablated by a Ti:sapphire laser ( $\lambda = 800$  nm,  $\tau = 70$  fs, and  $F = 0.1$ – $1$  J/cm<sup>2</sup>) [138]. They reported a bi-modal ion kinetic energy distribution with the lower distribution following the shifted Maxwell-Boltzmann, attributed to thermal ionization, whereas, the higher distribution was non-Maxwellian, attributed to space-charge effects within the plume [138]. Donnelly *et al.* studied the expansion dynamics and the various plume components in laser ablation ( $\lambda = 527$  nm,  $\tau = 250$  fs, and maximum  $F \sim 0.8$  J/cm<sup>2</sup>) of a Ni target. Ion TOF profiles and thickness map of deposition on a transparent substrate were obtained. The ion energy normal to target was  $\sim 35$  and  $\sim 100$  eV for laser fluences of  $\sim 0.1$  and  $\sim 0.8$  J/cm<sup>2</sup>, respectively [139].

Generation of energetic MCIs by femtosecond laser pulse irradiation of a solid target with moderate powers was previously reported [104, 140, 141]. Gordienko *et al.* generated up to Si<sup>12+</sup> by ablation of a Si target with a femtosecond dye-laser ( $\lambda = 616$  nm,  $\tau = 200$  fs, and maximum intensity  $I = 3 \times 10^{16}$  W/cm<sup>2</sup>) [140]. The surface of the Si target was cleaned by

ablating it with a nanosecond laser pulse of fluence  $3 \text{ J/cm}^2$  prior to femtosecond laser ablation. Fast and slow components of the Si ions were observed; the fast ions gain energy according to their charge state, while for the slow ions, the energy gain increases with the charge state. This was explained by recombination, which occurs at a faster rate for the slower ions since slower ions spend more time to reach the detector [140]. In that experiment, the residual gas pressure was  $\leq 2 \times 10^{-5}$  Torr [62]. Zheng *et al.*, used a Langmuir probe and electrostatic ion energy analyzer to study the Al plasma characteristics generated by a nanosecond Nd:YAG laser ( $\lambda = 1064 \text{ nm}$ ,  $\tau = 6 \text{ ns}$ , and  $F = 1.3 \text{ J/cm}^2$ ) and a femtosecond Ti:sapphire laser ( $\lambda = 780 \text{ nm}$ ,  $\tau = 100 \text{ fs}$ , and  $F = 0.4 \text{ J/cm}^2$ ). The maximum charge states achieved by the nanosecond and the femtosecond lasers were  $\text{Al}^{2+}$  and  $\text{Al}^{3+}$ , respectively [104]. The plasma characteristics generated by these two lasers were studied for comparable ablation flux using a Langmuir probe and an ion energy analyzer. The nanosecond laser pulse produced a greater concentration of low energy and low charge state ions compared to the femtosecond laser. Chutko *et al.*, used an ion energy/charge cylindrical analyzer combined with TOF analysis to study ion generation from ablation of Si by a femtosecond laser ( $\lambda = 616 \text{ nm}$ ,  $\tau = 200 \text{ fs}$ , and  $I \leq 2 \times 10^{16} \text{ W/cm}^2$ ) [141]. Generation of charge states up to  $\text{Si}^{6+}$ ,  $\text{O}^{4+}$ , and  $\text{C}^{6+}$  was reported. The O and C ions were attributed to impurities on the Si surface.

We report on aluminum MCI generation by a Ti:sapphire femtosecond laser ( $\lambda = 800 \text{ nm}$ ,  $\tau \sim 100 \text{ fs}$ ,  $F \leq 7.6 \text{ J/cm}^2$ ) ablation without and with ion acceleration in an external electric field between the target and a grounded mesh. The velocity and the charge state of the MCIs are determined by using ion TOF and electrostatic retarding field ion energy analyzer. The electric field generated in the plume-vacuum interface that is responsible for the ion acceleration is estimated from the deconvolution of the ion pulse into individual ion species. Distinct higher order charge states along with the increase in the total number of ions generated are observed with the increase in the laser pulse energy. Ions up to  $\text{Al}^{6+}$  were observed. These results are compared to our earlier nanosecond Al MCI generation using a Q-switched Nd:YAG laser (wavelength  $\lambda = 1064 \text{ nm}$ , pulse width  $\tau \sim 7 \text{ ns}$ , and Fluence  $F \leq 38 \text{ J/cm}^2$ ) [54, 55]. The extracted MCIs from femtosecond laser ablation gain more energy from the external electric field compared to nanosecond ablation due to the lower plasma shielding effect in the femtosecond case.

## 6.2 EXPERIMENTAL

A Spectra-Physics femtosecond amplified Ti:sapphire laser is used to ablate the Al target. The laser produces  $\sim 100$  fs (measured with a single shot auto-correlator) laser pulses at 800 nm with a repetition rate of 1 kHz and laser fluence up to  $7.6 \text{ J/cm}^2$ . The ions are generated in a vacuum chamber where the femtosecond laser irradiates the Al target. The generated ions are then accelerated towards the Faraday cup (FC) through a drift tube. The diameter of the ion generation chamber is 30 cm. A 125 cm long transport tube with an inner diameter of 10 cm is connected to the chamber. An illustration of the MCI source is shown in Fig. 6.1.

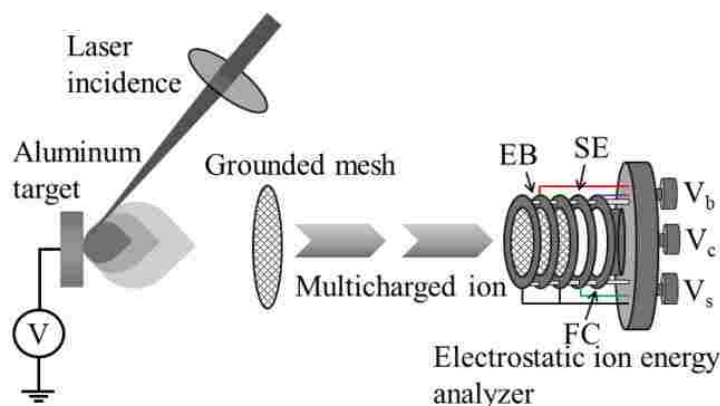


Fig. 6.1 An illustration of the laser MCI ion source showing the laser irradiating the Al target, and the electrostatic TOF energy analyzer. EB is the electrostatic barrier electrode, SE suppressor electrode, and FC Faraday cup.

The Al target ( $\sim 1$  cm square, 0.5 mm thick, 99.97% pure Al foil) was placed on a multi-axes translational stage. The laser beam is focused on the Al target surface at an angle of  $45^\circ$  with the surface using a lens of 32-cm focal length positioned on a horizontal translation stage. The laser spot area at focus was  $\sim 8 \times 10^{-5} \text{ cm}^2$ , as obtained using the knife-edge method at target-equivalent plane with the edge scanned at  $45^\circ$  to the laser beam. The Al target support is placed inside the MCI generating chamber using an insulated connector. This arrangement allows for applying an accelerating voltage directly to the Al target while keeping the experimental chamber at ground. The femtosecond laser pulses pass to the Al target through a viewport which

has ~8% loss in optical power due to Fresnel reflections. For ion extraction, a nickel mesh of diameter 10-cm, thickness of 100  $\mu\text{m}$ , and with an open area of 70% is placed 15-cm in front of the target. The generated ions are accelerated in the gap between the Al target and the extraction mesh. The ions are accelerated by the combined effect of the expanding plasma, the electric field developed in the plasma-vacuum interface due to double-layer formation [54], and the external applied electric field. After passing the extraction mesh, the ions drift in the transport tube with a constant velocity. The MCIs are detected at the end of the transport tube using an Al Faraday cup (FC) with a diameter of 5 cm. To suppress the secondary electrons from the FC due to positive ion collisions, the suppressor electrode ring, located 1 cm before the FC, is biased with -140 V [111]. Throughout the experiment, the FC voltage was maintained at -70 V. The retarding field ion energy analyzer consists of three nickel meshes, like the extraction mesh but with a diameter of 5 cm, each separated by 1 cm and placed with the closest mesh to target at 130 cm away from the Al target. To analyze the ion energy distribution, a variable voltage is applied to the electrostatic barrier (EB) electrode, which is the central electrode of the three-grid retarding field analyzer. The 1-kHz femtosecond laser pulses are gated by a fast-mechanical shutter to select only a single laser pulse that irradiates the Al target. The oscilloscope is triggered by a fast photodiode detector observing the optical leak in the last mirror before the focusing lens. Inside the vacuum chamber, the loss of MCIs by charge transfer with the background gas is negligible under our experimental conditions (background gas in UHV chamber is in the low  $10^{-9}$  Torr). The total scattering cross section for ions with different charge states was previously measured [89-91]. The mean free path of the Al ions depends on their charge state, but for background pressures as in our vacuum chamber is  $\geq 10$  km for Al ions up to 6+. As the travel distance of the ions from the target to the Faraday cup is 1.4 m, ion recombination in the drift tube is negligible.

### 6.3 RESULTS AND DISCUSSIONS

The ion signal recorded on the oscilloscope from the FC was analyzed using Origin Pro version 9.1 software to determine the total charge of the Al ions delivered to the FC. Origin software allows processing the data recorded by the oscilloscope using a Fast Fourier Transform filter with a 5-point window to filter and smooth noise in the measured signal. The total charge

delivered to the FC  $Q_i$  is given by  $Q_i = \frac{1}{R_L} \int V_F(t) dt$ , where  $V_F(t)$  is the voltage signal detected by the FC and  $R_L$  is the 50  $\Omega$  internal resistance of the oscilloscope.

To observe the effect of consecutive laser pulses hitting the same spot on the target, we calculated the total ion generation per pulse for each laser pulse starting with a fresh target surface area. The femtosecond laser pulse fluence 7.6 J/cm<sup>2</sup> was focused on the surface of the Al target. The ion signal was observed, and the number of ions produced was calculated for an accelerating voltage of 0 – 6 kV. The general behavior of the number of ions detected with consecutive laser pulses is that it increases after the first or second laser pulse due to surface cleaning, followed by a slight reduction with laser pulses interacting with the same surface area due to drilling of the target. For the laser conditions used, the highest ion yield occurs at the 3<sup>rd</sup> laser pulse. Although there are pulse-to-pulse fluctuations in the magnitude of the ion signal due to a certain charge, the ion energy and energy distribution, as detected by TOF, remains consistent. For example, the peak amplitude of Al<sup>1+</sup> was observed to fluctuate by 23% over four consecutive laser pulses while the TOF of the ions, which is indicative of ion energy, remained almost unchanged. The reported data is collected for the 3<sup>rd</sup> pulse to avoid the effect of any oxide or contaminants on the surface of the Al target. A different target spot was used for each data point; each target spot was located at least 1 mm radially from the previous one so that no two spots overlap. The voltage on target was measured with a fast-high voltage probe.

### **6.3.1 Ions detected without external acceleration**

The interaction of the femtosecond laser pulse with the surface of the target creates dense hot plasma within the time scale of the laser pulse. Subsequently, the plasma expands adiabatically into the vacuum. In the plume, the ion kinetic energy can range from hundreds of eV to several keV depending on laser fluence [142]. The plume expansion is mainly perpendicular to the sample surface. To characterize the generated ions from the laser plasma without applying accelerating voltage to the target, the voltage bias on the electrostatic barrier (EB) was incrementally increased from 0 V to a voltage that resulted in complete suppression of the ions detected. Fig. 6.2 shows the TOF spectrum for 0, 50, 100, 200, and 325 V positive voltages applied to the EB. The laser fluence of 7.6 J/cm<sup>2</sup> was used to ablate the Al target. The plasma ion peak drifts towards the FC with a velocity of  $\sim 3.8 \times 10^4$  ms<sup>-1</sup> when no barrier voltage

is applied. The inset of Fig. 6.2 shows the reduction in the total number of charges reaching the FC with the increase of the electrostatic barrier voltage. The ion bunch generated by pulsed laser ablation that reaches the FC contains different ionic states. The double-layer potential, developed in the laser-generated plasma plume, at the plasma vacuum interface, accelerates the ions [23]. Higher charge state ions reach the FC earlier than those with a lower charge since the ions with higher charge gain more kinetic energy from the double-layer potential. From Fig. 6.2, we observe that the EB bias of  $\sim 325$  V stops most ( $\sim 95\%$ ) of the Al ions generated.

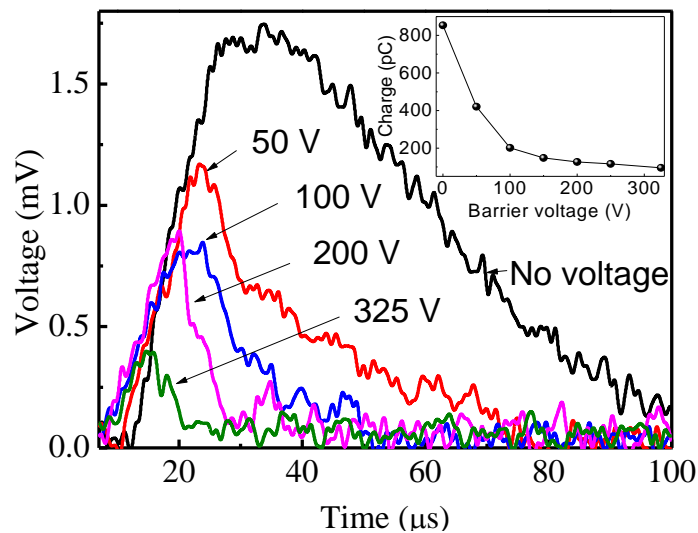


Fig. 6.2 Ion signal for various EB voltage biases at laser fluence of  $7.6 \text{ J/cm}^2$ . Inset shows the reduction of total charge with the increase of barrier voltage when no accelerating voltage is applied to the target.

Many factors affect the ion energy, most importantly, plasma temperature, adiabatic expansion of the plasma plume, and the Coulomb acceleration due to the double-layer potential at the plasma-vacuum interface of the expanding plume [23, 143]. The emitted ion charge states are identified from their TOF signal. Also, the ion energy distribution is obtained from the retarding energy analyzer and from the TOF signal. Therefore, deconvolution of the TOF signal into individual ion charge signals can be accomplished based on the assumption of local thermodynamic equilibrium (LTE) in the expanding laser plume [143]. The velocity distributions of the laser ablated ions far from the irradiated target, where the ion charge-states are frozen, is



characterized by a shifted Coulomb-Boltzmann (SCB) distribution for each ion species. This SCB distribution is given in Eq. 6.1 [143, 144]:

$$F(v) = A_0 \left( \frac{m}{2\pi kT} \right)^{3/2} (v)^3 \exp \left[ -\frac{m}{2kT} (v - v_k - v_c)^2 \right] \quad (6.1)$$

where  $v = v_t + v_k + v_c$  denotes the total velocity along the normal to the target surface,  $v_t$  is the mean thermal velocity for monoatomic neutral species,  $v_k$  is the adiabatic expansion velocity,  $v_c$  is the velocity due to Coulomb acceleration, and  $A_0$  is a normalization constant. These velocities are obtained from the following:

$$v_t = \sqrt{(3kT/m)}; \quad v_k = \sqrt{(YkT/m)}; \quad v_c = \sqrt{(2zeV_0/m)}$$

where  $m$  is the mass of ablated ion,  $Y$  is the adiabatic coefficient which, for a monoatomic metal, e.g., aluminum, has the value of 5/3,  $z$  is the charge state,  $kT$  is the equivalent ion plasma temperature (in eV), and  $V_0$  is the equivalent accelerating voltage developed inside the plasma. In Eq. 6.1, the condition of LTE ( $T_i \sim T_e \sim T$ ) is assumed. For a transient plasma, such as in laser-plasma, the LTE condition requires that electron-atom and electron-ion collisions are faster than radiative processes. These collisions establish equilibrium with particle velocities in the plasma following a Maxwell-Boltzmann distribution [16, 145]. The validity of LTE for laser plasma was previously considered for femtosecond laser ( $\lambda = 800$  nm,  $\tau = 100$  fs, and  $F = 0.9 - 18$  J/cm<sup>2</sup>) ablation [146], which is nearly same laser conditions used in our present experiment.

The Kelley and Dreyfus function, expressing the ion current based on the SCB distribution including the effect of Coulomb energy in terms of an equivalent accelerating voltage, can be applied for analysis of the ion current if the TOF of ions is much longer than the duration of the laser pulse [113, 114]. The SCB model considers both thermal and Coulomb interactions. TOF signal of each ion species can be written as  $F(t) = F(v) \frac{dv}{dt}$ , where  $F(v)$  is given in Eq. 6.1. Therefore, the overall distribution of the ejected ions is a sum of individual SCB distributions with their characteristics equivalent accelerating voltage and ion plasma temperature:

$$F(t) = \sum_i A_i \left( \frac{m}{2\pi kT} \right)^{3/2} \left( \frac{L^4}{t^5} \right) \exp \left[ -\frac{m}{2kT} \left( \frac{L}{t} - \sqrt{YkT/m} - \sqrt{2zeV_0/m} \right)^2 \right] \quad (6.2)$$

In Eq. 6.2,  $A_i$  are normalization constants,  $t$  is the time-of-flight, and  $L$  is the total distance from the target to the Faraday cup [109]. Eq. 6.2 applies under the condition of absence of significant recombination and collisional excitation processes, i.e., ion species are frozen and freely drifting in the vacuum. Such properties were observed for expanding laser plasma outside the recombination zone limited by the critical distance  $L_{cr}$  (i.e.,  $L > L_{cr}$ ), where the ion charges  $z$  decreases with distance  $L$  such that  $z \propto L^{-2}$  and the ion current follows  $j_{IC} \propto L^{-3}$  due to rarefaction of the expanding plasma [115]. The parameters used to fit the TOF ion signal with Eq. 6.2 are mostly sensitive to the equivalent ion plasma temperature  $kT$  and the equivalent acceleration voltage  $V_0$  developed in the plume due to the double-layer potential formed at the plasma-vacuum interface. From this fit of the measured TOF signal with Eq. 6.2, we can estimate  $kT$  and  $V_0$ .

The ion pulse detected by the FC, shown in Fig. 6.2, consists of ions with different charge states. In order to determine the contribution of each ion charge to the TOF signal, deconvolution of the ion pulse signal for each ion charge state is performed. To obtain the best fit to the TOF signal, a combination of  $kT$  and  $V_0$  is used. These two parameters are used to estimate the effects of thermal, adiabatic, and Coulomb potential on the different ion charges. The deconvolution of the ion pulse into different ion charges is conducted as follows: (1) The ion energy distribution of each charge state is assumed to follow the SCB distribution described in Eq. 6.1; (2) The maximum charge state  $z$  generated is based on the TOF measurement conducted by separating the charge states temporally using an externally applied electric field between the target and the grounded mesh, as discussed in Section III. B; (3) The equivalent accelerating voltage developed inside the plasma due to the double-layer potential  $V_0$  and the equivalent ion plasma temperature  $kT$  are set as free variables conditional upon the total energy (sum of thermal, adiabatic and Coulomb) matching with the ion energy measured by the three-grid retarding field analyzer; (4) The most probable energy of each ion charge is separated by  $V_0$  since the ions gain energy from  $V_0$  that is proportional to their charge  $z$ ; and (5) The sum of the TOF signal due to the different ion charges fits the TOF signal of the observed ion pulse that is composed of all ions.

In laser-generated ions, two energy distributions for  $\text{Al}^{1+}$  and  $\text{Al}^{2+}$  were reported using Nd:YAG laser ( $\lambda = 532$  nm,  $\tau = 5$  ns, and  $F = 0.8 - 6$  J/cm<sup>2</sup>) [19]. Also, slow and fast Si MCI generation using a femtosecond laser ( $\lambda = 616$  nm,  $\tau = 200$  fs, and maximum intensity  $I = 3 \times 10^{16}$

W/cm<sup>2</sup>) was reported [62]. The faster group was attributed to multiphoton laser ionization, while the slow group was attributed to collisional processes [19]. Within the expanding plume, collisions among ions, electrons, and neutrals lead to ionization, recombination, and charge transfer resulting in ions with different charge states than the source ion species. Since, ions are accelerated depending on their charge state and their energy also depends on their formation process. Therefore, an ion charge can have more than one independent SCB distributions [19]. The acceleration of these ions also depends on the location between the target and grounded mesh at which the ion is generated and can experience the external electric field. Plasma shielding reduces ion acceleration by the external electric field. For example, if recombination is the dominant process ( $\text{Al}^{2+} + e \rightarrow \text{Al}^{1+} + h\nu$ ), the  $\text{Al}^{2+}$  and  $\text{Al}^{1+}$  involved in this reaction will contribute to the energy distribution for the  $\text{Al}^{1+}$  ions. We considered slow  $\text{Al}^{1+}$  and  $\text{Al}^{2+}$  generation along with the fast ions, since multiple peak structures in the TOF signal are observed for these ion groups.

The deconvolution of the ion pulse into individual ion species, shown in Fig. 6.3, results in a temporal distribution of ion states throughout the ion pulse. The higher charge state ions have higher energy and reach the FC earlier than the lower charge states. The sum of the signals from different ion charges gives the total ion signal which is fitted to the experimental TOF signal. From Figs. 6.2 and 6.3, each ion charge is always affected by the retarding field according to its charge state resulting in a reduction in the ion pulse amplitude, throughout the ion pulse, due to the temporal separation of the different ion charges. From the deconvolution, we recover charge states up to  $\text{Al}^{6+}$ . This is confirmed by the individual ion charge signals observed after separation of the different ion charges with a voltage applied on the target making it possible to identify each by their time-of-flight.

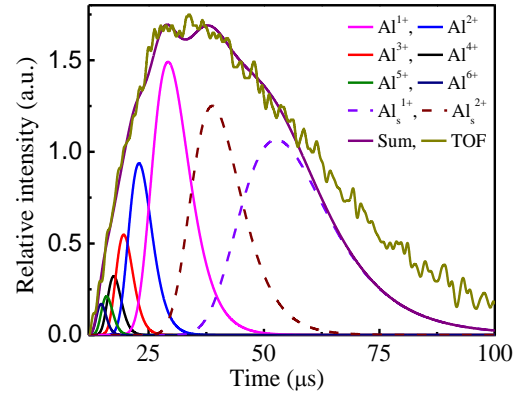


Fig. 6.3 Deconvolution of TOF spectrum into individual ion species for laser fluence of  $7.6 \text{ J/cm}^2$  when no accelerating voltage is applied to target.  $\text{Al}_s^{1+}$  and  $\text{Al}_s^{2+}$  are the slower ions.

The curve fit for the extracted Al ions in Fig. 6.3 was done for  $V_0 = 250 \text{ V}$  and  $kT = 25 \text{ eV}$  for the fast ions. For the slow  $\text{Al}^{1+}$  and  $\text{Al}^{2+}$  ions,  $V_0 = 90 \text{ V}$  and  $kT = 18 \text{ eV}$ . The stretched tail of the ion pulse indicates the possibility of more groups of slow ions. The total energy of the Al ions without externally applied electric field is  $E_{zT} = (E_t + E_k) + zE_c$ , where  $E_{zT}$  is the total energy gain for charge state  $z$ ,  $E_t = \frac{3}{2}kT$  is the thermal energy,  $E_k = \frac{\gamma}{2}kT$  is the adiabatic energy, and  $E_c = eV_0$  is the Coulomb energy associated with the equivalent accelerating voltage due to the double-layer potential. In Fig. 6.3, the most probable energy of different ion species are separated by  $\sim 250 \text{ eV}$ . The calculated most probable energy of the TOF signal and the adiabatic and thermal energy obtained by the deconvolution are in good qualitative agreement with the results found for ablation using femtosecond lasers [117, 147, 148].

The sensitivity of the ion signals for each charge state, obtained by the deconvolution process, is checked by performing the fit to the detected TOF signal using different values of  $z$ ,  $V_0$ , and  $kT$ . The maximum ion charge  $z$  is experimentally known from the TOF signal with the external accelerating field because the ions with different charges are temporally well separated. In performing the deconvolution, the sum of the ion signals of all charges detected is fitted to the measured TOF signal. This fit is best at time scales extending from the onset of the fast ions detected by the FC and extends past the peak of the TOF signal. The slower ions forming the tail of the TOF signal are not as well fitted to the SCB distribution, representing the sum of the ion charges. This is because there are secondary mechanisms forming these slower ions, as was

previously discussed [19, 62]. The ion pulse width for each charge state gives the value of  $kT$ . Higher  $kT$  results in a wider ion pulse for each charge state. The Coulomb energy associated with  $V_0$  determines the ion pulse energy shift, with higher  $V_0$  corresponds to an increased ion energy shift of the SCB distribution. The fit is more sensitive to changes in  $V_0$  compared to changes in  $kT$ , with changes in  $V_0$  affecting the higher charge states more profoundly. Sensitivity to fitting parameters are discussed in Section III. B for ion extraction with an external electric field.

### 6.3.2 Ions detected with external acceleration

Since  $\text{Al}^{1+}$  has the lowest velocity among the Al ions with different charge states, the  $\text{Al}^{1+}$  ions have the longest TOF. The effective accelerating potential that the  $\text{Al}^{1+}$  experience is obtained by calculating the accelerating potential required to achieve this TOF for  $\text{Al}^{1+}$ . This potential is then used to determine the TOF of ions with other charge states. The estimated TOF for MCIs with different charge states matches the TOF signal well.

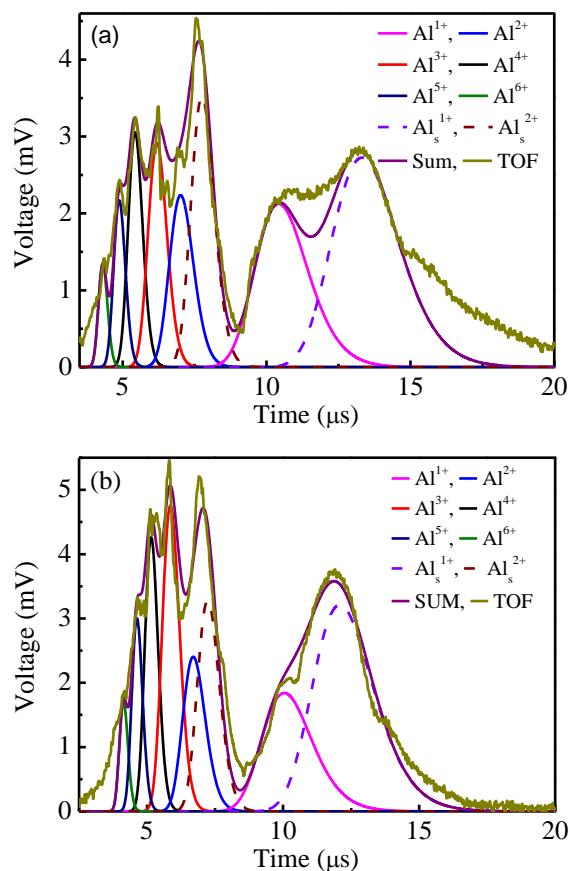
When an external electric field is present, the ions experience the double-layer potential plus the external field. The extent of which the ions experience the external field depends on the distance away from the target that they are separated from the shielding plasma. We, therefore, can extend the SCB distribution for an applied external field by adding the effective external field potential to the double-layer potential. A modified Eq. 6.2 is used to fit the extracted ion TOF signal, which also follows the SCB distribution, by replacing the term  $V_0$  with total accelerating voltage ( $V_0 + V_{eff}$ ), where  $V_{eff}$  is the effective voltage that accelerates the ions by the external field. For the extracted ions, the total accelerating energy is equal to the sum of accelerating voltage developed inside the plasma and the effective external accelerating voltage. To obtain the best fit to the TOF signal, a combination of  $kT$  and ( $V_0 + V_{eff}$ ) is used. This analysis results in temporally separating the TOF signal into different peak positions, each corresponding to a different charge state. The signal observed by the FC is the sum of these separated ion signals. By deconvolving the TOF signal, it is possible to obtain the energy distribution for each ion charge state. Integrating over the signal from a certain charge state and dividing the integral by the  $50 \Omega$  terminal resistance of the oscilloscope gives the total charge for that charge state delivered to the FC. The energy distribution for each charge state is calculated from the selected peak position. Peak position of temporally separated ions, as observed from the TOF signal, can also be used. These two approaches give almost similar energy distribution for

each charge state. The most probable energy of each charge state is calculated from the TOF signal.

The thermal interactions, the adiabatic expansion, and the Coulomb interactions are responsible for the ion acceleration during the plasma plume expansion [51]. In our geometry, plasma plume expansion occurs in a region with external electric field. Applying an electric field between the target and the grounded mesh accelerates the ions according to their charge state causing them to separate and, therefore, can be identified from the TOF signal collected by the FC. The ions are not accelerated to the full potential applied between the target and the grid due to plasma shielding prior to ion separation from the plume. If plasma shielding is not considered, an ion generated at the target with zero energy would reach the FC after a TOF of  $t = t_a + t_d = \sqrt{\frac{2m}{zeV}}d + \sqrt{\frac{m}{2zeV}}S$ , where  $t$  is the time taken by the ion to travel from target to the FC,  $t_a$  is the time that an ion is accelerated from zero velocity at target to velocity  $v$  at the extraction mesh,  $t_d$  is the time that an ion drifts at constant velocity  $v$  from the extraction mesh to the FC,  $d$  is the distance from the target to the extraction mesh,  $S$  is the distance from the extraction mesh to the FC,  $m$  is the mass of the Al atom,  $e$  is the electron charge,  $z$  is the charge state, and  $V$  is the applied accelerating voltage. The above equation for TOF does not account for the ion acceleration in the expanding plume, which is mainly due to acceleration by the double-layer potential, the adiabatic and thermal velocity, and the effect of plasma shielding limiting the ion acceleration by the external electric field. The ion accelerating time  $t_a$  is small compared to the ion drift time  $t_d$ .

Figs. 6.4(a) and (b) show the ion signal for the accelerating voltage of 5 and 6 kV, respectively, using a laser fluence of 7.6 J/cm<sup>2</sup>. Due to plasma shielding, the electric field established between the Al target and the grounded mesh does not fully penetrate the plasma plume resulting in ion energies less than the potential applied to the target. In Fig. 6.4(a), for Al<sup>1+</sup>, we detect ~0.3 nC with most probable energy  $E_{mp}$  ~2.4 keV; for Al<sup>2+</sup> ~0.12 nC with  $E_{mp}$  ~4.7 keV; for Al<sup>3+</sup> ~0.08 nC with  $E_{mp}$  ~7 keV; for Al<sup>4+</sup> ~0.08 nC with  $E_{mp}$  ~9.2 keV; for Al<sup>5+</sup> ~0.006 nC with  $E_{mp}$  ~11.5 keV; and for Al<sup>6+</sup> 0.06 nC with  $E_{mp}$  ~13.7 keV. The peak ion energies are separated by ~2.3 keV for 5 kV applied to target, while for 6 kV applied to target, the peak ion energy separation increases to ~2.6 keV. The total energy of the ion with charge-state  $z$  when

the external accelerating electric field is applied  $E_{z-Total} = E_T + E_K + zE_c + zE_{eff}$ , where  $E_{eff}$  is the effective acceleration energy experienced by the ion from the external electric field after considering plasma shielding. The deconvolution in Fig. 6.4(a) and (b) are fitted for the total accelerating voltage ( $V_0 + V_{eff}$ ) of  $\sim 2.3$  and  $\sim 2.6$  kV and  $kT = \sim 40$  and  $\sim 45$  eV, respectively. Figs. 6.4(a) and (b) also show the presence of slow  $Al^{1+}$  and  $Al^{2+}$ . In Fig 6.4(a), the TOF signal for the slow ions was fitted for  $(V_0 + V_{eff}) \sim 1100$  V for  $Al^{1+}$  and  $\sim 1900$  V for  $Al^{2+}$  with  $kT \sim 25$  eV, while in Fig. 6.4(b), slow  $Al^{1+}$  and  $Al^{2+}$  experience  $(V_0 + V_{eff})$  of  $\sim 1300$  and  $\sim 2100$  V, respectively, with  $kT \sim 30$  eV. In Figs. 6.4(a) and (b), the shoulders present at  $\sim 15$  and  $\sim 14 \mu s$  in the TOF signal indicates the possibility that more slow ions contribute to the TOF signal.



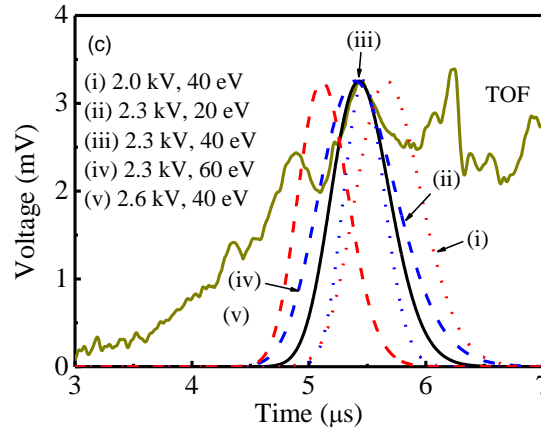


Fig. 6.4 Al MCI detected with (a) 5 kV and (b) 6 kV accelerating voltage. The laser fluence is  $7.6 \text{ J/cm}^2$ .

The deconvolution of the extracted ion is based on a shifted Coulomb-Boltzmann distribution. (c) The effect of varying the total accelerating voltage ( $V_0 + V_{eff}$ ) and equivalent plasma temperature  $kT$  on the deconvolution of the ion pulse when 5 kV accelerating voltage is applied. In (c), the  $\text{Al}^{4+}$  ion pulse obtained by deconvolution is shown for ( $V_0 + V_{eff}$ ) = 2300 V and  $kT = 40$  eV (black straight line), 2300 V and 20 eV (blue dot line), 2300 V and 60 eV (blue dash line), 2000 V and 40 eV (red dot line), and 2600 V and 40 eV (red dash line).

The same deconvolution procedure is applied when the target is biased at a positive potential. In this case, the value of  $V_{eff}$  is adjusted to account for the external electric field. In Fig. 6.4(c), the fit was performed for  $\text{Al}^{4+}$  signal using different values of ( $V_0 + V_{eff}$ ) and of  $kT$ . For a fixed  $kT$ , ( $V_0 + V_{eff}$ ) determines the energy shift in the SCB distribution. Whereas, for a fixed ( $V_0 + V_{eff}$ ),  $kT$  mainly determines the ion pulse width. Changing  $kT$  has a small effect on ( $E_t + E_k$ ) that is negligible compared to the effect of changing the accelerating potential ( $V_0 + V_{eff}$ ). The effect of ( $E_t + E_k$ ) on the ion signal is constant irrespective of ion charge state. As shown in Fig. 6.4(c), changes in the value of ( $V_0 + V_{eff}$ ) by 300 V shifts the  $\text{Al}^{4+}$  ion most probable energy by 1200 eV. This shift is easily noticeable. On the other hand, changes in  $kT$  by 20 eV mostly affects the ion pulse width. The accuracy of the fitting parameter ( $V_0 + V_{eff}$ ) increases for higher ion charge states.

For a laser fluence of  $7.6 \text{ J/cm}^2$ , increasing the accelerating voltage from 1 to 6 kV, increases the total charge detected from 20 to 720 pC. In the ion transport region, the main loss of detected ions is due to ion divergence resulting in ions falling outside of the FC area. The retrograde motion of the plasma edge exposes more ions to the accelerating field and repels the



electrons [52]. This is the main reason for the enhancement of the ion extraction with increasing electric field between the Al target and the extraction grounded mesh. The space-charge limited flow due to the retrograde motion of the plasma and the ion current introduction in the presheath affects ion extraction [53].

### 6.3.3 Effect of laser fluence

In a laser produced plasma, the plasma density, temperature, ablated mass, and the ion and electron energies are affected by the laser parameters (pulse energy, intensity, and width). The laser fluence on the Al target was varied while all other conditions kept fixed, as described in the experimental section. The voltage applied to the Al target was 5 kV. Fig. 6.5(a) shows the TOF spectra detected by the FC for a laser fluence from 1.4 to 7.4 J/cm<sup>2</sup>.

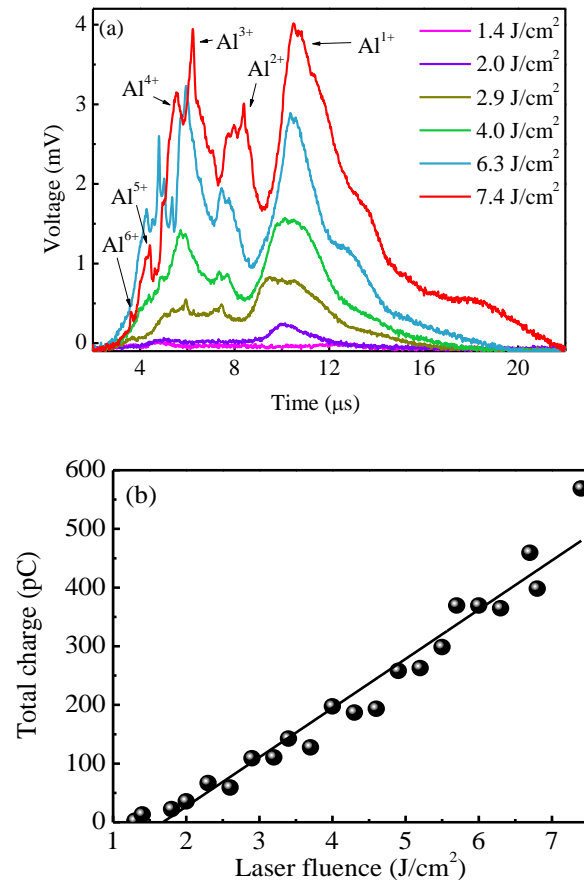


Fig. 6.5 (a) TOF spectrum of MCIs for laser fluence variation from 1.4 to 7.4 J/cm<sup>2</sup>, (b) total charge generation as a function of laser fluence. The accelerating voltage applied to the target was 5 kV.

From Fig 6.5(a), we observe that, for a laser fluence of  $1.4 \text{ J/cm}^2$ , a very small ion signal is detected. It is not until the laser fluence is  $\sim 2 \text{ J/cm}^2$  that ion peaks at 5 and 10  $\mu\text{s}$  are detected. As the laser fluence is increased, the number of ions detected is increased along with detection of higher charge state ions. Increasing the laser fluence increases the temporal spread of the  $\text{Al}^{1+}$  ions, possibly due to the increase in the generation of slow ions. For the lower fluences of 1.4 and  $2 \text{ J/cm}^2$ ,  $>80\%$  of the total ion yield is  $\text{Al}^{1+}$ , while for laser fluences above  $4 \text{ J/cm}^2$ , only  $\sim 50\%$  of the ions are  $\text{Al}^{1+}$ . The TOF signal shows a stretched low energy tail, which becomes clear for laser fluences above  $6.3 \text{ J/cm}^2$  probably due to the contribution of the slower ions to the TOF signal. The shape of the ion signal depends on the energy distribution of ions, which are generated by different mechanisms. Fig. 6.5(b) shows the total charge detected as a function of the laser fluence. In Fig. 6.5(b), a linear fit was applied to determine the threshold fluence for detecting Al ions. The point at which the fitted curve intersects with the x-axis indicates the laser fluence threshold for Al ion detection is  $1.6 \text{ J/cm}^2$ . For longer laser pulses (picosecond and nanosecond, depending of the thermal diffusivity of the target), thermal diffusion determines the ablation depth, whereas, for femtosecond laser ablation both the optical penetration depth and the mean free path of nonequilibrium carriers (electrons or phonons, depending on the material) plays the vital role [144]. For a metal such as Al, the nonequilibrium electrons carry the energy from the optical penetration depth to a deeper region under the surface. For femtosecond laser ablation of Al, low laser fluence produces relatively low hot electron density and the laser energy is mainly deposited in the shallow region defined by the optical penetration depth. With increased laser fluence, the contribution of the heat transport by hot electrons becomes significant resulting in a fast rise in the lattice temperature and the heat affected zone is defined by the hot electron penetration depth. With the increase in the femtosecond laser fluence, explosive evaporation takes place causing less localized energy deposition, which results in the increase in total ion yield [144, 149].

#### **6.3.4 Effect of focal length**

The focusing lens was moved longitudinally along the optical axis of the incident laser beam from the focal length position of 324 mm by  $\pm 7$  mm in 1 mm incremental steps. Throughout this experiment, the voltage applied to the Al target was 5 kV and the laser fluence was at  $6.9 \text{ J/cm}^2$  when the target was positioned at the focal length of the lens. The diameter of

the laser beam waist changes due to the change in the distance between the Al target surface and the focusing lens, resulting in a reduction in the laser fluence on the Al target surface when the lens position is moved away from focus.

Fig. 6.6 shows the effect of changing the focusing lens position on the total Al charge delivered to the FC as a function of the Al target distance from the focal length of the lens. The zero position corresponds to when the Al target is placed at the focal length of the lens (324 mm); positive positions are when the laser is focused in front of the surface, and negative positions are when the laser is focused behind the surface of the target.

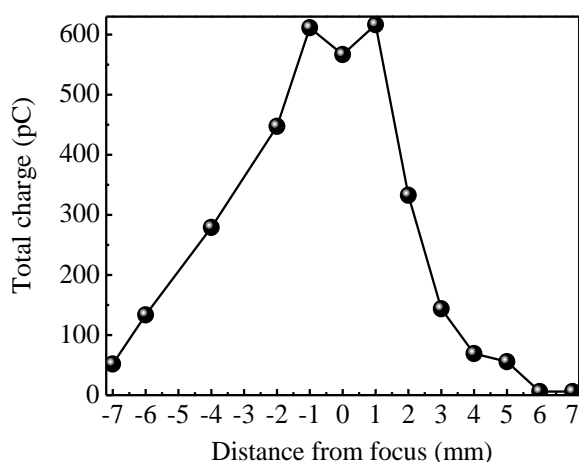


Fig. 6.6 Al total ion charge detected versus distance from optical focus of the lens on target surface.

It is evident from Fig. 6.6 that the best focus position for ion production is when the laser is focused 1 mm in front or behind the surface of the target. Moving the position of focus away from the surface of the target increases the spot diameter and reduces the laser fluence on the target. When focusing the laser at a position of  $\pm 7$  mm away from the surface of the target, the laser fluence becomes insufficient to ablate the Al target. For ablation of Al using a 120-fs laser pulse with an intensity of  $1.5 \times 10^{14}$  W/cm<sup>2</sup>, the plume expansion velocity is  $\sim 3 \times 10^4$  ms<sup>-1</sup> leading to a length of expanding plume of  $\sim 3$  nm in front of the target surface [147]. The femtosecond laser pulse does not interact with the expanding plasma as in the case of a nanosecond laser pulse. The absence of interaction of the expanding plasma with the laser pulse makes the ion yield dependence on the focal position similar when the focal spot is before or after the target surface.

The mechanism of material ablation and plasma production by femtosecond laser-matter interaction in vacuum is different from that for nanosecond laser interaction. The duration of interaction of the femtosecond laser pulse with the surface is substantially shorter than the time necessary for the thermal and hydrodynamic mechanisms that dominate during a nanosecond laser pulse [144, 150]. We have previously reported on the generation of Al MCI using a Q-switched Nd:YAG laser ( $\lambda = 1064$  nm,  $\tau \sim 7$  ns, and maximum fluence  $F = 38$  J/cm<sup>2</sup>) in the same experimental chamber presently used [54]. To remove the same amount of material by laser ablation with a femtosecond pulse requires higher laser intensity than a nanosecond pulse, approximately inversely proportional to the laser pulse duration [150]. For example, to extract a total charge of  $\sim 0.7$  nC when 5 kV is applied to the target, an intensity of  $\sim 8 \times 10^{13}$  W/cm<sup>2</sup> is required for Al ablation with 100 fs laser pulses, whereas with 7 ns laser pulses an intensity of  $\sim 5 \times 10^9$  W/cm<sup>2</sup> is sufficient [54]. Lower plasma shielding effect is observed for femtosecond laser-generated ions compared to when nanosecond pulses are used. This results in the extracted ions gaining more energy from the external electric field when the femtosecond laser is used. The plasma decays faster for the femtosecond laser due to the difference in the energy coupling mechanism and because of the absence of laser-plasma interaction for the femtosecond laser ablation [151]. Also, at the early stage of the plasma expansion, the femtosecond laser ablated plume is more directed perpendicular to the surface compared to nanosecond ablation resulting in less ion loss due to ion divergence [151]. Higher ablation efficiency is achieved for femtosecond laser ablation due to lack of interaction between the laser and the plasma compared to nanosecond laser ablation [152]. Table I summarizes results obtained for Al MCI generation by femtosecond and nanosecond laser ablation.

TABLE 6.1. Comparison of Al MCI generated by femtosecond and nanosecond laser

Characteristics	Femtosecond laser ( $\lambda = 800$ nm)	Nanosecond laser ( $\lambda = 1064$ nm) [54]
Ion detection threshold	1.6 J/cm <sup>2</sup>	22 J/cm <sup>2</sup>
Maximum ion energy gain in the double layer	~325 eV/charge for laser fluence of 7.6 J/cm <sup>2</sup>	~70 eV/charge for laser fluence of 38 J/cm <sup>2</sup>
Maximum charge state achieved	Al <sup>4+</sup> , Al <sup>5+</sup> , Al <sup>6+</sup> for laser fluence of 4.0, 6.3, and 7.6 J/cm <sup>2</sup> , respectively	Al <sup>2+</sup> , Al <sup>3+</sup> , and Al <sup>4+</sup> for laser fluence of 25, 28, and 38 J/cm <sup>2</sup> , respectively
Ion yield with laser fluence	Increases with fluence up to 7.6 J/cm <sup>2</sup> with no charge saturation observed in this region	Increases with fluence up to 27 J/cm <sup>2</sup> then saturates due to self-absorption
Plasma shielding effect	5 kV accelerating voltage produce Al ions with ~2.3 keV per charge state	5 kV accelerating voltage produces Al ions with ~1.8 keV per charge state

For a laser fluence of 7.6 J/cm<sup>2</sup>, the equivalent  $kT$  of the ejected ions, as evaluated by deconvolving the TOF signal, is 25 eV when no voltage is applied to the target. However, using a femtosecond Ti:sapphire laser ( $\lambda = 800$  nm,  $\tau = 100$  fs), which is similar to the one we used, the electron temperature calculated from the optical spectrum was ~1.4 eV for a laser fluence of 20 J/cm<sup>2</sup> [153]. The large difference in the measured plasma temperatures by the two methods is due to the difference in the plasma region probed. The ion TOF contains information on the plasma core zone, where the thermal and Coulomb interactions occur (Knudsen layer). Near the target surface, the plasma density of the inner core is comparable to solid density and the plasma temperature is expected to be much higher than that for the external zone of the expanding plasma [109]. Optical spectroscopy probes the electron temperature of the external zone of the plasma, where lower plasma densities and temperatures are expected. The outer zone of the plasma is formed by the colder neutral and ions of lower charge. Also, the decrease in the temperature in the outer zone is due to the conversion of the thermal energy into kinetic energy with the plasma attaining its maximum expansion velocity [26].

## 6.4 SUMMARY

A Ti:sapphire femtosecond laser (wavelength  $\lambda = 800$  nm, laser pulse width  $\tau \sim 100$  fs, laser fluence  $F \leq 7.6$  J/cm<sup>2</sup>) was used to generate Al multicharged ions by laser ablation. Al

charge state up to 6+ were detected in the faraday cup. The energy distribution of the extracted ions is fitted to a SCB distribution. The equivalent ion plasma temperature is estimated from the SCB distribution. When an external potential of 5 kV applied to the target to accelerate the ions setting an electric field in the plasma expansion region, the estimated ion plasma temperature increases from 25 to 40 eV. The ion energy depends on the sum of  $E_T + E_K + zE_c + zE_{eff}$ , where  $z$  is the charge state, indicating that ions are subjected to a Coulomb acceleration proportional to their charge state by the electric field generated in the plasma-vacuum interface of the expanding plume. For higher charge state ions, the effect of thermal energy is negligible compared to the Coulomb energy and effective external energy to accelerate the ions. For an accelerating voltage of 5 kV, optimal conditions for Al MCI production occurs when the Al target surface is positioned  $\pm 1$  mm about the focal length of the lens. The laser fluence threshold for Al ion detection with the femtosecond laser was determined to be  $1.6 \text{ J/cm}^2$ . Comparison of Al ion generation by the  $\sim 100$  fs laser pulses to that previously reported with  $\sim 7$  ns laser pulses shows that the femtosecond laser has a significantly lower threshold for ion generation, resulting in a higher maximum charge state production, and higher ion acceleration per charge.

## CHAPTER 7

### GENERATION OF B<sup>5+</sup> IONS

#### 7.1 INTRODUCTION

There is an interest in a lab-scale source of B ions. In addition to its wide application for introducing p-type acceptor impurity in silicon, B ion implantation is used in many other device applications [154-161]. All these applications were conducted with B<sup>1+</sup> ions. The use of MCIs provides control on both ion potential and kinetic energy. Since each ion is accelerated according to its charge state, MCIs require less acceleration potential and smaller bending magnets allowing the development of a compact and cost-effective implanter. Also, the use of ions with different charge states for implantation makes it possible to implant with different ion kinetic energies in one step. This feature can be used to control the implanted ion depth profile producing a uniform concentration over a certain depth or a tailored gradient when needed.

Sources of boron MCIs were previously developed and used for various applications. Up to B<sup>3+</sup> was obtained from an electron cyclotron resonance ion source (ECRIS) [162]. This ion source was used for structural modification of fullerene thin films by irradiation with B<sup>1+</sup> and B<sup>3+</sup> ions at a similar dose [162]. The optical bandgap of the fullerene films was reduced from 1.7 to 0.7 eV for films irradiated by B<sup>1+</sup> and to 1.06 eV for films irradiated by B<sup>3+</sup> ions [162]. Other studies of B<sup>3+</sup> ion irradiation of fullerene showed significant reduction of surface order and formation of new bonds [163, 164]. Implantation of 45 keV B<sup>3+</sup> ions in glassy carbon increased its hardness by more than 30% [165]. An ECRIS was used to generate up to B<sup>3+</sup> using boron fluoride generated by boron interaction with SF<sub>6</sub> plasma [166]. Up to B<sup>3+</sup> was generated by an indirectly-heated cathode arc discharge ion source using BF<sub>3</sub> gas [167].

We report on boron MCI generation by a Q-switched Nd:YAG laser ( $\lambda = 1064$  nm,  $\tau = 7$  ns, and maximum  $E = 175$  mJ) ablation. The charge state and the energy distribution of the ions are determined by their TOF and a three-grid retarding field ion energy analyzer. With the increase in laser fluence, higher order charge states are observed along with the increase in the number of ions generated. Fully-stripped B ions are observed. The electrostatic ion bending stage allows for separating the B ions for ion implantation.

## 7.2 EXPERIMENTAL

The laser ion source is composed of a Q-switched Nd:YAG laser with associated laser beam delivery optics, target ablation chamber, ion drift tube, three-grid retarding field ion energy-to-charge analyzer, two Faraday cups, and an ion deflection stage. The 99.9% pure B target is 2-inch diameter and 0.25-inch-thick (Kurt J. Lesker, part number EJTBXXX302A4). A schematic of the experimental setup used is shown in Fig. 7.1. The laser beam irradiates the target through a hole in the plasma expansion chamber (EC) made out of aluminum, which allows the plume to expand in a region with no applied external electric field (Region I). In Region I, the ions are accelerated by the double-layer potential developed at the plasma-vacuum interface. The EC has dimensions of 30 cm in length, 5 cm in width, and 5 cm in height. The beam strikes the B target surface at an angle  $\theta = 45^\circ$  with a laser spot area at focus of  $1.3 \times 10^{-3}$  cm<sup>2</sup>, as measured by the knife-edge method at target-equivalent plane with the edge scanned at  $45^\circ$  to the laser beam. The knife-edge was used to scan the laser beam in both horizontal and vertical directions. The front end of the EC has a 30 mm hole covered with a 70% opening nickel mesh. An accelerating region (Region II) is formed by placing a grounded mesh in front of the EC end grid, resulting in an electric field from the EC grid to the grounded grid that accelerates the ions towards the Faraday cup (FC-1). The suppressor electrode (SE) is biased with a negative voltage to suppress the secondary electron emission from the Faraday cup due to positive ion bombardment. Throughout the experiment, the Faraday cup voltage was maintained at -70 V, and the suppressor electrode voltage was at -140 V. The distance from the B target to the FC-1 is 150 cm. The accelerating gap is 4 cm. Four buffer capacitors, each 1 nF, are placed between the EC and the ground to minimize fluctuations in the accelerating voltage. A high voltage power supply (Glassman High Voltage, Inc Model PS/KL010R300-22) is used to bias the target. A fast-high voltage probe (Tektronix P6015A) is used to observe the voltage fluctuations of the biased target during plasma plume expansion. Upon exiting the grounded mesh at the end of Region II, the ions enter a field-free drift region (Region III) till they reach the three-grid retarding field analyzer. The pressure in the vacuum chamber is maintained in the low  $10^{-6}$  Torr using a 250 l/s turbomolecular pump.



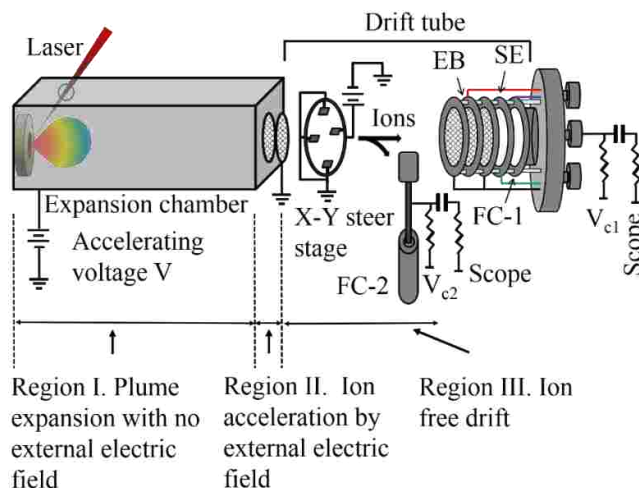


Fig. 7.1 An illustration of the laser ion source showing the laser irradiating the B target, and the electrostatic TOF energy analyzer. EC expansion chamber, EB electrostatic barrier, SE suppressor electrode, FC-1 Faraday cup-1, and FC-2 is Faraday cup-2. In Region I, the plasma plume expands in a field-free region and the ions separate from the plume and are accelerated by the double-layer potential at the plasma-vacuum interface. In Region II, the ions can be accelerated by an external electric field between the end of the EC and the grounded mesh parallel to it. Region III is a field-free ion drift region.

In a set of experiments conducted to separate the B ions from the neutrals, as discussed in Section 7.3.5, the vacuum chamber is modified. In this configuration, a movable Faraday cup (FC-2) of dimension  $1 \times 1$  cm is placed parallel to the target with a linear motion feed-through to move it in a direction perpendicular to the ion beam path. Deflection plates are placed to deflect the ions away from the path of the neutrals. The distances from the B target to the center of the deflection plates to FC-1 and to FC-2 are 27, 76, and 42 cm, respectively. The EC and target were grounded, and the length of the EC was reduced to 10 cm. Also, the circular opening at the front end of the EC was replaced by a rectangular opening of  $1.5 \text{ cm} \times 1 \text{ cm}$ . Deposition of the neutral B on the FC-2 is avoided by placing it away from the neutral path and deflecting the ions to it. The deflection plates have a length of 2 cm and width of 1 cm. This configuration separates the ions from the neutrals so that the ions can be used for ion implantation without neutral deposition.

The density of the laser-ablated plasma decreases during its free expansion in the EC. In the drift region, the ion pulse temporal width is increased, and ion recombination is reduced due

to the reduced plasma density. The ion signal is acquired by a fast-digital oscilloscope triggered by a photodiode detecting part of the laser pulse. This arrangement provides a TOF ion signal that can be used to determine the ion energies, mass-to-charge ratios, and abundance of the different ion charges generated. The adiabatic expansion, thermal interactions, and the Coulomb acceleration due to the double-layer potential formed at the plasma-vacuum interface are responsible for the ion acceleration in the EC [23]. After leaving the EC, the ions experience the external electric field applied between the EC and a grounded grid placed in front of it and are accelerated according to their charge state.

Pulse-to-pulse fluctuations were compensated for by averaging the ion signal obtained by 50 consecutive laser pulses hitting the same target spot. Fig. 7.2 shows the TOF signal for pulses from the first to the 1800<sup>th</sup>, when the distance between the target and FC-1 is 76 cm. For a laser pulse energy of 135 J/cm<sup>2</sup>, the total charge delivered to FC-1 (integrated signal) for the 1<sup>st</sup> to the 50<sup>th</sup> laser pulse varies by up to ~10%, while the ion signal maintains nearly the same most probable velocity. Significant reduction in the amplitude of the ion signal occurs after hundreds of laser pulses interact with the same spot. For the 600<sup>th</sup>, 1200<sup>th</sup>, and 1800<sup>th</sup> laser pulse, the total charge delivered to the FC-1 decreased to 0.64, 0.52, and 0.35 of the value obtained for the 1<sup>st</sup> laser pulse. The most probable velocity of the ion signal for the 1<sup>st</sup> laser pulse of  $\sim 5.5 \times 10^4 \text{ ms}^{-1}$  also decreased to  $\sim 4.4 \times 10^4$ ,  $\sim 3.3 \times 10^4$ , and  $\sim 2.9 \times 10^4 \text{ ms}^{-1}$  for the 600<sup>th</sup>, 1200<sup>th</sup>, and 1800<sup>th</sup> laser pulses. A different target spot, obtained by moving the B target by the XY manipulator, was used for each datum acquired, and each target spot was located at 2 mm from the previous one so that no two spots overlap.

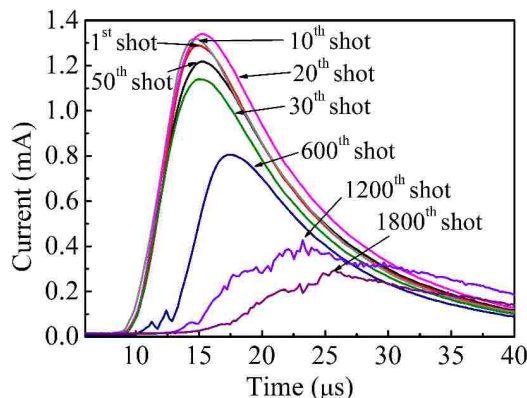


Fig. 7.2 TOF signal for 1800 consecutive laser pulses hitting on the same target spot for a laser fluence of  $135 \text{ J/cm}^2$ .

## 7.3 RESULTS AND DISCUSSIONS

### 7.3.1 Ions detected without external acceleration

Fig. 7.3(a) shows the TOF ion signal for laser fluence of 77, 96, 115, and  $135 \text{ J/cm}^2$ . The plume expansion is mainly perpendicular to the sample surface. The ions reach the FC-1 as a bunch containing different ionization states. Higher charge state ions reach the FC earlier than those with a lower charge since the ions with the higher charge gain more kinetic energy from the double-layer potential. Using retarding field ion energy analysis and assuming that the ions are thermalized and, therefore, their energy can be described by an equivalent ion plasma temperature, it is possible to deconvolute the TOF signal to obtain the energy distribution for each ion charge state [98, 168]. Integrating over the signal from and dividing the integral by the  $50 \text{ } \Omega$  terminal resistance of the oscilloscope gives the total charge delivered to the FC-1. From analysis of the shape of the ion signal, we show that, with the increase in the laser fluence, the peak position of the TOF signal shifted to shorter delays indicating an increase in the ion energy. Increasing the laser fluence from 77 to  $135 \text{ J/cm}^2$  increases the peak ion drift velocity from  $\sim 4.5 \times 10^4$  to  $\sim 5.5 \times 10^4 \text{ ms}^{-1}$ , and the total charge detected from 9 to 20 nC. For a laser fluence of  $135 \text{ J/cm}^2$ , the ion bunch contains 7.6, 4.6, 3.6, 1.8, and 2.4 nC of  $\text{B}^{1+}$  to  $\text{B}^{5+}$  ions, respectively. These values are estimated from the ratio of ions accelerated by an external electric field causing ion separation according to their charge, as discussed in Section 7.3.2. The ion dose per pulse is  $3.76 \times 10^9 \text{ ions/cm}^2$ . For a moderate dose of  $10^{14} \text{ ions/cm}^2$  [156], it would take  $\sim 45$  minutes to implant that dose. The dose can be further increased by implanting before the ions

pass the three meshes of the retarding field ion energy analyzer, which combined allow only 34% of the ions to pass to the FC-1. The energy spread  $\frac{\Delta E}{E}$  depends on the laser fluence, where  $\Delta E$  is the full-width at half-maximum of the energy distribution and  $E$  is the most probable ion energy. Increasing the laser fluence from 77 to 135 J/cm<sup>2</sup> increases  $\frac{\Delta E}{E}$  from 0.68 to 1.16. To characterize the ions from the laser plasma with the target and the EC grounded, the voltage bias on the central mesh of the electrostatic barrier (EB) of the three-grid energy analyzer was incrementally increased from 0 V to a voltage that resulted in complete suppression of the ions detected. Fig. 7.3(b) shows the TOF signal for 0 to 150 V applied to the EB. The laser fluence used to ablate the B target was 135 J/cm<sup>2</sup>. The applied barrier voltage stops the singly-charged ions with kinetic energy lower than the barrier voltage. Whereas, higher charge state ions lose kinetic energy according to their charge state. The retarding field affects each ion charge according to its charge state. The temporal separation of the different ion charges results in a reduction in the amplitude of the ion pulse throughout its temporal width. The inset in Fig. 7.3(b) shows the total charge reduction with the increase of the barrier voltage. From Fig. 7.3, we observe that ~50% of the ions generated with a laser fluence of 135 J/cm<sup>2</sup> are retarded by a potential of 25 V. Almost all the ions are retarded by a potential of ~150 V. In another experiment (not shown in Fig. 7.3) with the target to FC-1 separation of 76 cm and EC front opening of 1.5 x 1 cm, showed that ~20% of the ions has energies less than 5 eV. The TOF signal for a laser fluence of 135 J/cm<sup>2</sup> shows near flat-top profile due to the ions with different charge separation in time while drifting and, possibly, due to the space-charge effect.

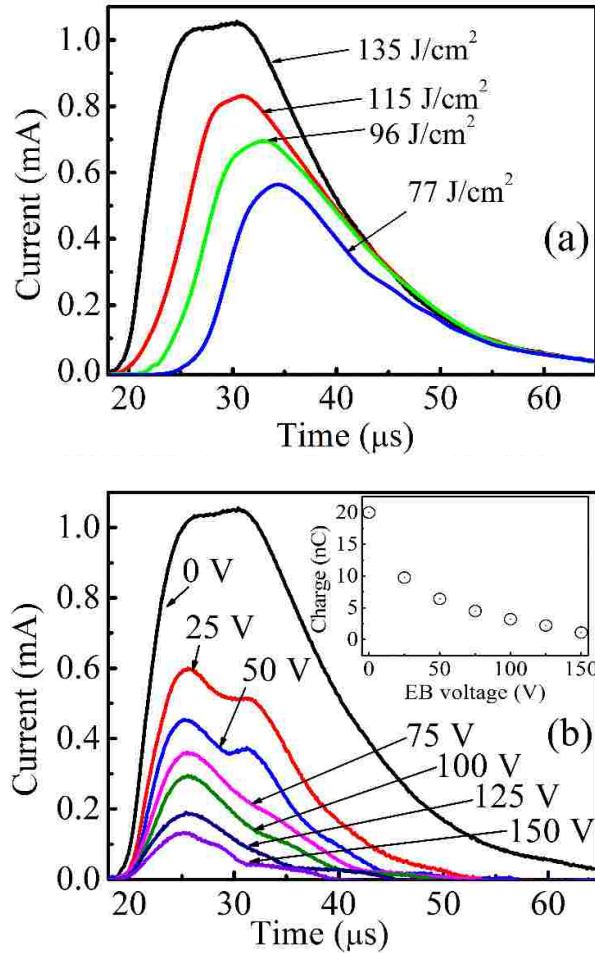


Fig. 7.3 (a) Ion signal detected by the FC-1 for increasing laser fluence. (b) Ion signal for a laser fluence of 135  $\text{J}/\text{cm}^2$  with different applied barrier voltages. Inset shows the total charge detected with the increase of barrier voltage.

### 7.3.2 Ions detected with external acceleration

When a voltage is applied to the EC, an electric field is established between the grid at the exit of the EC and the grounded grid. In this case, the ions are accelerated by the external electric field in addition to the double-layer potential at the plasma-vacuum interface. In our geometry, plasma plume expansion occurs in the EC, a region without an external electric field. Applying an electric field between the EC and the grounded mesh accelerates the ions according to their charge state causing them to separate in time and, therefore, the different ion charges can be identified from their TOF signal collected by the FC-1. The total energy of the ion with charge-state  $z$  when the external electric field is applied is  $E_{z-Total} = E_T + E_K + zE_c + zE_{eff}$ ,

where  $E_T$  is the thermal energy,  $E_K$  is the energy due to adiabatic expansion,  $E_C$  is the Coulomb energy associated with the equivalent accelerating voltage due to the double-layer potential, and  $E_{eff}$  is the effective acceleration energy experienced by the ion from the external electric field after considering the voltage drop of the power supply used to bias the target and EC. The procedure to identify the ions are as follows: first, using retarding field analysis, we determine the ion energy obtained from the plasma expansion and the double-layer potential. Then, the effective accelerating potential is measured from the voltage curve of the biased EC. We calculate the time required for each ion charge to travel from the target to the FC. The calculated time matches well with the experimental ion peak positions in the TOF signal for different charge states.

Fig. 7.4 shows the ion signal for the accelerating voltage of 5, 6, and 7 kV, respectively, for a laser fluence of  $135 \text{ J/cm}^2$ . Increasing the bias voltage increases their energy and, therefore, reduces the TOF of the ions to reach the FC-1. Boron has two stable isotopes,  $^{11}\text{B}$  and  $^{10}\text{B}$  with an abundance of  $\sim 80$  and  $\sim 20\%$ , respectively. The ion TOF depends on their energy and mass. Ions are accelerated, by the double-layer potential and the external electric field, to an energy proportional to their charge. Therefore, higher charge ions arrive at the FC-1 earlier. Moreover, for ions with a certain charge, a  $^{10}\text{B}$  ion arrives earlier than a  $^{11}\text{B}$  ion with an equivalent energy. Because each ion state has a distribution of ion energy, which mainly develops by collisional processes in the plasma, the signal from the  $^{10}\text{B}$  ions can overlap with the  $^{11}\text{B}$  ions for certain ion charges. In the TOF signals in Fig. 7.4, two distinct  $\text{B}^{5+}$  peaks can be observed, one corresponding to  $^{11}\text{B}^{5+}$  while the other to  $^{10}\text{B}^{5+}$ .  $\text{B}^{5+}$  has the highest  $\sqrt{\frac{\text{Energy}}{\text{Mass}}}$  of the different ion charges, which allows for identifying each isotope by its TOF. The TOF of the peak identified as  $^{10}\text{B}^{5+}$  is slightly faster than expected from a simple calculation, however, we note that previous work on boron ablation has shown differences in the angular distribution of the ablated boron ion isotopes, which can affect the TOF [169]. Increasing the bias voltage on the EC increases not only the ion acceleration energy but also the number of ions extracted. Increasing the EC voltage from 5 to 7 kV increases the  $\text{B}^{1+}$  detected from 0.60 to 0.83 nC,  $\text{B}^{2+}$  from 0.35 to 0.40 nC,  $\text{B}^{3+}$  from 0.26 to 0.37 nC,  $\text{B}^{4+}$  from 0.14 to 0.23 nC, and  $\text{B}^{5+}$  from 0.10 to 0.16 nC. When the ions are accelerated by the electric field established between the target and the grid by biasing the target at 7 kV, the ion dose per pulse is  $3.9 \times 10^8 \text{ ions/cm}^2$ . For a moderate dose of  $1 \times 10^{14} \text{ ions/cm}^2$

[156], it would take  $\sim 7$  hours to implant that dose when the laser is operated at 10 Hz. In the vacuum chamber, the main ion transport loss is ion divergence rather than recombination. Increasing the electric field between the EC and the grounded mesh reduces ion diversion causing more ions to be incident on the FC-1 [54].

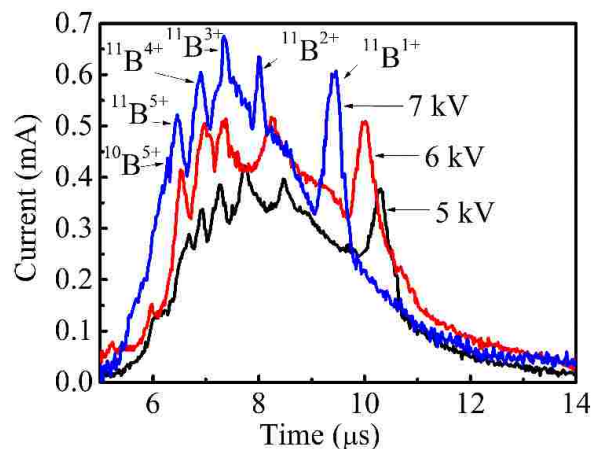


Fig. 7.4 External acceleration voltage accelerates and separate the ions in their TOF. The accelerating voltage applied is 5 – 7 kV, and the laser fluence is  $135 \text{ J/cm}^2$ .

### 7.3.3 Effect of laser fluence

In a laser plasma, the plasma density, temperature, ablated mass, and the ion and electron energies are affected by the laser parameters (pulse energy, fluence, and width) [22]. In ns laser plasma, the leading part of the laser pulse interacts with the target surface resulting in the formation of a plasma plume containing energetic species. The remaining part of the laser pulse reheats the plasma. After the plume generation, the target surface is partially or totally shielded from the remaining part of the laser pulse because of the laser absorption in the plasma by inverse bremsstrahlung. This laser-plasma interaction eventually reheats the plasma, and more ions with higher charge are produced. The laser fluence on the B target was varied while all other conditions were fixed, as described in the experimental section. The EC was biased at 5 kV to accelerate the ions. Fig. 7.5 shows the TOF ion signal detected by the FC-1 for a laser fluence from  $77 - 135 \text{ J/cm}^2$ . We observe that, for a laser fluence of  $77 \text{ J/cm}^2$ , distinct peaks for charge states up to  $\text{B}^{3+}$  are detected. It is not until the laser fluence of  $115 \text{ J/cm}^2$  that the fully-stripped

$B^{5+}$  ions are detected. Increasing the laser fluence from 77 to 135 J/cm<sup>2</sup>, increases the total ions detected from 0.7 to 1.5 nC. As the laser fluence is increased, the number of ions detected is increased along with the detection of higher charge state ions. With the increase in the laser fluence, higher charge state ions are generated due to the increase in the laser energy deposited in the plasma plume causing more plasma heating. The higher laser fluence also increases the ablated material per pulse providing denser plume that can absorb more of the laser pulse generating more ions.

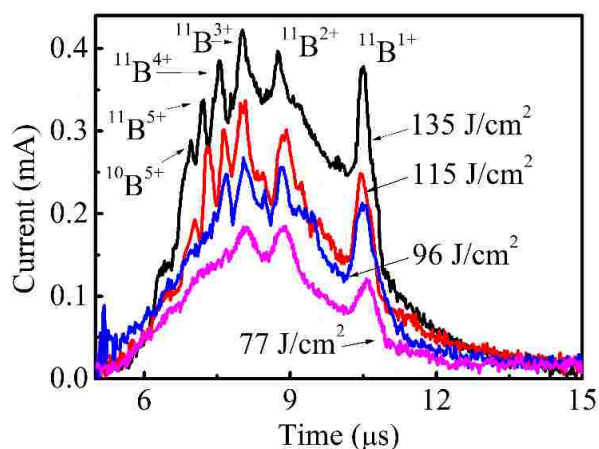


Fig. 7.5 Higher charge states are generated with the increase of the laser fluence from 77 to 135 J/cm<sup>2</sup>.

The accelerating voltage applied to the EC is 5 kV.

### 7.3.4 Ion energy

The ion kinetic energy was measured by the retarding field ion energy analyzer combined with the TOF ion signal. The EB potential  $V_{EB}$  retards the ions, according to their charge state  $z$ , and suppresses all ions having kinetic energies lower than  $zeV_{EB}$ , whereas ions with higher kinetic energies lose energy during their drift to the central grid of the three-grid analyzer. This energy loss is then gained after the ions reach the last grid of the analyzer. During retardation the voltage applied to the EB was incrementally increased from 0 V to a voltage, which resulted in complete suppression of the ions detected. Ion with Fig. 7.6 shows the TOF signal for 0 – 5 kV applied to the EB. The laser fluence was 135 J/cm<sup>2</sup> and the voltage applied to the EC was 5 kV. The ions always affected by the EB voltage resulting in an ion pulse amplitude reduction



throughout the ion pulse due to the temporal separation of the different ion charges. From Fig. 7.6, we observe that, for each charge state, ions with a lower kinetic energy are detected. Although 5 kV accelerating voltage is applied to the EC, most of the ions (~ 83%) have an energy of 4.5 to 5.0 kV/charge. The lowered energy ions could be due to the voltage drop in the power supply during plasma expansion in the EC.

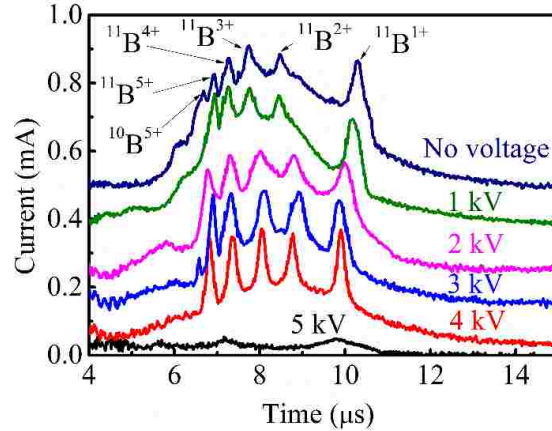


Fig. 7.6 Time-of-flight ion signals for different barrier voltages applied to the central grid of the retarding field analyzer.

### 7.3.5 Ion deflection out of the neutral beam

To utilize the B ions for ion implantation, the experimental chamber is modified as discussed in Section II to allow deflection of the ions out of the neutral beam path. The Faraday cup FC-2 is used to detect the deflected ions. The deflecting plates deflect the ions out of the neutral beam path, which is defined by the opening of the EC and FC-1. Fig. 7.7 shows the TOF signals for ions detected by both FC-1 and FC-2 for a laser fluence of  $135 \text{ J/cm}^2$  when no potential is applied to the target and the EC. The total ions detected by the FC-1 is ~17 nC, consisting of B ions up to  $\text{B}^{5+}$ , when no deflecting voltage is applied. The deflection of ions due to the electric field of the deflection plates can be calculated from  $S = \frac{V_d L}{2dV_{acc}} \left( D + \frac{L}{2} \right)$ , where  $S$  is the deflection of an ion from the center of the two plates at a distance  $D$  from the end of the deflection plates,  $V_d$  is the deflecting voltage,  $L$  is the deflection plate length,  $d$  is the separation between the plates, and  $V_{acc}$  is the ion accelerating voltage. In our experiment,  $D = 6.5 \text{ cm}$ ,  $V_d =$

150 V,  $L = 2$  cm,  $d = 2$  cm, and  $V_{acc} = 150$  V. Ions with different charges are deflected together as long as they experience the same accelerating voltage, as their kinetic energy is proportional to their charge. When 150 V is applied across a set of deflection plates, the ions with similar energy-to-charge ratio are deflected by the same angle. At the location of FC-2, the ions are deflected by 3.75 cm away from the center of the neutral beam. This distance is enough to assure that only ions reach FC-2. The total charge detected by the FC-2 is  $\sim 9.50$  nC, while  $\sim 4.50$  nC is detected by FC-1. Since the dimension of the gap between the deflection plates are smaller than the ion beam path dimension defined by the rectangular opening of the EC, some of the ions continue undeflected in the drift tube to FC-1.

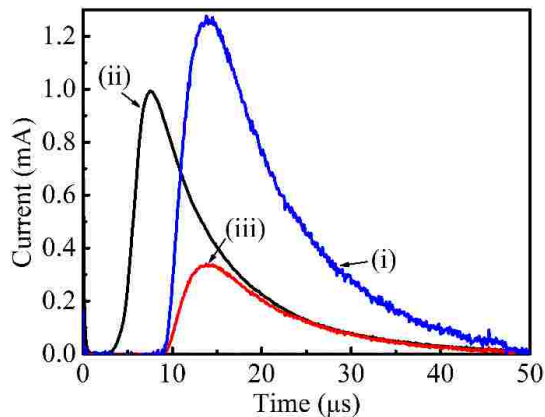


Fig. 7.7 Ion signal detected by the two Faraday cups with and without ion deflection. The TOF signal shown are for (i) FC-1 without ion deflection, (ii) FC-2 with ion deflection, and (iii) FC-1 with ion deflection.

## 7.4 SUMMARY

Boron multicharged ion generation from a laser-ablated target was studied by ion TOF. Fully stripped boron ions were generated using Nd:YAG laser ( $\lambda = 1064$  nm,  $\tau = 7.4$  ns) operated at a fluence of  $\geq 115$  Jcm<sup>-2</sup>. The ions extracted from the laser plasma are characterized in terms of laser fluence and accelerating voltage applied between the EC and grounded grid. The plasma plume expands in a field free region resulting that allows the separation of the ions from the decaying plasma. Increasing the laser fluence increases the ions generation along with producing

higher charge states. Two distinct ion peaks for  $B^{5+}$  are observed corresponding to  $^{11}B$  and  $^{10}B$ . The EC bias voltage fluctuates during the plasma expansion, which affects the ion kinetic energy. For EC biasing voltage of 5 kV, the ions are accelerated with an energy  $>4.5$  keV/charge. The ion deflection stage allows the ion source to be used for implantation without neutrals deposition.

## CHAPTER 8

### SHALLOW IMPLANTATION ON SILICON CARBIDE

#### 8.1. INTRODUCTION

Under the VMEC seed funding, we modified a laser multicharged ion (MCI) source to implant boron and barium ions in SiC and characterized the ion implanter for boron MCI generation. The experimental chamber used is composed of (i) plasma generation chamber, (ii) drift tube, (iii) X-Y steering stage to steer the ion beam towards sample location, (iv) linearly movable sample holder across the drift tube, and (v) two Faraday cups (FC) to detect the ions. FC 1 (area  $20 \text{ cm}^2$ ) is placed at the end of the drift tube, and a small linearly movable FC 2 (area  $1 \text{ cm}^2$ ), placed across the drift tube, is used to detect the deflected ions. There is a slit (width  $\sim 1 \text{ cm}$ ) at the end of the plasma generation chamber to limit the ion beam size in the drift tube region and avoid wall sputtering. A Q-switched Nd:YAG ( $\lambda = 1064 \text{ nm}$ ,  $\tau = 7 \text{ ns}$ ) is used to ablate the boron target. Fig. 8.1 shows the image and schematic of the experimental chamber. The distance from the B target to FC 1 and FC 2 is  $150 \text{ cm}$  and  $40 \text{ cm}$ , respectively.

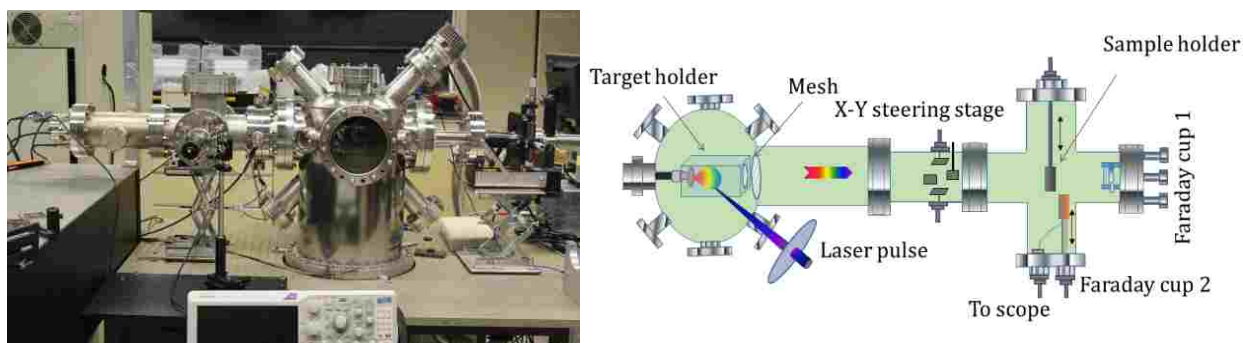


Fig. 8.1 Image and schematic of the laser ion implanter showing the plasma generation chamber, ion deflecting stage, sample holder, and Faraday cup to detect the MCI.

## 8.2 PROCEDURE

The procedure followed to fabricate and characterize the SiC-MOSCAP is depicted in the block diagram of Fig. 8.2. Boron and barium multicharged ions were generated from the laser ion source. The substrates were 4H-SiC (5 x 5 x 0.33 mm, with two sides polished, Item # SC4HZ0505033S2, MTI Corporation). Shallow implantation was conducted using the laser multicharged ion source. The SiO<sub>2</sub> and metal layers were grown by sputtering.

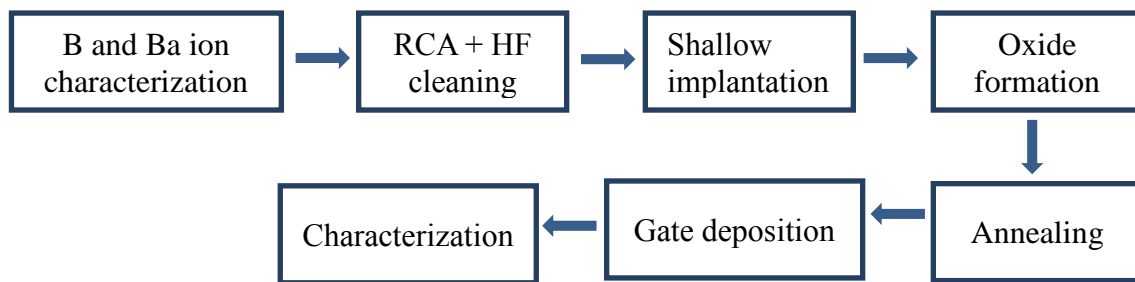


Fig. 8.2 Block diagram shows the steps followed to fabricate MOSCAP.

## 8.3 SRIM SIMULATION OF BORON ION IMPLANTATION ON SILICON CARBIDE

The Stopping and Range of Ions in Matter (SRIM) simulation is used to check the profile of the implanted B atom. Fig. 8.3 (a)-(e) shows the SRIM simulation result of the B atoms implantation in SiC with energies of 150 to 750 eV, with an increasing step of 150 eV. The number of atoms in each group are 2000. Fig. 8.3(f) shows the profile of the implanted B ions with five energy groups of 150, 300, 450, 600, and 750 eV with each group containing ~2000 atoms. The model shows that 80% of the implanted atoms travelled up to ~60 Å inside the SiC.

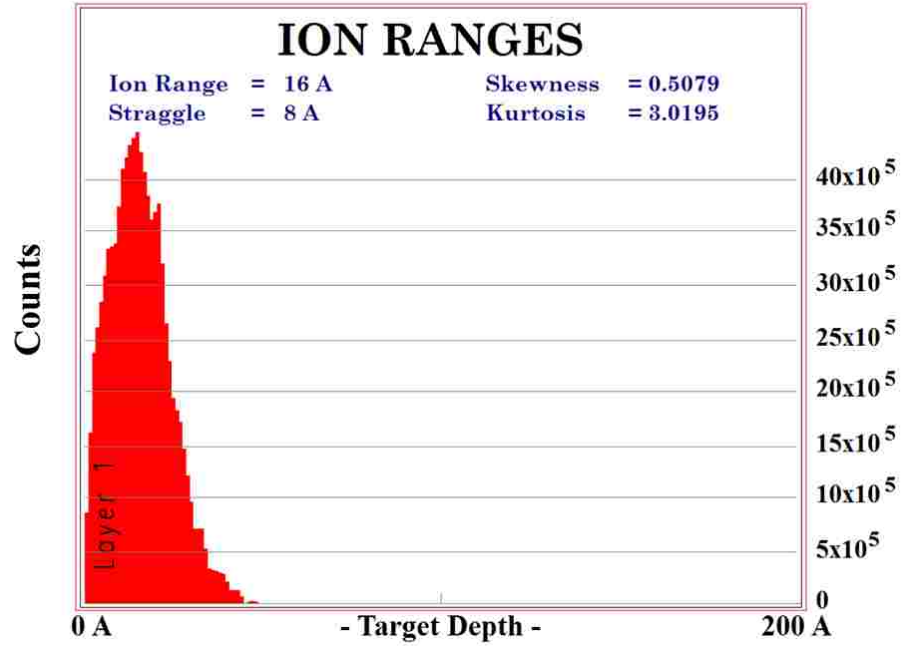


Fig. 8.3(a) SRIM simulation of 2000 B ions implanted in the SiC wafer with energy 150 eV

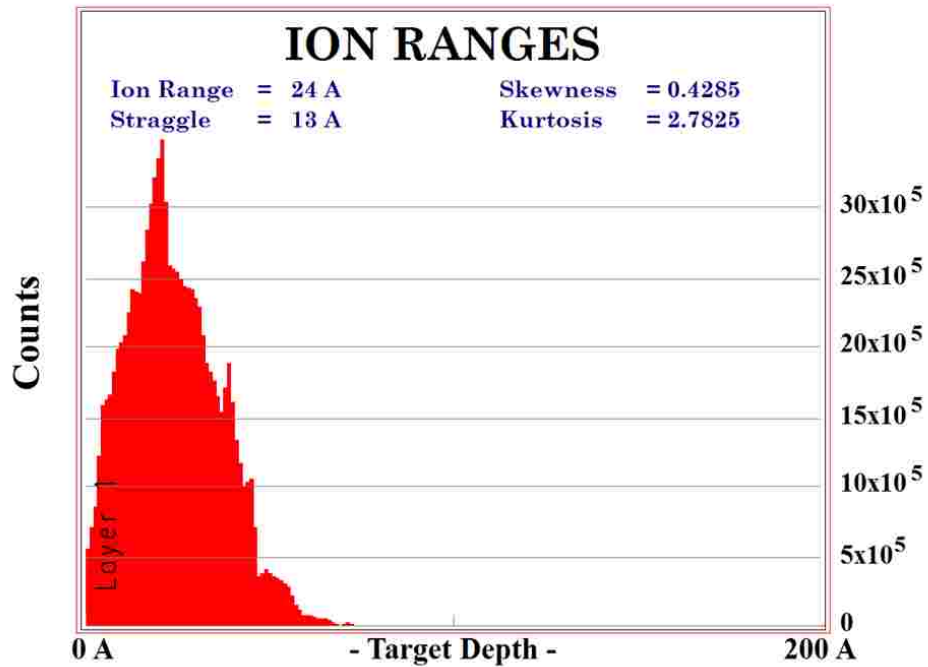


Fig. 8.3(b) SRIM simulation of 2000 B ions implanted in the SiC wafer with energy 300 eV

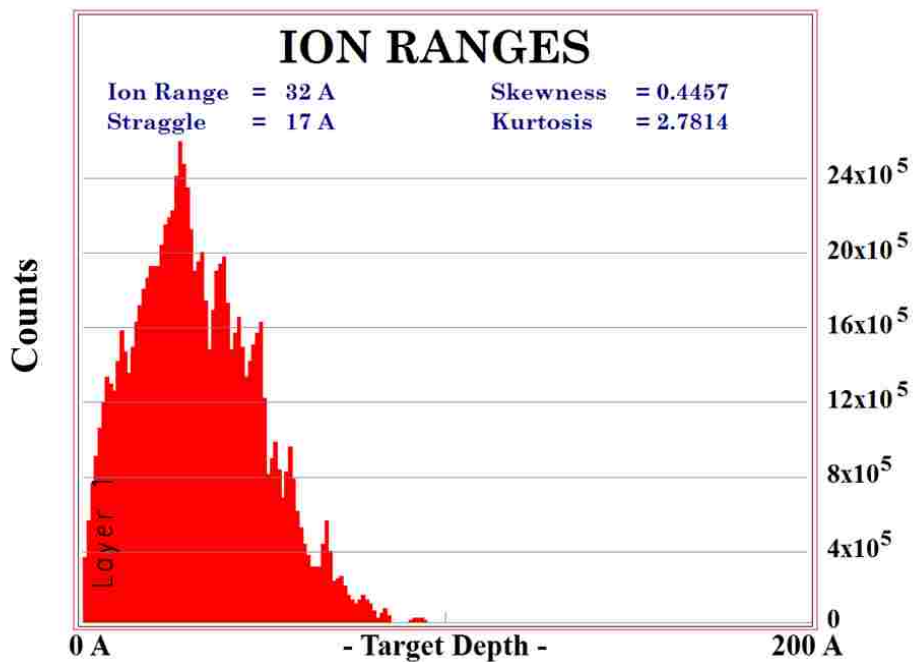


Fig. 8.3(c) SRIM simulation of 2000 B ions implanted in the SiC wafer with energy 450 eV

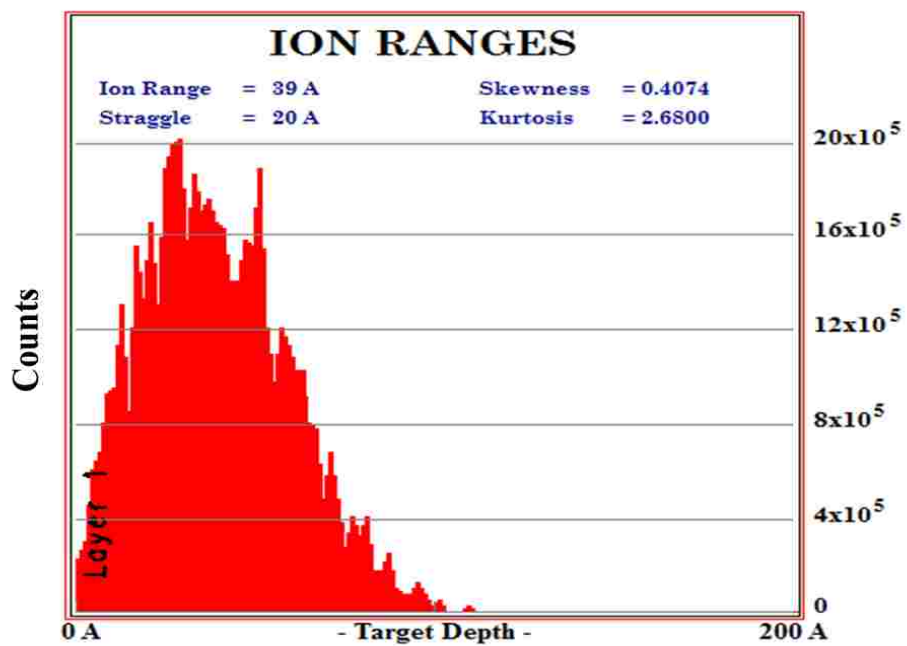


Fig. 8.3(d) SRIM simulation of 2000 B ions implanted in the SiC wafer with energy 600 eV

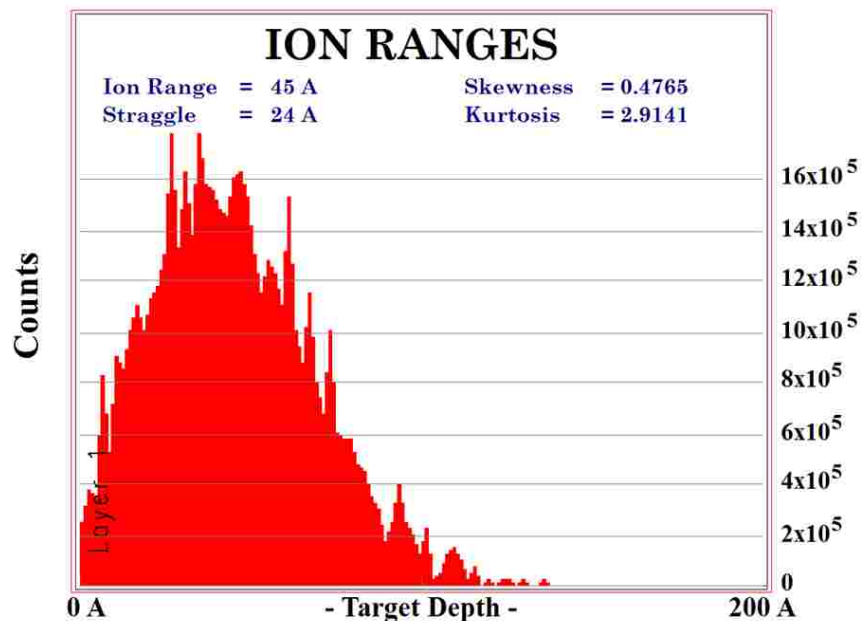


Fig. 8.3(e) SRIM simulation of 2000 B ions implanted in the SiC wafer with energy 750 eV

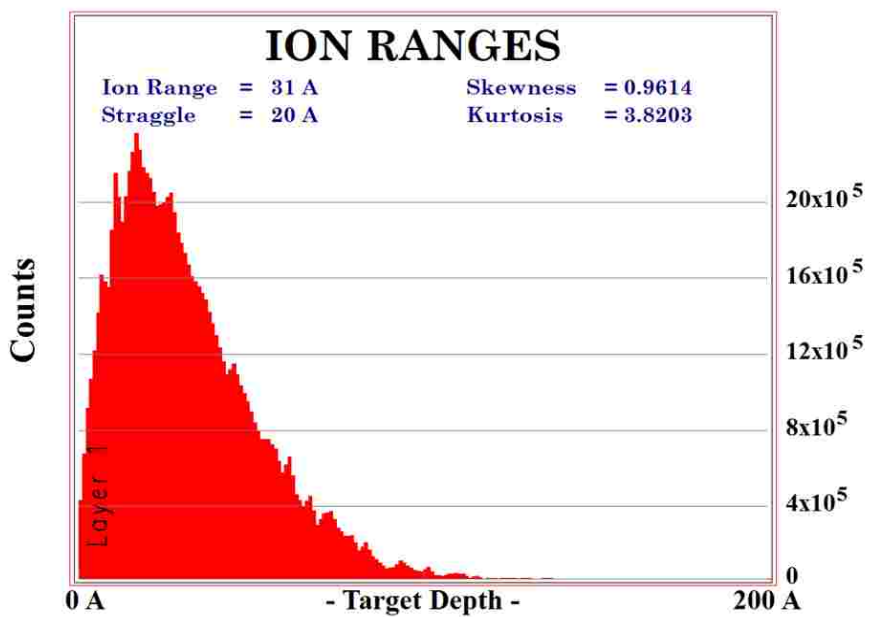


Fig. 8.3(f) SRIM simulation of 10,000 B ions with five energy groups of (a)–(e), with 2000 B ions in each group



## 8.4 IMPLANTATION OF B ION ON SILICON

Boron MCIs with energy  $\sim 150$  eV/charge were implanted in intrinsic silicon (University wafer, ID 2648, Orientation:  $\langle 100 \rangle$ , Resistivity:  $>10,000$   $\Omega\text{-cm}$ ). The MCIs were deflected by the X-Y steering stage towards FC 2 (area  $1\text{ cm}^2$ ). X-Y steering stage was activated, and the ion beam was  $\sim 2$  cm away from the main axis in order to avoid deposition of neutrals on the Si substrate. Total charge measured is  $\sim 7$  nC/pulse. The ion bunch contained 2.66, 1.61, 1.26, 0.63, and 0.84 nC of  $B^{1+}$  to  $B^{5+}$ , respectively. The implantation continued for 10 hours with 10 Hz pulse repetition rate, resulting in a dose of  $5.9 \times 10^{15}$ ,  $1.8 \times 10^{15}$ ,  $9.45 \times 10^{14}$ ,  $3.5 \times 10^{14}$ , and  $9.45 \times 10^{13}$  ions/ $\text{cm}^2$  of  $B^{1+}$  to  $B^{5+}$ , respectively. The total number of ions implanted during the experiment was  $9 \times 10^{15}/\text{cm}^2$ . The implanted film thickness was estimated from the total number of ion to be  $\sim 11$  nm. Fig. 8.4 shows the field-emission scanning electron microscope (FESEM) image and UV-Vis absorption spectra of the film deposited on a microscope glass slide that was placed next to the Si substrate.

A Hall measurement system (Ecopia: HMS-5500) was employed to characterize the B implanted sample. The sheet resistance decreased from  $3.9 \times 10^5$  to  $3.2 \times 10^5$   $\Omega/\text{square}$ , and resistivity decreased from  $2 \times 10^4$  to  $1.5 \times 10^4$   $\Omega\text{-cm}$  due to the B ion implantation.

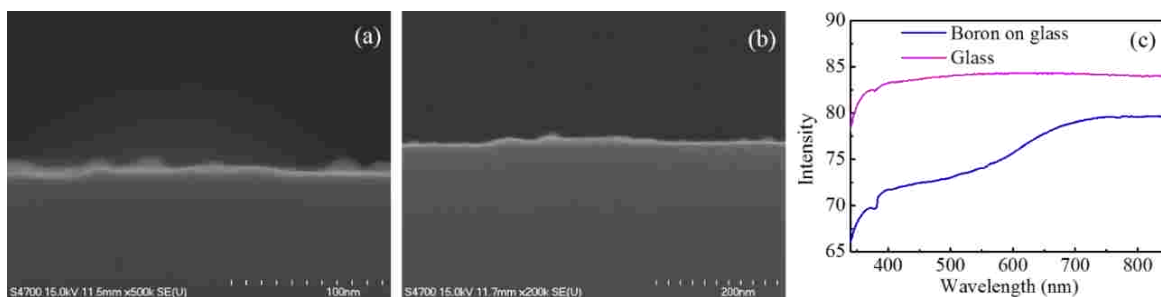


Fig. 8.4 (a) and (b) FESEM image of the boron film on Si, (c) transmission characteristics of the film on glass sample measured using UV-Vis spectrophotometer.

To calibrate the film thickness growth with time, films were grown for variable time and their cross-sections measured with FESEM. Fig. 8.5 shows the Ba film of  $\sim 40$  nm grown on silicon in 2 hours.

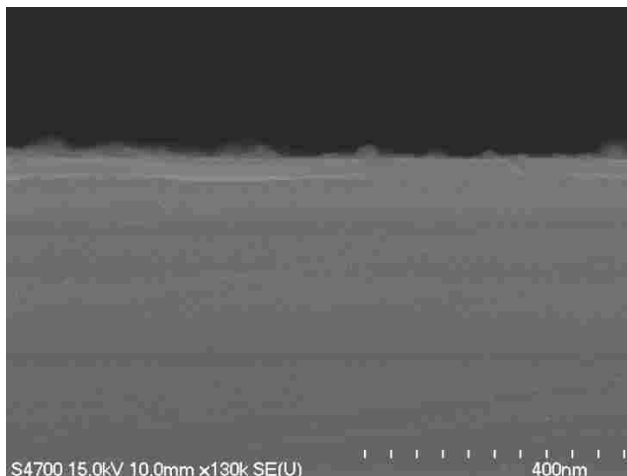


Fig. 8.5 Film thickness measured by FESEM of ~40 nm Ba film.

## 8.5 B AND Ba SHALLOW ION IMPLANTATION ON SiC

B and/or Ba shallow ion implantation on N-type 4H-SiC ( $4^\circ$  off axis) (orientation  $\langle 0001 \rangle$ , dimension  $5 \times 5 \times 0.33$  mm, surface roughness  $< 10 \text{ \AA}$ ) was performed after RCA + HF cleaning.

### 8.5.1 Optical bandgap measurement

The transmission spectrum and the Tauc plot method were used to determine the optical bandgap of 4H-SiC samples with 2 nm B film and without B ion implantation, as shown in Fig. 8.6. The transmission characteristics are measured using a LAMBDA 45 UV/Vis System (PerkinElmer). As expected, the transmission (%) decreases due to boron shallow implantation, as shown in Fig. 8.6 (a). The coefficient of optical absorption  $\alpha$  is obtained from [170]:  $\alpha = 1/d \ln(I_0/I)$ , where  $d$  is the thickness of SiC sample, and  $I_0$  and  $I$  are the intensities of the incident and transmitted light, respectively. The optical bandgap  $E_g$  is calculated using the Tauc relation [170]:  $\alpha h\nu = A(h\nu - E_g)^{1/2}$  where  $h\nu$  is the photon energy. By extending the linear region of the  $(\alpha h\nu)^2$  term versus energy ( $h\nu$ ), in Fig. 8.6(b), the optical bandgap of the 4H-SiC substrate is obtained to be  $\sim 3.24$  eV. The bandgap is reduced to  $\sim 3.2$  eV for SiC with 2 nm B film.

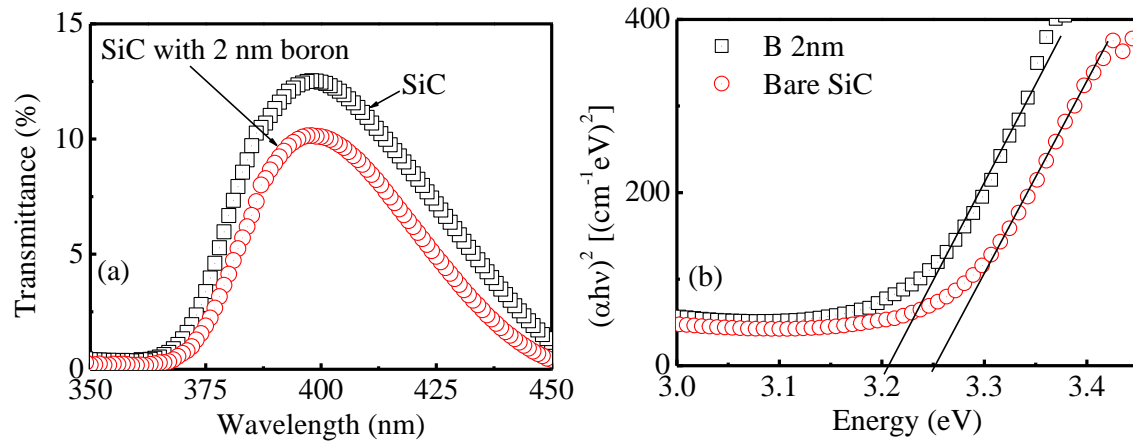


Fig. 8.6 Effect of B implantation on the bandgap of SiC, (a) UV-Vis photo-spectroscopy of the bare SiC and SiC with 2 nm boron layer, (b) Tauc plot to calculate the optical bandgap.

### 8.5.2 MOSCAP preparation

After RCA + HF cleaning, 6 samples were shallow implanted with B and Ba ions. The samples prepared as a part of this experiment are:

1. No implantation, bare SiC
2. Boron 2 nm
3. Barium 2 nm
4. Boron 1 nm and barium 1 nm
5. Boron 2 nm and barium 2 nm
6. Barium 1 nm and boron 1 nm

Using reactive sputtering, ~47-nm thick silicon dioxide ( $\text{SiO}_2$ ) layer was formed at 250 °C. The thickness of the oxide was measured using an ellipsometer (M2000 J.A. Woollam Co.). A high temperature vacuum tube furnace (MTI Corporation GSL-1100X) was used to anneal the samples at 950 °C for 30 min. Aluminum gate contact of diameter ~3 mm and thickness of ~150 nm was deposited. Fig. 8.7 shows the cross-section schematic of the MOSCAP.

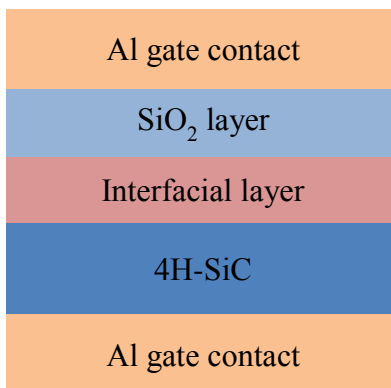


Fig. 8.7 Cross-section schematic of the MOSCAP.

### 8.5.3 MOSCAP characterization

High-low C-V characterization technique was performed by measuring the capacitance from a small amplitude (10 mV) high-frequency and low-frequency AC signal centered on the DC voltage applied to the gate. In the high-low C-V characterization, the voltage is swept from the accumulation to the depletion region of the MOSCAP. In the accumulation region, the electron traps are filled since the conduction band edge is below the Fermi level. The metal Fermi level increases with decreasing DC voltage applied to the MOSCAP gate causing bending of the semiconductor bands upwards [171]. The AC signal is shifted by the DC voltage. The electrons cannot respond to the high frequency by moving into and out of the traps with the voltage change. However, for low frequency CV characterization, the electrons respond to the voltage and move into and out of the traps as the voltage changes. The condition of trapped electron and out of the traps creates the differences in charge resulting in higher low frequency capacitance than the high frequency capacitance [171].

High-frequency capacitance-voltage (C-V) (using Agilent B1500A Semiconductor Device Parameter Analyzer) characteristics for a frequency of 100 kHz at room temperature for n-MOS capacitor with difference B and Ba doses are shown in Fig. 8.8. With increasing B dose, the oxide thickness increases, as evident by the reduction of the oxide capacitance, and the C-V curve becomes increasingly left-shifted. While with the increase of Ba shallow implantation dose, the oxide thickness increases with the shift in the C-V curve negligible. Under flat band condition the effective interfacial charge causes the deviation of the experimental flat-band

voltage. The left shift of the C-V curve is due to the interfacial charge carrier change with the doping.

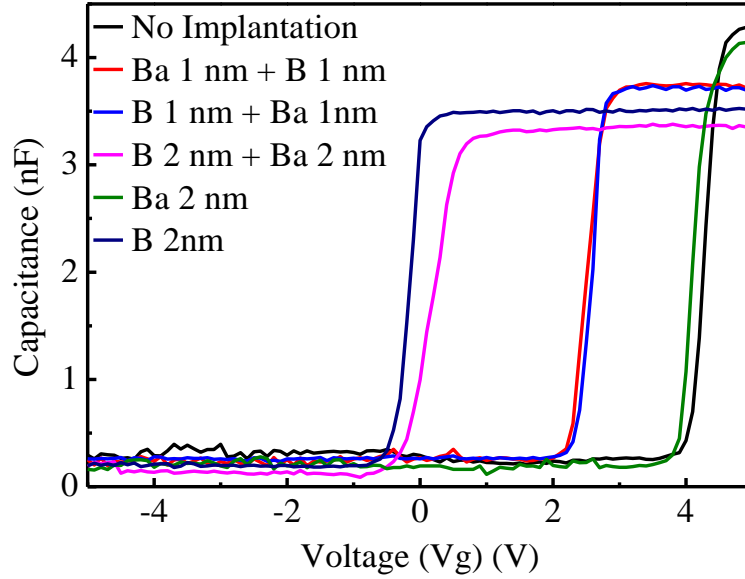


Fig. 8.8 100 kHz C-V for n-type MOS capacitor with different B and Ba dose.

The flat-band voltage is calculated from the C-V curve using Eq. 8.1 [172]:

$$C_{FB} = \frac{C_{OX} \cdot C_{sFB}}{C_{OX} + C_{sFB}} \quad (8.1)$$

where  $C_{OX}$  is the oxide capacitance and  $C_{sFB}$  is the semiconductor surface capacitance in  $F/cm^2$ , and can be calculated Eq. 8.2 [172]:

$$C_{sFB} = \frac{\epsilon_s \epsilon_0}{L_D} \quad (8.2)$$

where  $\epsilon_s$  and  $\epsilon_0$  is the dielectric permittivity of the semiconductor and the vacuum in  $F/cm$ .  $L_D$  is the Debye's length in cm,  $L_D$  can be calculated using Eq. 8.3 [172]:

$$L_D = \sqrt{\frac{kT \epsilon_s \epsilon_0}{q^2 N_D}} \quad (8.3)$$

where  $k$  is the Boltzmann constant (J/K),  $T$  is the temperature in K,  $q$  is the electron charge in C,  $N_D$  is the doping concentration in  $\text{cm}^{-3}$ . The doping concentration can be calculated from the C-V curve. Using the slope ( $d/dV$ ). ( $1/C^2$ ) of the linear part of the ( $1/C^2$ ) versus  $V$  characteristics and the  $N_D$  value is calculated by Eq. 8.4 [172]:

$$N_D = \frac{2}{q\epsilon_s\epsilon_0} / (|\text{slope}| \cdot A^2) \quad (8.4)$$

where  $A$  is the gate area in  $\text{cm}^2$ .

The change in the flat-band voltage with varying implantation is given in Table 1. We observe that shallow implantation of B affects the flat-band voltage significantly while the effect of implanting Ba ions is negligible.

Table 8.1. Flat-band voltage with the implantation variation.

SiC MOSCAP	Flat-band voltage
No Implantation	4.5
Ba 2 nm	4.4
Ba 1 nm + B 1nm	2.8
B 1 nm + Ba 1nm	2.7
Ba 2 nm + B 2 nm	0.2
B 2 nm	0.04

High-low C-V measurement of bare SiC and 2-nm B implanted MOSCAP is given Fig. 8.9. For high and low frequency 1 MHz and 1 kHz signals are used. From the Fig. 8.9 we observe that the deviation of the high and low C-V curve is increased with the shallow implantation, indicating the possibility of an interface trap density increase.

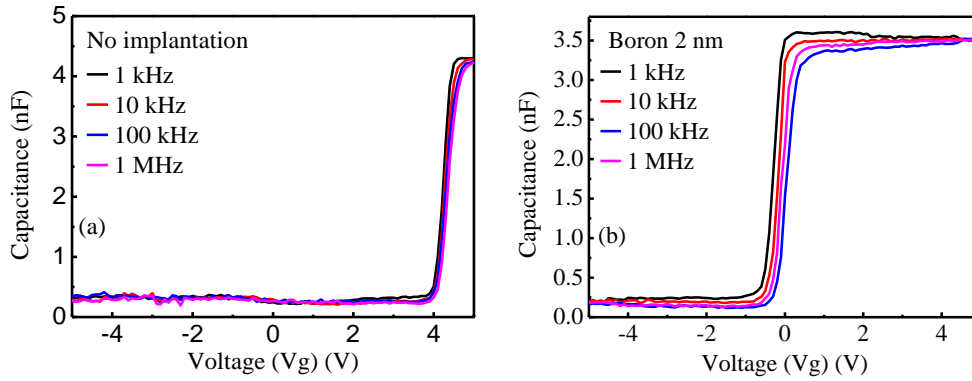


Fig. 8.9 High-Low C-V curve for bare SiC (a) and 2 nm boron implanted SiC (b).

## 8.6 SUMMARY

Shallow implantation of boron and barium multicharged ion in SiC/SiO<sub>2</sub> is performed. Six different MOSCAPs, with varying boron and barium implantation dose, are fabricated and characterized using high-low CV method. According to SRIM simulation, for ion energy of 150 eV/charge, the ion range is up to  $\sim 50$  Å (FWHM). Two nm thick boron shallow implantation reduced the optical bandgap of the 4H SiC and reduced the flatband voltage noticeably. While the effect of the barium implantation is negligible.

## CHAPTER 9

### CONCLUSION

A Q-switched Nd:YAG laser was used to generate Al multicharged ions by laser ablation in UHV. We characterized the dependence of extracted Al MCIs from laser plasma on laser pulse energy, accelerating voltage, and incident laser angle. Singly-charged ions were the dominant charge extracted. The charge state of the laser-generated ions and their kinetic energy are influenced significantly by the incident laser pulse energy. With 5 kV voltage applied to the target and a laser pulse energy of 90 mJ, we can extract up to  $\text{Al}^{4+}$  ions. The most probable energy of  $\text{Al}^{4+}$  is 6 keV applied to the target. Under these conditions, the total charge that reaches the Faraday cup is  $\sim 0.65$  nC. Significant plasma shielding in the target-to-extraction grid region is observed. The results show that ion charge extraction is enhanced by stronger electric field applied between the target and extraction grid. The spatial distribution of the generated MCIs appears to be strongly dependent on ion charge.

Components of a transport line for a LMCI source are constructed and tested. These components are an einzel lens for ion focusing, parallel deflection plates with pulsed voltage source for MCI charge selection, electrostatic cylindrical ion energy analyzer for MCI  $E/z$  selection, three-grid ion energy analyzer, and a Faraday cup for TOF ion detection. We are able to focus the ion beam down to  $\sim 1.5$  mm depending on ion charge. Ion pick-up from TOF with variable pulse width allows for selecting an ion charge and a narrow energy distribution of the selected charge if the pick-up pulse is shortened below the ion pulse width. Ion selection by pulsed deflection plates can be used for ion pick-up in tandem TOF instruments and avoids transport of contamination ions produced from the target surface during laser-target interaction. A high voltage pulse generator with programmable narrow pulse width is necessary for the ion selection. The EIA combined with TOF measurement are used to resolve both  $E/z$  and ion charge and obtain the energy distribution of each charge. The transport line components discussed are all built on standard ConFlat flanges making them highly modular. This design provides the flexibility to modify each component, reconfigure the transport line, and add other beam forming and beam steering components in addition to a substrate processing chamber.



A spark discharge coupled laser multicharged ion source was developed and tested. A 7.4 ns Nd:YAG laser is used to ablate an Al target generating a plasma plume. The spark discharge is triggered by the laser plume which significantly simplifies the design and provides synchronization of the spark discharge with the laser plume. The spark discharge amplifies the total charge generation and results in higher charge states. The charge state depends mostly on the spark energy deposited rather than on the laser ablation energy. For a laser pulse energy of 72 mJ and spark energy of 1.25 J, charge states up to  $\text{Al}^{6+}$  were detected. Under this condition, the total charge delivered to the Faraday cup was  $\sim 9.2$  nC when the target was at 5 kV. The SD-LMCI source is an effective method to generate high charge states of MCIs with small laser pulse energies. This approach also minimizes target damage by the laser pulse since the laser is mainly used to introduce the vapor into the spark while the energy delivered by the spark is used to heat the plasma, which increases the MCI state along with total charge production.

A combined ion TOF and OES study of laser-generated Al plasma was conducted. The 1064 nm laser ablation source providing 7 ns pulses was operated at a fluence of 21 – 38 J/cm<sup>2</sup>. The energy distributions of the ejected ions were fitted to SCB distribution. The ions are subjected to a Coulomb acceleration proportional to their charge state by the electric field generated at the plasma-vacuum interface of the expanding plume, in addition to the external electric field after their separation from the plasma. The results show significant deviation in the plasma temperature measured by ion energy versus that measured by OES. From the ion TOF measurement, the  $kT_i$  increases with the laser fluence from about 6 – 10 eV for the studied laser fluence range. However, applying the line emission intensity analysis method to OES yields  $kT_e$  of about 1.1 – 1.8 eV. Since the laser plasma is considered at LTE, the present results show that measurements of  $kT_e$  by OES does not reflect the initial high temperature of the plasma in which the ions are produced, and the condition of optically thin plasma might not be maintained. Also, the OES data were obtained under temporal and spatial averaging of plasma emission. This averaging also influences the measurements and gives a lower plasma temperature than that achieved in the early part of plume formation, where the plasma is densest and hottest, which are the conditions at which the MCIs are generated. When the plume expands in an applied electric field, ion energy spread, in addition to that due to the plasma ion temperature, is observed due to the interaction of the plume with the external field causing temporal and spatial distortion to the field. Applying voltage to the target had no effect on  $kT_e$  as measured by OES.

Ablation of Al target with 800 nm, 100 fs laser pulse of intensity  $10^{13} - 10^{14}$  W/cm<sup>2</sup> is used to generate Al ions. Production of Al ions up to Al<sup>6+</sup> is observed. The energy distributions of the ejected ions are fitted to a SCB distribution. From this fit, the equivalent plasma ion temperature is found to increase from 25 to 40 eV when an external accelerating voltage of 5 kV is applied to the target setting an electric field in the plasma expansion region. The ion energy depends on the sum of  $E_T + E_K + zE_c + zE_{eff}$ , where  $z$  is the charge state, and  $E_T$ ,  $E_K$ ,  $E_c$ , and  $E_{eff}$  is the thermal, adiabatic, Coulomb, and external effective energy. For higher charge state ions, the Coulomb contribution to the ion velocity is much higher than the thermal ion velocity. Plasma shielding and secondary ion generation in the target-to-extraction grid region results in ion energies less than the voltage applied to the target. Comparison of Al ion generation by the ~100 fs laser pulses with ~7 ns laser pulses shows that the femtosecond laser has significantly lower threshold for ion detection, results in a higher ion charge state, and ion acceleration. For 5 kV accelerating voltage charge state up to Al<sup>6+</sup> detected at 7.6 J/cm<sup>2</sup> with 2.3 keV per charge state for the femtosecond laser, while only Al<sup>4+</sup> with 1.8 keV per charge state is detected at a fluence of 38 J/cm<sup>2</sup> for the nanosecond laser.

Ion emission from laser-ablated B target was studied by ion time-of-flight. B<sup>5+</sup> ions are generated using a 7 ns, 1064 nm laser pulse operated at a fluence of  $\geq 115$  J/cm<sup>2</sup>. By allowing the plume to expand in a field-free region, where the ions separate from the decaying plasma plume and then accelerating the ions, it is possible to separate, in time, ions with a different charge-to-mass ratio. Increasing the laser fluence increases the ions generation along with producing higher charge states. For B<sup>5+</sup>, clear ion pulses corresponding to <sup>11</sup>B and <sup>10</sup>B are observed. The ion kinetic energy is affected by the bias voltage fluctuations during the plasma expansion. For 5 kV accelerating voltage applied to the EC, most of the ions have an energy  $>4.5$  kV/charge. Ion deflecting out of the plume direction allows the laser ion source to be used for implantation without deposition of B neutrals. The results show that a relatively small laser source can produced up to the fully-stripped B<sup>5+</sup> ions that can be accelerated by an external electric field. This approach offers a design of a compact B ion source for implantation.

The multicharged ion source was used to perform shallow implantation boron and barium ions. To calibrate the film thickness growth with time, films were grown for variable time and their cross-sections measured with FESEM. The depth to which ions are implanted were

simulated using SRIM, and for 150 eV/charge boron ions the FWHM depth is  $\sim 50$  Å. Implantation of boron ions affects the optical bandgap and flatband voltage noticeably, while the effect of barium is negligible. Several MOSCAPs were fabricated with a combination of boron and barium ions. The MOSCAPs are characterized using high-low CV method.

### **Future work**

Optimization of ion extraction and considering the ion energy and spatial distributions are needed for design of ion lenses and other components of the ion transport line in laser MCI systems. The proof-of-concept presented here shows the significant potential of the SD-LMCI source which can be used to generate MCIs out of practically any solid target. Further optimization of the SD-LMCI source is possible by shortening the discharge energy deposition time in the plume to increase the plasma density and temperature. This can be achieved through improvement of the pulse forming network. Also, providing control on discharge trigger time can lead to better coupling of discharge energy with the laser plasma. Other geometries for coupling the discharge energy to the plasma plume and for MCI extraction can also lead to further improvements in MCI yield and energy distribution.

Also, the interfacial treatment of the SiC/SiO<sub>2</sub> can be repeated with 4H-SiC with high density epitaxial layer. In the current experiment, the n-type 4H-SiC used has very low carrier concentration resulting in reduced effect of boron and barium implantation.

## REFERENCES

- [1] T. Schenkel, A. V. Hamza, and D. D. Schneider, “Interaction of slow, very highly charged ions with surface”, *Prog. Surf. Sci.* 62, 23 (1999).
- [2] H. Gnaser, *Springer Tracts in Modern Physics* (Springer, Berlin, Heidelberg, New York, 1999), Vol. 146.
- [3] J. D. Gillaspay, “Highly charged ions” *J. Phys. B: At., Mol. Opt. Phys.* 34, 93 (2001).
- [4] Y. Higurashi, T. Nakagawa, M. Kidera, T. Aihara, K. Kobayashi, M. Kase, A. Goto, and Y. Yano, “Effect of the plasma electrode position and shape on the beam intensity of the highly charged ions from RIKEN 18 GHz electron-cyclotron-resonance ion source” *Rev. Sci. Instrum.* 77, 03A329 (2006).
- [5] V. Skalyga, V. Zorin, I. Izotov, S. Razin, A. Sidorov, and A. Bohanov, “Gasdynamic ECR source of multicharged ions based on a cusp magnetic trap”, *Plasma Sources Sci. Technol.* 15, 727 (2006).
- [6] F. Ullman, F. Grossmann, V. P. Ovsyannikov, J. Gierak, and G. Zschornack, “Production of a helium beam in a focused ion beam machine using an electron beam ion trap”, *Appl. Phys. Lett.* 90, 083112 (2007).
- [7] G. Zschornack, M. Kreller, V. P. Ovsyannikov, F. Grossman, U. Kentsch, M. Schmidt, F. Ullmann, and R. Heller, “Compact electron beam ion sources/traps: Review and prospects”, *Rev. Sci. Instrum.* 79, 02A703 (2008).
- [8] D. Bleiner, A. Bogaerts, F. Belloni, and V. Nassisi, “Laser-induced plasmas from the ablation of metallic targets: the problem of the onset temperature, and insights on the expansion dynamics”, *J. Appl. Phys.* 101, 083301 (2007).
- [9] H. Daido, M. Nishiuchi, and A. S. Pirozhkov, “Review of laser-driven ion sources and their applications”, *Rep. Prog. Phys.* 75, 056401 (2012).
- [10] A. Lorusso, L. Velardi, V. Nassisi, F. Paladini, A. M. Visco, N. Campo, L. Torrisi, D. Margarone, L. Giuffrida, and A. Rainò, “Polymer processing by a low energy ion accelerator”, *Nucl. Instrum. Methods Phys. Res., Sect. B* 266, 2490 (2008).

- [11] J. Krása, L. Laska, K. Rohlena, M. Pfeifer, J. Skala, B. Kralikova, P. Straka, E. Woryna, and J. Wolowski, “The effect of laser-produced plasma expansion on the ion population”, *Appl. Phys. Lett.* 75, 2539 (1999).
- [12] V. Dubenkov, B. Sharkov, A. Golubev, A. Shumshurov, O. Shamaev, I. Roudskoy, A. Streltsov, Y. Satov, K. Makarov, Y. Smakovasky, D. Hoffmann, W. Laus, R. W. Muller, P. Spadtke, C. Stockl, B. Wolf, and J. Jacoby, “Acceleration of Ta<sup>10+</sup> ions produced by laser ion source in RFQ MAXILAC”, *Laser Part. Beams* 14, 385 (1996).
- [13] B. Y. Sharkov, S. Kondrashev, I. Roudskoy, S. Savin, A. Shumshurov, H. Haseroth, H. Kugler, K. Langbein, N. Lisi, H. Magnusson, R. Scrivens, J. C. Schnuringer, J. Tambini, S. Homenko, K. Markov, V. Roerich, A. Stepanov, and Yu. Satov, “Laser ion source for heavy ion synchrotrons”, *Rev. Sci. Instrum.* 69, 1035 (1998).
- [14] S. Kondrashev, N. Mescheryakov, B. Sharkov, A. Shumshurov, S. Khomenko, K. Makarov, Yu. Satov, and Y. Smakovskii, “Production of He-like light and medium mass ions in laser ion source”, *Rev. Sci. Instrum.* 71, 1409 (2000).
- [15] L. Laska, K. Jungwirth, B. Kralikova, J. Krasa, M. Pfeifer, K. Rohlena, J. Skala, J. Ullschmied, J. Badziak, P. Parys, J. Wolowski, E. Woryna, S. Gammino, L. Torrisi, F. P. Boody, and H. Hora, “Generation of multiply charged ions at low and high laser-power densities”, *Plasma Phys. Controlled Fusion* 45, 585 (2003).
- [16] S. S. Harilal, B. O’shay, M. S. Tillack, and M. V. Mathew, “Spectroscopic characterization of laser-induced tin plasma”, *J. Appl. Phys.* 98, 013306 (2005).
- [17] R. Fabbro, C. Max, and E. Fabre, “Planar laser-driven ablation: Effect of inhibited electron thermal conduction”, *Phys. Fluids* 28, 1463 (1985).
- [18] S. J. Gitomer, R. D. Jones, F. Begay, A. W. Ehler, J. F. Kephart, and R. Kristal, “Fast ions and hot electrons in the laser-plasma interaction”, *Phys. Fluids* 29, 2679 (1986).
- [19] J. I. Apinaniz, B. Sierra, R. Martinez, A. Longarte, C. Redondo, and F. Castano, “Ion kinetic energy distribution and mechanism of pulsed laser ablation on Al”, *J. Phys. Chem. C* 112, 16556 (2008).
- [20] P. Ecija, M. S. Rayo, R. Martinez, B. Sierra, C. Redondo, F. J. Basterretxea, and F. Castano, “Fundamental processes in nanosecond pulsed laser ablation of metals in vacuum”, *Phys. Rev. A* 77, 032904 (2008).

- [21] S. Amoruso, M. Armenante, V. Berardi, R. Bruzzese, G. Pica, and R. Velotta, “Charged species analysis as a diagnostic tool for laser produced plasma characterization”, *Appl. Surf. Sci.* 106, 507 (1996).
- [22] X. Wang, S. Zhang, X. Cheng, E. Zhu, W. Hang, and B. Huang, “Ion kinetic energy distribution in laser-induced plasma”, *Spectrochim. Acta B* 99, 101 (2014).
- [23] N. M. Bulgakova, A. V. Bulgakov, and O. F. Bobrenok, “Double layer effects in laser-ablation plasma plumes”, *Phys. Rev. E* 62, 5624 (2000).
- [24] E. Woryna, P. Parys, J. Wolowski, and W. Mroz, “Corpuscular diagnostics and processing methods applied in investigation of laser-produced plasma as a source of highly charged ions”, *Laser Part. Beams* 14, 293 (1996).
- [25] D. Mascali, S. Tudisco, N. Gambino, A. Pluchino, A. Anzalone, F. Musumeci, A. Rapisarda, and A. Spitaleri, “Prompt electrons driving ion acceleration and formation of a two-temperature plasma in nanosecond laser-ablation domain”, *Europhys. Lett.* 100, 45003 (2012).
- [26] G. Abdellatif and H. Imam, “A study of the laser plasma parameters at different laser wavelengths”, *Spectrochim. Acta B* 57, 1155,073304 (2002).
- [27] V. Nassisi, A. Pedone, and A. Rainò, Nucl. “Preliminary experimental results on an excimer laser ion source”, *Instrum. Methods Phys. Res., Sect. B* 188, 267 (2002).
- [28] D. Doria, A. Lorusso, F. Belloni, V. Nassisi, L. Torrisci, and S. Gammino, “A study of the parameters of particles ejected from a laser plasma”, *Laser Part. Beams* 22, 461 (2004).
- [29] L. Velardi, M. V. Siciliano, D. Delle Side, and V. Nassisi, “Production and acceleration of ion beams by laser ablation”, *Rev. Sci. Instrum.* 83, 02B717 (2012).
- [30] L. Torrisci, F. Caridi, D. Margarone, A. Picciotto, A. Mangione, and J. J. Beltrano, “Carbon-plasma produced in vacuum by 532 nm-3 ns laser pulses ablation”, *Appl. Surf. Sci.* 252, 6383 (2006).
- [31] L. Láska, K. Jungwirth, J. Krása, M. Pfeifer, K. Rohlena, J. Ullschmied, J. Badziak, P. Parys, J. Wolowski, S. Gammino, L. Torrisci, and F. P. Boody, “Charge-state and energy enhancement of laser-produced ions due to nonlinear processes in preformed plasma”, *Appl. Phys. Lett.* 86, 081502 (2005).

- [32] Y. Wada, Y. Shigemoto, and A. Ogata, “Ion production enhancement by rear-focusing and prepulse in ultrashort-pulse laser interaction with foil targets”, *Jpn. J. Appl. Phys.*, 43, L996 (2004).
- [33] L. Laska, K. Jungwirth, J. Krasa, E. Krouský, M. Pfeifer, K. Rohlena, J. Ullschmied, J. Badziak, P. Parys, J. Wolowski, S. Gammino, L. Torrissi, and F. P. Boody, “Self-focusing in processes of laser generation of highly-charged and high-energy heavy ions”, *Laser Part. Beams* 24, 175 (2006).
- [34] S. Gammino, L. Torrissi, L. Andò, G. Ciavola, L. Celona, L. Laska, J. Krasa, M. Pfeifer, K. Rohlena, E. Woryna, J. Wolowski, P. Parys, and G. D. Shirkov, “Production of low energy, high intensity metal ion beams by means of a laser ion source”, *Rev. Sci. Instrum.* 73, 650 (2002).
- [35] E. Woryna, J. Wolowski, B. Králiková, J. Krása, L. Laska, M. Pfeifer, K. Rohlena, J. Skala, V. Perina, F. P. Boody, R. Hopfl, and H. Hora, “Laser produced Ag ions for direct implantation”, *Rev. Sci. Instrum.* 71, 949 (2000).
- [36] K. Rohlena, B. Králiková, J. Krása, L. Laska, K. Mašek, M. Pfeifer, J. Skala, J. Farny, P. Parys, J. Wolowski, E. Woryna, W. Mroz, I. Roudskoy, O. Shamaev, B. Sharkov, A. Shumshurov, B. A. Bryunetkin, H. Haseroth, J. Collier, A. Kutteneberger, K. Langbein, and H. Kugler, “Ion production by lasers using high-power densities in a near infrared region”, *Laser Part. Beams* 14, 335 (1996).
- [37] H. Haseroth, H. Kugler, K. Langbein, N. Lisi, A. Lombardi, H. Magnusson, W. Pirkl, J. C. Schnuriger, R. Scrivens, J. Tambini, E. Tanke, S. Homenko, K. Makarov, V. Roerich, A. Stepanov, Y. Satov, S. Kondrashev, S. Savin, B. Sharkov, A. Shumshurov, J. Krasa, L. Laska, M. Pfeifer, and E. Woryna, “Developments at the CERN laser ion source”, *Rev. Sci. Instrum.* 69, 1051 (1998).
- [38] A. Lorusso, F. Belloni, D. Doria, V. Nassisi, J. Wolowski, J. Badziak, P. Parys, J. Krasa, L. Laska, F. P. Boody, L. Torrissi, A. Mezzasalma, A. Picciotto, S. Gammino, G. Quarta, and D. Bleiner, “Modification of materials by high energy plasma ions”, *Nucl. Instrum. Methods Phys. Res., Sect. B* 240, 229 (2005).
- [39] Ueda, M., Tan, I., Dallaqua, R., Rossi, J., Barroso, J., and Tabacniks, M., “Aluminum plasma immersion ion implantation in polymers,” 13<sup>th</sup> International Conference on Ion Beam Modification of Materials, *Nucl. Instr. and Meth. B*, 206, 760–766, (2003).

- [40] Kohiki, S., Nishitani, M., and Wada, T., "Enhanced electrical conductivity of zinc oxide thin films by ion implantation of gallium, aluminum, and boron atoms," *J. Appl. Phys.*, 75 (4), 2069–2072 (1994).
- [41] Liu, C., Xin, Y., Tian, X., and Chu, P.K., "Corrosion behavior of AZ91 magnesium alloy treated by plasma immersion ion implantation and deposition in artificial physiological fluids," *Thin Solid Films*, 516 (2–4), 422–427 (2007).
- [42] Wu, G., Xu, R., Feng, K., Wu, Sh., Wu, Z., Sun, G., Zheng, G., Li, G., and Chu, P.K., "Retardation of surface corrosion of biodegradable magnesium-based materials by aluminum ion implantation," *Appl. Surf. Sci.* 258 7651–7657 (2012).
- [43] Sen, B., Yang, B.-L., Wong, H., Kok, C.-W., Chu, P., and Huang, A., "Effects of aluminum incorporation on hafnium oxide film using plasma immersion ion implantation," *Microelectron. Reliab.* 48 (11–12), 1765–1768, (2008).
- [44] Boutopoulos, C., Terzis, P., Zergioti, I., Kantos, A.G., Zekentes, K., Giannakopoulos, K., and Raptis, Y. S., "Laser annealing of Al implanted silicon carbide: Structural and optical characterization," *Appl. Surf. Sci.* 253 (19), 7912–7916 (2007).
- [45] Mitra, S, Rao, M.V., Jones, K., Papanicolaou, N., and Wilson, S., "Deep levels in ion implanted field effect transistors on SiC," *Solid-State Electronics* 47, 193–198 (2003).
- [46] Rao, M.V. "Maturing ion-implantation technology and its device applications in SiC," *Solid-State Electronics* 47, 213–222 (2003).
- [47] Woryna, E., Parys, P., Wolowski, J., and Mroz, W., "Corpuscular diagnostics and processing methods applied in investigations of laser-produced plasma as a source of highly ionized ions," *Laser Part. Beams*, 14 (03), 293–321, (1996).
- [48] Láska, L., Badziak, J., Gammino, S., Jungwirth, K., Kasperczuk, A., Krása, J., Krouský, E., Kubeš, P., Parys, P., Pfeifer, M., Pisarczyk, T., Rohlena, K., Rosinski, M., Ryc, L., Skála, J., Torrisi, L., Ullschmied, J., Velzhan, A., and Wolowski, J., "The influence of an intense laser beam interaction with preformed plasma on the characteristics of emitted ion streams," *Laser Part. Beams*, 25 (04), 549–556 (2007).
- [49] Vadillo, J.M., Fernández Romero, J.M., Rodríguez, C, and Laserna, J.J., "Effect of plasma shielding on laser ablation rate of pure metals at reduced pressure" *Surf. Interface Anal.* 27, 1009–1015 (1999).



- [50] Moscicki, T., Hoffman, J., and Szymanski, Z., “Modelling of plasma formation during nanosecond laser ablation,” *Arch. Mech.* 63(2), 99–116 (2011).
- [51] Torrisci, L., Gammino, S., Andò, L., and Laska, L., “Tantalum ions produced by 1064 nm pulsed laser irradiation,” *J. Appl. Phys.*, 91, 4685–4692, (2002).
- [52] F. F. Chen, “Decay of a plasma created between negatively biased walls,” *Phys. Fluids* 25, 1385–2387 (1982).
- [53] Yamada, K., Tetsuka, T., and Deguchi, Y., “New scaling relation for ion extraction by external electric field on a barium plasma produced between parallel-plate electrodes,” *J. Appl. Phys.* 69, 6962–6967 (1991).
- [54] M. H. A. Shaim, and H. E. Elsayed-Ali, “Aluminum multicharged ion generation from laser plasma”, *Nucl. Instrum. Methods Phys. Res. Sect. B* 356 (2015) 75.
- [55] M. H. A. Shaim, and H. E. Elsayed-Ali, “Spark discharge coupled laser multicharged ion source”, *Rev. Sci. Instrum.* 86 (2015) 073304.
- [56] S. Prasad, K. Tang, D. Manura, D. Papanastasiou, and R. D. Smith, “Simulation of ion motion in FAIMS through combined use of SIMION and modified SDS”, *Anal. Chem.* 81 (2009) 8749.
- [57] M. Trinczek, A. Werdich, V. Mironov, P. Guo, A.J. González Martínez, J. Braun, J.R. Crespo López-Urrutia, J. Ullrich, “A laser ion source for an electron beam ion trap”, *Nucl. Instrum. Methods Phys. Res. Sect. B* 251 (2006) 289.
- [58] P. Yeates, J. T. Costello, and E. T. Kennedy, “The DCU laser ion source”, *Rev. Sci. Instrum.* 81 (2010) 043305.
- [59] T. Nagaya, T. Nishiokada, S. Hagino, T. Uchida, M. Muramatsu, T. Otsuka, F. Sato, A. Kitagawa, Y. Kato, and Y. Yoshida, “Producing multicharged fullerene ion beam extracted from the second stage of tandem-type ECRIS”, *Rev. Sci. Instrum.* 87 (2016) 02A723.
- [60] N. S. Saks, A. K. Agarwal, S. H. Ryu, and J. W. Palmour, “Low-dose aluminum and boron implants in 4H and 6H silicon carbide”, *J. Appl. Phys.* 90 (2001) 2796.
- [61] B. Sharkov, and R. Scrivens, “Laser ion sources”, *IEEE Trans. plasma sci.* 33 (2005) 1778.

- [62] V. Gordienko, I. Lachko, A. Rusanov, A. Savel'Ev, D. Uryupina, and R. Volkov. "Enhanced production of fast multi-charged ions from plasmas formed at cleaned surface by femtosecond laser pulse", *Appl. Phys. B* 80 (2005) 733.
- [63] R. Volkov, V. Gordienko, I. Lachko, A. Rusanov, A. Savel'ev, and D. Uryupina. "Formation of fast multicharged heavy ions under the action of a superintense femtosecond laser pulse on the cleaned surface of a target", *J.Exp.Theor. Phys.* 103 (2006) 303.
- [64] O. Balki, and H. E. Elsayed-Ali. "Multicharged carbon ion generation from laser plasma", *Rev. Sci. Instrum.* 87 (2016) 113304.
- [65] W. Lu, C. Qian, L. T. Sun, X. Z. Zhang, X. Fang, J. W. Guo, Y. Yang, Y. C. Feng, B. H. Ma, B. Xiong, L. Ruan, H. W. Zhao, W. L. Zhan, and D. Xie, "High intensity high charge state ion beam production with an evaporative cooling magnet ECRIS", *Rev. Sci. Instrum.* 87 (2016) 02A738.
- [66] L. Sun, J. Guo, W. Lu, W. Zhang, Y. Feng, Y. Yang, C. Qian, X. Fang, H. Ma, X. Zhang, and H. Zhao, "Advancement of highly charged ion beam production by superconducting ECR ion source SECRA", *Rev. Sci. Instrum.* 87(2016) 02A707.
- [67] Ady I. Herscovitch, "Eliminating unwanted electrons in EBIS devices", *Rev. Sci. Instrum.* 87 (2016) 02A918.
- [68] S. Schwarz and A. Lapierre, "Recent charge-breeding developments with EBIS/T devices", *Rev. Sci. Instrum.* 87 (2016) 02A910.
- [69] A. C. Villari, "Latest trends in ECR technology and Pantechnik ECRIS", In Proceedings of the DAE-BRNS Indian particle accelerator conference, 2011.
- [70] G. Zschornack, M. Kreller, V. P. Ovsyannikov, F. Grossman, U. Kentsch, M. Schmidt, F. Ullmann, and R. Heller, "Compact electron beam ion sources/traps: Review and prospects (invited) <sup>a)</sup>", *Rev. Sci. Instrum.* 79 (2008) 02A703.
- [71] H. Kashiwagi, M. Fukuda, M. Okamura, R. A. Jameson, T. Hattori, N. Hayashizaki, K. Sakakibara, J. Takano, K. Yamamoto, Y. Iwata, and T. Fujimoto, "Acceleration of high current fully stripped carbon ion beam by direct injection scheme", *Rev. Sci. Instrum.* 77 (2006) 03B305.
- [72] D. W. Heddle, *Electrostatic lens systems*. CRC Press, Institute of Physics publishing, Bristol and Philadelphia (2000).

- [73] O. Sise, M. Ulu, and M. Dogan, "Multi-element cylindrical electrostatic lens systems for focusing and controlling charged particles", *Nucl. Instrum. Methods Phys. Res. Sect. A* 554 (2005) 114.
- [74] O. Sise, M. Ulu, and M. Dogan, "Characterization and modeling of multi-element electrostatic lens systems", *Radiat. Phys. Chem.* 76 (2007) 593.
- [75] M. M. Abdelrahman, "Ion Beam Simulation Using a Three-Electrode Diaphragm Einzel Lens System", *J. Nucl. Radiation Phys.* 3 (2008) 93.
- [76] M. H. Rashid, "Simple analytical method to design electrostatic einzel lens", In *Proceedings of the DAE Symp. on Nucl. Phys.*, vol. 56 (2011) 1132.
- [77] A. Thum-Jaeger, B. K. Sinha, and K. P. Rohr, "Time of flight measurements on ion-velocity distribution and anisotropy of ion temperatures in laser plasmas", *Phys. Rev. E.* 63 (2000) 016405.
- [78] L. Torrisi, S. Gammino, L. Andò, V. Nassisi, D. Doria, and A. Pedone, "Comparison of nanosecond laser ablation at 1064 and 308 nm wavelength", *Appl. Surf. Sci.* 210 (2003) 262.
- [79] D. A. Dahl, J. E. Delmore, and A. D. Appelhans, "SIMION PC/PS2 electrostatic lens design program", *Rev. Sci. Instrum.* 61 (1990) 607.
- [80] P. R. Vlasak, D. J. Beussman, M. R. Davenport, and C. G. Enke, "An interleaved comb ion deflection gate for  $m/z$  selection in time-of-flight mass spectrometry", *Rev. Sci. Instrum.* 67 (1996) 68.
- [81] M. Guilhaus, *Spectrochim.*, "Essential elements of time-of-flight mass spectrometry in combination with the inductively coupled plasma ion source", *Acta B* 55 (2000) 1511.
- [82] Y. Toker, N. Altstein, O. Aviv, M. L. Rappaport, O. Heber, D. Schwalm, D. Strasser, and D. Zajfman, "The kick-out mass selection technique for ions stored in an Electrostatic Ion Beam Trap", *J. Instrum.* 4 (2009) P09001.
- [83] D. Wayne, and J. Olivares, "Selective removal of matrix ion peaks in plasma source time-of-flight mass spectrometry: ion deflection and detector gating", *J. Anal. At. Spectrom.* 14 (1999) 1523.
- [84] L. Torrisi, D. Mascali, R. Miracoli, S. Gammino, N. Gambino, L. Giuffrida, and D. Margarone, "Measurements of electron energy distribution in tantalum laser-generated plasma", *J. Appl. Phys.* 107 (2010) 123303.

- [85] D. P. Hale, and W. D. Allen, "An electrostatic electron energy analyser for 3-20 keV electrons", *J. Phys. E* 4 (1971) 311.
- [86] L. Torrisci, F. Caridi, D. Margarone, and A. Borrielli, "Plasma-laser characterization by electrostatic mass quadrupole analyzer", *Nucl. Instrum. Methods Phys. Res. Sect. B* 266 (2008) 308.
- [87] S. Shan, J. Qian-Yu, L. Zhang-Min, G. Xiao-Hong, Z. Lun-Cai, C. Guo-Zhu, S. Liang-Ting, Z. Xue-Zhen, Z. Huan-Yu, C. Xi-Meng, and Z. hong-Wei, "Charge state distribution analysis of Al and Pb ions from the laser ion source at IMP", *Chin. Phys. C* 37 (2013) 117006.
- [88] O. A. Nassef, & H. E. Elsayed-Ali, "Spark discharge assisted laser induced breakdown spectroscopy", *Spectrochim. Acta B* 60, 1564 (2005).
- [89] H. A. Sakaue, K. Hosaka, H. Tawara, I. Yamada, N. Nakamura, S. Ohtani, A. Danjo, M. Kimura, A. Matumoto, M. Sakurai, and M. Yoshino, "Total electron transfer cross sections for highly charged ion-alkali metal atom collisions", *J. Plasma Fusion Res.* 7, 195 (2006).
- [90] H. Ryufuku and T. Watanabe, "Total and partial cross sections for charge transfer in collisions of multicharged ions with atomic hydrogen", *Phys. Rev. A* 20, 1828 (1979).
- [91] D. H. Crandall, R. A. Phaneuf, and F. W. Meyer, "Electron capture by slow multicharged ions in atomic and molecular hydrogen", *Phys. Rev. A* 19, 504 (1979).
- [92] P. Persephonis, K. Vlachos, C. Georgiades, and J. Parthenios, "The inductance of the discharge in a spark gap", *J. Appl. Phys.*, 71, 4755 (1992).
- [93] A. Descoedres, C. Hollenstein, R. Demellayer, and G. Walder, *J. Mater.* "Optical emission spectroscopy of electrical machining plasma" *Process. Technol.* 149, 184 (2004).
- [94] M. L. Vestal, "Methods of ion generation", *Chem. Rev.* 101, 361 (2001).
- [95] M. F. Artamonov, V. I. Krasov, & V. L. Paperny, "Generation of multiply charged ion from a cathode jet of a low-energy vacuum spark", *J. Phys. D: Appl. Phys.* 34, 3364 (2001).
- [96] A. H. Lutey, "An improved model for nanosecond pulsed laser ablation of metals", *J. Appl. Phys.* 114, 083108 (2013).

- [97] Y. K. Kim and P. M. Stone, "Ionization of boron, aluminum, gallium, and indium electron impact", *Phys. Rev. A*, 64, 052707 (2001).
- [98] M. H. A. Shaim, F.G. Wilson, and H.E. Elsayed-Ali, "Aluminum multicharged ion generation from femtosecond laser plasma", *J. Appl. Phys.* 121, 185901 (2017).
- [99] J. R. Freeman, S.S. Harilal, P. K. Diwakar, B. Verhoff, and A. Hassanein, "Comparison of optical emission from nanosecond and femtosecond laser produced plasma in atmosphere and vacuum conditions", *Spectrochim. Acta B* 87, 43 (2013).
- [100] A. Roy, S. S. Harilal, M. P. Polek, S. M. Hassan, A. Endo, and A. Hassanein, "Influence of laser pulse duration on extreme ultraviolet and ion emission features from tin plasmas", *Phys. Plasmas* 21, 033109 (2014).
- [101] R. A. Burdt, Y. Tao, M. S. Tillack, S. Yuspeh, N. M. Shaikh, E. Flaxer, and F. Najmabadi, "Ion kinetic energy distributions in laser-induced plasma", *J. Appl. Phys.* 107, 043303 (2010).
- [102] L. Torrisi, F. Caridi, and L. Giuffrida, "Comparison of Pd plasmas produced at 532 nm and 1064 nm by Nd:YAG laser ablation", *Nucl. Instrum. Meth. Phys. Res. B* 268, 2285 (2010).
- [103] S. S. Harilal, "Influence of spot size on propagation dynamics of laser-produced tin plasma", *J. Appl. Phys.*, 102, 123306 (2007).
- [104] Z. Zhang, P. A. VanRompay, J. A. Nees, and P. P. Pronko, "Multi-diagnostics comparison of femtosecond and nanosecond pulsed laser plasmas", *J. Appl. Phys.*, 92, 2867 (2002).
- [105] S. Canulescu, E. Papadopoulou, D. Anglos, T. Lippert, M. J. Montenegro, S. Georgiou, M. Döbeli, and A. Wokaun, "Nanosecond and femtosecond ablation of  $\text{LaO}_{0.6}\text{CaO}_{0.4}\text{CoO}_3$ : a comparison between plume dynamics and composition of this films", *Appl. Phys. A* 105, 167 (2011).
- [106] B. Toftmann, B. Doggett, C. Budtz-Jørgensen, J. Schou, and J. G. Lunney, "Femtosecond ultraviolet laser ablation of silver and comparison with nanosecond ablation", *J. Appl. Phys.*, 113, 083304 (2013)
- [107] A. M. Elsieid, P. K. Diwakar, M. Polek, and A. Hassanein, "Dynamics of low-and high-Z metal ions emitted during nanosecond laser-produced plasmas", *J. Appl. Phys.*, 120, 173104 (2016).

- [108] J. R. Freeman, S. S. Harilal, B. Verhoff, A. Hassanein, and B. Rice, “Laser wavelength dependence on angular emission dynamics of Nd:YAG laser-produced Sn plasmas”, *Plasma Sources Sci. Technol.*, 21, 055003 (2012).
- [109] F. Caridi, L. Torrasi, and L. Giuffrida, “Time-of-flight and UV spectroscopy characterization of laser-generated plasma”, *Nucl. Instrum. Methods Phys. Res. B* 268, 499 (2010).
- [110] E. Hontzopoulos, D. Charalambidis, C. Fotakis, G. Farkas, Z. G. Horváth, and C. Toth, “Enhancement of ultraviolet laser plasma emission produced in a strong static electric field”, *Opt. commun.*, 67, 124 (1988).
- [111] M. H. A. Shaim, M. M. Rahman, O. Balki, A. Sarkissian, M. L. KorwinPawlowski, and H. E. Elsayed-Ali, “Transport line for laser multicharged ion source”, *Vacuum* 137, 14 (2017).
- [112] S. Gurlui, M. Agop, P. Nica, M. Ziskind, and C. Focsa, “Experimental and theoretical investigations of a laser-produced aluminum plasma”, *Phys. Rev. E* 78, 026405 (2008).
- [113] R. Kelly and R. Dreyfus, “On the effect of knudsen-layer formation on studies of vaporization, sputtering, and deposition”, *Surf. Sci.* 198, 263 (1988).
- [114] A. Miotello and R. Kelly, “On the origin of the different velocity peaks of particles sputtered from surfaces by laser pulses or charged-particle beams”, *Appl. Surf. Sci.* 138–139, 44 (1999)..
- [115] A. Lorusso, J. Krasa, K. Rohlena, V. Nassisi, F. Belloni, and D. Doria, “Charge losses in expanding plasma created by an XeCl laser”, *Appl. Phys. Lett.* 86, 081501 (2005).
- [116] N. Farid, S. S. Harilal, H. Ding, and A. Hassanein, “Kinetics of ion and prompt electron emission from laser-produced plasma”, *Phys. Plasmas*, 20, 073114 (2013).
- [117] R. Teghil, L. d’Alessio, A. Santagata, M. Zaccagnino, D. Ferro, and D. Sordelet, “Picosecond and femtosecond pulsed laser ablation and deposition of quasicrystals”, *Appl. Surf. Sci.* 210, 307 (2003).
- [118] S. S. Harilal, C. V. Bindhu, M. S. Tillack, F. Najmabadi, and A. C. Gaeris, “Internal structure and expansion dynamics of laser ablation plumes into ambient gases”, *J. Appl. Phys.*, 93, 2380 (2003).

- [119] A. Kramida, Yu. Ralchenko, J. Reader, and NIST ASD Team, NIST Atomic Spectra Database (ver. 5.3), [2017, July 11]. Available: <http://physics.nist.gov/asd>, National Institute of Standards and Technology, Gaithersburg, MD., (2015).
- [120] H. Griem, *Spectral Line Broadening by Plasmas*, Academic Press, New York, 1974.
- [121] L. J. Radziemski, T. R. Loree, D. A. Cremers, and N. M. Hoffman, "Time-resolved laser-induced breakdown spectroscopy of aerosols", *Anal. Chem.*, **55**, 246 (1983).
- [122] A. M. El Sherbini, T. M. El Sherbini, H. Hegazy, G. Cristoforetti, S. Legnaioli, V. Palleschi, L. Pardini, A. Salvetti, and E. Tognoni, "Evaluation of self-absorption coefficients of aluminum emission lines in laser-induced breakdown spectroscopy measurements", *Spectrochim. Acta B*, **60**, 1573 (2005).
- [123] C. Colon, G. Hatem, E. Verdugo, P. Ruiz, and J. Campos, "Measurement of the Stark broadening and shift parameters for several ultraviolet lines of singly ionized aluminum", *J. Appl. Phys.*, **73**, 4752 (1993).
- [124] A. W. Allen, M. Blaha, W. W. Jones, A. Sanchez, and H. R. Griem, "Stark-broadening measurement and calculations for a singly ionized aluminum line", *Phys. Rev. A*, **11**, 477 (1975).
- [125] M. Tillack, D. Blair, and S. Harilal, "The effect of ionization on clusters formation in laser ablation plumes", *Nanotechnology* **15**, 390 (2004).
- [126] S. Amoruso, "Modelling of UV pulsed-laser ablation of metallic targets", *Appl. Phys. A* **69**, 323 (1999).
- [127] S. Amoruso, M. Armenante, V. Berardi, R. Bruzzese, and N. Spinelli, "Absorption and saturation mechanisms in aluminum laser ablated plasmas", *Appl. Phys. A* **65**, 265 (1997).
- [128] R. E. Russo, X. Mao, J. J. Gonzalez, V. Zorba, and J. Yoo, *Laser ablation in analytical chemistry*, ACS Publications (2013).
- [129] S. A. Irimiciuc, S. Gurlui, G. Bulai, P. Nica, M. Agop, and C. Focsa, "Langmuir probe investigation of transient plasmas generated by femtosecond laser ablation of several metals: Influence of the target physical properties on the plume dynamics", *Appl. Surf. Sci.* **417**, 108 (2017).

- [130] E. Gamaly, A. Rode, B. Luther-Davies, and V. Tikhonchuk, "Ablation of solids by femtosecond laser: Ablation mechanism and ablation thresholds for metals and dielectrics", *Phys. Plasmas* 9, 949 (2002).
- [131] H. E. Elsayed-Ali, T. B. Norris, M. A. Pessot, and G. A. Mourou, "Time-resolved observation of electron-photon relaxation in copper" *Phys. Rev. Lett.* 58, 1212 (1987).
- [132] W. MG. Ibrahim, H. E. Elsayed-Ali, C. E. Bonner, and M. Shinn, Int. "Ultrafast investigation of electron dynamics in multi-layer metals", *J. Heat Mass Transfer* 47, 2261, (2004).
- [133] J. Chen, I. V. Tomov, H. E. Elsayed-Ali, and P. M. Rentzepis, "Hot electrons blast wave generated by femtosecond laser pulses on thin Au (1 1 1) crystals, monitored by subpicosecond X-ray diffractions", *Chem. Phys. Lett.* 419,374 (2006).
- [134] X. Liu, D. Du, and G. Mourou, "Laser ablation and micromachining with ultrashort laser pulses", *IEEE J. Quant. Electron.* 33 1706 (1997).
- [135] S. Musazzi, and U. Perini, *Laser-induced breakdown spectroscopy, in Theory and Applications.* 2014, Springer.
- [136] S. S. Harilal, J. R. Freeman, P. K. Diwakar, and A. Hassanein., *Femtosecond laser ablation: Fundamentals and applications.*" In *Laser-Induced Breakdown Spectroscopy*, Springer Berlin Heidelberg, (2014).
- [137] K. K. Anoop, S. S. Harilal, R. Philip, R. Bruzzese, and S. Amoruso, "Laser fluence dependence on emission dynamics of ultrafast laser induced copper plasma", *J. Appl. Phys.* 120, 185901 (2016).
- [138] T. J. Kelly, T. Butler, N. Walsh, P. Hayden, and J. T. Costello., "Features in the ion emission of Cu, Al, and C plasmas produced by ultrafast laser ablation", *Phys. Plasmas* 22, 123112 (2015).
- [139] T. Donnelly, J. G. Lunney, S. Amoruso, R. Bruzzese, X. Wang, and X. Ni., *J.* "Dynammmics of the plumes produced by ultrafast laser ablation of metals", *Appl. Phys.* 108, 043309 (2010).
- [140] V. Gordienko, I. Lachko, A. Rusanov, A. Savel'Ev, D. Uryupina, and R. Volkov, "Enhancement production of fast multi-charged ions from plasmas formed at cleaned surface by femtosecond laser pulse", *Appl. Phys. B* 80, 733 (2005).



- [141] Z. Zhang, P. A. VanRompay, J. A. Nees, and P. P. Pronko, “Multi-diagnostic comparison of femtosecond and nanosecond pulsed laser plasmas”, *J. Appl. Phys.* 92, 2867 (2002).
- [142] O. Chutko, V. Gordienko, I. Lachko, B. Mar’in, A. Savel’ev, and R. Volkov, “High-energy negative ions from expansion of high-temperature femtosecond laser plasma”, *Appl. Phys. B* 77, 831 (2003).
- [143] J. Krása, K. Jungwirth, S. Gammino, E. Krouský, L. Láska, A. Lorusso, V. Nassisi, M. Pfeifer, K. Rohelna, L. Torrisi, and J. Ullschmied, “Partial currents of ion species in an expanding laser-created plasma”, *Vacuum* 83, 180 (2008).
- [144] M. Ye and C. P. Grigoropoulos, “Time-of-flight and emission spectroscopy study of femtosecond laser ablation of titanium”, *J. Appl. Phys.* 89, 5183 (2001).
- [145] B. Verhoff, S. S. Harilal, J. R. Freeman, P. K. Diwakar, and A. Hassanein. “Dynamics of femto- and nanosecond laser ablation plumes investigated using optical emission spectroscopy”, *J. Appl. Phys.* 112, 093303 (2012).
- [146] D. Grojo, J. Hermann, and A. Perrone, “Plasma analysis during femtosecond laser ablation of Ti, Zr, and Hf”, *J. Appl. Phys.* 97, 063306 (2005).
- [147] Y. Okano, K. Oguri, T. Nishikawa, and H. Nakano, “Observation of femtosecond-laser-induced ablation plumes of aluminum using space- and time-resolved soft x-ray absorption spectroscopy”, *Appl. Phys. Lett.* 89, 221502 (2006).
- [148] B. Verhoff, S. Harilal, and A. Hassanein, “Angular emission of ions and mass deposition from femtosecond and nanosecond laser-produced plasmas”, *J. Appl. Phys.* 111, 123304 (2012).
- [149] S. Nolte, C. Momma, H. Jacobs, A. Tünnermann, B. N. Chichkov, B. Wellegehausen, and H. Welling, “Ablation of metals by ultrashort laser pulses”, *JOSA B* 14, 2716 (1997).
- [150] E. Gamaly, A. Rode, B. Luther-Davies, and V. Tikhonchuk, “Ablation of solids by femtosecond laser: Ablation mechanism and ablation thresholds for metals and dielectrics”, *Phys. Plasmas* 9, 949 (2002).
- [151] X. Zeng, X. Mao, R. Greif, and R. Russo, “Experimental investigation of ablation efficiency and plasma expansion during femtosecond and nanosecond laser ablation of silicon”, *Appl. Phys. A* 80, 237 (2005).
- [152] A. Semerok, C. Chaléard, V. Detalle, J.-L. Lacour, P. Mauchien, P. Meynadier, C. Nouvellon, B. Salle, P. Palianov, M. Perdrix, and G. Petite, “Experimental investigation

- of laser ablation efficiency of pure metals with femto, pico, and nanosecond pulses”, *Appl. Surf. Sci.* 138, 311 (1999).
- [153] B. Le Drogoff, J. Margot, M. Chaker, M. Sabsabi, O. Barthelemy, T. W. Johnston, S. Laville, F. Vidal, and Y. Von Kaenel. “Temporal characterization of femtosecond laser pulses induced plasma for spectrochemical analysis of aluminum alloys”, *Spectrochim. Acta part B* 56, 987 (2001).
- [154] N. Bateman, P. Sullivan, C. Reichel, J. Benick, and M. Hermle, High quality ion implanted boron emitters in an interdigitated back contact solar cell with 20% efficiency, *Energy Procedia* 8, (2011) 509.
- [155] C. W. Jang, J. H. Kim, D. H. Lee, D. H. Shin, S. Kim, S. H. Choi, E. Hwang, and R. G. Elliman, Effect of stopping-layer-assisted boron-ion implantation on the electrical properties of graphene: Interplay between strain and charge doping, *Carbon* 118, (2017) 343.
- [156] M. D. Ynsa, F. Agulló-Rueda, N. Gordillo, A. Maira, D. Moreno-Cerrada, and M. A. Ramos, Study of the effects of focused high-energy boron ion implantation in diamond, *Nucl. Instrum. Meth. B.* 404, (2017) 207.
- [157] T. Hamaguchi, H. Nakajima, M. Ito, J. Mitomo, S. Satou, N. Fuutagawa, and H. Narui, Lateral carrier confinement of GaN-based vertical-cavity surface-emitting diodes using boron ion implantation, *Jpn. J. Appl. Phys.* 55, (2016) 122101.
- [158] D. Okamoto, M. Sometani, S. Harada, R. Kosugi, Y. Yonezawa, and H. Yano, Improved channel mobility in 4H-SiC MOSFETs by boron passivation, *IEEE Electron Device Lett.* 35, (2014) 1176.
- [159] S. Miyazaki, K. Morino, and M. Hirose, Influence of boron and fluorine incorporation on the network structure of ultrathin SiO<sub>2</sub>, *Sol. St. Phen.* 76, (2001) 149.
- [160] Y. C. Zhu, S. Ohtani, Y. Sato, and N. Iwamoto, Influence of boron ion implantation on the oxidation behavior of CVD-SiC coated carbon-carbon composites, *Carbon* 38, (2000) 501.
- [161] Y. C. Zhu, K. Fujita, N. Iwamoto, H. Nagasaka, and T. Kataoka, Influence of boron ion implantation on the wear resistance of TiAlN coatings, *Surf. Coat. Technol.* 158, (2002) 664.

- [162] B. Todorović-Marković, I. Draganić, D. Vasiljević-Radović, N. Romčević, M. Romčević, M. Dramićanin, and Z. Marković, Synthesis of amorphous boron carbide by single and multiple charged boron ions bombardment of fullerene thin films. *Appl. Surf. Sci.* 253, (2007) 4029.
- [163] I. Draganic, T. Nedeljkovic, J. Jovovic, M. Siljegović, and A. Dobrosavljević, Multiply charged ions from solid substances with the mVINIS Ion Source. In *J. Phys. Conf. Ser.* 58, (2007) 427.
- [164] R. Pincak, and M. Pudlak. *Progress in Fullerene Research*. Milton Lang, Nova Science Publisher (2007) 375-388.
- [165] A. Kalijadis, Z. Jovanović, M. Laušević, and Z. Laušević, The effect of boron incorporation on the structure and properties of glassy carbon. *Carbon*, 49, (2011) 2671.
- [166] Y. Saitoh, K. Ohkoshi, and W. Yokota, Production of multiply charged metallic ions by compact electron cyclotron resonance ion source with SF<sub>6</sub> plasma. *Rev. Sci. Instrum.* 69, (1998) 703.
- [167] T. N. Horsky, Indirectly heated cathode arc discharge source for ion implantation of semiconductors." *Rev. Sci. Instrum.* 69, (1998) 840.
- [168] M. H. A. Shaim, and H. E. Elsayed-Ali, Characterization of laser-generated aluminum plasma using ion time-of-flight and optical emission spectroscopy, *J. Appl. Phys.* 122, (2017) 203301.
- [169] P. Pronko, P. VanRompay, Z. Zhang, and J. Nees, Isotope enrichment in laser-ablation plumes and commensurately deposited thin films, *Phys. Rev. Lett.* 83, (1999) 2596.
- [170] W. Lien, A. P. Pisano, D. Tsai, Jr-H. He, and D. G. Senesky. "Extreme temperature 4H-SiC metal-semiconductor-metal ultraviolet photodetectors." *Solid-State Device Research Conference (ESSDERC), 2012 Proceedings of the European, IEEE*, pp. 234-237. 2012.
- [171] A. Modic, "Novel Interface Trap Passivation and Channel Counter-doping for 4H-SiC MOSFETs". Dissertation, 2015.
- [172] K. Piskorski, and H. M. Przewlocki. "The methods to determine flat-band voltage  $V_{FB}$  in semiconductor of a MOS structure." *MIPRO, 2010 Proceedings of the 33rd International Convention, IEEE*, pp. 37-42. 2010.

## APENDIX A

### VACUUM SYSTEM

#### **Pumping down the system**

To pump down the system do the followings:

1. Tighten all the flanges so that there is no leak. Close the gate valve.
2. First turn on the mechanical pump and, after a short delay, the turbo pump. Monitor the speed of the turbo pump during start up.
3. Wait 15 minutes before turning on the pressure gauge monitor. This gauge does not work above  $10^{-3}$  Torr.
4. Leave the whole system to be pumped down by the turbo for 1-2 hours.
5. In ~ 2 hour the pressure should reach  $\sim 10^{-6}$  Torr.
6. Leave the turbo and mechanical pumps on during the experiment.
7. If it requires bake-out, use light bulbs around the vacuum chamber symmetrically and use aluminum foil to wrap the system.

#### **Opening the system**

1. Turn off the Turbo pump then mechanical pump.
2. Leave the chamber for 20 minutes and then open the gate valve slowly.

## APPENDIX B

### MULTICHARGED ION SOURCE

The multicharged ion source developed at ODU is shown in Fig B. 1. This ion source comprises a laser ion source and a separate spark discharge system to amplify the laser plasma ionization.



Fig. B. 1 The MCI system with its transport line components.

The energy analyzer, used to detect the multicharged ions, shown in Fig B. 2. Are composed of a Faraday cup, suppressor electrode and three-grid retarding field ion energy analyzer.

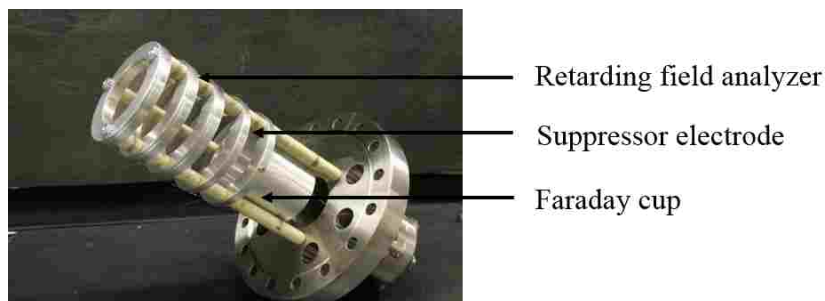


Fig. B.2 The ion energy analyzer

The schematic of the energy analyzer is shown in Fig. B.3.

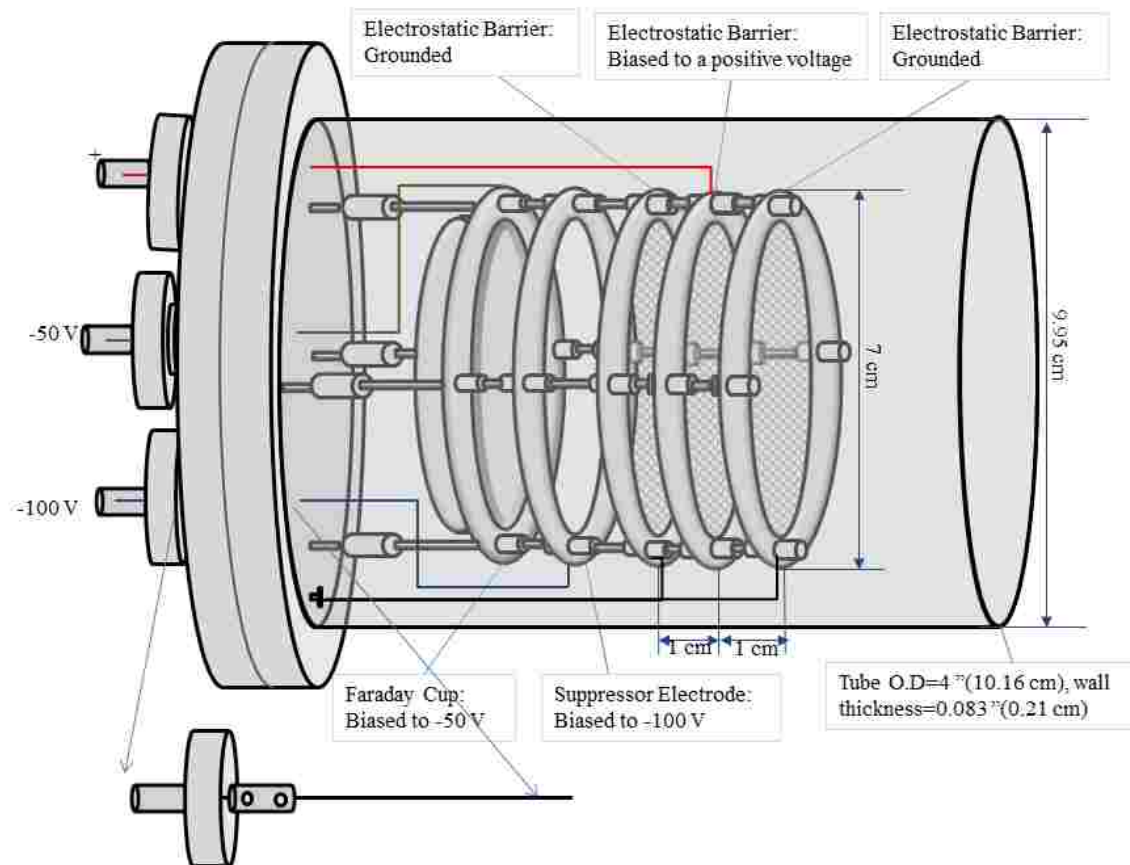

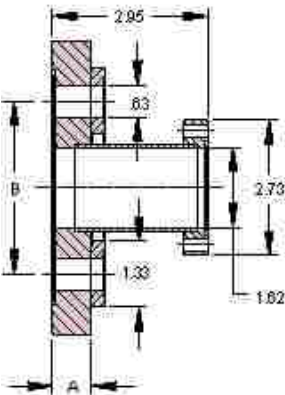
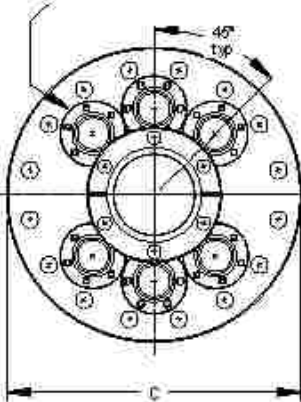


Fig. B.3 Schematic of the faraday cup.

The energy analyzer is built on a standard CF flange from Kurt J. Lesker. Fig. B.4 shows the image from the company website and the specifications.



1-1/3" Del-Seal™ CF flanges, tapped, typical 6 places

**Features**

- UHV rated to  $1 \times 10^{-13}$
- High temperature rated to 450°C
- OFE Copper or optional Viton® elastomer gaskets
- Clearance bolt holes
- Conflat® compatible design
- Standard matte finish
- Includes six straight-in tapped mini flanges around a 2-3/4" Del-Seal CF port
- Assemblies are fully electropolished

**Specifications**

<b>Material</b>	
Flanges	304ss
Gaskets	OFE copper
Bolts	300ss and 300ss silver plated
<b>Fastening</b>	
Bolt Type	Hexagonal, 12-point or socket head
Nut Type	Hexagonal or two hole plate nuts
Size / Torque	See individual flange specs.
Vacuum Range	$1 \times 10^{-13}$
Leak Test	$2 \times 10^{-10}$ cc/sec of He
Temperature Range	-200°C to 450°C

Fig. B.4 Image and schematic of the CF flange used from Kurt J. Lesker

DESCRIPTION	A	B	C	WT LB	Part Number	UOM	List Price	Net Price	Lead Time
6" DEL-SEAL FLANGE	0.78	3.50	5.97	7	409006 REF# MAF500-6-133T	EACH	\$680.00	\$680.00	25 days

Link: <http://www.mdcvacuum.com/DisplayProductContent.aspx?d=MDC&p=m.1.2.8.1>

The 6" flange bought from Kurt. J. Lesker is customized in the machine shop to build the Faraday cup. Fig. B.5 shows the drawing of the design.

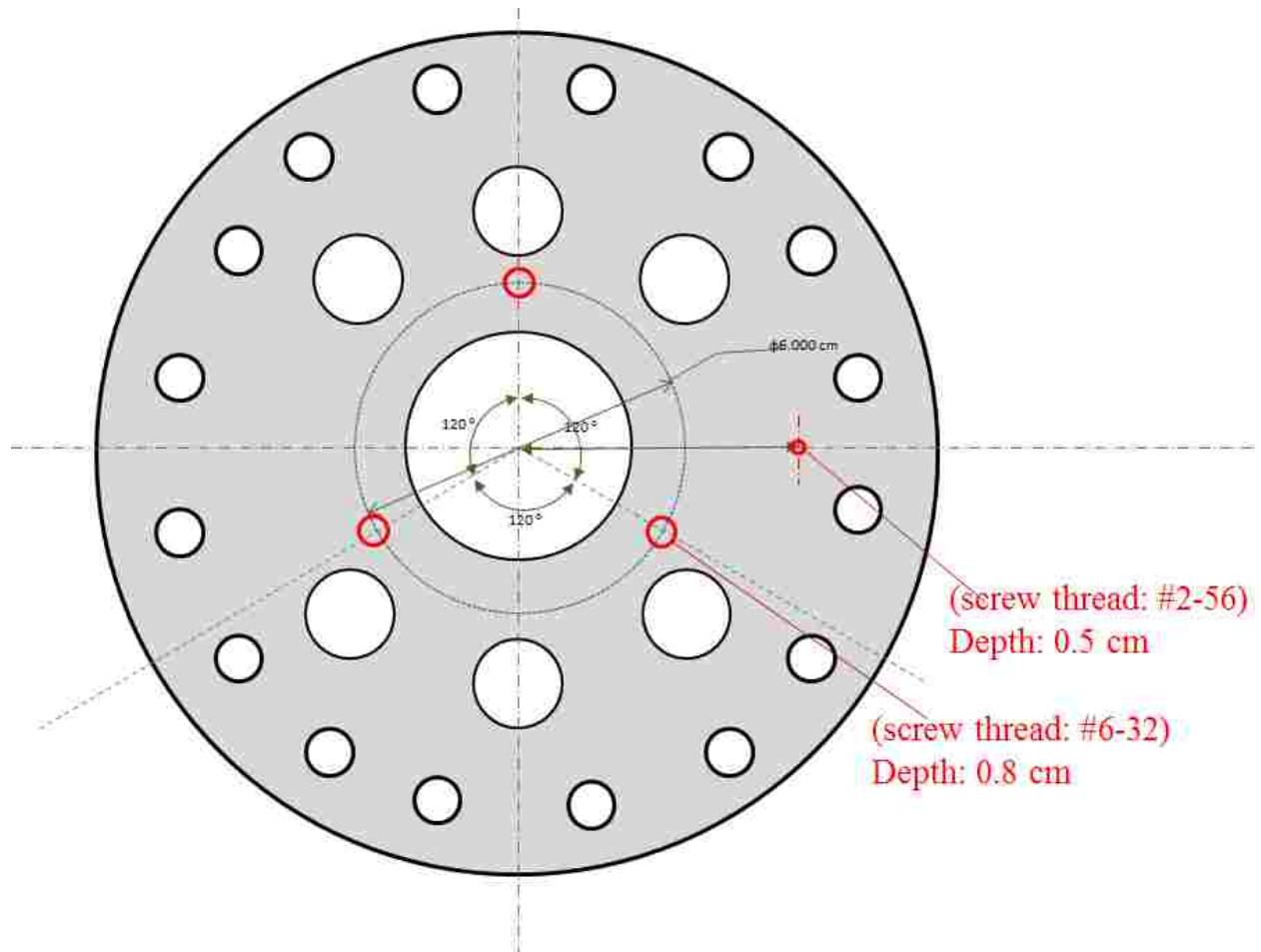


Fig. B.5 Schematic of the top view of the customized CF flange.



Several components are machined to develop the FC. Following figures, Fig. B.6 – B.8 shows the design parameters of the components. All the components are made of aluminum.

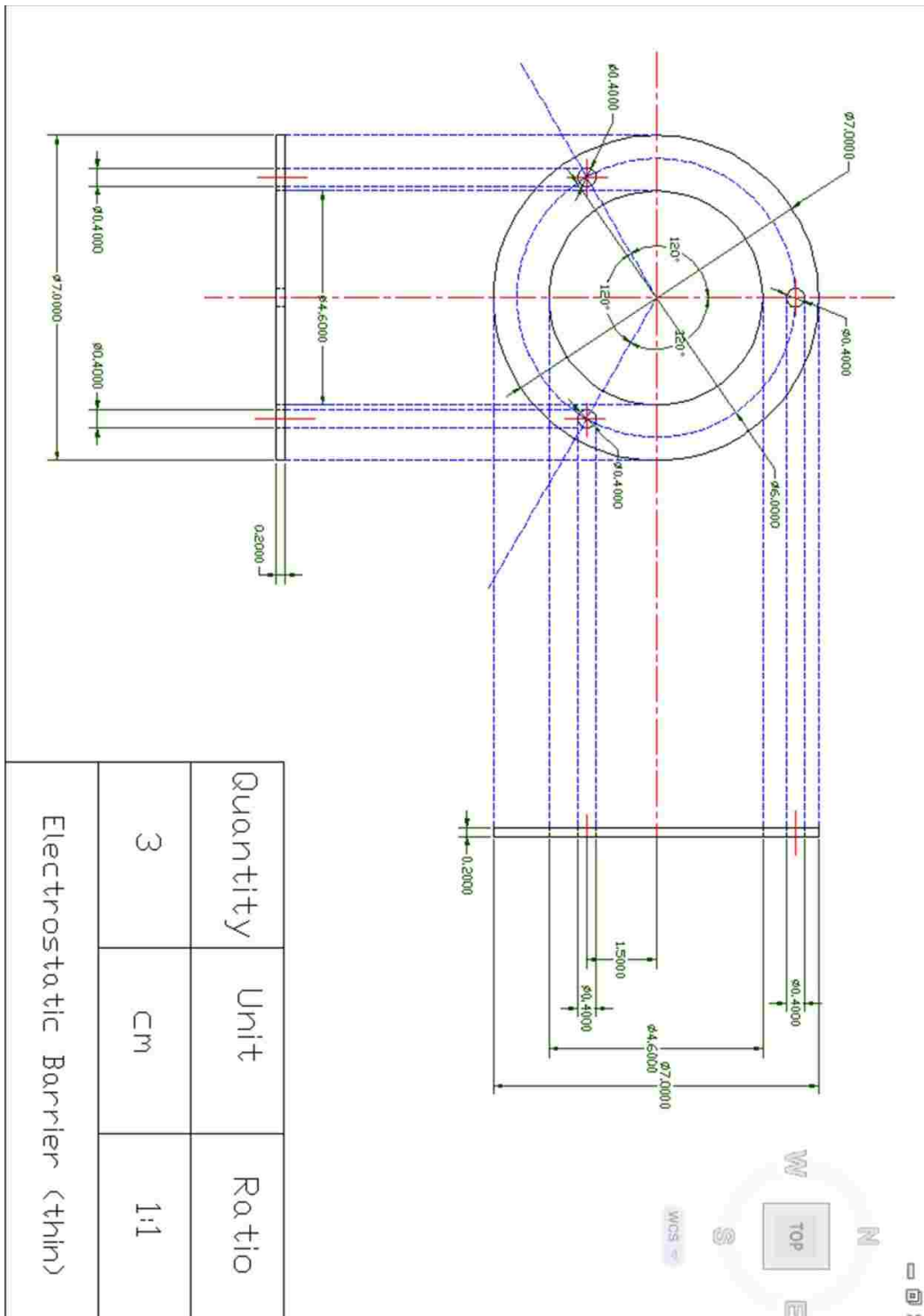


Fig. B.6 AutoCAD schematic of the FC components.

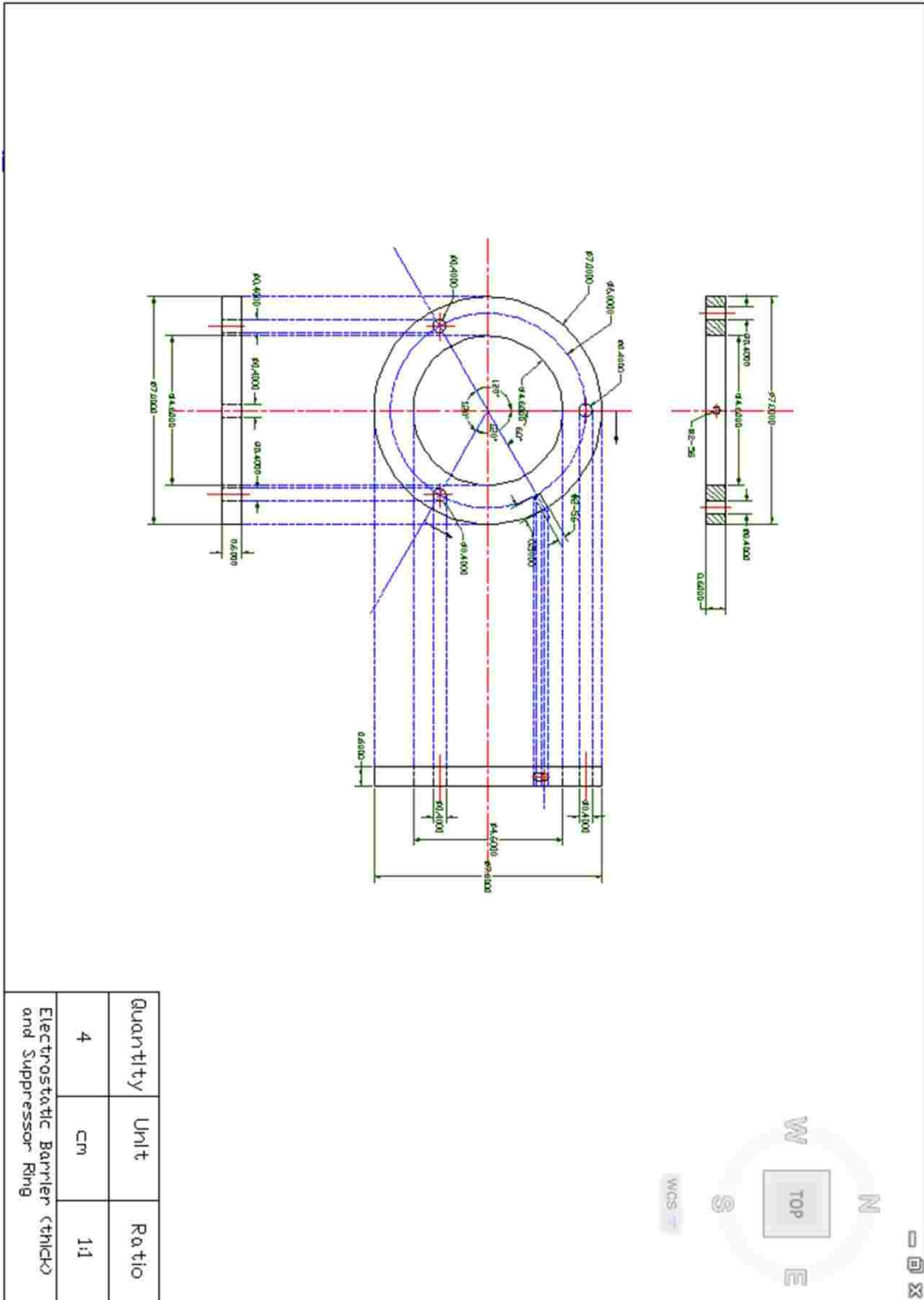
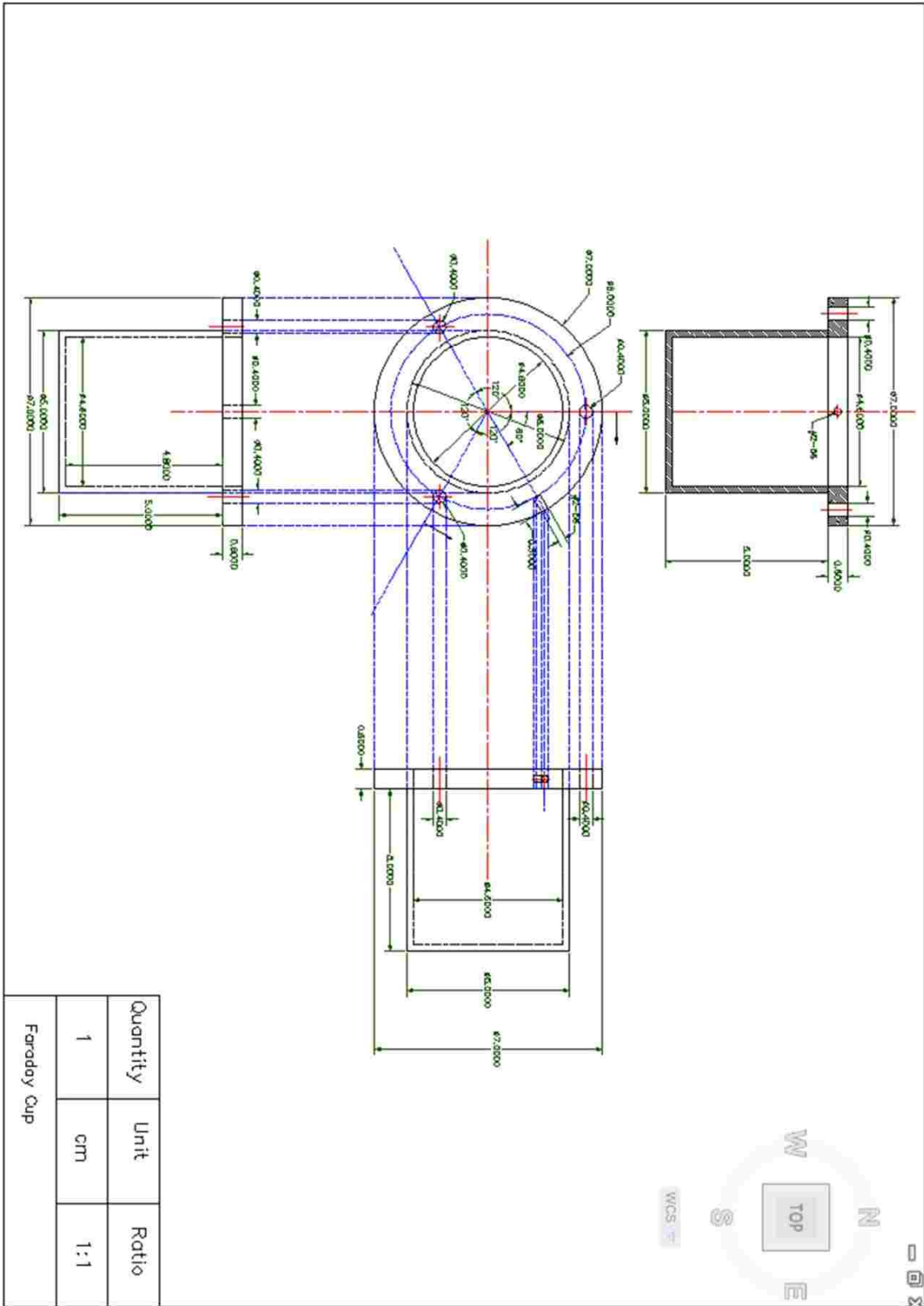


Fig. B.7 AutoCAD schematic of the FC components.



.Fig B.8 AutoCAD schematic of the FC components

Fig B.9. shows the three electrode einzel lens that focuses the ion beam without changing the ion energy.



Fig. B.9 Einzel lens.

The AutoCAD design done by Prof. Michael Korwin-Powloski and Andranik Sarkissian of the einzel lens is given in Fig. B.10.

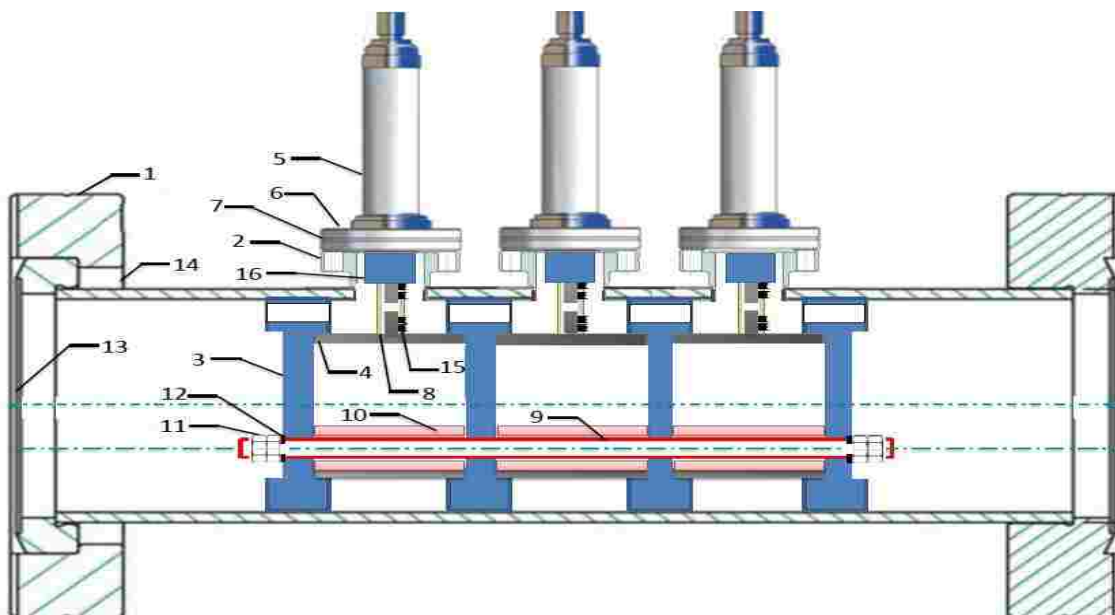


Fig. B.10 Design of the einzel and its components. 1. CF Full Nipple; 2. 1-1/3" OD CF Flanges; 3. Ceramic spacer; 4. 304 Stainless steel 2"OD seamless tubes; 5. Power Feedthroughs CF Flanged 20 000V; 6. 8-32x3/4" Bolt & Nut Sets; 7. Annealed Copper Gaskets 1-1/3" CF; 8. Barrel Connector for 0,120" wire; 9. UNC 1/4" stainless steel connecting rods; 10. Ceramic isolating tubes; 11. Stainless steel hex nuts; 12. Stainless steel washers; 13. Annealed copper gaskets 6"CF; 14. Stainless steel hex bolt/plate -nut sets; 15. Socket head screws 4-40; 16. Isolating tube.

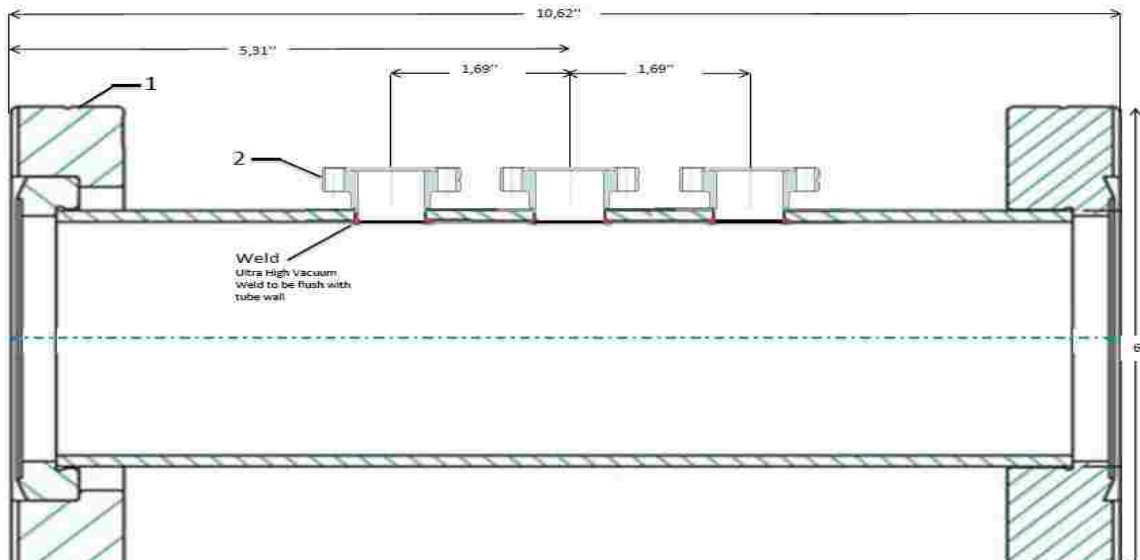


Fig. B.11 AutoCAD drawing of the CF flange.

The required components for the einzel lens are:

1. CF Full nipple 304L-SS Kurt J. Lesker FN-0600 Qty = 1
2. 1 1/3" OD CF flange tapped 304L-SS Kurt J. Lesker F0133X075NTW Qty = 3
3. Seamless stainless-steel tube electropolished 304/304L Qty = 3
4. Connector pin 304L-SS Qty = 3
5. Power feedthrough CF flanged 20,000 V, Kurt J. Lesker, Product # EFT2011092, Qty = 3
6. Custom ceramic spacer (Fig A.12 shows below)

The AutoCAD schematic of the ceramic spacer is shown in Fig. B.12.

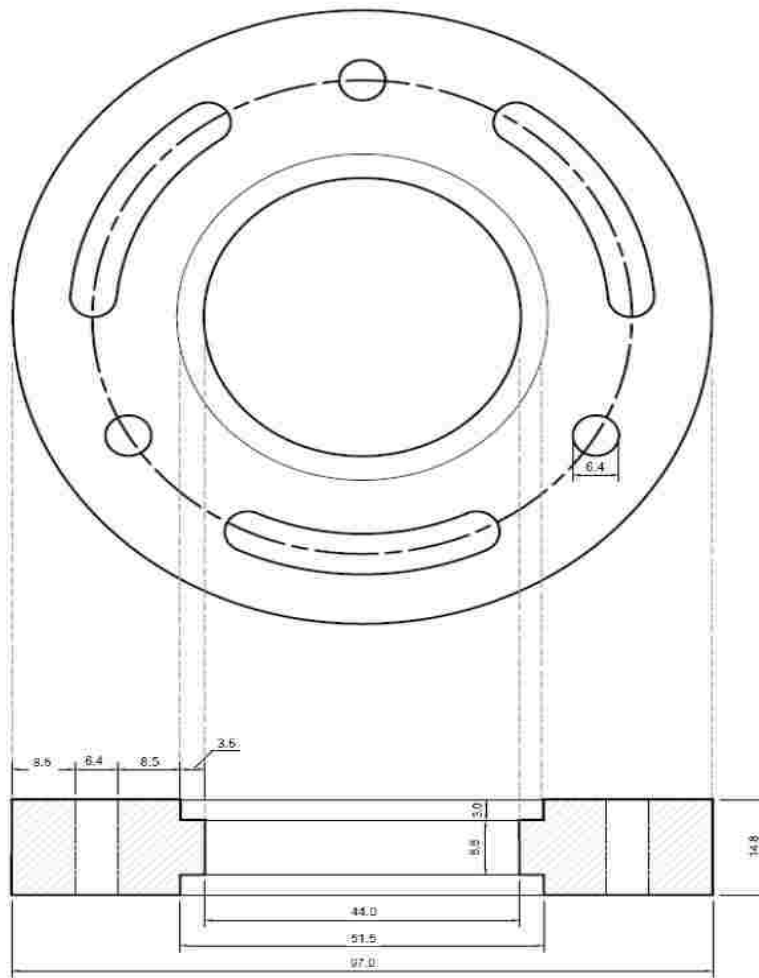


Fig. B.12 AutoCAD drawing of customized ceramic Spacer

Cylindrical ion deflector selects ions according to the energy/charge ratio. Fig B.13. shows the image of the cylindrical ion deflector during construction stage.

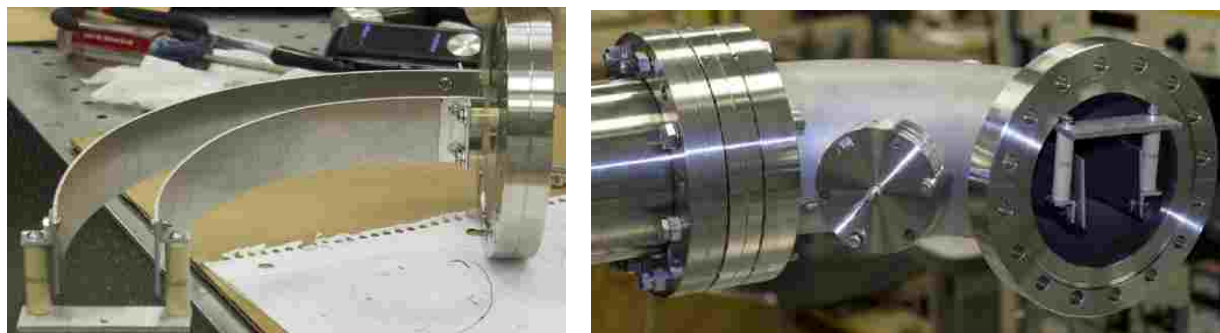


Fig. B.13 Cylindrical ion deflector.

The MCI system is modified to implant ions without neutral deposition. A pair of deflection plates deflect the ions out of neutral beam path. The schematic and the image of the system is shown in Fig. B.14.

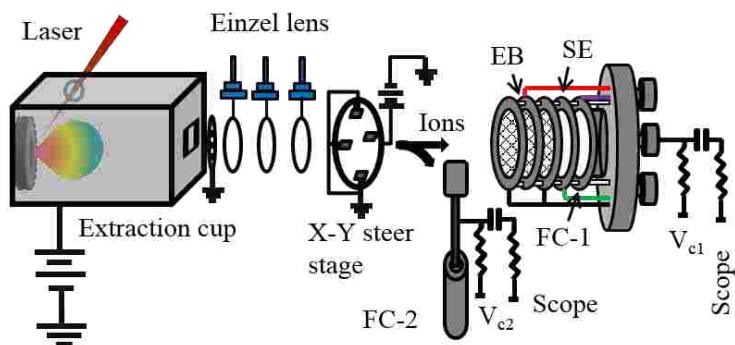


Fig. B.14 Schematic and image of the MCI system with ion deflection plates to avoid neutral deposition.

## APPENDIX C

### ND:YAG NANOSECOND LASER OPERATION AND MAINTENANCE

The Nd:YAG nanosecond laser has the following specifications; wavelength 1064 nm, pulse duration 7.4 ns, maximum laser energy 600 mJ/pulse, repetition rate 10 Hz. The below procedures should be followed for proper operation and maintenance of the laser.

1. To turn ON the system, rotate the key to ON position, press “start/stop” and wait for 30 minutes.
2. Press “shutter” to get laser output.
3. To turn OFF, turn off the “shutter” first then start/stop button and rotate the key to OFF position.
4. The cooling water should be changed every six-month, cooling water was last changed on July 18, 2018. To change the Colling water, open the side frame of the laser power supply.
5. Logbook should be maintained to follow the laser energy change over time.
6. We have spare “flash lamp” for the Nd:YAG laser.
7. One problem that happened earlier is the with “Marx Bank”. If the problem arises, Q-switched will be turn ON but the “shutter does not work”. We tried to open the shutter manually, but there was no laser beam. The Marx bank was replaced.



## APPENDIX D

### Ti:SAPPHIRE FEMTOSECOND LASER

The femtosecond laser system has a pumping oscillator called the Tsunami and ReGen amplifier called Darwin. The ReGen amplifier consists of a stretcher, amplifier, and compressor. We do have two chillers - both work to cool the pumping oscillator and the ReGen amplifier. The procedure to turn on the oscillator and amplifier is given below. The oscillator chiller, pumping oscillator and ReGen are shown in Fig. D.1.

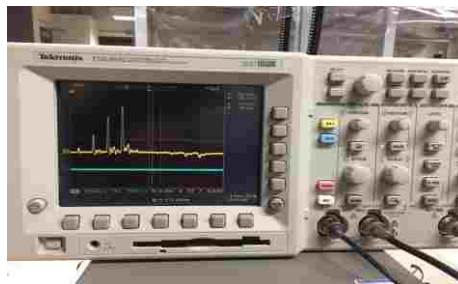


Fig. D.1. (a) power supply with chiller, (b) chiller temperature, (c) chiller for regen and oscillator and (d) pumping oscillator, oscillator, and regen.

The other components of the Ti:Sapphire femtosecond laser are shown in Fig. D.2.



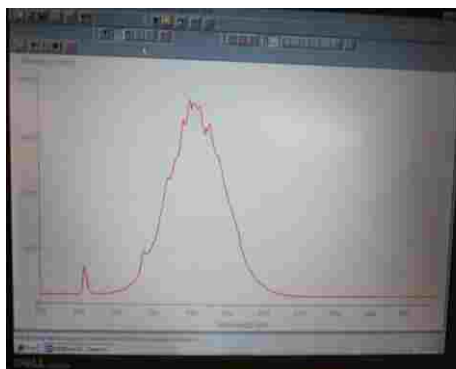
(a)



(b)



(c)



(d)

Fig. D.2 (a) Pulse generator, (b) oscilloscope, (c) Q-switched controller, (d) mode locked output in the computer screen.

### Procedure to Turn-on the laser

1. Turn on power supply in the big chiller by rotating the key properly.
2. Check the water level and allow the chiller to cool down the oscillator. Initially, a red LED will be on the control panel, wait some time until the red LED is off and a green LED comes on.
3. Keep the temperature of the smaller chiller around 23° C.
4. Turn on the signal generator and oscilloscope.
5. Turn on the Q-switch controller, it will ask to set the power as 5W. Increase the power to 5 W.

6. Open the software in the computer. In the software initially, we will see some spectrum from the incandescent light of room. To remove these, set the “auto scale” as minimum 750 nm.
7. In the controller, set PRF values for external. The current will be 29 mA and the temperature will be 22.3°C.
8. Turn on the laser shutter
9. The system is an active mode lock system. It should be in mode lock automatically. If not, adjust the knob initially to move the spectrum to the left up to value 729 nm and then lightly hit the table to make it mode lock. Rotate the other knob the move the center of the spectrum to 793 nm.
10. Mode locking will provide 1 KHz repetition rate.
11. Move the switch to enable the output.
12. Turn on the power meter

**Procedure to turn off the laser:**

1. Turn of the shutter and rotate the key.
2. Turn off the Q-switched controller.
3. Turn of the software in the computer
4. Turn off the chiller
5. Turn off the oscilloscope and power meter.

## Beam path in the ReGEN

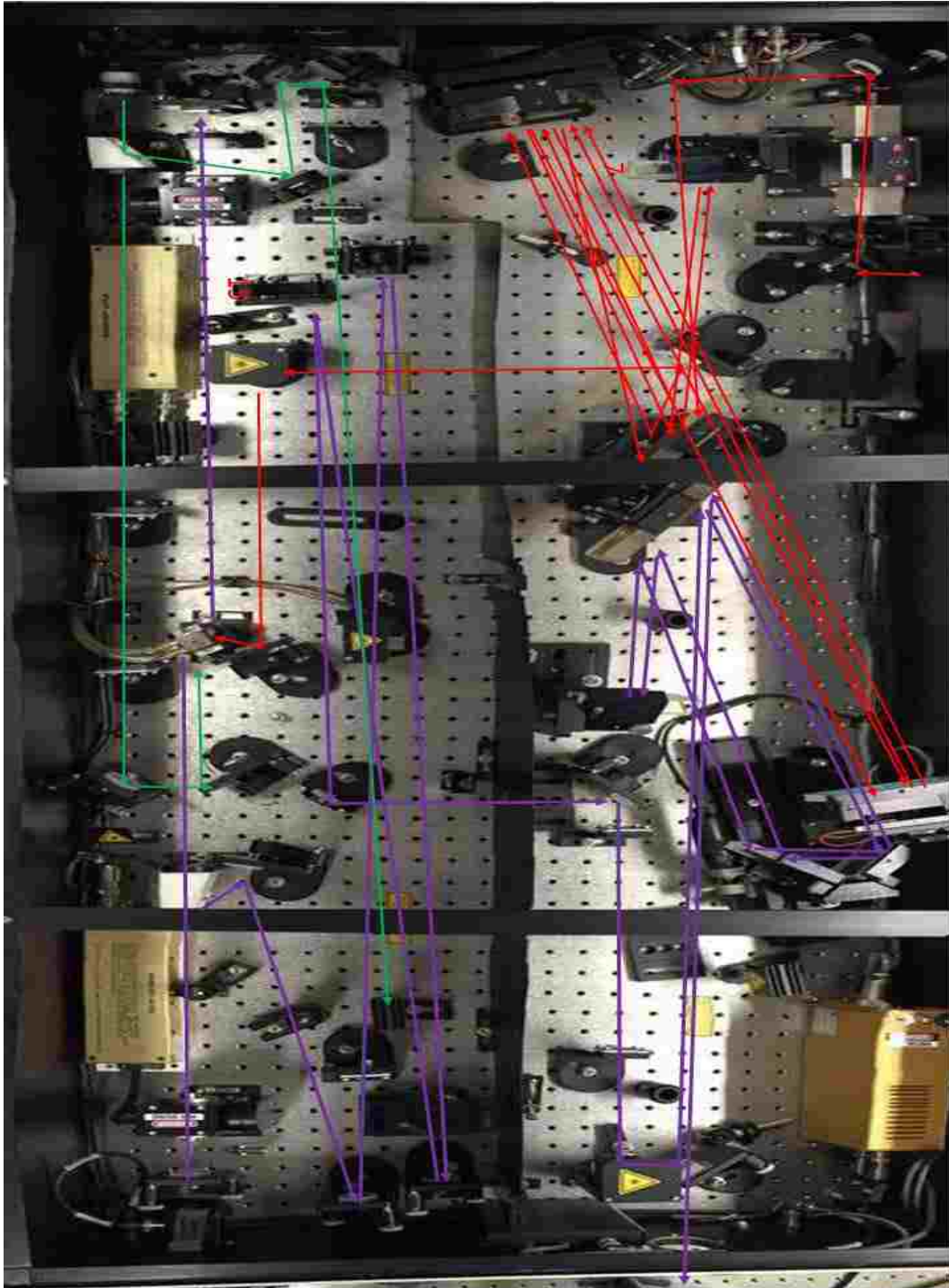


Fig. D.3 Beam path in the Regen

Beam spot on different optics of the Regen.

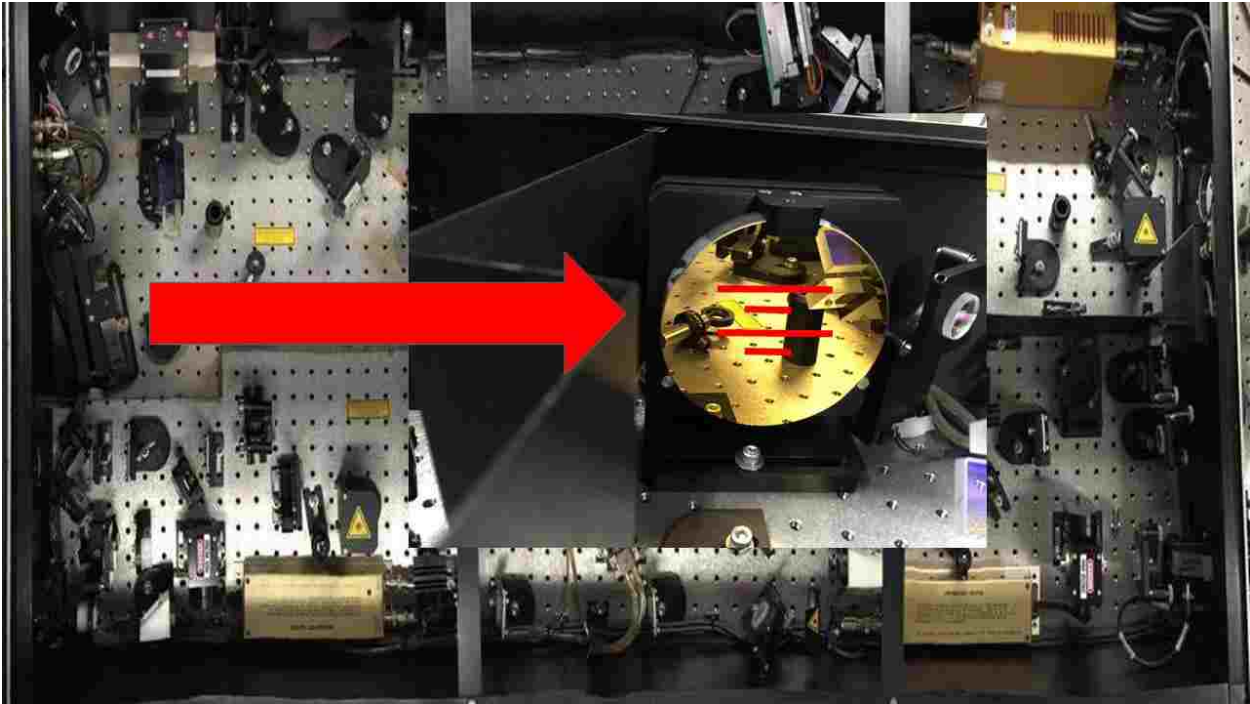


Fig. D.4 Beam shape observed in the concave mirror (compressor).

Following figures shows the beam shape observed in different mirrors during laser operation.

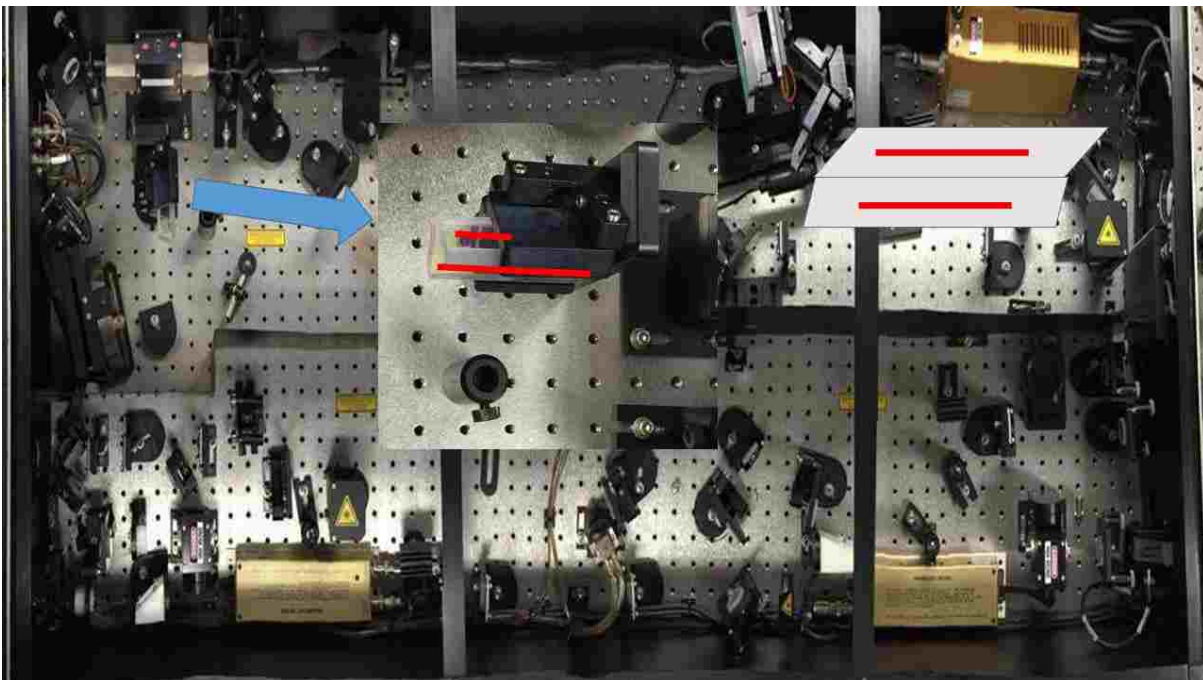


Fig. D.5 Beam shape observed in the compressor Retro-reflector

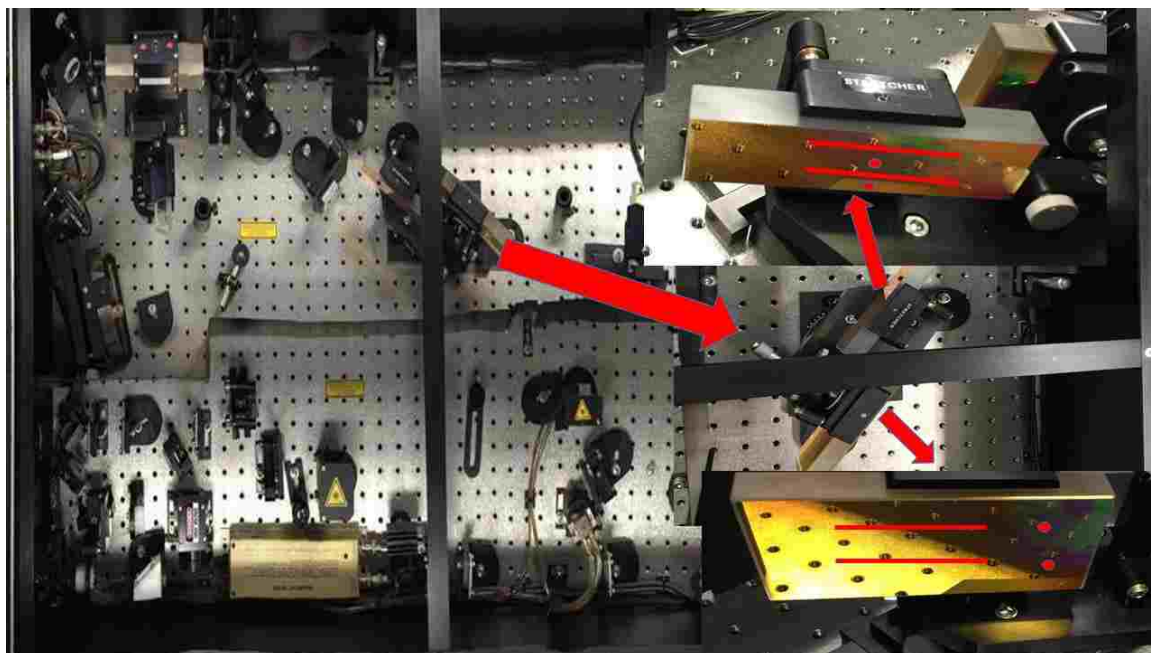


Fig. D.6 Beam shape in the stretcher grating

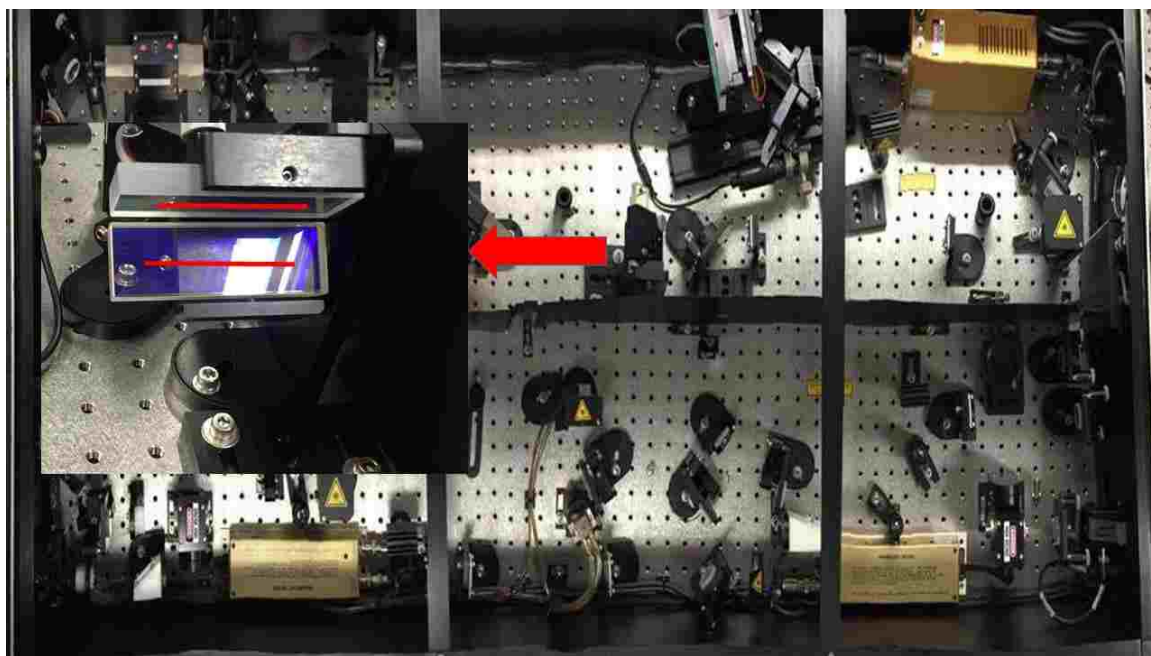


Fig. D.7 Beam shape in the retro-reflector mirror (compressor).

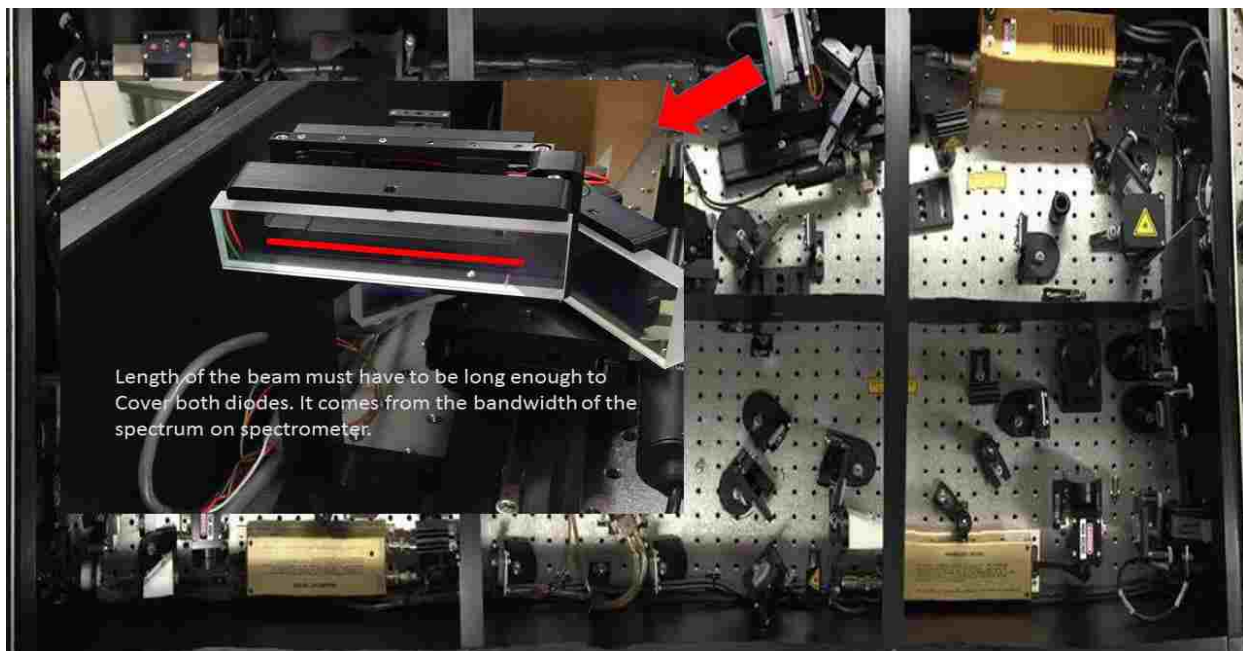


Fig. D.8 Beam shape on the mirror (stretcher).

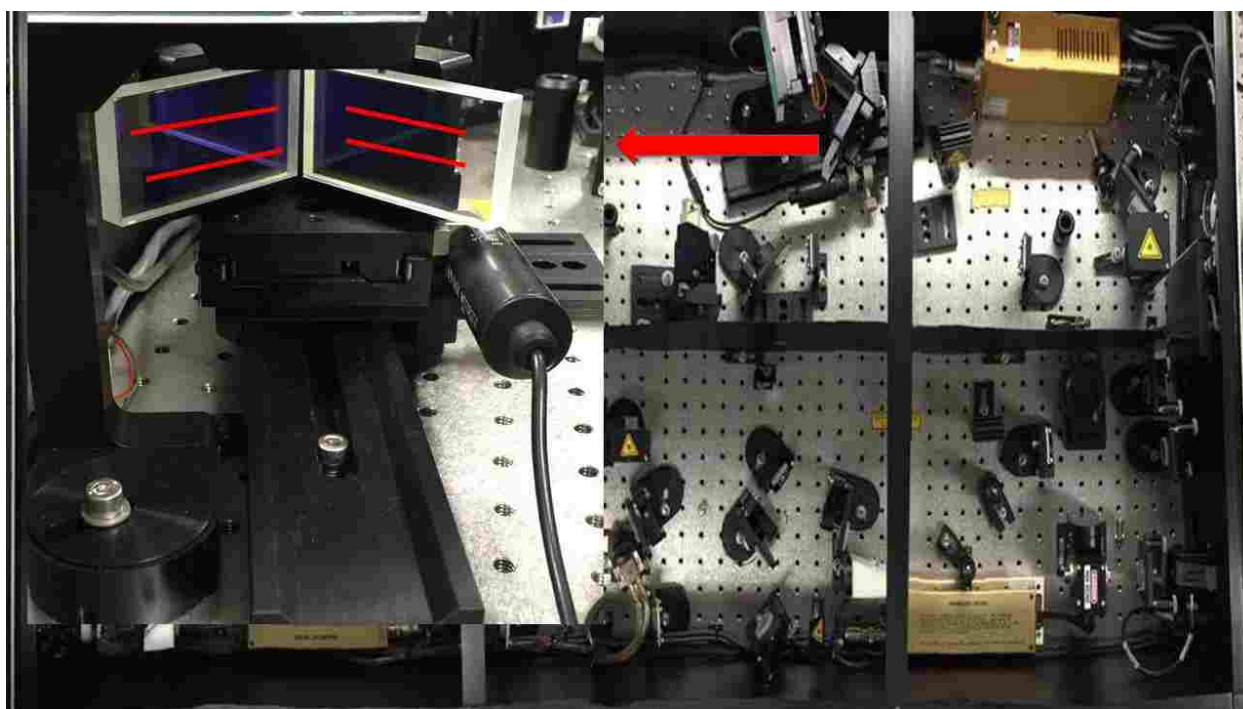


Fig. D.9 Beam shape on the mirror (stretcher)

## APPENDIX E

## ION ENERGY DISTRIBUTION MEASUREMENT

The procedure to estimate the energy distribution of the ion from their TOF is discussed below. First draw a curve fit using peak fitting option in Origin-lab 9.1 software. Separate the TOF signal for individual MCI using the selected peak position (red curve shown in Fig. E.1. for  $\text{Al}^{4+}$ ) obtained by Origin-lab. Integrating the area gives us the total charge for that MCI.

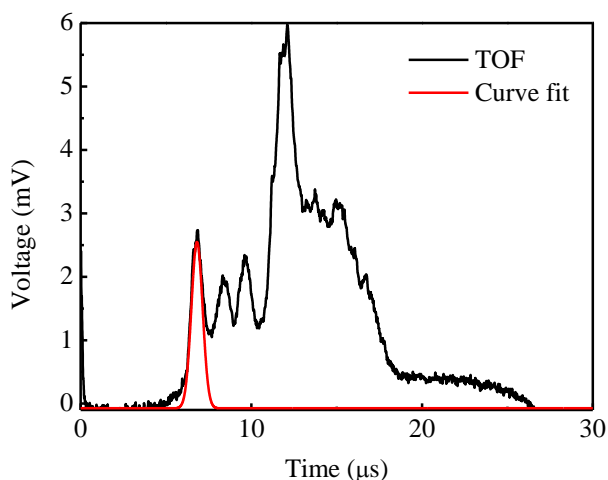


Fig. E.1 Deconvolution of the TOF spectrum.

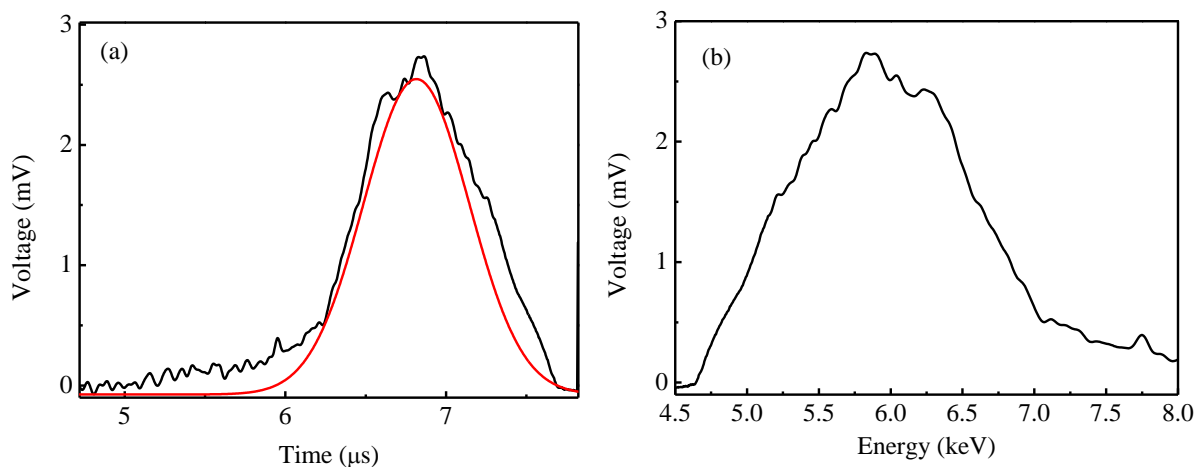


Fig. E.2 Extension of the signal to the base line, (b) energy distribution of the  $\text{Al}^{4+}$ .



The Fig. E.1. above shows an example of how we calculate the total charge of  $Al^{4+}$ . For simplicity we show the curve fit for  $Al^{4+}$ . The curve for  $Al^{4+}$  has TOF distribution from  $\sim 5.7$  to  $\sim 7.7$   $\mu s$ . Integrating the curve over this time range and dividing the integral by the scope resistance of  $50 \Omega$  gives the total charge of  $Al^{4+}$ . Integrating within the TOF for individual MCIs obtained from the graph directly without curve fitting can be also used and gives total charge for each MCI about similar to those from the curve fit with only  $\sim 5$  % deviation which is within the experimental error.

Energy distribution is calculated using the following steps:

1. Curve fit the desired charge state to get the time range of the peak.
2. Extend the signal of the overlapped region up to the base line.
3. Select the time range and create another column in Origin Lab.
4. Convert the time scale to energy, eV.
5. Plot energy vs voltage curve.

## APPENDIX F

### FABRICATION OF SiC MOSCAP

The following process is performed to fabricate the SiC-MOSCAP.

1. The SiCs are cleaned with RCA + HF to remove the organic and ionic contaminations.
2. Boron and barium shallow implantation are performed without neutral boron deposition. For boron implantation, at laser fluence of  $135 \text{ J/cm}^2$ , it takes 2 hours to grow 1 nm of boron film and 3 minutes to make 1 nm barium film. The sample holder is  $\sim 3.75 \text{ cm}$  away from the center axis and 150 V is applied to deflecting plates.
3. The samples are annealed at  $950 \text{ }^\circ\text{C}$  for 30 minutes.
4. The film thickness is measured using ellipsometer (M2000 J.A. Woollam Co.).
5.  $\text{SiO}_2$  layer was grown by sputtering. For 200 W RF power with  $\text{SiO}_2$  target, it takes 60 minutes to grow  $\sim 47 \text{ nm}$  of  $\text{SiO}_2$ . The oxygen flow rate is 6 ccm and argon flow rate is 20 ccm. Nitrogen is purged to protect the vacuum pumps. Substrate was heated to  $250^\circ\text{C}$ .
6. During  $\text{SiO}_2$  sputtering, if the system stops automatically and RF power supplies shows high reflected power, from the previous observation, I can say it's possible that the  $\text{SiO}_2$  has another crack.  $\text{SiO}_2$  target has several cracks but it still working.
7. Aluminum gate contacts are sputtered at a rate of  $0.5 \text{ \AA/min}$ .
8. CV characterization is performed using Agilent B1500A Semiconductor Device Parameter Analyzer.
9. UV-Vis spectroscopy is performed using LAMBDA 45 UV/Vis System (PerkinElmer).
10. We sent the samples for SIMS and GAXRD to NC State University and are waiting for the results.

APPENDIX G

XY DEFLECTING STAGE FLANGE DESIGN

The AutoCAD drawing the XY deflecting stage is shown below in Fig. G.1

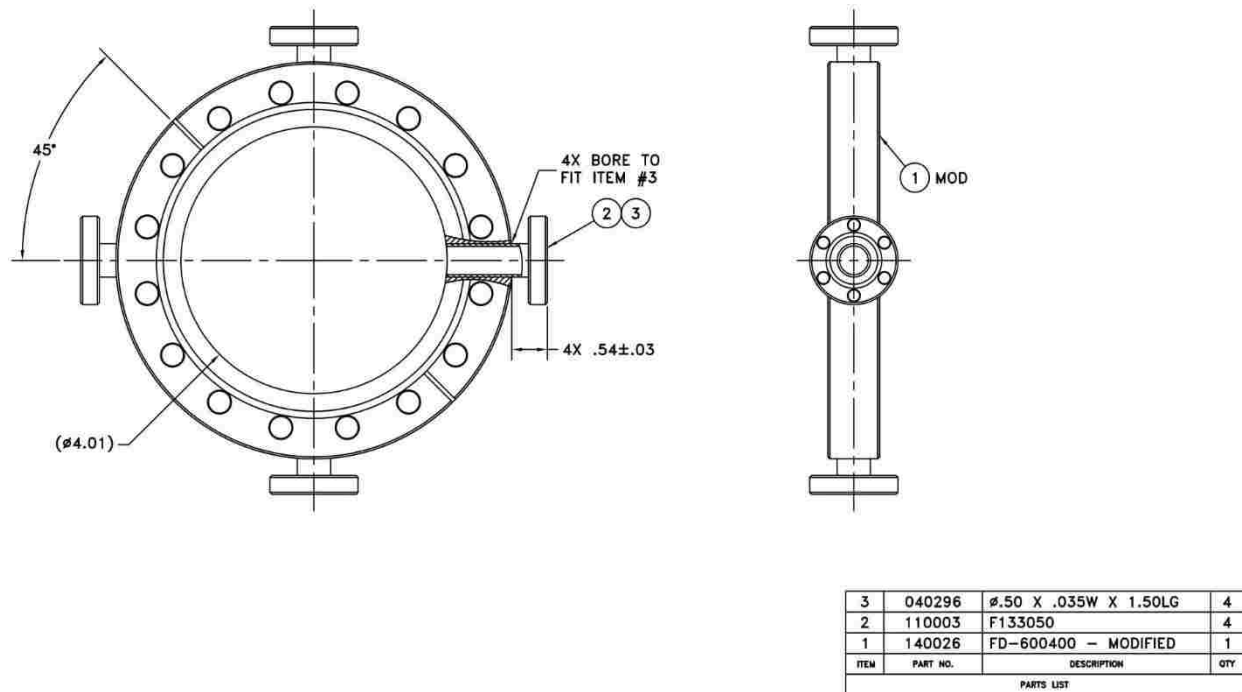


Fig. G.1 AutoCAD drawing of XY deflecting flange.

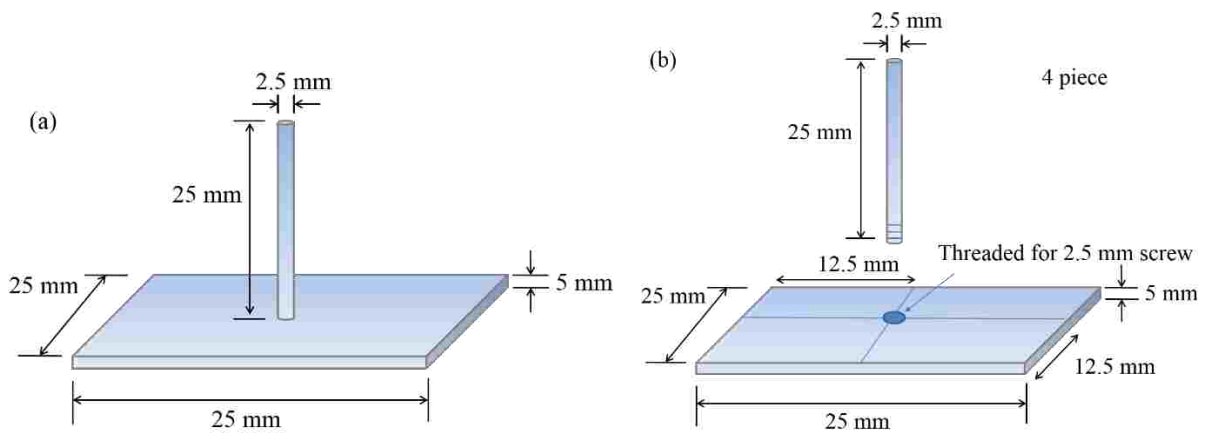


Fig. G.2 (a) assembled deflecting plate design and (b) separate plate and rod.

## APPENDIX H

### ION SELECTION STEPS

The steps to select specific ion using the deflector is as follows:

1. Connect the laser external trigger cable to the pulse generator.
2. Connect the pulse generator to the “high voltage pulsar”.
3. For positive pulse, connect the “positive high voltage input” of the “high voltage pulsar” to the high voltage power supply. Ground the negative high voltage input.
4. Reverse the polarity for negative pulse.
5. Connect the “high voltage output” of the pulsar to the deflecting plates.
6. Select the delay time, pulse width, rise time and fall time in the pulse generator.
7. Apply required voltage of the output pulse in the power supply.
8. Calculate delay time from the TOF equation and select the deflecting voltage pulse width according to the desired ion pulse width.
9. If the obtained TOF signal is noisy, smooth the signal using OriginLab.

## APPENDIX I

### LIST OF VENDORS AND DIFFERENT COMPONENTS USED

<b>Unit description</b>	<b>Part number</b>	<b>Vendor</b>
XYZ manipulator	EMC-B6C-T275T-1.39-2	Thermionic Northwest
Mechanical pump	1201006408	Franklin Electric
Turbo Pump	Varian 250 l/s	Varian
Ion pump	ULTEK D-I 220 l/s	Perkin Elmer
Nickel mesh	70% opening, thickness 100 $\mu\text{m}$ ,	Precision Eforming
Pulse generator	PVX-4110	Directed Energy Incorporated
Aluminum target	99.9 % pure, 0.5 mm thick	Alfa Aesar
Shield box for Faraday cup bias	2392	Digi-key
Oscilloscope	MDO3054C	Tektronix
Current pickup coil	4418	Pearson Electronics Inc.
Pressure monitor	500200-CG	MKS GRANVILLE- PHOLLIPS

**VITA***for***MD HAIDER ALI SHAIM**

mshai001@odu.edu, 757-275-5543,

www.linkedin.com/in/md-haider-shaim

512 Oscar Loop, 202H, Newport News, VA-23606

**EDUCATION**

---

Ph. D. Electrical Engineering, Old Dominion University, Norfolk, VA, 2018

M. S. Applied Physics, University of Chittagong, Chittagong, Bangladesh, 2008

B. Sc. Applied Physics, University of Chittagong, Chittagong, Bangladesh, 2006

**WORK EXPERIENCE**

---

Lecturer, Applied Physics, University of Chittagong, Chittagong, Bangladesh, 2008-2013

**KEY AWARDS**

---

- Meredith Construction Company Scholarship-2017 of \$7614 for excellence.
- ODU-Electrical and Computer Engineering Faculty Award-2016 for excellence.
- Engineering Dean's Graduate Fellowship-2015 of \$18,000 for research achievements.
- SEES travel award from Old Dominion University: AVS 64<sup>th</sup> International Symposium and Exhibition-2017, Tampa, Florida.
- Society of Vacuum Coaters Foundation Scholarship-2014 of \$3500.
- Travel award: SVC TechCON 2014, Chicago, Illinois.
- Travel award: AVS 63<sup>rd</sup> International Symposium and Exhibition-2016, Nashville, Tennessee.
- 3 times poster competition award in AVS Mid-Atlantic Regional Meeting 2015 - 2017, Jefferson Lab, Newport News, Virginia.
- GEC award: Gaseous Electronics Conference-2014, APS, Raleigh, North Carolina.

## REFERRED JOURNAL PUBLICATIONS

---

1. **MHA Shaim**, and HE Elsayed-Ali, "*Generation of B5+ ions from a nanosecond laser plasma*" Vacuum, 154, 32, 2018.
2. **MHA Shaim**, and HE Elsayed-Ali, "*Characterization of laser-generated aluminum plasma using ion time-of flight and optical emission spectroscopy*" Journal of Applied Physics. 122, 2017.
3. **MHA Shaim**, F Wilson, and HE Elsayed-Ali, "*Aluminum Multicharged Ion Generation from femtosecond laser plasma*", Journal of Applied Physics. 121, 185901, 2017
4. **MHA Shaim**, O Balki, MM Rahman, A Sarkissian, M Korwin-Pawlowski, and HE Elsayed-Ali, "*Transport Line Components of a Multicharged Ion Source*", Vacuum, 137 March. 2017.
5. **MHA Shaim**, and HE Elsayed-Ali, "*Spark Discharged Coupled Laser Multicharged Ion Source*", Review of Scientific Instrumentation 86 (7) July 2015.
6. **MHA Shaim**, and HE Elsayed-Ali, "*Aluminum multicharged ion generation from laser plasma*," Nuclear Instruments and Methods B, 356-357, Aug. 2015.
7. **MHA Shaim**, and DK chy, "*Real time Correlation Filter for Optical Particle Counter*". Optical and Quantum Electronics, Springer, 15 (5), May 2013.
8. **MHA Shaim**, and DK chy, "*Development of Online Correlation Filter for Optical Particle Counter*" Journal of Optics, Springer, 41(1), March 2012.

## PRESENTATIONS AND POSTERS

---

1. **MHA Shaim**, MM Rahman, O Balki, and HE Elsayed-Ali, "*Spark-discharge Coupled Laser Multicharged Ion Implantation and Deposition System*," AVS 64th International Symposium & Exhibition, Tampa, Florida, 2017
2. **MHA Shaim**, O Balki, MM Rahman, A Sarkissian, M Korwin-Pawlowski, and HE Elsayed-Ali, "*Transport Line for Laser Multicharged Ion Implantation and Deposition System*", AVS 63rd International Symposium & Exhibition, Nashville Tennessee, 2016.
3. **MHA Shaim**, MM Rahman, O Balki, and HE Elsayed-Ali, "*Transport line Components of a Laser Multicharged Ion Implantation and Deposition System*" AVS Mid-Atlantic Regional Meeting - 2016, Jefferson Lab, Newport news, Virginia.

4. **MHA Shaim**, and HE Elsayed-Ali, “*Aluminum Multicharged Ion Generation Using Spark-Assisted Laser Ion Source*” 16th International Conference on Ion Source-2015, Brookhaven National Laboratory, New York.
5. **MHA Shaim**, and HE Elsayed-Ali, “*Spark-assisted laser aluminum multicharged ion source in an ultra-high vacuum chamber*”, 8th International Workshop on Microplasma-2015, Seton Hall University, Newark, New Jersey.
6. **MHA Shaim**, and HE Elsayed-Ali, “*Enhancement of Aluminum Multicharged Ion Generation Using Spark assisted Laser Ion Source*”, AVS Mid-Atlantic Regional Meeting – 2015, Jefferson Lab, Newport News, Virginia.
7. P Rainey, S Berl, Z Adams, B Bishop, D Jung, **MHA Shaim**, and HE Elsayed-Ali, “*Design of a Multicharged Ion Transport Line and Diagnostic System*”, AVS Mid-Atlantic Regional Meeting - 2014, Jefferson Lab, Newport news, Virginia.
8. **MHA Shaim**, W Chen, A Bugayev, and HE Elsayed-Ali, “*Characterization of Q-Switched Nd:YAG laser Generated Aluminum Multicharged Ions*”, AVS Mid-Atlantic Regional Meeting - 2014, Jefferson Lab, Newport news, VA.
9. **MHA Shaim**, A Bugayev and HE Elsayed-Ali, “*Energy Distribution of Aluminum Multicharged Ions Generated from Laser Plasma*”, 67th Gaseous Electronics Conference-2014, American Physical Society, North Carolina State University, Raleigh, North Carolina.
10. **MHA Shaim**, W Chen, A Bugayev, W Cao, and HE Elsayed-Ali, “*A Laser Multicharged Ion Deposition and Implantation System based on an Ultrahigh Vacuum Pulsed Laser Deposition Chamber*”, Society of Vacuum Coaters TechCon-2014, Chicago, Illinois.
11. KT Ahmmmed, **MHA Shaim**, MKH Majumdar, and H Biswas, “*Automated Energy Saving and Safety System*”, 1st International Conference on Electrical Engineering and Information & Communication Technology-2014, MIST, Dhaka, Bangladesh.
12. **MHA SHAIM** and RH Khan, “*Design and Simulation of a Low Loss Optical Fiber Coupler*”, International Conference on Electronics, Computer and Communication (ICECC - 2008), Rajshahi, Bangladesh.